

000  
 001  
 002 **MULTIPLICATIVE DIFFUSION MODELS:**  
 003 **BEYOND GAUSSIAN LATENTS**  
 004  
 005  
 006

007 **Anonymous authors**  
 008 Paper under double-blind review  
 009  
 010  
 011

012 **ABSTRACT**  
 013  
 014  
 015  
 016  
 017  
 018  
 019  
 020  
 021  
 022  
 023  
 024  
 025  
 026  
 027  
 028  
 029  
 030  
 031  
 032

We introduce a new class of generative models based on multiplicative score-driven diffusion. In contrast to classical diffusion models that rely on additive Gaussian noise, our construction is driven by skew-symmetric multiplicative noise. It yields conservative forward-backward dynamics inspired by the principles of physics. We prove that the forward process converges exponentially fast to a tractable non-Gaussian latent distribution, and we characterize this limit explicitly. A key property of our diffusion is that it preserves the distribution of data norms, resulting in a latent space that is inherently data-aware. Unlike the standard Gaussian prior, this structure better adapts to heavy-tailed and anisotropic data, providing a closer match between latent and observed distributions. On the algorithmic side, we derive the reverse-time stochastic differential equation and associated probability flow, and show that sliced score matching furnishes a consistent estimator for the backward dynamics. This estimation procedure is equivalent to maximizing an evidence lower bound (ELBO), bridging our framework with established variational principles. Empirically, we demonstrate the advantages of our model in challenging settings, including correlated Cauchy distributions and experimental fluid dynamics images ( $d = 1024$ ). Across these tasks, our approach more accurately captures extreme events and tail behavior than classical diffusion models, particularly in the low-data regime. Our results suggest that multiplicative conservative diffusions open a principled alternative to current score-based generative models, with strong potential for domains where rare but critical events dominate.

033  
 034 **1 INTRODUCTION**  
 035  
 036

037 athematically equivalent (Song et al., 2021), diffusion models and score-based generative models  
 038 demonstrate impressive skills and are among the current state-of-the-art for the generation of two-  
 039 and three-dimensional images. Unconditioned sampling scores can be easily modified to conditioned  
 040 sampling scores to address various inverse problems (Rybchuk et al., 2023; Rozet & Louppe, 2023;  
 041 Daras et al., 2024; Bao et al., 2025). However, both learning and inference come with significant  
 042 computational costs. In addition, even with large computational power, the generation of rare and  
 043 extreme events remains a difficult task (Li et al., 2024; Stamatelopoulos & Sapsis, 2025). Those  
 044 generative AI challenges may be more easily addressed by introducing physical-based inductive bias  
 045 in the fully-data-driven approaches. In this paper, we take inspiration from physics and its conservative  
 046 structure to build a multiplicative score-based generative model. It is inspired by transport noises in  
 047 fluid dynamics (Kraichnan, 1968; Brzežniak et al., 1991; Klyatskin, 1994; Piterbarg & Ostrovskii,  
 048 1997; Mikulevicius & Rozovskii, 2004; Mémin, 2014; Holm, 2015; Resseguier et al., 2021; Zhen  
 049 et al., 2023) and, more generally, from slow-fast systems with multiplicative noise (Majda et al.,  
 050 1999; Franzke et al., 2005; Gottwald & Melbourne, 2013; Gottwald & Harlim, 2013). Transport noise  
 051 models may be understood as generative models based on stochastic fluid dynamics rather than fitted  
 052 neural networks. As other generative models, they suit particularly well to Bayesian inverse problems  
 053 (Cotter et al., 2020b;a; Resseguier et al., 2022; Dufée et al., 2022).

Here, we might address problems outside the scope of fluid dynamics, though keeping the conservative structure of transport noise. The noising and denoising procedures that we propose maintain a part of

054 the data information: the distribution of norm of the data point. The latent distribution is hence both  
 055 tractable and close to the data distribution. ore specifically, our contributions are the following.  
 056

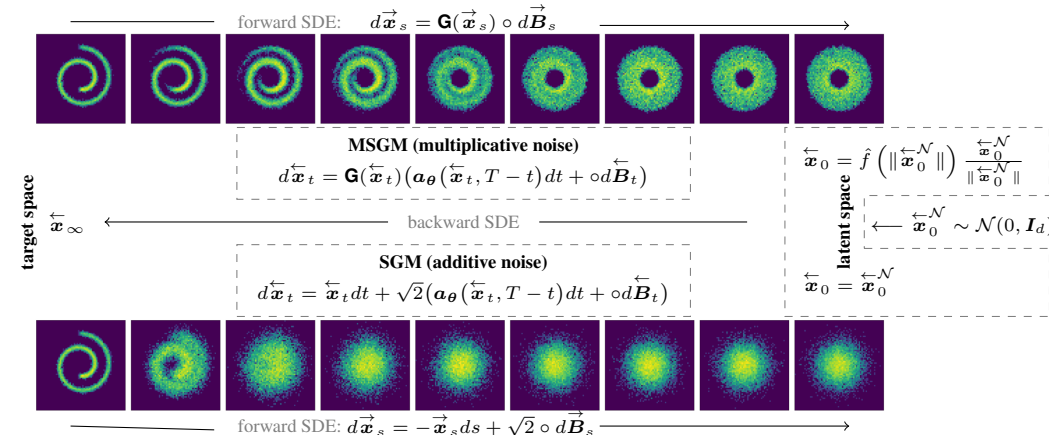
057 **New generative model paradigm:** We introduce a new type of diffusion model where the noising  
 058 process is multiplicative. We call it a Multiplicative Score-based Generative Model (MSGM).  
 059 Involving random rotations around the origin, it greatly differs from previous diffusion models and  
 060 opens a new research path. The key aspects are summarized in Figure 1.

061 **Deep theoretical analysis of MSGM:** Assuming a skew-symmetric structure and a rank condition  
 062 for this noise, we proved several theoretical results, guiding the use of this new generative tool. The  
 063 first theorem provides the Fokker-Planck equation of forward diffusion and its invariant measures.  
 064 Then, we separately analyze the norm and direction of the diffusion. The norm is steady, whereas the  
 065 direction follows a similar multiplicative stochastic differential equation (SDE). Two other theorems  
 066 show that distributions of the direction and thus of the whole diffusion converge exponentially fast to  
 067 a white noise in the weak sense. Asymptotically, the norm and direction are independent, and the  
 068 latter is uniformly distributed over the  $d$ -sphere.

069 **General algorithm for MSGM:** We propose to estimate the scaled diffusion score by a neural  
 070 network using sliced score matching, and our last theorem shows that it is equivalent to maximizing  
 071 the ELBO. Sampling the non-Gaussian latent vectors reduces to a one-dimensional problem that we  
 072 address with eCDF. For the denoising process, both SDE and ordinary differential equation (ODE)  
 073 formulations are proposed.

074 **Application to extremes in moderate dimension:** We propose a numerical procedure to mimic  
 075 the heavy-tail distribution with MSGM. We add a first layer to the neural network to perform a  
 076 spherical decomposition with log-norm, and the latent distribution is characterized by the law of  
 077 the data log-norm. Compared numerically with a standard diffusion model, MSGM better mimics  
 078 multidimensional Cauchy distributions and measured fluid vorticity. The proximity between latent  
 079 and data distributions facilitates the forward and the backward diffusions, and implicitly encompasses  
 080 the correct distribution tail decays.

081 **Application in high dimension:** As a first step, we focus on MSGM scalability and design of sparse  
 082 underlying tensors in the diffusion. While the latter is not covered completely by the theoretical  
 083 analysis, our numerical experiments show promising image generation results.



103 Figure 1: Illustration of multiplicative score-based generative modeling (ours) compared to additive  
 104 score-based generative modeling.

108 

## 2 ADDITIVE SCORE-BASED GENERATIVE MODEL

109 

### 2.1 FORWARD AND BACKWARD SDEs

110 Diffusion models or score-based generative models (SGM) can be expressed in continuous time with  
111 stochastic differential equation (SDE) (Song et al., 2021). The forward SDE is

112 
$$d\vec{\mathbf{x}}_s = -\vec{\mathbf{x}}_s ds + \sqrt{2}d\vec{\mathbf{B}}_s, \quad (2.1)$$

113 where  $\vec{\mathbf{x}}_s \in \mathbb{R}^d$  is distributed according to some density  $p_s$  for  $s > 0$ ,  $s \mapsto \vec{\mathbf{B}}_s$  is  $d$ -dimensional  
114 Brownian motion, and  $\vec{\mathbf{x}}_0$  distributed according to the dataset of interest. It is an Ornstein-Uhlenbeck  
115 process: the continuous-time version of a first-order autoregressive (AR) model and the distribution  
116  $p_s$  converges to a standard Gaussian density exponentially for  $s \rightarrow \infty$ , e.g. in total variation or  
117 Wasserstein distance. We can then define for  $t \in [0, T]$  the backward equation

118 
$$d\overleftarrow{\mathbf{x}}_t = \overleftarrow{\mathbf{x}}_t dt + 2\nabla \log p_{T-t}(\overleftarrow{\mathbf{x}}_t) dt + \sqrt{2}d\overleftarrow{\mathbf{B}}_t, \quad (2.2)$$

119 with  $t \mapsto \overleftarrow{\mathbf{B}}_t$  another  $d$ -dimensional Brownian motion and  $\overleftarrow{\mathbf{x}}_0 \sim p_T$  (identifying the density  $p_T$   
120 with its distribution). Then for any  $s \in [0, T]$ ,  $\overleftarrow{\mathbf{x}}_{T-s}$  and  $\vec{\mathbf{x}}_s$  have the same law  $p_s$ . In practice, when  
121 an approximate score  $\nabla \log p_{T-t}$  is available we initialize equation 2.2 with a standard Gaussian  
122 distribution  $\overleftarrow{\mathbf{x}}_0 \sim \mathcal{N}(0, I_d)$  and integrate the backward SDE from  $t = 0$  to  $t = T$  (i.e. from  $s = T$   
123 to  $s = 0$ ), ideally letting  $\overleftarrow{\mathbf{x}}_T$  become statistically similar to our dataset of interest.124 

### 2.2 A NEURAL NETWORK TO FIT THE SCORE

125 In practice, the score  $\nabla \log p_{T-t}(\mathbf{x})$  is approximated by a surrogate model,  $\mathbf{s}_\theta(\mathbf{x}, T-t)$ , e.g., a fitted  
126 artificial neural network (ANN). Alternatively, one can work on  $\mathbf{a}_\theta(\mathbf{x}, T-t) = \sqrt{2}\mathbf{s}_\theta(\mathbf{x}, T-t)$   
127 (Huang et al., 2021). For large-dimensional problems, Song et al. (2020) proposes to learn this neural  
128 network by *Sliced Score Matching* (SSM). Here,  $\mathbf{a}_\theta$  is obtained by minimizing the loss function

129 
$$\mathcal{L}_{\text{SSM}}^{\text{SGM}}(\theta) = \int_0^T \mathbb{E}_{\vec{\mathbf{x}}_s} \mathbb{E}_{\mathbf{v} \sim \text{Rad}(d)} \left[ \frac{1}{2} \|\mathbf{a}_\theta(\vec{\mathbf{x}}_s, s)\|^2 + (\mathbf{v} \cdot \nabla)((\sqrt{2}\mathbf{a}_\theta(\vec{\mathbf{x}}_s, s) - \vec{\mathbf{x}}_s) \cdot \mathbf{v}) \right] ds. \quad (2.3)$$

130 where  $\|\cdot\|$  is the Euclidean norm,  $\text{Rad}(d)$  denotes the  $d$ -dimensional Rademacher distribution and  
131  $\mathbb{E}_{\vec{\mathbf{x}}_s}$  is the expectation along each path realization  $\vec{\mathbf{x}}_s$ . Appendix A details the most common score  
132 matching losses and their link to the concept of the Evidence Lower Bound (ELBO).133 

## 3 MULTIPLICATIVE SCORE-BASED GENERATIVE MODEL

134 Rather than relying on additive SDE equation 2.1, we propose a multiplicative SDE and the associated  
135 score-based generative model. Taking inspiration from physics, this approach introduces physical-  
136 based inductive bias and yields tractable latent distributions closer to the dataset distribution. In  
137 this section, we introduce our forward SDE based on skew-symmetric multiplicative noise, its  
138 corresponding latents, and backward SDE and analyze the limit properties of the process distribution.  
139 To share didactic similarities of the forward and backward processes as in the additive noise case, we  
140 will keep the same notation for the forward process  $\vec{\mathbf{x}}_s$  and the backward process  $\overleftarrow{\mathbf{x}}_s$ , respectively.141 

### 3.1 FORWARD SDE

142 Instead of considering a forward SDE with additive noise, we rely on *multiplicative noise model*

143 
$$d\vec{\mathbf{x}}_s = \mathbf{G}(\vec{\mathbf{x}}_s) \circ d\vec{\mathbf{B}}_s, \quad (3.1)$$

144 where  $d \geq 2$ ,  $\mathbf{G} : \mathbb{R}^d \rightarrow \mathbb{R}^{d \times d}$  is linear and  $\circ$  stands for the *Stratonovich* notation. The readers  
145 unfamiliar with this notation may interpret the Stratonovich noise  $s \mapsto \circ d\vec{\mathbf{B}}_s$  as a process with short  
146 correlation time but respecting the usual rules of differential calculus – says the chain rule. The  
147 discretized version of equation 3.1 – with an infinitely small time step  $ds$  – may also provide insight:

148 
$$\frac{1}{2}(\vec{\mathbf{x}}_{s+ds} - \vec{\mathbf{x}}_{s-ds}) = \mathbf{G}(\vec{\mathbf{x}}_s) \frac{1}{2}(\vec{\mathbf{B}}_{s+ds} - \vec{\mathbf{B}}_{s-ds}). \quad (3.2)$$

For deeper understanding, Appendix B recalls some important notions of stochastic calculus, including the Stratonovich notation and the relationship to Itô calculus. Let  $\mathbf{G}$  be represented by a third-order tensor  $[\mathbf{G}_{i,j}^k] \in \mathbb{R}^{d,d,d}$  and define the random matrix  $\mathbf{Z}_s = \sum_{k=1}^d \mathbf{G}^k (\vec{\mathbf{B}}_s)_k$ . Then, equation 3.1 can be written more explicitly as:

$$d\vec{\mathbf{x}}_s = \sum_{k=1}^d (\mathbf{G}^k \vec{\mathbf{x}}_s) (\circ d\vec{\mathbf{B}}_s)_k = \sum_{k=1}^d \mathbf{G}^k (\circ d\vec{\mathbf{B}}_s)_k \vec{\mathbf{x}}_s = \circ d\mathbf{Z}_s \vec{\mathbf{x}}_s \approx \frac{1}{2} (\mathbf{Z}_{s+ds} - \mathbf{Z}_{s-ds}) \vec{\mathbf{x}}_s, \quad (3.3)$$

where the time increments of the random matrix,  $\circ d\mathbf{Z}_s \approx \frac{1}{2} (\mathbf{Z}_{s+ds} - \mathbf{Z}_{s-ds})$ , are uncorrelated.

Additionally, we will impose two assumptions valid throughout the paper:

Skew-symmetry : For any  $k \in \{1, \dots, d\}$ , the matrix  $\mathbf{G}^k = (\mathbf{G}_{i,j}^k)_{i,j}$  is skew-symmetric. (A1)

Rank condition : For any  $\mathbf{x} \in \mathbb{R}^d \setminus \{0\}$ ,  $\text{rank}(\mathbf{G}(\mathbf{x})) = d - 1$ . (A2)

In particular equation 3.1 does not describe a geometric Brownian motion, as the noise term  $\mathbf{Z}_s$  is not diagonal. It includes zeros on the diagonal due to the skew-symmetry of  $\mathbf{G}^k$ . A geometric Brownian motion would necessitates  $\mathbf{Z}_s = \text{diag}(\vec{\mathbf{B}}_s)$ . A strategy to obtain a tensor  $\mathbf{G}$  that matches assumptions A1 and A2 will be discussed in Section 6. By linearity, the skew-symmetry of all  $\mathbf{G}^k$  (assumption A1) implies the skew-symmetry of the whole multiplicative noise matrix  $\circ d\mathbf{Z}_s$ . This structure is inspired by transport noises in fluid dynamics (Kraichnan, 1968; Piterbarg & Ostrovskii, 1997; Resseguier et al., 2021). In this analogy,  $\vec{\mathbf{x}}_s$  would represent an image of temperature, advected by an incompressible fluid flow. Incompressibility leads to the skew-symmetry of the advection operator, and eventually to energy conservation of  $\vec{\mathbf{x}}_s$ . Here, we might address problems outside the scope of fluid dynamics, though maintaining the noise skew-symmetry (assumption A1) and thus the energy conservation, as discussed in Section 3.2.

With assumption A2, the noise spreads in a large space:  $\text{Im}(\mathbf{G}(\vec{\mathbf{x}}_s)) = \vec{\mathbf{x}}_s^\perp$ . It ensures sufficient variability in the noising process and, in turn, a tractable distribution for  $\vec{\mathbf{x}}_T$  when  $T$  becomes large.

**Theorem 3.1.1.** *Let the assumptions A1 and A2 hold. Then, the Fokker-Planck equation of equation 3.1 reads*

$$\frac{\partial}{\partial s} p_s(\mathbf{x}) = \nabla_\perp \cdot \left( \frac{1}{2} \Sigma(\mathbf{x}) \nabla_\perp p_s(\mathbf{x}) \right), \quad \mathbf{x} \in \mathbb{R}^d, \quad (3.4)$$

with conditional noise covariance  $\Sigma(\mathbf{x}) := \mathbf{G}(\mathbf{x}) \mathbf{G}(\mathbf{x})^\top$  and  $\nabla_\perp$  denoting the orthogonal projection of nabla  $\nabla$  on the tangent plane  $\mathbf{x}^\perp$ , i.e.

$$\nabla_\perp := (\mathbf{I}_d - \mathbf{x}^n(\mathbf{x}^n)^\top) \nabla, \quad (3.5)$$

for  $\mathbf{x}^n := \mathbf{x} / \|\mathbf{x}\|$  with  $\mathbf{x} \in D := \mathbb{R}^d \setminus \{0\}$  and 0 otherwise, the unit vector orthogonal to the  $d$ -sphere. Moreover, any stationary density  $p_\infty$  of equation 3.4 is rotation-invariant on  $\mathbb{R}^d$ .

The proof is detailed in Appendix D.2. In order to highlight the connection to diffusion models on Riemannian manifolds, we note that  $\nabla_\perp$  is the Riemannian gradient on the unit  $d$ -sphere:  $\mathbb{S}^{d-1} = \{\mathbf{x} \in \mathbb{R}^d \mid \|\mathbf{x}\| = 1\}$ , see Appendix H.1. For a possible extension of the considered diffusion equation 3.1 to the case of non-zero drift, we refer to section D.6.

### 3.2 DYNAMICS OF NORM AND DIRECTION

We now consider for any  $s \geq 0$  and  $\vec{\mathbf{x}}_s \neq 0$ , the spherical decomposition

$$\vec{\mathbf{x}}_s = \|\vec{\mathbf{x}}_s\| \vec{\mathbf{x}}_s^n \quad \text{with} \quad \vec{\mathbf{x}}_s^n := \vec{\mathbf{x}}_s / \|\vec{\mathbf{x}}_s\| \in \mathbb{S}^{d-1}. \quad (3.6)$$

First, we note that the norm,  $\|\vec{\mathbf{x}}_s\|$ , remains constant throughout the noising process. Indeed, the skew-symmetry of  $\circ d\mathbf{Z}_s$  implies that  $d\vec{\mathbf{x}}_s = \circ d\mathbf{Z}_s \vec{\mathbf{x}}_s$  is orthogonal to  $\vec{\mathbf{x}}_s$  and hence:

$$d\|\vec{\mathbf{x}}_s\|^2 = 2\vec{\mathbf{x}}_s \cdot \circ d\vec{\mathbf{x}}_s = 0, \quad \forall s \geq 0. \quad (3.7)$$

Consequently,  $\|\vec{\mathbf{x}}_s\| \equiv \|\vec{\mathbf{x}}_0\|$ . The vector  $\vec{\mathbf{x}}_s$  moves randomly on  $\|\vec{\mathbf{x}}_0\| \mathbb{S}^{d-1}$ , the  $d$ -sphere of radius  $\|\vec{\mathbf{x}}_0\|$ . Therefore, the distribution of the norms of the latent variable is exactly the distribution of

216 the norms of the points of the dataset. We refer to Appendix D.3 for more details. This property  
 217 will have important consequences for our learning procedure and on the possibility of generating  
 218 extreme events. **Indeed, the property of likely large norm events will be conserved along the diffusion.**  
 219 In particular, the norm distribution is one-dimensional and we can rely on advanced techniques  
 220 available for this setup, without worrying about the curse of dimensionality. In practice, we will  
 221 fit the distribution of the log-norm,  $F_{\log|\cdot|_\epsilon}$ , with eCDF. We refer to Appendix C for details and an  
 222 overview of sampling from one-dimensional distributions.

223 We now focus on  $p_s^n$ , the distribution of the direction,  $\vec{x}_s^n$ , in particular as  $s \rightarrow \infty$ . For better  
 224 readability, we postpone the full discussion and the main theorems to Appendix D.4. Lemma D.4.1  
 225 introduces the Fokker-Planck equation of the direction on  $\mathbb{S}^{d-1}$  and its unique invariant measure,  
 226  $p_\infty^n$ . Then, Theorem D.4.2 shows the exponential convergence of the initial distribution  $p_0^n$  to  $p_\infty^n$ ,  
 227 the uniform distribution on the unit sphere  $\mathbb{S}^{d-1}$ . Consequently, since  $\mathbb{S}^{d-1}$  is compact, this implies  
 228 convergence in total variation of  $p_s^n$  to  $p_\infty^n$  and convergence in distribution of  $\vec{x}_s^n$  to  $\vec{x}_\infty^n \sim \mathcal{U}(\mathbb{S}^{d-1})$ .  
 229

### 230 3.3 NON-GAUSSIAN LATENT SPACE

232 In this section, we characterize the generally non-Gaussian latent distribution. Although this sounds  
 233 intractable at first glance, it will turn out that we can easily sample it.

234 In general, the latent space of MSGM is not Gaussian. It becomes Gaussian if and only if the  
 235 distribution of the squared norms of the dataset points has  $\chi^2$  distributions with  $d$  degrees of freedom  
 236 (see Appendix E.2). This property differs from the usual SGM. SGM latent variables are Gaussian,  
 237 leading to  $\chi^2$  distributions for the norms of the latent variables regardless of the data set. According  
 238 to Lafon et al. (2023), without a heavy tail distribution for the latent variables, it is unlikely that the  
 239 final samples will be generated with a heavy tail distribution, at least with **variational autoencoders**  
 240 (**VAE**). With our approach, the distribution of the norms of the latent variables has heavy tails if  
 241 and only if the distribution of the norms of dataset points has heavy tails. Therefore, we expect a  
 242 significant improvement from our method in generating extreme events. In fact, for heavy-tailed data  
 243 the KL divergence to the SGM latent distribution is infinite, whereas MSGM yields a finite value,  
 244 see Appendix E.6. ore generally, Appendix E.5 shows that the KL divergence from data to the latent  
 245 distribution is always smaller under MSGM than SGM. So, only few time steps may be sufficient to  
 246 integrate the forward and the backward MSGM diffusions. In any case, the MSGM latent vectors  
 247 are still white noise in the weak sense (see Appendix E.1). Moreover, the norm and direction are  
 248 independent from each other, which will drastically facilitate the sampling procedure. These results  
 249 hold for latent vectors  $\vec{x}_\infty \sim p_\infty$ . In practice, integrations of forward and backward diffusions are  
 250 only possible over a finite time  $T$ . However, the following theorem states that the law of the solution,  
 251  $\vec{x}_T$ , will become close to  $p_\infty$  exponentially as fast as  $T \rightarrow +\infty$ . So, we can confidently rely on  
 252 finite-time integration.

253 **Theorem 3.3.1.** *Let assumptions A1 and A2 hold. Let  $\vec{x}_0 \sim p_0 \in \mathcal{C}^2(D)$  and let  $p_{|\cdot|}$  be the (radial)  
 254 density of  $\|\vec{x}_0\|$ . Then, the Fokker-Planck equation 3.4 has a unique solution  $p_s \in \mathcal{C}^2(D) \cap L^2(D)$   
 255 for all  $s > 0$ . Moreover, the Fokker-Planck equation has the stationary distribution*

$$256 \quad p_\infty(\mathbf{x}) = \frac{p_{|\cdot|}(\|\mathbf{x}\|)}{\|\mathbf{x}\|^{d-1}} \frac{1}{|\mathbb{S}^{d-1}|}. \quad (3.8)$$

259 *In particular,  $\|\vec{x}_s\|$  and  $\vec{x}_s^n$  are asymptotically independent for  $s \rightarrow +\infty$ . oreover, there exists  
 260  $\alpha = \alpha(\mathbf{G}, d) > 0$  such that*

$$261 \quad \|p_s - p_\infty\|_{L^2(\mathbb{R}^d)}^2 \leq \exp(-\alpha s) \|p_0 - p_\infty\|_{L^2(\mathbb{R}^d)}^2. \quad (3.9)$$

263 The proof and details on  $\alpha$  are given in Appendix D.5 and a specific case is discussed in Appendix J.3.  
 264 The factor  $\|\mathbf{x}\|^{1-d}$  in equation 3.8 is expected. Indeed,  $\frac{|\mathbb{S}^{d-1}|}{\|\mathbf{x}\|^{1-d}}$  is the volume of the scaled  $d$ -sphere  
 265  $\|\mathbf{x}\|\mathbb{S}^{d-1}$ , i.e. it corresponds to the uniform distribution on the scaled  $d$ -sphere  $\|\mathbf{x}\|\mathbb{S}^{d-1}$ .

266 We will now consider the practical question on how to draw samples from the latent distribution  
 267 with density  $\rho_\infty$  from equation 3.8. It is of product structure between the radial and the directional  
 268 component. So, we can sample the norm  $R_\infty$  and the direction  $\vec{x}_\infty^n$  separately and multiply them. The

270 norm  $R_\infty$  can be sampled from an one-dimensional approximation of the data norm (see Appendix C)  
 271 and the direction  $\vec{x}_\infty^n$  is uniform. So, we can sample a  $\vec{x}_\infty^n \sim \mathcal{N}(0, I_d)$  and set  
 272

$$273 \quad \vec{x}_\infty = R_\infty \vec{x}_\infty^n \quad \text{with} \quad \vec{x}_\infty^n = \vec{x}_\infty / \|\vec{x}_\infty\|, \quad R_\infty = \hat{f}(\|\vec{x}_\infty\|), \quad (3.10)$$

$$274 \quad \text{and} \quad \hat{f}(r) := \exp\left(\hat{F}_{\log|\cdot|_\epsilon}^{-1}(F_{\chi^2(d)}(r^2))\right) - \epsilon, \quad \forall r > 0. \quad (3.11)$$

277 If  $\vec{x}_\infty^n = 0$ , we set  $\vec{x}_\infty = 0$ . Proposition E.3.2 shows that this procedure leads to samples with the  
 278 correct distribution, up to the approximation of the log-norm CDF  $\hat{F}_{\log|\cdot|_\epsilon} \approx F_{\log|\cdot|_\epsilon}$ . oreover, the  
 279 direct map  $\hat{F}_{\log|\cdot|_\epsilon}$  can transform a latent vector,  $\vec{x}_T$ , into a Gaussian one (see Appendix E.4). This  
 280 transformation may be useful for future applications like inverse problems or time evolution fittings.  
 281

### 282 3.4 REVERSE ODE/SDE AND SCORE MATCHING

283 From the Itô forward SDE (see [Lemma D.1.2](#)), we know that the Stratonovich reverse SDE writes  
 284

$$285 \quad d\vec{x}_t = \mathbf{G}(\vec{x}_t) \left( \mathbf{G}(\vec{x}_t)^\top \nabla \log p_{T-t}(\vec{x}_t) dt + \circ d\vec{B}_t \right), \quad (3.12)$$

286 and the reverse probability flow ODE is given as  
 287

$$288 \quad \frac{d\vec{x}_t}{dt} = \frac{1}{2} \mathbf{G}(\vec{x}_t) \left( \mathbf{G}(\vec{x}_t)^\top \nabla \log p_{T-t}(\vec{x}_t) \right). \quad (3.13)$$

289 The corresponding [derivations](#) are formulated in Proposition F.1 and Proposition F.2 and are proven in  
 290 the appendix using Anderson (1982); Song et al. (2021). Following Huang et al. (2021), we directly  
 291 model  $\mathbf{G}(\vec{x}_t)^\top \nabla \log p_{T-t}(\vec{x}_t)$  by a neural network  $\mathbf{a}_\theta(\vec{x}_t, T-t)$ . Additionally, we incorporate a  
 292 spherical input layer, see Appendix L.4.1. We fit the parameters  $\theta$  by sliced score matching (SSM)  
 293 (Song et al., 2020), because in the multiplicative case we do not have an analytic formula for the  
 294 conditional score  $\nabla \log p_s(\vec{x}_s | \vec{x}_0)$  and because of the better scalability of SSM to high-dimensional  
 295 problems that we would like to address in the future. To this end, we minimize the loss function:  
 296

$$297 \quad \mathcal{L}_{\text{SSM}}(\theta) = \mathbb{E}_{s \sim \mathcal{U}[0, T]} \mathbb{E}_{\vec{x}_s} \mathbb{E}_{\mathbf{v} \sim \text{Rad}(d)} \left[ \frac{1}{2} \|\mathbf{a}_\theta(\vec{x}_s, s)\|^2 + (\mathbf{v} \cdot \nabla)(\mathbf{G}(\vec{x}_s) \mathbf{a}_\theta(\vec{x}_s, s)) \cdot \mathbf{v} \right], \quad (3.14)$$

300 where  $\text{Rad}(d)$  denotes the Rademacher distribution in  $\mathbb{R}^d$ . The following theorem states that even  
 301 in our multiplicative case, score matching is equivalent to maximize the ELBO,  $\mathcal{E}_\infty$ . [In line with](#)  
 302 [Benton et al. \(2024\); Ren et al. \(2025\)](#), this theorem generalizes the result of Huang et al. (2021) and  
 303 gives a theoretical justification for our score-matching loss equation 3.14. [The derivation of this loss](#)  
 304 [from the ELBO below is detailed in Appendix G.7](#).

305 **Theorem 3.4.1.** *Let assumption A1 holds. Then, there exists a constant  $C$  such that*

$$306 \quad p_0(\mathbf{x}) \geq \mathcal{E}_\infty(\mathbf{x}) := C - \int_0^T \mathbb{E}_{\vec{x}_s} \left[ \frac{1}{2} \|\mathbf{a}_\theta(\vec{x}_s, s)\|^2 + \nabla \cdot (\mathbf{G}(\vec{x}_s) \mathbf{a}_\theta(\vec{x}_s, s)) \middle| \vec{x}_0 = \mathbf{x} \right] ds. \quad (3.15)$$

313 We proof this theorem in Appendix G. The first term  $C := \mathbb{E} \left[ \log p_T(\vec{x}_T) | \vec{x}_0 = \mathbf{x} \right]$  is a constant  
 314 w.r.t. to  $\theta$ . So, it has no effect on the optimization procedure. Therefore, even with our multiplicative  
 315 noise, the minimization of the ELBO corresponds precisely to Implicit Score Matching (ISM), which  
 316 is itself equivalent to explicit score matching (ESM), denoising score matching (DSM), and SSM  
 317 (Huang et al., 2021). [Note that formally replacing  \$\mathbf{G}\$  by  \$\sqrt{2}\$ , we get the SGM SSM loss. For an easier](#)  
 318 [numerical comparison in Section 6, we will also rely on SSM to train our baseline SGM.](#)  
 319

## 320 4 WORKFLOW

321 Algorithm 1 summarizes the proposed MSGM procedure. Here we make use of [color](#) to highlight the  
 322 differences compared to SGM. For more details, we refer to Appendix L.

324

**Algorithm 1: MSGM (Multiplicative Score-Based Generative Model).**

325

---

326 **Input:** tensor  $\mathbf{G}$ , one-dimensional distribution model  $\hat{f}_\gamma$ , data  $\{\vec{\mathbf{x}}_0^m\}_{m=1}^M$ ,  $t_\epsilon$ , time horizon  $T$ , time  
 327 steps  $N_T^f$  and  $N_T^b$ , time scheduler  $g$ , score model  $\mathbf{a}_\theta$ , initial ANN parameter  $\theta_0$ , iterations  $N_{\text{iter}}$

328 **— Training stage —**

329 1:  $\gamma^* \leftarrow \text{fit\_distribution}(\hat{f}_\gamma, \{\|\vec{\mathbf{x}}_0^m\|\}_{m=1}^M)$  {Fitting of  $\hat{f}_\gamma$ , see Appendix C}

330 2: **for**  $n = 0$  to  $N_{\text{iter}} - 1$  **do**

331 3:  $\vec{\mathbf{x}}_0 \sim \frac{1}{M} \sum_{m=1}^M \delta_{\vec{\mathbf{x}}_0^m}$  {Random mini-batch from dataset}

332 4:  $s \sim \mathcal{U}(I(t_\epsilon, T))$  {Sample uniform gridded time}

333 5:  $\vec{\mathbf{x}}_s \leftarrow \text{SRK4}(s, \lfloor \frac{s}{T} N_T^f \rfloor, \vec{\mathbf{x}}_0, 0, g\mathbf{G})$  {Forward diffusion integration via Algorithm 2}

334 6:  $\mathbf{v} \sim \text{Rad}(d)$  {Slicing directions}

335 7:  $\ell(\theta_n) \leftarrow \mathcal{L}_{\text{SSM}}^{\text{MSGM}}(s, \vec{\mathbf{x}}_s, \mathbf{G}, g\mathbf{a}_{\theta_n}, \mathbf{v})$  {Score-matching loss, from equation 3.14}

336 8:  $\theta_{n+1} \leftarrow \text{optimizer\_update}(\theta_n, \ell(\theta_n))$  {e.g. via ADAM}

337 9: **end for**

338 10:  $\theta^* \leftarrow \theta_{N_{\text{iter}}}$  {Set final ANN parameter}

339 **— Generative sampling stage —**

340 11:  $\overset{\leftarrow}{\mathbf{x}}_0 \sim \mathcal{N}(0, \mathbf{I}_d)$  {Sample strong white noise}

341 12:  $\overset{\leftarrow}{\mathbf{x}}_0 = \hat{f}_{\gamma^*} \left( \left\| \overset{\leftarrow}{\mathbf{x}}_0 \right\| \right) \frac{\overset{\leftarrow}{\mathbf{x}}_0}{\left\| \overset{\leftarrow}{\mathbf{x}}_0 \right\|}$  {Sample weak white noise, see equation 3.11}

342 13:  $\overset{\leftarrow}{\mathbf{x}}_T \leftarrow \text{SRK4}(T, N_T^b, \overset{\leftarrow}{\mathbf{x}}_0, g\mathbf{G}\mathbf{a}_{\theta^*}, g\mathbf{G})$  {Reverse diffusion integration via Algorithm 2}

343 14: **return**  $\gamma^*, \theta^*, \overset{\leftarrow}{\mathbf{x}}_T$

---

344

345

346

## 5 RELATED WORKS

347

348

349 Combining machine learning and mechanistic approaches is now a common approach. We may cite  
 350 physics-informed neural networks (PINNs) (Raissi et al., 2019; Lu & Xu, 2024), physics-based prior  
 351 covariance (Beauchamp et al., 2025; Clarotto et al., 2024), deep augmentation (Holzschuh et al.,  
 352 2023; Fan et al., 2025), neural Galerkin (Lee & Carlberg, 2020; Chen et al., 2021; Romor et al.,  
 353 2023; Finzi et al., 2023; Bruna et al., 2024; Kim et al., 2022), and **chaos from energy-based models**  
 354 (Fournier & Pierfrancesco, 2025) among others. Here, we shall focus on score-based generative  
 355 models. Bastek et al. (2024) add the physical equations inside their score matching loss. Holzschuh  
 356 et al. (2023) fit a score to correct a backward physical equation but does not propose any generative  
 357 model. To denoise corrupted images, several authors (e.g. Zhou et al., 2014; Shan et al., 2022;  
 358 Guha & Acton, 2023) encode the multiplicative structure of speckle noise. Since this noise is not  
 359 correlated between pixels, this approach strongly differs from ours. Most of these works do not  
 360 deal with score or generative models. Guha & Acton (2023); Ren et al. (2025); Shetty et al. (2025)  
 361 do, but their framework simplifies to SGM by considering the pixel-wise logarithm of images. Guth  
 362 et al. (2022); Lempereur & Mallat (2024) encode a target multiscale structure (e.g. turbulence) by a  
 363 hierarchy of normalized wavelets conditioned by the larger scales. Chen & Vanden-Eijnden (2025)  
 364 adapt the noise to that multiscale structure in a stochastic interpolant context. Lobbe et al. (2023;  
 365 2025) replaced the Gaussian process involved in the transport-noise equations (Kraichnan, 1968;  
 366 Piterbarg & Ostrovskii, 1997; Resseguier et al., 2021) by a Shrodinger bridge (De Bortoli et al., 2021).  
 367 They inserted a SGM inside a transport noise dynamics, whereas we inserted a dynamics similar  
 368 to transport noise inside a SGM. Following general Bayesian approaches, some of the literature on  
 369 transport-noise relies on the Girsanov theorem to fit a drift modification or evaluate a likelihood  
 370 (Cotter et al., 2020a; Singh et al., 2025)(see Appendix G.9). By extending the ELBO of (Huang et al.,  
 371 2021) to SDEs inspired by transport noise, Theorem 3.4.1 justifies our fit of the backward SDE drift.

372

373

374

375

376

377

Several authors have recently proposed Langevin equations (Arnaudon et al., 2019; Luesink & Street, 2025; Ayala et al., 2025) and SGM (De Bortoli et al., 2022; Huang et al., 2022; Lou et al., 2023; Benton et al., 2024) on Riemannian manifolds in order to generate data lying on a particular manifold. Clearly different, our goal is more classical: generating data in  $\mathbb{R}^d$ . In our work, neither data nor their noisy versions are restricted to a single manifold. However, each solution path of our forward and backward SDE lies on its particular Riemannian manifold, the scaled  $d$ -sphere  $\|\vec{\mathbf{x}}_0\| \mathbb{S}^{d-1}$ . De Bortoli et al. (2022) describes diffusions and SGM in the  $d$ -sphere  $\mathbb{S}^{d-1}$ . A detailed comparison is given in Appendix H.

378 Regarding extremes generation, using variational autoencoders (VAE), Lafon et al. (2023) argue  
 379 that Gaussian latent restricts the generated samples to light-tail distributions. Accordingly,  
 380 they propose to use fat-tailed latent distributions (see also Jaini et al. (2020); Huster  
 381 et al. (2021) for normalizing flows (NF) and generative adversarial models (GAN) respectively).  
 382 Yoon et al. (2023); Shariati et al.; Pandey et al. (2024); Ren et al. (2025) proposed SGMs with ad  
 383 hoc heavy-tailed (Lévy and Student- $t$ ) latent distributions. Our approach automatically makes the  
 384 tails of the latent distribution fat when necessary. It learns it from the distribution of the data norm,  
 385  $p_{\|\cdot\|}$ . Similarly, the diffusion proposed by Dharmakeerthi et al. (2025) adapt to data but through a  
 386 nonlinear drift and an additive noise. Li et al. (2024); Price et al. (2025); Stamatelopoulos & Sapsis  
 387 (2025) and references therein show that the usual SGM may correctly represent extremes, especially  
 388 in "interpolation mode", that is, when extremes lie on the interior of the dataset but have difficulties  
 389 with extremes lying on the dataset boundaries. Our numerical experiments in Section 6 suggest that  
 390 our method probably overcomes this limitation. To represent the directionality of extremes, many  
 391 authors decompose norms and directions of extreme events (Engelke et al., 2019; Palacios-Rodríguez  
 392 et al., 2020; Lafon et al., 2023; Naveau & Segers, 2024). Large-amplitude criterion (e.g. exceeding a  
 393 high threshold) or fat-tail model can be applied on the norm. Extreme directions may or may not  
 394 become asymptotically independent of their magnitude (Engelke et al., 2019; Lafon et al., 2023).  
 395 Build on random rotations, MSGM naturally suggests such a polar decomposition. The extreme  
 396 direction of the MSGM latent vector is asymptotically independent of its magnitude. However, the  
 397 direction of the reverse process does depend on the magnitude (see Appendix H.2).

## 398 6 EXPERIMENTS

400 For our numerical experiments, we choose to define a tensor  $\mathbf{G}^k$  in a simple way. We sample  $d$   
 401 random matrices, keep only their skew-symmetric parts, and normalize:

$$402 \quad \mathbf{G} = \frac{\sqrt{d}}{\|\mathbf{G}\|_2} \tilde{\mathbf{G}} \quad \text{with} \quad \tilde{G}_{i,j}^k = \frac{1}{2}(M_{i,j}^k - M_{j,i}^k) \quad \text{and} \quad M_{i,j}^k \stackrel{iid}{\sim} \mathcal{N}(0, 1). \quad (6.1)$$

404 In Appendix J we show that this random tensor  $\mathbf{G}$  respects conditions A1 and A2 almost surely.  
 405 Appendix K proposes alternative tensor definitions with sparse structures that allow high-dimensional  
 406 applications. Following Appendix K.2.2, MSGM can generate images as in Appendix M.6.2. For the  
 407 test cases below, we also checked in Appendix M.6.2 and Appendix M.6.1 that the MSGM generation  
 408 skills are equivalent with these sparse and dense tensors. However, these sparse tensors do not match  
 409 the framework of Section 3.1 so we postpone the associated numerical evaluations to future works.  
 410

### 411 6.1 MULTIVARIATE CAUCHY DISTRIBUTION

413 We first illustrate our method with a vector of Cauchy variables,  $\mathbf{x}_{\text{Ca}}$ , with scale parameter  $\gamma$ :

$$414 \quad (x_{\text{Ca}})_i \stackrel{iid}{\sim} p_{\text{Ca}} \quad \text{with} \quad p_{\text{Ca}}(x) := \frac{\gamma/\pi}{x^2 + \gamma^2}. \quad (6.2)$$

417 It is an extreme case of fat-tailed distributions with a power-law tail:  $p_{\text{Ca}}(x) \propto |x|^{-2}$  for large  $|x|$ .  
 418 Real problems often involve both correlation and dimensionality  $d > 2$ . So, we correlate Cauchy  
 419 variables, as  $\mathbf{x}_0 = \mathbf{A}\mathbf{x}_{\text{Ca}}$ , with a fixed matrix,  $\mathbf{A}$ , initialized with i.i.d. coefficients  $A_{i,j} \sim \mathcal{N}(0, 1)$ .  
 420 Figure 2 confirms that, for  $d = 4$ , SGM hardly reproduces fat tails and extreme directionality, unlike  
 421 MSGM. An explanation is the strong dissimilarity between the data distribution and the latent SGM  
 422 distribution; see Appendix E.5 and Appendix E.6. For a larger number of ADAMS iterations, MSGM  
 423 becomes more accurate, whereas SGM diverges (see Figure 4a). For plots, numerical comparisons,  
 424 and experiments with variants of the state-of-the-art SGM can be found in Appendix M.6.1.

### 425 6.2 MEASURED VORTICITY FIELDS

427 We also test our algorithm on fluid dynamics experimental data: small images of vorticity fields.  
 428 These fields are two-dimensional curl of fluid velocity measured by Particle Image Velocimetry (PIV)  
 429 in wind tunnels. Vorticity quantifies the local rotation speed of fluid and is known to have point-  
 430 wise distributions with tails fatter than Gaussian ones (Wilczek & Friedrich, 2009). We focus on a  
 431 benchmark fluid flow: a wake flow at Reynolds number 3900 created by a circular cylinder embedded  
 in a mean stream (Parnaudeau et al., 2008). Each vorticity sample is evaluated at  $d = 16$  spatial

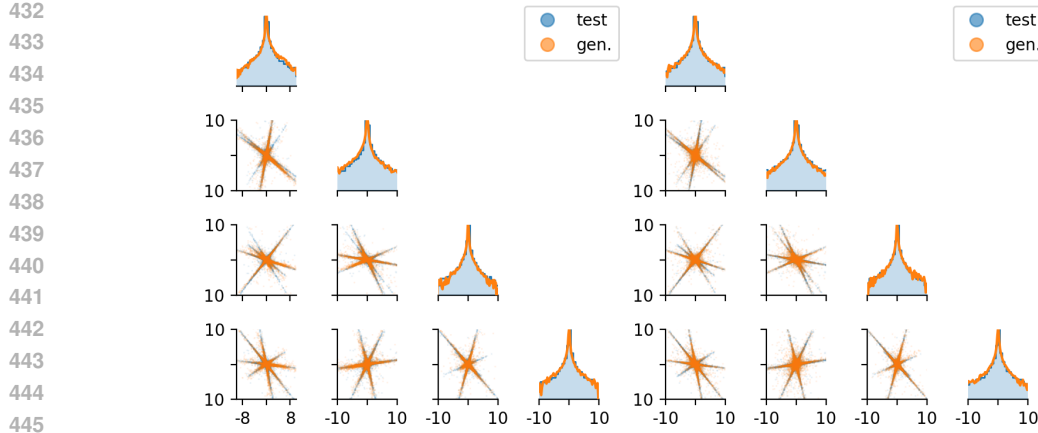


Figure 2: Pair plots of generated data (orange lines and dots) compared to ground truth data (blue lines and dots) with the SGM (left) and MSGM (right) for a vector of 4 correlated Cauchy variables. On the diagonal, log-histogram and logarithm of the pdf KDE estimation are superimposed.

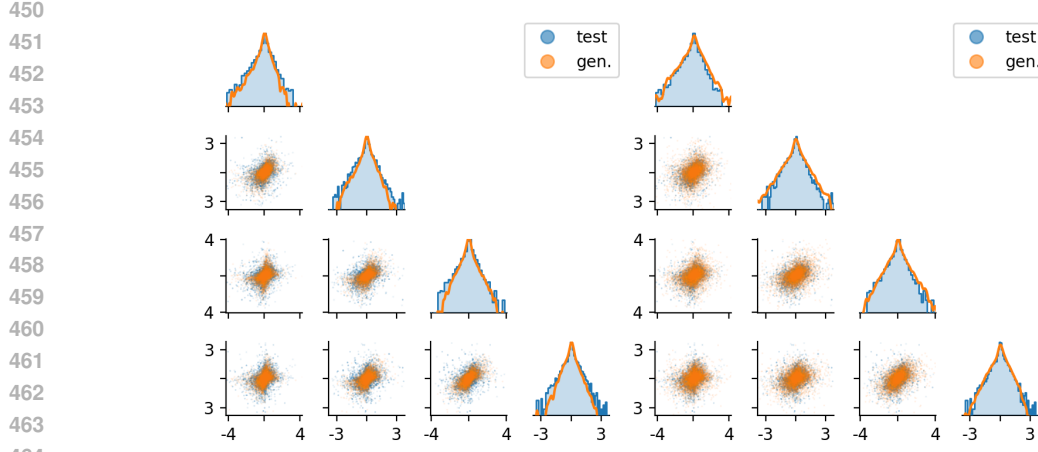
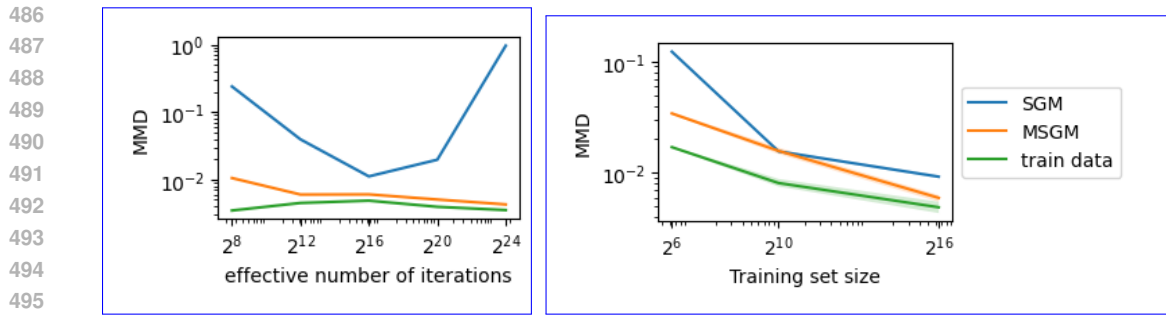


Figure 3: Pair plots of generated data (orange lines and dots) compared to ground truth data (blue lines and dots) with the SGM (left) and MSGM (right) trained on 1024 16-dimensional measured vorticity fields. On the diagonal, log-histogram and logarithm of the pdf KDE estimation are superimposed.

points to ensure low dimensionality. We use limited training data (1024 data points) to make rare events even more rare and learning more challenging. Appendix M.7 provides a deeper description of this experimental dataset. Figure 3 highlights a larger concentration of points generated by SGM in the center of the ground truth distribution. Accordingly, the tails of the marginals – i.e. the tails of the vorticity point-wise distributions – are underestimated : SGM underestimates rare large vorticity events. SGM performs better since the MSGM latent distribution – easy to learn – is much closer to the data distribution than SGM latent distribution, as theoretically suggested by Appendix E.5 and experimentally verified in Appendix M.7. In particular, the MSGM latent distribution seems to have Laplace tails and to be more accurate in the low-data regime (see Figure 4). Additional we carried out high-dimensional experiments with  $d = 1024$  in Appendix M.6.2 based on sparse tensor  $G$  developed in Appendix K. More details on data, preprocessing, illustrations, and other numerical experiments are given in Appendix M.

## 7 CONCLUSION AND DISCUSSION

We have proposed a new type of diffusion model with multiplicative noise. After a theoretical analysis of this ansatz, an algorithm is specified to mimic fat-tailed distributions, surpassing SGM in this task.



(a) Single MMD value for the correlated Cauchy distribution ( $d = 4$ ) as a function of the number of effective ADAMS iterations.

(b) Mean and 80% CI of MMD for the vorticity measurements distribution ( $d = 16$ ) as a function of the number of training samples.

Figure 4: Convergence behaviors of the Maximum Mean Discrepancy (MMD) for two different test cases.  $10^4$  samples are used for each MMD evaluation.

At this point, limitations of the general MSGM framework may be difficult to know. We rather discuss the limitations of the first numerical procedure applied in Section 6. First, the forward SDE has to be integrated numerically since we do not know an analytic solution for [large-rank tensors](#) (see [Appendix I](#) for the solution [with low-rank tensors](#)). It implies either a slower training or a reduced number of iterations compared to SGM. Moreover, we do not know of any analytic solution for the score in finite time. This prevents the use of DSM and force us to use ISM or SSM, a less stable approach. In the next future, we can hope that the active communities of generative models on symmetric Riemannian manifolds and, more generally, of stochastic differential geometry could come up with more efficient sampling algorithms and score evaluation procedures for our diffusions on  $d$ -spheres. In addition, random matrix theory and free probabilities (Biane, 1997; Delyon & Yao, 2006; Demni, 2008; Lévy, 2008; Delyon, 2010; Demni & Hmidi, 2012; Cébron, 2014) may provide alternative sampling methods and helpful results for large-dimension cases. Indeed, for some choices of  $\mathbf{G}$ , the semigroup of our forward SDE may be expressed as a unitary Brownian matrix, converging for large dimensions to a free multiplicative Brownian matrix. Both theories could facilitate the sampling and the score evaluation of the MSGM forward diffusion. Moreover, a dense third-order tensor  $\mathbf{G}$  prevents image processing and other large-dimensional applications, related to, say, turbulent fluid dynamics. In fact, dimensions  $d$  of such problems are very large – typically  $d = O(10^5)$  or more. A dense tensor  $\mathbf{G}$  as we use in our numerical experiments has  $d^3$  coefficients, and the memory and computational costs would become prohibitive in these cases. To address this issue, [Appendix K](#) proposes several sparse tensors and alternative to assumptions A1 and A2. [Appendix M.6.2](#) shows first MSGM generated images in dimension  $d = 1024$ . Furthermore, we are currently developing physics-based sparse tensors  $\mathbf{G}$ . Here, MSGM forward SDE is the spatial discretization of a stochastic partial differential equation involving transport noises (Kraichnan, 1968; Piterbarg & Ostrovskii, 1997; Resseguier et al., 2021). We expect that the physical inductive bias will facilitate both inference and learning, especially in low-data mode. Alternatively, the rank assumption A2 may be expressed more simply with the algebraic properties of  $\mathbf{G}$ , eventually producing simple examples of sparse and efficient tensors.

In addition to the improvements discussed above, many paths remain to be explored. First, our theoretical results could be generalized to other multiplicative diffusions. We have considered [dense](#) linear maps  $\mathbf{x} \mapsto \mathbf{G}(\mathbf{x})$  with  $\text{Im}(\mathbf{G}(\mathbf{x})) = \mathbf{x}^\perp$  for any  $\mathbf{x} \neq 0$ . We believe that [sparse](#) linear maps of [Appendix K](#) and non-linear Lipschitz-continuous maps can yield [similar](#) theoretical results as long as that image condition is fulfilled [for almost every](#)  $\mathbf{x} \in \mathbb{R}^d$  (see [Appendix K.1](#)). The non-linear case would include in particular sphere-wise diffusions of De Bortoli et al. (2022) (see [Appendix H.2](#)). Second, we could address dynamical system forecasting. With the Gaussianization of MSGM latent vectors (see [Appendix E.4](#)) complex nonlinear dynamics could simplify to uncoupled one-dimensional linear dynamics as in Arbab & Sapsis (2022). A third path to explore involves Bayesian inverse problems and data assimilation (Rozet & Louppe, 2023; Bao et al., 2025). Finally, [our analytic solution issue could be bypassed by a normalizing flow approach](#): spherical decomposition, stochastic interpolants and flow along scaled  $d$ -spheres, taking inspiration from normalizing flow along Riemannian manifolds (e.g., Gemici et al., 2016; Mathieu & Nickel, 2020; Wu et al., 2025).

540 REFERENCES  
541

542 Ronald J Adrian and Jerry Westerweel. *Particle image velocimetry*. Number 30. Cambridge university  
543 press, 2011.

544 Brian DO Anderson. Reverse-time diffusion equation models. *Stochastic Processes and their  
545 Applications*, 12(3):313–326, 1982.

546 Hassan Arbabi and Themistoklis Sapsis. Generative stochastic modeling of strongly nonlinear flows  
547 with non-gaussian statistics. *SIAM/ASA Journal on Uncertainty Quantification*, 10(2):555–583,  
548 2022.

549 Alexis Arnaudon, Alessandro Barp, and So Takao. Irreversible langevin mcmc on lie groups. In  
550 *Geometric Science of Information: 4th International Conference, GSI 2019, Toulouse, France,  
551 August 27–29, 2019, Proceedings 4*, pp. 171–179. Springer, 2019.

552 Ludwig Arnold. *Stochastic differential equations: theory and applications*. Wiley, 1974.

553 Mario Ayala, Nicolas Dirr, Grigorios A Pavliotis, and Johannes Zimmer. Reversibility, covariance  
554 and coarse-graining for langevin dynamics: On the choice of multiplicative noise. *arXiv preprint  
555 arXiv:2511.03347*, 2025.

556 Feng Bao, Hristo G Chipilski, Siming Liang, Guannan Zhang, and Jeffrey S Whitaker. Nonlinear  
557 ensemble filtering with diffusion models: Application to the surface quasigeostrophic dynamics.  
558 *Monthly Weather Review*, 153(7):1155–1169, 2025.

559 Jan-Hendrik Bastek, WaiChing Sun, and Dennis M Kochmann. Physics-informed diffusion models.  
560 *arXiv preprint arXiv:2403.14404*, 2024.

561 Maxime Beauchamp, Ronan Fablet, Simon Benaichouche, Pierre Tandeo, Nicolas Desassis, and  
562 Bertrand Chapron. Neural variational data assimilation with uncertainty quantification using spde  
563 priors. *Artificial Intelligence for the Earth Systems*, 4(3):240060, 2025.

564 Joe Benton, Yuyang Shi, Valentin De Bortoli, George Deligiannidis, and Arnaud Doucet. From  
565 denoising diffusions to denoising markov models. *Journal of the Royal Statistical Society Series B:  
566 Statistical Methodology*, 86(2):286–301, 2024.

567 Philippe Biane. Free brownian motion, free stochastic calculus and random matrices. *Free probability  
568 theory (Waterloo, ON, 1995)*, 12:1–19, 1997.

569 Joan Bruna, Benjamin Peherstorfer, and Eric Vanden-Eijnden. Neural galerkin schemes with active  
570 learning for high-dimensional evolution equations. *Journal of Computational Physics*, 496:112588,  
571 2024.

572 Zdzisław Brzeźniak, Marek Capiński, and Franco Flandoli. Stochastic partial differential equations  
573 and turbulence. *Mathematical Models and Methods in Applied Sciences*, 1(01):41–59, 1991.

574 Francesco Paolo Cantelli. Sulla determinazione empirica delle leggi di probabilita. *Giorn. Ist. Ital.  
575 Attuari*, 4(421–424), 1933.

576 Guillaume Cébron. *Processes on the unitary group and free probability*. PhD thesis, Université Pierre  
577 et Marie Curie-Paris VI, 2014.

578 Yanlai Chen, Sigal Gottlieb, Lijie Ji, and Yvon Maday. An eim-degradation free reduced basis method  
579 via over collocation and residual hyper reduction-based error estimation. *Journal of Computational  
580 Physics*, 444:110545, 2021.

581 Yifan Chen and Eric Vanden-Eijnden. Scale-adaptive generative flows for multiscale scientific data.  
582 *arXiv preprint arXiv:2509.02971*, 2025.

583 Lucia Clarotto, Denis Allard, Thomas Romary, and Nicolas Desassis. The spde approach for  
584 spatio-temporal datasets with advection and diffusion. *Spatial Statistics*, pp. 100847, 2024.

594 Colin Cotter, Dan Crisan, Darryl Holm, Wei Pan, and Igor Shevchenko. Data assimilation for a quasi-  
 595 geostrophic model with circulation-preserving stochastic transport noise. *Journal of Statistical*  
 596 *Physics*, 179(5):1186–1221, 2020a.

597

598 Colin Cotter, Dan Crisan, Darryl D Holm, Wei Pan, and Igor Shevchenko. A particle filter for  
 599 stochastic advection by lie transport: a case study for the damped and forced incompressible two-  
 600 dimensional euler equation. *SIAM/ASA Journal on Uncertainty Quantification*, 8(4):1446–1492,  
 601 2020b.

602 Colin J Cotter, Dan Crisan, and Maneesh Kumar Singh. Data assimilation for the stochastic camassa-  
 603 holm equation using particle filtering: a numerical investigation. In *Stochastic Transport in Upper*  
 604 *Ocean Dynamics Annual Workshop*, pp. 137–160. Springer Nature Switzerland Cham, 2023.

605 Giannis Daras, Hyungjin Chung, Chieh-Hsin Lai, Yuki Mitsufuji, Jong Chul Ye, Peyman Milanfar,  
 606 Alexandros G Dimakis, and Mauricio Delbracio. A survey on diffusion models for inverse problems.  
 607 *arXiv preprint arXiv:2410.00083*, 2024.

608

609 Valentin De Bortoli, James Thornton, Jeremy Heng, and Arnaud Doucet. Diffusion schrödinger  
 610 bridge with applications to score-based generative modeling. *Advances in Neural Information*  
 611 *Processing Systems*, 34:17695–17709, 2021.

612 Valentin De Bortoli, Emile Mathieu, Michael Hutchinson, James Thornton, Yee Whye Teh, and  
 613 Arnaud Doucet. Riemannian score-based generative modelling. *Advances in Neural Information*  
 614 *Processing Systems*, 35:2406–2422, 2022.

615

616 Bernard Delyon. Concentration inequalities for the spectral measure of random matrices. *Electronic*  
 617 *Communications in Probability*, 15:549–562, 2010.

618

619 Bernard Delyon and Jian-Feng Yao. On the spectral distribution of gaussian random matrices. *Acta*  
 620 *Mathematicae Applicatae Sinica*, 22(2):297–312, 2006.

621

622 Nizar Demni. Free jacobi process. *Journal of Theoretical Probability*, 21(1):118–143, 2008.

623

624 Nizar Demni and Taoufik Hmidi. Spectral distribution of the free unitary brownian motion: another  
 625 approach. In *Séminaire de Probabilités XLIV*, pp. 191–206. Springer, 2012.

626

627 Prafulla Dhariwal and Alexander Nichol. Diffusion models beat gans on image synthesis. *Advances*  
 628 *in neural information processing systems*, 34:8780–8794, 2021.

629

630 Kulunu Dharmakeerthi, Yousef El-Laham, Henry H Wong, Vamsi K Potluru, Changhong He, and  
 631 Taosong He. Beyond linear diffusions: Improved representations for rare conditional generative  
 632 modeling. *arXiv preprint arXiv:2510.02499*, 2025.

633

634 Benjamin Dufée, Etienne Mémin, and Dan Crisan. Stochastic parametrization: An alternative to  
 635 inflation in ensemble kalman filters. *Quarterly Journal of the Royal Meteorological Society*, 148  
 636 (744):1075–1091, 2022.

637

638 Sebastian Engelke, Thomas Opitz, and Jennifer Wadsworth. Extremal dependence of random scale  
 639 constructions. *Extremes*, 22(4):623–666, 2019.

640

641 Xiantao Fan, Deepak Akhare, and Jian-Xun Wang. Neural differentiable modeling with diffusion-  
 642 based super-resolution for two-dimensional spatiotemporal turbulence. *Computer Methods in*  
 643 *Applied Mechanics and Engineering*, 433:117478, 2025.

644

645 Marc Anton Finzi, Andres Potapczynski, Matthew Choptuik, and Andrew Gordon Wilson. A  
 646 stable and scalable method for solving initial value pdes with neural networks. In *The Eleventh*  
 647 *International Conference on Learning Representations*, 2023.

648

649 Samantha J. Fournier and Urbani Pierfrancesco. Generative modeling through internal high-  
 650 dimensional chaotic activity. *Physical Review E*, 111.4:045304, 2025.

651

652 Christian Franzke, Andrew Majda, and Eric Vanden-Eijnden. Low-order stochastic mode reduction  
 653 for a realistic barotropic model climate. *Journal of the atmospheric sciences*, 62(6):1722–1745,  
 654 2005.

648 Avner. Friedman. *Partial differential equations of parabolic type*. Prentice-Hall, Englewood Cliffs,  
 649 N.J, 1964.  
 650

651 Mevlana C Gemici, Danilo Rezende, and Shakir Mohamed. Normalizing flows on riemannian  
 652 manifolds. *arXiv preprint arXiv:1611.02304*, 2016.

653 Valery Glivenko. Sulla determinazione empirica delle leggi di probabilita. *Gion. Ist. Ital. Attauri.*, 4:  
 654 92–99, 1933.

655

656 Fabián González, O Deniz Akyildiz, Dan Crisan, and Joaquín Míguez. Nudging state-space models  
 657 for bayesian filtering under misspecified dynamics: F. gonzález et al. *Statistics and Computing*, 35  
 658 (4):112, 2025.

659 Georg Gottwald and John Harlim. The role of additive and multiplicative noise in filtering complex  
 660 dynamical systems. *Proceedings of the Royal Society A: Mathematical, Physical and Engineering*  
 661 *Science*, 469(2155):20130096, 2013.

662

663 Georg Gottwald and Ian Melbourne. Homogenization for deterministic maps and multiplicative noise.  
 664 *Proceedings of the Royal Society of London A: Mathematical, Physical and Engineering Sciences*,  
 665 469(2156), 2013.

666

667 Georg Gottwald, Daan Crommelin, and Christian Franzke. Stochastic climate theory. In *Nonlinear*  
 668 *and Stochastic Climate Dynamics*. Cambridge University Press, 2015.

669 Arthur Gretton, Karsten M Borgwardt, Malte J Rasch, Bernhard Schölkopf, and Alexander Smola. A  
 670 kernel two-sample test. *The journal of machine learning research*, 13(1):723–773, 2012.

671

672 Soumee Guha and Scott T Acton. Sddpm: Speckle denoising diffusion probabilistic models. *arXiv*  
 673 *preprint arXiv:2311.10868*, 2023.

674

675 Florentin Guth, Simon Coste, Valentin De Bortoli, and Stephane Mallat. Wavelet score-based  
 676 generative modeling. *Advances in neural information processing systems*, 35:478–491, 2022.

677

678 Darryl Holm. Variational principles for stochastic fluid dynamics. *Proceedings of the Royal Society*  
 679 *of London A: Mathematical, Physical and Engineering Sciences*, 471(2176), 2015.

680

681 Benjamin Holzschuh, Simona Vegetti, and Nils Thuerey. Solving inverse physics problems with  
 682 score matching. *Advances in Neural Information Processing Systems*, 36, 2023.

683

684 Elton P Hsu. *Stochastic analysis on manifolds*. Number 38. American Mathematical Soc., 2002.

685

686 Chin-Wei Huang, Jae Hyun Lim, and Aaron C Courville. A variational perspective on diffusion-based  
 687 generative models and score matching. *Advances in Neural Information Processing Systems*, 34:  
 688 22863–22876, 2021.

689

690 Chin-Wei Huang, Milad Aghajohari, Joey Bose, Prakash Panangaden, and Aaron C Courville.  
 691 Riemannian diffusion models. *Advances in Neural Information Processing Systems*, 35:2750–2761,  
 692 2022.

693

694 Todd Huster, Jeremy Cohen, Zinan Lin, Kevin Chan, Charles Kamhoua, Nandi O Leslie, Cho-  
 695 Yu Jason Chiang, and Vyas Sekar. Pareto gan: Extending the representational power of gans to  
 696 heavy-tailed distributions. In *International Conference on Machine Learning*, pp. 4523–4532.  
 697 PMLR, 2021.

698

699 Aapo Hyvärinen and Peter Dayan. Estimation of non-normalized statistical models by score matching.  
 700 *Journal of Machine Learning Research*, 6(4), 2005.

701

Priyank Jaini, Ivan Kobyzev, Yaoliang Yu, and Marcus Brubaker. Tails of lipschitz triangular flows.  
 In *International Conference on Machine Learning*, pp. 4673–4681. PMLR, 2020.

Youngkyu Kim, Youngsoo Choi, David Widemann, and Tarek Zohdi. A fast and accurate physics-  
 informed neural network reduced order model with shallow masked autoencoder. *Journal of*  
*Computational Physics*, 451:110841, 2022.

702 Peter E Kloeden, Eckhard Platen, Peter E Kloeden, and Eckhard Platen. *Stochastic differential*  
 703 *equations*. Springer, 1992.  
 704

705 Valerii I Klyatskin. Statistical description of the diffusion of a passive tracer in a random velocity  
 706 field. *Physics-Uspekhi*, 37(5):501, 1994.  
 707

708 Robert Kraichnan. Small-scale structure of a scalar field convected by turbulence. *Physics of Fluids*  
 709 (1958-1988), 11(5):945–953, 1968.  
 710

711 Hiroshi Kunita. *Stochastic flows and stochastic differential equations*, volume 24. Cambridge  
 712 university press, 1997.  
 713

714 Nicolas Lafon, Philippe Naveau, and Ronan Fablet. A vae approach to sample multivariate extremes.  
 715 *arXiv preprint arXiv:2306.10987*, 2023.  
 716

717 John M Lee. *Introduction to Riemannian manifolds*, volume 2. Springer, 2018.  
 718

719 Kookjin Lee and Kevin T Carlberg. Model reduction of dynamical systems on nonlinear manifolds  
 720 using deep convolutional autoencoders. *Journal of Computational Physics*, 404:108973, 2020.  
 721

722 Etienne Lempereur and Stéphane Mallat. Hierarchic flows to estimate and sample high-dimensional  
 723 probabilities. *arXiv preprint arXiv:2405.03468*, 2024.  
 724

725 Thierry Lévy. Schur–weyl duality and the heat kernel measure on the unitary group. *Advances in*  
 726 *Mathematics*, 218(2):537–575, 2008.  
 727

728 Tianyi Li, Luca Biferale, Fabio Bonacorso, Martino Andrea Scapolini, and Michele Buzzicotti.  
 729 Synthetic lagrangian turbulence by generative diffusion models. *Nature Machine Intelligence*, 6  
 730 (4):393–403, 2024.  
 731

732 Alexander Lobbe, Dan Crisan, and Oana Lang. Generative modelling of stochastic rotating shallow  
 733 water noise. In *Stochastic Transport in Upper Ocean Dynamics Annual Workshop*, pp. 1–23.  
 734 Springer Nature Switzerland Cham, 2023.  
 735

736 Alexander Lobbe, Dan Crisan, and Oana Lang. Bayesian inference for geophysical fluid dynamics  
 737 using generative models. *Philosophical Transactions A*, 383(2299):20240321, 2025.  
 738

739 Aaron Lou, Minkai Xu, Adam Farris, and Stefano Ermon. Scaling riemannian diffusion models.  
 740 *Advances in Neural Information Processing Systems*, 36:80291–80305, 2023.  
 741

742 Yulong Lu and Wuzhe Xu. Generative downscaling of pde solvers with physics-guided diffusion  
 743 models. *Journal of Scientific Computing*, 101(3):1–23, 2024.  
 744

745 Erwin Luesink and Oliver D Street. Symplectic techniques for stochastic differential equations on  
 746 reductive lie groups with applications to langevin diffusions. *arXiv preprint arXiv:2504.02707*,  
 747 2025.  
 748

749 Calvin Luo. Understanding diffusion models: A unified perspective. *arXiv preprint arXiv:2208.11970*,  
 750 2022.  
 751

752 Andrew Majda, Ilya Timofeyev, and Eric Vanden-Eijnden. Models for stochastic climate prediction.  
 753 *Proceedings of the National Academy of Sciences*, 96(26):14687–14691, 1999.  
 754

755 Emile Mathieu and Maximilian Nickel. Riemannian continuous normalizing flows. *Advances in*  
 756 *neural information processing systems*, 33:2503–2515, 2020.  
 757

758 Etienne Mémin. Fluid flow dynamics under location uncertainty. *Geophysical & Astrophysical Fluid*  
 759 *Dynamics*, 108(2):119–146, 2014. doi: 10.1080/03091929.2013.836190.  
 760

761 Remigijus Mikulevicius and Boris Rozovskii. Stochastic Navier–Stokes equations for turbulent flows.  
 762 *SIAM Journal on Mathematical Analysis*, 35(5):1250–1310, 2004.  
 763

764 Robb J Muirhead. *Aspects of multivariate statistical theory*. John Wiley & Sons, 2009.  
 765

756 Philippe Naveau and Johan Segers. Multivariate extreme value theory. *arXiv preprint*  
 757 *arXiv:2412.18477*, 2024.

758

759 Bernt Oksendal. *Stochastic differential equations*. Springer-Verlag, 1998.

760

761 Fátima Palacios-Rodríguez, Gwladys Toulemonde, Julie Carreau, and Thomas Opitz. Generalized  
 762 pareto processes for simulating space-time extreme events: an application to precipitation  
 763 reanalyses. *Stochastic Environmental Research and Risk Assessment*, 34:2033–2052, 2020.

764

765 Kushagra Pandey, Jaideep Pathak, Yilun Xu, Stephan Mandt, Michael Pritchard, Arash Vahdat, and  
 766 Morteza Mardani. Heavy-tailed diffusion models. *arXiv preprint arXiv:2410.14171*, 2024.

767

768 Philippe Parnaudeau, Johan Carlier, Dominique Heitz, and Eric Lamballais. Experimental and  
 769 numerical studies of the flow over a circular cylinder at reynolds number 3900. *Physics of fluids*,  
 20(8), 2008.

770

771 Leonid Piterbarg and Alexander Ostrovskii. *Advection and Diffusion in Random Media: Implications  
 for Sea Surface Temperature Anomalies*. Springer Science & Business Media, 1997.

772

773 Ilan Price, Alvaro Sanchez-Gonzalez, Ferran Alet, Tom R Andersson, Andrew El-Kadi, Dominic  
 774 Masters, Timo Ewalds, Jacklynn Stott, Shakir Mohamed, Peter Battaglia, et al. Gencast: Diffusion-  
 775 based ensemble forecasting for medium-range weather. In *105th Annual AMS Meeting 2025*,  
 776 volume 105, pp. 449275, 2025.

777

778 Maziar Raissi, Paris Perdikaris, and George E Karniadakis. Physics-informed neural networks: A  
 779 deep learning framework for solving forward and inverse problems involving nonlinear partial  
 differential equations. *Journal of Computational physics*, 378:686–707, 2019.

780

781 Yinuo Ren, Grant M Rotskoff, and Lexing Ying. A unified approach to analysis and design of  
 782 denoising markov models. *arXiv preprint arXiv:2504.01938*, 2025.

783

784 Valentin Resseguier. Maximum likelihood estimation of subgrid flows from tracer image sequences.  
 785 In *Stochastic Transport in Upper Ocean Dynamics Annual Workshop*, pp. 269–285. Springer  
 Nature Switzerland Cham, 2023.

786

787 Valentin Resseguier, Long Li, Gabriel Jouan, Pierre Dérian, Etienne Mémin, and Bertrand Chapron.  
 788 New trends in ensemble forecast strategy: uncertainty quantification for coarse-grid computational  
 789 fluid dynamics. *Archives of Computational Methods in Engineering*, 28:215–261, 2021.

790

791 Valentin Resseguier, Matheus Ladvig, and Dominique Heitz. Real-time estimation and prediction  
 792 of unsteady flows using reduced-order models coupled with few measurements. *Journal of  
 Computational Physics*, 471:111631, 2022.

793

794 Francesco Romor, Giovanni Stabile, and Gianluigi Rozza. Non-linear manifold reduced-order models  
 795 with convolutional autoencoders and reduced over-collocation method. *Journal of Scientific  
 Computing*, 94(3):74, 2023.

796

797 François Rozet and Gilles Louppe. Score-based data assimilation. *Advances in Neural Information  
 798 Processing Systems*, 36:40521–40541, 2023.

799

800 Alex Rybchuk, Malik Hassanaly, Nicholas Hamilton, Paula Doubrava, Mitchell J Fulton, and Luis A  
 801 Martínez-Tossas. Ensemble flow reconstruction in the atmospheric boundary layer from spatially  
 802 limited measurements through latent diffusion models. *Physics of Fluids*, 35(12), 2023.

803

804 Xiujie Shan, Jiebao Sun, Zhichang Guo, Wenjuan Yao, and Zhenyu Zhou. Fractional-order diffusion  
 805 model for multiplicative noise removal in texture-rich images and its fast explicit diffusion solving.  
*BIT Numerical Mathematics*, 62(4):1319–1354, 2022.

806

807 Dario Shariatian, Umut Simsekli, and Alain Oliviero Durmus. Heavy-tailed diffusion with denoising  
 808 levy probabilistic models. In *The Thirteenth International Conference on Learning Representations*.

809

Nishanth Shetty, Madhava Prasath, and Chandra Sekhar Seelamantula. Dale meets langevin: A  
 810 multiplicative denoising diffusion model. *arXiv preprint arXiv:2510.02730*, 2025.

810 Maneesh Kumar Singh, Joshua Hope-Collins, Colin J Cotter, and Dan Crisan. Data assimilation  
 811 using a global girsanov nudged particle filter. *arXiv preprint arXiv:2507.17685*, 2025.  
 812

813 Yang Song, Sahaj Garg, Jiaxin Shi, and Stefano Ermon. Sliced score matching: A scalable approach  
 814 to density and score estimation. In *Uncertainty in Artificial Intelligence*, pp. 574–584. PMLR,  
 815 2020.

816 Yang Song, Jascha Sohl-Dickstein, Diederik P Kingma, Abhishek Kumar, Stefano Ermon, and Ben  
 817 Poole. Score-based generative modeling through stochastic differential equations. In *International  
 818 Conference on Learning Representations*, 2021.

819 Stamatis Stamatelopoulos and Themistoklis P Sapsis. Can diffusion models capture extreme event  
 820 statistics? *Computer Methods in Applied Mechanics and Engineering*, 435:117589, 2025.

821 Michael E. Taylor. *Partial Differential Equations III: Nonlinear Parabolique Equations*, volume  
 822 117 of *Applied Mathematical Sciences*. Springer-Verlag, New York, 2nd edition, 2011. ISBN  
 823 978-1-4419-7048-0.

824 Surya T Tokdar, Sheng Jiang, and Erika L Cunningham. Heavy-tailed density estimation. *Journal of  
 825 the American Statistical Association*, 119(545):163–175, 2024.

826 Howard G Tucker. A generalization of the glivenko-cantelli theorem. *The Annals of Mathematical  
 827 Statistics*, 30(3):828–830, 1959.

828 Michael Wilczek and Rudolf Friedrich. Dynamical origins for non-gaussian vorticity distributions in  
 829 turbulent flows. *Physical Review E—Statistical, Nonlinear, and Soft Matter Physics*, 80(1):016316,  
 830 2009.

831 Jiawen Wu, Bingguang Chen, Yuyi Zhou, Qi Meng, Rongchan Zhu, and Zhi-Ming Ma. Riemannian  
 832 neural geodesic interpolant. *arXiv preprint arXiv:2504.15736*, 2025.

833 Eun Bi Yoon, Keehun Park, Sungwoong Kim, and Sungbin Lim. Score-based generative models with  
 834 lévy processes. *Advances in Neural Information Processing Systems*, 36:40694–40707, 2023.

835 Yicun Zhen, Valentin Resseguier, and Bertrand Chapron. Physically constrained covariance inflation  
 836 from location uncertainty. *Nonlinear Processes in Geophysics*, 30(2):237–251, 2023.

837 Zhenyu Zhou, Zhichang Guo, Gang Dong, Jiebao Sun, Dazhi Zhang, and Boying Wu. A doubly  
 838 degenerate diffusion model based on the gray level indicator for multiplicative noise removal.  
 839 *IEEE Transactions on Image Processing*, 24(1):249–260, 2014.

840

841

842

843

844

845

846

847

## 848 Appendix

### 849 Table of Contents

850	<b>A Losses for score matching</b>	<b>18</b>
851		
852	<b>B Stochastic Calculus and Stratonovich Integrals</b>	<b>18</b>
853	B.1 Itô Integrals and SDEs . . . . .	19
854	B.2 Stratonovich Integrals and Chain rule . . . . .	19
855	B.3 Conversion between Itô and Stratonovich forms . . . . .	19
856	B.4 Fokker–Planck equation . . . . .	19
857		
858	<b>C Sampling from 1D distributions</b>	<b>20</b>
859		
860	<b>D The Fokker-Planck equation and its invariant measures</b>	<b>20</b>
861	D.1 Itô form of the forward SDE . . . . .	20
862		
863		

864	D.2 Fokker-Planck equation and Theorem 3.1.1 . . . . .	21
865	D.3 Distribution of the norms . . . . .	23
866	D.4 Fokker-Planck equation of the direction . . . . .	25
867	D.5 Proof of Theorem 3.3.1 : Convergence of Fokker-Planck equation . . . . .	27
868	D.6 Beyond pure Stratonovich noise . . . . .	31
869		
870	<b>E Latent distribution</b>	<b>31</b>
871	E.1 The invariant measures define white noises in the weak sense . . . . .	31
872	E.2 Condition of Gaussianity for the latent vector . . . . .	32
873	E.3 A tractable algorithm to sample latent vectors . . . . .	32
874	E.4 Gaussianization of the latent vectors . . . . .	33
875	E.5 A shorter distance between latent and data distribution . . . . .	33
876	E.6 Relevance of MSGM latent space for heavy-tail distributions. . . . .	34
877		
878	<b>F Backward diffusion</b>	<b>38</b>
879		
880	<b>G Proof of Theorem 3.4.1: equivalence between ELBO and score matching</b>	<b>39</b>
881	G.1 Statement of the theorem . . . . .	39
882	G.2 Notations correspondence . . . . .	39
883	G.3 Marginal density from Feynman-Kac representation . . . . .	40
884	G.4 Change of measure and Jensen’s inequality . . . . .	40
885	G.5 Girsanov theorem . . . . .	40
886	G.6 ELBO evaluation . . . . .	41
887	G.7 From ELBO to our SSM loss . . . . .	41
888	G.8 Remark on the score parametrization . . . . .	42
889	G.9 Girsanov theorem in the transport noise literature . . . . .	43
890		
891	<b>H Comparison with diffusions on Riemannian manifolds</b>	<b>43</b>
892	H.1 Riemannian Manifolds and Differentiation . . . . .	43
893	H.2 Conditional diffusions on scaled $d$ -spheres . . . . .	44
894	H.3 Link with neural network architecture . . . . .	46
895		
896	<b>I Analytic illustrations on simplified cases</b>	<b>46</b>
897	I.1 The two-dimensional case . . . . .	46
898	I.2 Tensor built from a single skew-symmetric matrix . . . . .	47
899	I.3 Non-commutativity in the general case . . . . .	52
900		
901	<b>J Rank and skew-symmetry conditions for random tensor <math>G</math></b>	<b>52</b>
902	J.1 Proof of the rank condition . . . . .	52
903	J.2 Tensor renormalization . . . . .	53
904	J.3 Mean speed of convergence with renormalized tensor . . . . .	53
905		
906	<b>K Going beyond the rank condition for MSGM scalability</b>	<b>54</b>
907	K.1 Weaker assumptions . . . . .	54
908	K.2 Sparse tensors . . . . .	56
909	K.3 Discussion about local and non local structure . . . . .	59
910		
911	<b>L Numerical scheme</b>	<b>60</b>
912	L.1 Numerical integration of SDEs . . . . .	60
913	L.2 Scheduling . . . . .	60
914	L.3 Loss evaluation . . . . .	63
915	L.4 Neural network architecture . . . . .	63
916	L.5 . . . . .	63
917		
	<b>M Details about our numerical experiments</b>	<b>65</b>
	M.1 Test cases . . . . .	65

918	M.2 Data preprocessing . . . . .	65
919	M.3 Comparison strategy . . . . .	65
920	M.4 Swiss roll . . . . .	66
921	M.5 <i>Anisotropic Gaussian distribution</i> . . . . .	68
922	M.6 Multivariate Cauchy distribution . . . . .	72
923	M.7 <i>Vorticity field from Particle Image Velocimetry measurements</i> . . . . .	80
924		
925	<b>N Summarized comparison of MSGM and SGM</b>	<b>83</b>
926	N.1 Theoretical aspects . . . . .	88
927	N.2 Empirical aspects . . . . .	88
928		
929		
930		
931	<b>A LOSSES FOR SCORE MATCHING</b>	
932		
933	This section presents some classical score-matching losses. In SGM backward SDE, the score	
934	$\nabla \log p_{T-t}(\mathbf{x})$ is replaced by a fitted neural network $s_{\theta}(\mathbf{x}, T-t)$ . This fitting is performed by	
935	minimizing some losses, like denoising, implicit, or slicing score-matching losses. Alternatively, one	
936	can work on $\mathbf{a}_{\theta}(\mathbf{x}, T-t) = \sqrt{2}s_{\theta}(\mathbf{x}, T-t)$ (Huang et al., 2021). It leads to this SGM backward	
937	SDE:	
938	$d\overleftarrow{\mathbf{x}}_t = \overleftarrow{\mathbf{x}}_t dt + \sqrt{2}(\mathbf{a}_{\theta}(\mathbf{x}, T-t)dt + d\overleftarrow{\mathbf{B}}_t),$	(A.1)
939		
940	A typical loss to learn this neural network is denoising score matching (DSM)	
941		
942	$\mathcal{L}_{\text{DSM}} = \int_0^T \frac{1}{2} \mathbb{E}_{\overrightarrow{\mathbf{x}}_s} \ \mathbf{a}_{\theta}(\overrightarrow{\mathbf{x}}_s, s) - \sqrt{2} \nabla \log p_s(\overrightarrow{\mathbf{x}}_s   \overrightarrow{\mathbf{x}}_0)\ ^2 ds.$	(A.2)
943		
944	where $\ \cdot\ $ is the Euclidian norm. By integration by part, we can show that DSM is equivalent to	
945	Implicit Score Matching (ISM) (Hyvärinen & Dayan, 2005)	
946		
947	$\mathcal{L}_{\text{ISM}} = \int_0^T \mathbb{E}_{\overrightarrow{\mathbf{x}}_s} \left( \frac{1}{2} \ \mathbf{a}_{\theta}(\overrightarrow{\mathbf{x}}_s, s)\ ^2 + \nabla \cdot (\sqrt{2} \mathbf{a}_{\theta}(\overrightarrow{\mathbf{x}}_s, s)) \right) ds.$	(A.3)
948		
949	A reference score $\nabla \log p_s$ is not needed anymore. However, the divergence term may be untractable	
950	for large-dimensional problems. Using the Hutchinson trick, Song et al. (2020) shows that this loss	
951	is equivalent to a trackable version : the Sliced Score Matching (SSM)	
952		
953	$\mathcal{L}_{\text{SSM}} = \int_0^T \mathbb{E}_{\overrightarrow{\mathbf{x}}_s} \mathbb{E}_{\mathbf{v} \sim \mathcal{N}(0, \mathbf{I}_d)} \left( \frac{1}{2} \ \mathbf{a}_{\theta}(\overrightarrow{\mathbf{x}}_s, s)\ ^2 + (\mathbf{v} \cdot \nabla)(\sqrt{2} \mathbf{a}_{\theta}(\overrightarrow{\mathbf{x}}_s, s) \cdot \mathbf{v}) \right) ds.$	(A.4)
954		
955		
956	Score matching is equivalent to maximizing the Evidence Lower Bound (ELBO) both in discrete time	
957	(Luo, 2022) and in continuous time (Huang et al., 2021). Indeed, denoting $\mathcal{E}_{\infty}$ the ELBO, Huang	
958	et al. (2021) shows that:	
959	$\mathcal{E}_{\infty}(\mathbf{x}) = \mathbb{E} \left[ \log p_0(\overrightarrow{\mathbf{x}}_T) \mid \overrightarrow{\mathbf{x}}_0 = \mathbf{x} \right]$	(A.5)
960	$- \int_0^T \mathbb{E}_{\overrightarrow{\mathbf{x}}_s} \left[ \frac{1}{2} \ \mathbf{a}_{\theta}(\overrightarrow{\mathbf{x}}_s, s)\ ^2 + \nabla \cdot (\sqrt{2} \mathbf{a}_{\theta}(\overrightarrow{\mathbf{x}}_s, s)) \mid \overrightarrow{\mathbf{x}}_0 = \mathbf{x} \right] ds.$	
961		
962		
963	The first term does not depends on the neural network parameters $\theta$ . The expectation of the second	
964	term over $\mathbf{x}$ following the dataset distribution is $\mathcal{L}_{\text{ISM}}$ . So, maximizing the ELBO is equivalent to	
965	minimize the ISM. Table 1 of Huang et al. (2021) summarizes the classical score matching losses.	
966		
967		
968	<b>B STOCHASTIC CALCULUS AND STRATONOVICH INTEGRALS</b>	
969		
970	This appendix provides a concise overview of essential stochastic calculus concepts from Oksendal	
971	(1998); Kunita (1997) relevant to our work, especially the Stratonovich interpretation of stochastic	
	differential equations (SDEs).	

972 B.1 ITÔ INTEGRALS AND SDES  
973

974 Let  $(\Omega, \mathcal{F}, \mathbb{P})$  be a probability space equipped with a filtration  $(\mathcal{F}_t)_{t \geq 0}$  satisfying the usual conditions,  
975 and let  $(\mathbf{B}_t)_{t \geq 0}$  be a standard  $m$ -dimensional Brownian motion. Given an adapted process  $\mathbf{X}_t \in$   
976  $\mathbb{R}^{d \times m}$  satisfying appropriate integrability conditions, the *Itô integral* of  $\mathbf{X}$  with respect to  $\mathbf{B}$  is  
977 defined as the mean-square limit:

$$978 \quad \int_0^T \mathbf{X}_s d\mathbf{B}_s := \lim_{|\Pi| \rightarrow 0} \sum_{[t_i, t_{i+1}] \in \Pi} \mathbf{X}_{t_i} (\mathbf{B}_{t_{i+1}} - \mathbf{B}_{t_i}), \quad (\text{B.1})$$

981 where the sum is taken over a partition  $\Pi$  of  $[0, T]$ .

982 An SDE interpreted in the Itô sense reads:

$$983 \quad d\mathbf{X}_t = \mathbf{f}(\mathbf{X}_t, t) dt + \mathbf{G}(\mathbf{X}_t, t) d\mathbf{B}_t, \quad (\text{B.2})$$

984 where  $\mathbf{f} : \mathbb{R}^d \times \mathbb{R}_+ \rightarrow \mathbb{R}^d$  is the drift, and  $\mathbf{G} : \mathbb{R}^d \times \mathbb{R}_+ \rightarrow \mathbb{R}^{d \times m}$  is the diffusion coefficient.

986 B.2 STRATONOVICH INTEGRALS AND CHAIN RULE  
987

988 Unlike the Itô integral, the *Stratonovich integral* is defined using a symmetric discretization:

$$989 \quad \int_0^T \mathbf{X}_s \circ d\mathbf{B}_s := \lim_{|\Pi| \rightarrow 0} \sum_{[t_i, t_{i+1}] \in \Pi} \frac{\mathbf{X}_{t_i} + \mathbf{X}_{t_{i+1}}}{2} (\mathbf{B}_{t_{i+1}} - \mathbf{B}_{t_i}). \quad (\text{B.3})$$

993 A Stratonovich SDE is written as:

$$994 \quad d\mathbf{X}_t = \mathbf{f}_S(\mathbf{X}_t, t) dt + \mathbf{G}(\mathbf{X}_t, t) \circ d\mathbf{B}_t. \quad (\text{B.4})$$

995 A key advantage of the Stratonovich formulation is that it satisfies the classical chain rule. For any  
996 smooth function  $\phi : \mathbb{R}^d \rightarrow \mathbb{R}$ , we have:

$$997 \quad d\phi(\mathbf{X}_t) = \nabla \phi(\mathbf{X}_t)^\top \mathbf{f}_S(\mathbf{X}_t, t) dt + \nabla \phi(\mathbf{X}_t)^\top \mathbf{G}(\mathbf{X}_t, t) \circ d\mathbf{B}_t. \quad (\text{B.5})$$

999 oreover, in multiscale deterministic or stochastic equations, if the fast component is a continuous  
1000 process with infinitesimal correlation time, the slow component generally converges to the solution  
1001 of another SDE. In this other SDE, the fast component is often replaced by a Stratonovich integral  
1002 (Arnold, 1974). Note that it is not always true for nonlinear dynamics (Gottwald & Melbourne, 2013;  
1003 Gottwald et al., 2015). Accordingly, the readers may interpret the Stratonovich noise  $s \mapsto \circ d\mathbf{B}_s$  as a  
1004 formal representation of a process with a short correlation time that nevertheless respects the classical  
1005 rules of differential calculus, in particular, the chain rule.

1006 B.3 CONVERSION BETWEEN ITÔ AND STRATONOVICH FORMS  
1007

1008 Given a Stratonovich SDE, it is always possible to convert it to the equivalent Itô form:

$$1009 \quad d\mathbf{X}_t = \left( \mathbf{f}_S(\mathbf{X}_t, t) + \frac{1}{2} \sum_{j=1}^m G_j(\mathbf{X}_t, t) \cdot \nabla G_j(\mathbf{X}_t, t) \right) dt + \mathbf{G}(\mathbf{X}_t, t) d\mathbf{B}_t, \quad (\text{B.6})$$

1013 where  $G_j(\mathbf{x}, t)$  is the  $j$ -th column of the diffusion matrix  $\mathbf{G}(\mathbf{x}, t)$ . The additional drift term arises  
1014 from the correction due to the non-zero quadratic variation of the noise.

1015 B.4 FOKKER-PLANCK EQUATION  
1016

1017 An Itô SDE of the form

$$1019 \quad d\mathbf{X}_t = \mathbf{f}(\mathbf{X}_t, t) dt + \mathbf{G}(\mathbf{X}_t, t) d\mathbf{B}_t, \quad (\text{B.7})$$

1020 induces a time-evolution equation for the probability density  $p(\mathbf{x}, t)$  of  $\mathbf{X}_t$ . This is known as the  
1021 *Fokker-Planck equation*, given by:

$$1022 \quad \partial_t p(\mathbf{x}, t) = -\nabla \cdot (\mathbf{f}(\mathbf{x}, t) p(\mathbf{x}, t)) + \frac{1}{2} \nabla \cdot (\nabla \cdot (\boldsymbol{\Sigma}(\mathbf{x}, t) p(\mathbf{x}, t))^\top), \quad (\text{B.8})$$

1024 where  $\boldsymbol{\Sigma}(\mathbf{x}, t) := \mathbf{G}(\mathbf{x}, t) \mathbf{G}(\mathbf{x}, t)^\top$  is the diffusion tensor. The Fokker-Planck equation describes  
1025 the deterministic evolution of the probability density associated with the stochastic process.

1026 **C SAMPLING FROM 1D DISTRIBUTIONS**  
 1027

1028 Let us denote by  $p_{|\cdot|}$  the distribution of the norms,  $\|\vec{\mathbf{x}}_T\|$ . In MSGM, it is also the distribution of  
 1029  $\|\vec{\mathbf{x}}_0\|$  (see Proposition D.3.2). This distribution is arbitrary, but is a one-dimensional distribution. So,  
 1030 it is straightforward to learn and sample from, e.g., using an empirical cumulative distribution function  
 1031 (eCDF) (Cantelli, 1933; Glivenko, 1933; Tucker, 1959). Norms are positive and might be close to zero,  
 1032 so in practice we work with a regularized log-norm:  $\log \|\mathbf{x}\|_\epsilon := \log(\|\mathbf{x}\| + \epsilon)$  with  $\epsilon$  small, typically  
 1033  $\epsilon = 10^{-6}$ . From a data set of the log-norms of  $M$  training samples,  $(\log \|\vec{\mathbf{x}}_T^{(i)}\|_\epsilon)_i = (\log \|\vec{\mathbf{x}}_0^{(i)}\|_\epsilon)_i$ ,  
 1034 we define eCDF  $\hat{F}_{\log |\cdot|_\epsilon}$  as  
 1035

$$\hat{F}_{\log |\cdot|_\epsilon} : \mathbb{R} \rightarrow [0, 1], \quad (\text{C.1})$$

$$R \mapsto \frac{1}{M} \sum_{i=1}^M \mathbf{1}_{\{R \geq \log \|\vec{\mathbf{x}}_T^{(i)}\|_\epsilon\}}. \quad (\text{C.2})$$

1042 Then, we approximate the distribution of the norms,  $p_{\log |\cdot|_\epsilon}(R) dR$ , by the empirical one,  
 1043  $\hat{p}_{\log |\cdot|_\epsilon}(R) dR := \hat{F}_{\log |\cdot|_\epsilon}(dR)$ . In particular, we can sample a new norm of latent variables,  $\|\vec{\mathbf{x}}_T\|$ ,  
 1044 from a uniform one-dimensional variable  $u \sim \mathcal{U}(0, 1)$  as follows  
 1045

$$\|\vec{\mathbf{x}}_T\| = \|\vec{\mathbf{x}}_0\| = \exp(\log \|\vec{\mathbf{x}}_0\|_\epsilon) - \epsilon = \exp\left(\hat{F}_{\log |\cdot|_\epsilon}^{-1}(u)\right) - \epsilon. \quad (\text{C.3})$$

1046 eCDF is an efficient tool, but it cannot generalize the distribution  $\hat{p}_{|\cdot|}$  outside the training set  $(\|\vec{\mathbf{x}}_T^{(i)}\|)_i$ .  
 1047 For better generalization, instead, one could use a one-dimensional kernel density estimation or fitting  
 1048 of parametric distributions. In the case of one-dimensional distributions with fat tails, classical kernel  
 1049 density estimation (KDE) suffers from bias in the tail estimation or peaks due to sparse data in the  
 1050 tails. In that case, one could consider more robust approaches that, in general, do not require the  
 1051 existence of moments of the target distribution Tokdar et al. (2024).  
 1052

1053 In this paper, we rely on the eCDF.  
 1054

1055 **D THE FOKKER-PLANCK EQUATION AND ITS INVARIANT MEASURES**  
 1056

1057 **D.1 ITÔ FORM OF THE FORWARD SDE**  
 1058

1059 Define the conditional noise covariance  $\Sigma(\mathbf{x})$  as  
 1060

$$\Sigma(\mathbf{x}) := \mathbf{G}(\mathbf{x})\mathbf{G}(\mathbf{x})^\top = \mathbb{E}[(d\vec{\mathbf{x}}_s)(d\vec{\mathbf{x}}_s)^\top | \vec{\mathbf{x}}_s = \mathbf{x}]. \quad (\text{D.1})$$

1061 We begin with a lemma.  
 1062

1063 **Lemma D.1.1.** *Let the skew-symmetry assumption A1 hold. Then,*  
 1064

$$\frac{1}{2} \nabla \cdot (\Sigma(\mathbf{x})) = \frac{1}{2} \sum_{k=1}^d (\mathbf{G}^k)^2 \mathbf{x}. \quad (\text{D.2})$$

1065 *Proof.* Let us explicitly state the matrix divergence. For  $k = 1, \dots, d$  define  $\Sigma^k(\mathbf{x}) = [\Sigma_{ij}^k(\mathbf{x})] :=$   
 1066  $\mathbf{G}^k \mathbf{x} \mathbf{x}^\top (\mathbf{G}^k)^\top$ , then we decompose  $\Sigma$  as  
 1067

$$\Sigma(\mathbf{x}) := \mathbf{G}(\mathbf{x})\mathbf{G}^\top(\mathbf{x}) = \sum_{k=1}^d \Sigma^k(\mathbf{x}). \quad (\text{D.3})$$

1080 Then, taking the divergence of the  $j$ -th column of  $\Sigma^k(\mathbf{x})$ , we obtain  
1081

$$1082 (\nabla \cdot (\Sigma^k(\mathbf{x})))_j = \nabla \cdot [\Sigma^k(\mathbf{x})]_{:,j} = \sum_{i=1}^d \frac{\partial}{\partial x_i} \Sigma_{ij}^k(\mathbf{x}), \quad (D.4)$$

$$1085 = \sum_{i=1}^d \frac{\partial}{\partial x_i} \sum_{p,q=1}^d G_{ip}^k x_p x_q G_{jq}^k, \quad (D.5)$$

$$1088 = \sum_{i,p,q=1}^d G_{ip}^k (\delta_{ip} x_q + x_p \delta_{iq}) G_{jq}^k, \quad (D.6)$$

$$1091 = \sum_{p,q=1}^d G_{pp}^k x_q G_{jq}^k + G_{qp}^k x_p G_{jq}^k, \quad (D.7)$$

$$1094 = [\text{tr}(\mathbf{G}^k) \mathbf{G}^k \mathbf{x} + \mathbf{G}^k(\mathbf{G}^k \mathbf{x})]_j. \quad (D.8)$$

1095 By skew-symmetry  $\text{trace}(\mathbf{G}^k) = 0$  and consequently  
1096

$$1097 \nabla \cdot (\Sigma(\mathbf{x})) = \sum_{k=1}^d (\nabla \cdot (\Sigma^k(\mathbf{x}))) = \sum_{k=1}^d \mathbf{G}^k(\mathbf{G}^k \mathbf{x}).$$

1100  $\square$

1101 **Lemma D.1.2. (Forward SDE - Itô)** *Let the skew-symmetry assumption equation A1 hold. Then,  
1102 the Itô form of the forward SDE equation 3.1 of  $\vec{\mathbf{x}}_s$  is given by*

$$1104 d\vec{\mathbf{x}}_s = \frac{1}{2} (\nabla \cdot \Sigma)(\vec{\mathbf{x}}_s) ds + \mathbf{G}(\vec{\mathbf{x}}_s) d\vec{\mathbf{B}}_s. \quad (D.9)$$

1105 *Proof.* Using the standard Stratonovich-to-Itô formula (e.g. Kunita, 1997), it holds

$$1107 d\vec{\mathbf{x}}_s = \frac{1}{2} d\langle \mathbf{G}(\vec{\mathbf{x}}_s), \vec{\mathbf{B}}_s \rangle_s + \mathbf{G}(\vec{\mathbf{x}}_s) d\vec{\mathbf{B}}_s, \quad (D.10)$$

$$1110 = \frac{1}{2} \sum_{k=1}^d d\langle \mathbf{G}^k \vec{\mathbf{x}}_s, (\vec{\mathbf{B}}_s)_k \rangle_s + \mathbf{G}(\vec{\mathbf{x}}_s) d\vec{\mathbf{B}}_s, \quad (D.11)$$

$$1113 = \frac{1}{2} \sum_{k=1}^d (\mathbf{G}^k)^2 \vec{\mathbf{x}}_s ds + \mathbf{G}(\vec{\mathbf{x}}_s) d\vec{\mathbf{B}}_s, \quad (D.12)$$

$$1115 = \frac{1}{2} (\nabla \cdot \Sigma)(\vec{\mathbf{x}}_s) ds + \mathbf{G}(\vec{\mathbf{x}}_s) d\vec{\mathbf{B}}_s, \quad (D.13)$$

1116 where the last equality comes from Lemma D.1.1.  $\square$   
1117

## 1118 D.2 FOKKER-PLANCK EQUATION AND THEOREM 3.1.1

1119 Let  $\vec{\mathbf{x}}_0 \sim p_{\vec{\mathbf{x}}_0}$  with  $p_{\vec{\mathbf{x}}_0} \in \mathcal{C}^2(\mathbb{R}^d)$  be twice continuously differentiable. Let  $p_s$  denote the density  
1120 of the distribution of  $\vec{\mathbf{x}}_s$ . For each  $\mathbf{x} \in \mathbb{R}^d$  we define the normalized vector  $\mathbf{x}^n := \frac{\mathbf{x}}{\|\mathbf{x}\|}$  for  $\mathbf{x} \neq 0$   
1121 and 0 otherwise, which is orthogonal to the  $d$ -sphere  $\mathbb{S}^{d-1}$ . Furthermore, let  $\nabla_{\perp}$  be the orthogonal  
1122 projection of the gradient  $\nabla$  in the tangent plane  $\mathbf{x}^{\perp} = \mathcal{T}_{\mathbf{x}} \mathbb{S}^{d-1}$ , the tangent space on the Riemannian  
1123 manifold  $\mathbb{S}^{d-1}$  at the point  $\mathbf{x}$ , defined for  $f \in \mathcal{C}^2(\mathbb{R}^d)$  as  
1124

$$1126 \nabla_{\perp} f := \nabla f - (\mathbf{x}^n \cdot \nabla f) \mathbf{x}^n. \quad (D.14)$$

1127 **Lemma D.2.1.** *It holds for any smooth vector field  $f$  that*

$$1129 \nabla \cdot f = (\mathbf{x}^n \cdot \nabla)(\mathbf{x}^n \cdot f) + \nabla_{\perp} \cdot f. \quad (D.15)$$

1130 *Proof.* Let  $f$  be a smooth vector field, then  
1131

$$1132 (\mathbf{x}^n (\mathbf{x}^n)^{\top} \nabla) \cdot f = \sum_{i=1}^d \sum_{j=1}^d x_i^n x_j^n \frac{\partial}{\partial x_j} f_i = \sum_{i=1}^d (\mathbf{x}^n)_i \langle \mathbf{x}^n, \nabla \rangle f_i = \langle \langle \mathbf{x}^n, \nabla \rangle f, \mathbf{x}^n \rangle. \quad (D.16)$$

1134 It holds for each  $j = 1, \dots, d$  that  
 1135

$$1136 \quad [(\mathbf{x}^n \cdot \nabla) \mathbf{x}^n]_j = \left[ \left( \sum_{i=1}^d (\mathbf{x}^n)_i \frac{\partial}{\partial x_i} \right) \frac{\mathbf{x}}{\|\mathbf{x}\|} \right]_j = (\mathbf{x}^n)_j \frac{1}{\|\mathbf{x}\|} - \sum_{i=1}^d (\mathbf{x}^n)_i \frac{x_i}{\|\mathbf{x}\|^3} x_j, \quad (D.17)$$

$$1139 \quad = x_j / \|\mathbf{x}\|^2 - \left( \sum_{i=1}^d x_i^2 / \|\mathbf{x}\|^4 \right) x_j, \quad (D.18)$$

$$1142 \quad = 0. \quad (D.19)$$

1143 Consequently,

$$1144 \quad (\mathbf{x}^n \cdot \nabla)(\mathbf{x}^n \cdot f) = (\mathbf{x}^n \cdot \nabla) \mathbf{x}^n \cdot f + (\mathbf{x}^n \cdot \nabla) f \cdot \mathbf{x}^n = (\mathbf{x}^n \cdot \nabla) f \cdot \mathbf{x}^n. \quad (D.20)$$

1146 Using the decomposition  $\nabla = \mathbf{x}^n (\mathbf{x}^n)^\top \nabla + (I - \mathbf{x}^n (\mathbf{x}^n)^\top) \nabla = \mathbf{x}^n (\mathbf{x}^n)^\top \nabla + \nabla_\perp$ , equation D.16  
 1147 and equation D.20 we conclude

$$1148 \quad \nabla \cdot f = (\mathbf{x}^n (\mathbf{x}^n)^\top \nabla + \nabla_\perp) \cdot f = (\mathbf{x}^n \cdot \nabla) f \cdot \mathbf{x}^n + \nabla_\perp \cdot f = (\mathbf{x}^n \cdot \nabla)(\mathbf{x}^n \cdot f) + \nabla_\perp \cdot f.$$

1150  $\square$   
 1151

1152 Define the conditional noise covariance  $\Sigma(\mathbf{x})$  as  
 1153

$$1154 \quad \Sigma(\mathbf{x}) := \mathbf{G}(\mathbf{x}) \mathbf{G}(\mathbf{x})^\top = \mathbb{E}[(d\vec{\mathbf{x}}_s)(d\vec{\mathbf{x}}_s)^\top | \vec{\mathbf{x}}_s = \mathbf{x}]. \quad (D.21)$$

1156 We can now state and proof Theorem 3.1.1.

1157 **Theorem D.2.1.** *Let the assumptions A1 and A2 hold. Then, the Fokker-Planck equation of equa-  
 1158 tion 3.1 reads*

$$1159 \quad \begin{cases} \frac{\partial}{\partial s} p_s(\mathbf{x}) &= \nabla_\perp \cdot \left( \frac{1}{2} \Sigma(\mathbf{x}) \nabla_\perp p_s(\mathbf{x}) \right), \\ p_0 &= p_{\vec{\mathbf{x}}_0}. \end{cases} \quad \mathbf{x} \in \mathbb{R}^d, \quad (D.22)$$

1162 *oreover, any stationary density  $p_\infty$  of equation D.22 is rotation-invariant on  $\mathbb{R}^d$ .*

1163

1164 *Proof.* From the Itô SDE equation D.9, the Fokker-Planck equation describing the evolution of  
 1165  $(p_s)_{s \geq 0}$  is given as

$$1166 \quad \frac{\partial}{\partial s} p_s = \nabla \cdot \left( -\frac{1}{2} \nabla \cdot (\Sigma(\mathbf{x})) p_s(\mathbf{x}) + \frac{1}{2} \nabla \cdot (\Sigma(\mathbf{x}) p_s(\mathbf{x})) \right), \quad (D.23)$$

$$1169 \quad = \nabla \cdot \left( -\frac{1}{2} \nabla \cdot (\Sigma(\mathbf{x})) p_s(\mathbf{x}) + \frac{1}{2} \nabla \cdot (\Sigma(\mathbf{x})) p_s(\mathbf{x}) + \frac{1}{2} \Sigma(\mathbf{x}) \nabla p_s(\mathbf{x}) \right), \quad (D.24)$$

$$1171 \quad = \nabla \cdot \left( \frac{1}{2} \Sigma(\mathbf{x}) \nabla p_s(\mathbf{x}) \right). \quad (D.25)$$

1173 The skew-symmetry condition in assumption A1 implies for any  $\mathbf{x} \in \mathbb{R}^d$  that  
 1174

$$1175 \quad ((\mathbf{x}^n)^\top \Sigma(\mathbf{x}))^\top = \Sigma(\mathbf{x}) \mathbf{x}^n = \sum_{k=1}^d G_k \mathbf{x} \|\mathbf{x}\| \underbrace{(\mathbf{x}^n)^\top G_k^\top \mathbf{x}^n}_{=0} = 0. \quad (D.26)$$

1178 Combining this with the result of equation D.16, it holds that  
 1179

$$1180 \quad \nabla \cdot (\Sigma(\mathbf{x}) \nabla p_s(\mathbf{x})) = (\mathbf{x}^n \cdot \nabla)(\mathbf{x}^n \cdot \Sigma(\mathbf{x}) \nabla p_s(\mathbf{x})) + \nabla_\perp \cdot (\Sigma(\mathbf{x}) \nabla p_s(\mathbf{x})). \quad (D.27)$$

1181 The decomposition  $\nabla = \mathbf{x}^n (\mathbf{x}^n)^\top \nabla + (I - \mathbf{x}^n (\mathbf{x}^n)^\top) \nabla = \mathbf{x}^n (\mathbf{x}^n)^\top \nabla + \nabla_\perp$  and equation D.26  
 1182 yields

$$1183 \quad \nabla_\perp \cdot (\Sigma(\mathbf{x}) \nabla p_s(\mathbf{x})) = \nabla_\perp \cdot (\Sigma(\mathbf{x}) \nabla_\perp p_s(\mathbf{x})) + \nabla_\perp \cdot (\Sigma(\mathbf{x}) \mathbf{x}^n (\mathbf{x}^n)^\top \nabla p_s(\mathbf{x})), \quad (D.28)$$

$$1185 \quad = \nabla_\perp \cdot (\Sigma(\mathbf{x}) \nabla_\perp p_s(\mathbf{x})). \quad (D.29)$$

1186 Hence, by linearity  
 1187

$$\frac{\partial}{\partial s} p_s = \nabla_\perp \cdot \left( \frac{1}{2} \Sigma(\mathbf{x}) \nabla_\perp p_s(\mathbf{x}) \right). \quad (D.30)$$

We shall now explore the set of possible invariant densities  $\rho_\infty$  of the Fokker-Planck equation D.22. We will show that  $\rho_\infty$  is stationary if and only if it is rotation-invariant.

Let  $p_\infty$  be rotation-invariant, i.e.  $\nabla_\perp p_\infty = 0$  then it is a stationary solution of the Fokker-Planck equation. The set of rotation-invariant measures is not empty, e.g. containing the isotropic normal distributions  $\mathcal{N}(0, \mathbf{I}_d)$ .

Conversely, let  $p_\infty$  be a stationary solution of the Fokker-Planck equation, in particular

$$\nabla_\perp \cdot \left( \frac{1}{2} \boldsymbol{\Sigma}(\mathbf{x}) \nabla_\perp p_\infty(\mathbf{x}) \right) = 0. \quad (\text{D.31})$$

Integrating over the test function  $\phi = p_\infty$  gives a necessary condition for  $p_\infty$  to be an invariant measure:

$$0 = - \int_{\mathbb{R}^d} p_\infty(\mathbf{x}) \nabla_\perp \cdot (\boldsymbol{\Sigma}(\mathbf{x}) \nabla_\perp p_\infty(\mathbf{x})) d\mathbf{x}, \quad (\text{D.32})$$

$$= \int_{\mathbb{R}^d} \nabla_\perp p_\infty(\mathbf{x})^\top \boldsymbol{\Sigma}(\mathbf{x}) \nabla_\perp p_\infty(\mathbf{x}) d\mathbf{x}, \quad (\text{D.33})$$

$$= \int_{\mathbb{R}^d} \underbrace{\|\mathbf{G}^\top(\mathbf{x}) \nabla_\perp p_\infty(\mathbf{x})\|^2}_{\geq 0} d\mathbf{x}. \quad (\text{D.34})$$

Hence, for a.e.  $\mathbf{x} \in \mathbb{R}^d$  it holds that  $\nabla_\perp p_\infty(\mathbf{x}) \in \ker(\mathbf{G}^\top(\mathbf{x}))$ . By assumption A2, this kernel has dimension 1. Moreover,  $\mathbf{G}^\top(\mathbf{x})\mathbf{x} = 0$  and by definition of  $\nabla_\perp$  we have that  $\nabla_\perp p_\infty(\mathbf{x}) \perp \mathbf{x}$ . That means

$$\nabla_\perp p_\infty(\mathbf{x}) \in \ker(\mathbf{G}^\top(\mathbf{x})) \cap \mathbf{x}^\perp = \text{span}\{\mathbf{x}\} \cap \mathbf{x}^\perp = \{0\}. \quad (\text{D.35})$$

We conclude that  $\nabla_\perp p_\infty(\mathbf{x}) = 0$  almost everywhere on  $\mathbb{R}^d$ , i.e. the measure is rotation-invariant.  $\square$

### D.3 DISTRIBUTION OF THE NORMS

In this section, we see more precisely that the norm of the MSGM SDE solution remains constant along the noising process whereas in SGM the norm dynamics is random with a mean going to  $\sqrt{d}$  asymptotically.

#### D.3.1 NORM DYNAMICS IN SGM

The dynamics of the SGM diffusion norm is stochastic. The following proposition states that the norm of the SGM latent concentrates around its mean,  $\sqrt{d}$ , for large dimension  $d$ .

**Proposition D.3.1.** *If  $\vec{\mathbf{x}}_s$  is an Ornstein Uhlenbeck process then*

$$\mathbb{E} \left[ \|\vec{\mathbf{x}}_s\|^2 \mid \vec{\mathbf{x}}_0 \right] = e^{-2s} \|\vec{\mathbf{x}}_0\|^2 + (1 - e^{-2s})d \xrightarrow[s \rightarrow \infty]{} d. \quad (\text{D.36})$$

and

$$\|\vec{\mathbf{x}}_s\|^2 = \mathbb{E} \left[ \|\vec{\mathbf{x}}_s\|^2 \mid \vec{\mathbf{x}}_0 \right] + \sqrt{d} I_s + e^{-s} K_s = d \left( 1 + \frac{1}{\sqrt{d}} \xrightarrow[s \rightarrow \infty]{} O(1) \right), \quad (\text{D.37})$$

with both  $\mathbb{E} K_s^2$  and  $\mathbb{E} I_s^2$  bounded for large time  $s$  and  $\mathbb{E} I_s^2$  independent of the dimension  $d$ .

*Proof.* To get the dynamics of the squared norm mean in SGM, we can take the expectation of the following Itô equation

$$d\|\vec{\mathbf{x}}_s\|^2 = 2\vec{\mathbf{x}}_s \cdot d\vec{\mathbf{x}}_s + d < \vec{\mathbf{x}}^\top, \vec{\mathbf{x}} >_s = 2(\|\vec{\mathbf{x}}_s\|^2 - d)ds + 2\sqrt{2}\vec{\mathbf{x}}_s \cdot d\vec{\mathbf{B}}_s, \quad \forall s \geq 0. \quad (\text{D.38})$$

Thus,

$$\mathbb{E} \left[ \|\vec{\mathbf{x}}_s\|^2 \mid \vec{\mathbf{x}}_0 \right] = e^{-2s} \|\vec{\mathbf{x}}_0\|^2 + (1 - e^{-2s})d \xrightarrow[s \rightarrow \infty]{} d. \quad (\text{D.39})$$

To obtain the full norm dynamics from equation D.38, we note that  $t \rightarrow e^{-2s}$  has finite variations. Accordingly,

$$d(e^{-2s}(\|\vec{\mathbf{x}}_s\|^2 - d)) = 2\sqrt{2}e^{-2s}\vec{\mathbf{x}}_s \cdot d\vec{\mathbf{B}}_s, \quad (\text{D.40})$$

1242 and a temporal integration and the analytic expression of the Ornstein Uhlenbeck process yields:  
1243

$$1244 \quad \|\vec{x}_s\|^2 = \mathbb{E} \left[ \|\vec{x}_s\|^2 \mid \vec{x}_0 \right] + 2\sqrt{2} \int_0^s e^{-2(s-s')} \vec{x}_{s'} \cdot d\vec{B}_{s'}, \quad (\text{D.41})$$

$$1246 \quad = \mathbb{E} \left[ \|\vec{x}_s\|^2 \mid \vec{x}_0 \right] + 2\sqrt{2} e^{-s} \vec{x}_0 \cdot \int_0^s e^{-(s-s')} d\vec{B}_{s'} \\ 1247 \quad + 2\sqrt{2} \int_0^s \int_0^{s'} e^{-(2s-s'-s'')} d\vec{B}_{s'} \cdot d\vec{B}_{s''}, \quad (\text{D.42})$$

$$1251 \quad = \mathbb{E} \left[ \|\vec{x}_s\|^2 \mid \vec{x}_0 \right] + \sqrt{d} I_s + e^{-s} K_s, \quad (\text{D.43})$$

1252 with the martingales  
1253

$$1254 \quad I_s = \sqrt{\frac{8}{d}} \int_0^s \int_0^{s'} e^{-(2s-s'-s'')} d\vec{B}_{s'} \cdot d\vec{B}_{s''}, \quad (\text{D.44})$$

$$1256 \quad K_s = \sqrt{8} \vec{x}_0 \cdot \int_0^s e^{-(s-s')} d\vec{B}_{s'}. \quad (\text{D.45})$$

1258  $K_s$  corresponds to the martingale part of the Ornstein Uhlenbeck solution projected on  $\vec{x}_0$ . It is well  
1259 known that  $\mathbb{E} K_s^2$  is bounded for large time  $s$ .  $\mathbb{E} I_s^2$  may be less known and we shall evaluate it below:  
1260

$$1261 \quad \mathbb{E} I_s^2 = \frac{8}{d} e^{-4s} \mathbb{E} \left( \sum_{p=1}^d \int_0^s \int_0^{s'} e^{s'+s''} d(\vec{B}_{s'})_p \cdot d(\vec{B}_{s''})_p \right)^2, \quad (\text{D.46})$$

$$1264 \quad = \frac{8}{d} e^{-4s} \mathbb{E} \sum_{p_1, p_2=1}^d \int_0^s \int_0^{s'_1} \int_0^s \int_0^{s'_2} e^{s'_1+s'_1 s'_2+s''_2} d(\vec{B}_{s'_1})_{p_1} \cdot d(\vec{B}_{s'_1})_{p_1} d(\vec{B}_{s'_2})_{p_2} \cdot d(\vec{B}_{s'_2})_{p_2}, \\ 1266 \quad (\text{D.47})$$

$$1268 \quad = \frac{8}{d} e^{-4s} \mathbb{E} \sum_{p_1, p_2=1}^d \int_0^s \int_0^{s'_1} \int_0^s \int_0^{s'_2} e^{s'_1+s''_1+s'_2+s''_2} \delta_{p_1, p_2} \delta(s'_1 - s'_2) \delta_{p_1, p_2} \delta(s''_1 - s''_2) ds'_1 ds''_1 ds'_2 ds''_2, \\ 1270 \quad (\text{D.48})$$

$$1272 \quad = 8e^{-4s} \int_0^s \int_0^{s'} e^{2(s'+s'')} ds' ds'', \quad (\text{D.49})$$

$$1275 \quad = 4e^{-4s} \int_0^s e^{2s'} (e^{2s'} - 1) ds', \quad (\text{D.50})$$

$$1277 \quad = e^{-4s} ((e^{4s} - 1) + 2(e^{2s} - 1)), \quad (\text{D.51})$$

$$1278 \quad \xrightarrow[s \rightarrow \infty]{} 1. \quad (\text{D.52})$$

□

### 1282 D.3.2 NORM DYNAMICS IN MSGM

1283 For MSGM, the norm follows totally different dynamics. We recall that the skew-symmetry of  $\circ d\vec{Z}_s$   
1284 implies that  $d\vec{x}_s = \circ d\vec{Z}_s \vec{x}_s$  is orthogonal to  $\vec{x}_s$  and hence:  
1285

$$1286 \quad d\|\vec{x}_s\|^2 = 2\vec{x}_s \cdot \circ d\vec{x}_s = 0, \quad \forall s \geq 0. \quad (\text{D.53})$$

1287 Consequently,  $\vec{x}_s$  moves randomly on  $\|\vec{x}_0\| \mathbb{S}^{d-1}$ , the  $d$ -sphere of radius  $\|\vec{x}_0\|$ , and the increments  
1288  $d\vec{x}_s$  are tangent to the  $d$ -sphere. In particular, we obtain the following result.  
1289

1290 **Proposition D.3.2.** *Let the skew-symmetry assumption A1 hold. Let  $\vec{x}_0$  be a random variable. Then,  
1291 for all  $s \geq 0$  the distribution of  $\|\vec{x}_s\|$  equals the distribution of  $\|\vec{x}_0\|$ .*

1292 Therefore, the distribution of the norms of the latent variable is exactly the distribution of the norms  
1293 of the points of the dataset. Moreover,  $\vec{x}_s \equiv 0$  if and only if  $\vec{x}_0 = 0$ . As a consequence, we can  
1294 exclude all points exactly equal to zero from a dataset, treat them aside, and hence consider, without  
1295 loss of generality, that  $\vec{x}_T \neq 0$  almost surely.

1296 D.4 FOKKER-PLANCK EQUATION OF THE DIRECTION  
12971298 This subsection is devoted to the analysis of the Fokker-Planck equation on the unit sphere  $\mathbb{S}^{d-1}$ , i.e.  
1299 the distribution of  $\vec{x}_s^n$ , in particular as  $s \rightarrow \infty$ .  
13001301 D.4.1 MAIN RESULTS ON THE DISTRIBUTION OF DIRECTIONS  
13021303 We saw in Appendix D.3 that  $\vec{x}_s$  moves randomly on the  $d$ -sphere of radius  $\|\vec{x}_0\|$  and that the  
1304 increments,  $d\vec{x}_s = \mathbf{G}(\vec{x}_s) \circ d\vec{B}_s$ , are tangent to the  $d$ -sphere. If the rank condition, assumption A2 is  
1305 verified, then the support of the noise distribution  $\mathbf{G}(\vec{x}_s) \circ d\vec{B}_s$  coincides with the  $d-1$ -dimensional  
1306 tangent space, i.e. it will likely explore all local directions around  $\vec{x}_s$ . With time, the support of the  
1307 solution distribution will gradually cover the whole  $d$ -sphere, i.e. every direction  $\vec{x}_s^n$  will become  
1308 equiprobable. Lemma D.4.1 illustrates and precises this claim.  
13091310 **Lemma D.4.1.** *Let assumptions A1 and A2 hold. Let a initial density  $p_0^n \in \mathcal{C}^2(\mathbb{S}^{d-1})$  and  $\Sigma(\mathbf{x}^n) :=$   
1311  $\mathbf{G}(\mathbf{x}^n)\mathbf{G}(\mathbf{x}^n)^\top$ . Then, the Fokker-Planck equation*

1312 
$$\frac{\partial}{\partial s} p_s^n(\mathbf{x}^n) = \nabla_{\perp} \cdot \left( \frac{1}{2} \Sigma(\mathbf{x}^n) \nabla_{\perp} p_s^n(\mathbf{x}^n) \right), \quad \mathbf{x}^n \in \mathbb{S}^{d-1}, \quad (\text{D.54})$$
  
1313

1314 has a unique density solution  $p_s^n \in \mathcal{C}^2(\mathbb{S}^{d-1})$  for all  $s > 0$ . oreover, there is a unique invariant  
1315 measure  $p_\infty^n$  of that Fokker-Planck equation, i.e. the uniform distribution on the  $d$ -sphere  $\mathcal{U}(\mathbb{S}^{d-1})$ ,  
1316 with density  
1317

1318 
$$p_\infty^n(\mathbf{x}^n) := \frac{1}{|\mathbb{S}^{d-1}|}, \quad \forall \mathbf{x}^n \in \mathbb{S}^{d-1}, \quad (\text{D.55})$$
  
1319

1320 with  $|\mathbb{S}^{d-1}| = 2\pi^{d/2}/\Gamma(\frac{d}{2})$  the volume of the  $d$ -sphere  $\mathbb{S}^{d-1}$  and  $\Gamma$  the gamma function.  
13211322 Lemma D.4.1 is a consequence of Theorem 3.1.1 as shown in Appendix D.4.2. Note that in this case  
1323  $\nabla_{\perp} = \nabla_{\mathbb{S}^{d-1}}$  is the Riemannian gradient on  $\mathbb{S}^{d-1}$ , see Appendix H.1.1324 Given the unique invariant measure of Fokker-Planck equation formulated on  $\mathbb{S}^{d-1}$ , we can also show  
1325 that we have exponential convergence of the initial distribution  $p_0^n$  to  $p_\infty^n$ , the uniform distribution on  
1326 the unit sphere  $\mathbb{S}^{d-1}$ .  
13271328 **Theorem D.4.1.** *Let assumptions A1 and A2 hold. Then, there exists  $\alpha = \alpha(\mathbf{G}, d) > 0$  with*

1329 
$$\|p_s^n - p_\infty^n\|_{L^2(\mathbb{S}^{d-1})}^2 \leq \exp(-\alpha s) \|p_0^n - p_\infty^n\|_{L^2(\mathbb{S}^{d-1})}^2. \quad (\text{D.56})$$
  
1330

1331 The convergence rate  $\alpha$  is given as  
1332

1333 
$$\alpha(\mathbf{G}, d) = (d-1) \min_{(\mathbf{x}, \mathbf{y}) \in S} \|\mathbf{G}^\top(\mathbf{x})\mathbf{y}\|^2, \quad S = \{(\mathbf{x}, \mathbf{y}) \in \mathbb{S}^{d-1} \times \mathbb{S}^{d-1} | \mathbf{x} \perp \mathbf{y}\}. \quad (\text{D.57})$$
  
1334

1335 Consequently, since  $\mathbb{S}^{d-1}$  is compact this implies convergence in total variation of  $p_s^n$  to  $p_\infty^n$  and  
1336 convergence in distribution of  $\vec{x}_s^n$  with  $\vec{x}_\infty^n \sim \mathcal{U}(\mathbb{S}^{d-1})$ . The full proof is detailed in Appendix D.4.3.  
13371338 D.4.2 PROOF OF LEMMA D.4.1  
13391340 *Proof. Existence and Uniqueness:*  
1341 Consider  $L(p_s^n) = \nabla_{\perp} \cdot \left( \frac{1}{2} \Sigma(\mathbf{x}) \nabla_{\perp} p_s^n(\mathbf{x}) \right) - \frac{\partial}{\partial s} p_s^n(\mathbf{x})$ .  $L$  is a parabolic type operator according to  
1342 Friedman (1964) since  $\mathbf{x} \mapsto \Sigma(\mathbf{x})$  is positive definite by assumption A2 on  $\mathbb{S}^{d-1}$ . Indeed, for any  
1343  $\mathbf{y} \in T_{\mathbf{x}} \mathbb{S}^{d-1}$  the tangential (linear) space of  $\mathbb{S}^{d-1}$  at  $\mathbf{x}$ ,

1344 
$$\mathbf{y}^\top \Sigma(\mathbf{x}) \mathbf{y} = \|\mathbf{G}^\top(\mathbf{x})\mathbf{y}\|^2 \geq 0. \quad (\text{D.58})$$
  
1345

1346 with equality if and only if  $\mathbf{G}^\top(\mathbf{x})\mathbf{y} = 0$ . Then, the rank condition A2 implies  $\mathbf{y} = 0$  as previously in  
1347 equation D.35. Consequently, the associated spatial operator  $L_0$  defined by  
1348

1349 
$$L_0 p_s^n = \nabla_{\perp} \cdot \left( \frac{1}{2} \Sigma(\mathbf{x}) \nabla_{\perp} p_s^n(\mathbf{x}) \right) \quad (\text{D.59})$$
  
1350

1351 is an elliptic operator on  $\mathbb{S}^{d-1}$ , a compact manifold without boundary such that the semi-group  $e^{sL_0}$   
1352 is strongly continuous on  $\mathcal{C}^2(\mathbb{S}^{d-1})$ ,  $s \geq 0$ . As  $p_0^n \in \mathcal{C}^2(\mathbb{S}^{d-1})$ , according to chapter 1, proposition

1350 1.1 in Taylor (2011), there exists a unique solution  $p_s^n \in \mathcal{C}^2(\mathbb{S}^{d-1})$ , for  $s \in [0, T]$  of [equation D.54](#).  
 1351 As the semigroup is well-defined for all  $s > 0$ , this extends the uniqueness of the solution to all  
 1352  $s > 0$ .

1353 *Invariant measure:* Repeating the lines in the proof of Theorem 3.1.1 given in Appendix D.2 it  
 1354 follows that  $p_\infty^n$  is rotation-invariant. The only rotation-invariant distribution on the  $d$ -sphere is the  
 1355 uniform distribution.  $\square$

1357 D.4.3 [PROOF OF THEOREM D.4.1 : LIMIT BEHAVIOR OF FOKKER-PLANCK EQUATION OF](#)  
 1358 [THE DIRECTION](#)

1360 **Theorem D.4.2.** *Let assumptions A1 and A2 hold. Then, there exists  $\alpha = \alpha(\mathbf{G}, d) > 0$  with*

$$1361 \|p_s^n - p_\infty^n\|_{L^2(\mathbb{S}^{d-1})}^2 \leq \exp(-\alpha s) \|p_0^n - p_\infty^n\|_{L^2(\mathbb{S}^{d-1})}^2. \quad (\text{D.60})$$

1363 *The convergence rate  $\alpha$  is given as*

$$1364 \alpha(\mathbf{G}, d) = (d-1) \min_{(\mathbf{x}, \mathbf{y}) \in S} \|\mathbf{G}^\top(\mathbf{x})\mathbf{y}\|^2, \quad S = \{(\mathbf{x}, \mathbf{y}) \in \mathbb{S}^{d-1} \times \mathbb{S}^{d-1} \mid \mathbf{x} \perp \mathbf{y}\}. \quad (\text{D.61})$$

1367 *Proof.* Let  $p_s^n$  denoting the density of  $\vec{\mathbf{x}}_s^n$ . Define  $e_s^n = p_s^n - p_\infty^n$  with  $p_\infty^n \equiv |\mathbb{S}^{d-1}|^{-1}$  being the  
 1368 uniform distribution on  $\mathbb{S}^{d-1}$ . Then, by linearity of the Fokker-Planck equation,  $e_t^n$  satisfies

$$1369 \partial_t e_t^n = \nabla_\perp \cdot \left( \frac{1}{2} \Sigma(\mathbf{x}) \nabla_\perp e_t^n(\mathbf{x}) \right). \quad (\text{D.62})$$

1371 Since  $p_s^n$  and  $p_\infty^n$  are densities on  $\mathbb{S}^{d-1}$ , we have  $\int_{\mathbb{S}^{d-1}} e_s^n d\mathbf{x} = 0$  for all  $s \geq 0$ . Consequently, since  
 1372  $\mathbb{S}^{d-1}$  is a compact manifold without boundary, Poincaré inequality holds, i.e.

$$1373 \|e_t^n\|_{L^2(\mathbb{S}^{d-1})}^2 \leq \frac{1}{d-1} \|\nabla_{\mathbb{S}^{d-1}} e_t^n\|_{L^2(\mathbb{S}^{d-1})}^2, \quad (\text{D.63})$$

1375 with

$$1376 \nabla_{\mathbb{S}^{d-1}} e_t^n(\mathbf{y})|_{\mathbf{y}=\mathbf{x}} = \text{Proj}_{\mathcal{T}_{\mathbf{x}, \mathbb{S}^{d-1}}} \nabla e_t^n(\mathbf{y})|_{\mathbf{y}=\mathbf{x}} = \nabla_\perp e_t^n(\mathbf{x}). \quad (\text{D.64})$$

1378 Consequently, integration by part on  $\mathbb{S}^{d-1}$  leads to

$$1379 \frac{1}{2} \frac{d}{dt} \|e_t^n\|_{L^2(\mathbb{S}^{d-1})}^2 = \int_{\mathbb{S}^{d-1}} e_t^n(\mathbf{x}) \nabla_\perp \cdot \left( \frac{1}{2} \Sigma(\mathbf{x}) \nabla_\perp e_t^n(\mathbf{x}) \right) d\mathbf{x}, \quad (\text{D.65})$$

$$1382 = - \int_{\mathbb{S}^{d-1}} \nabla_\perp e_t^n(\mathbf{x})^\top \Sigma(\mathbf{x}) \nabla_\perp e_t^n(\mathbf{x}) d\mathbf{x}. \quad (\text{D.66})$$

1384 We will now bound  $\mathbf{y}^\top \Sigma(\mathbf{x}) \mathbf{y}^\top$  from below for any  $\mathbf{y} \in \mathbf{x}^\perp$  and  $\mathbf{x} \in \mathbb{S}^{d-1}$ , in particular with a  
 1385 bound independent of  $\mathbf{x}$ . Since  $\Sigma(\mathbf{x})$  is symmetric, it is real diagonalizable with eigen-basis denoted  
 1386 as  $\mathbf{v}_1(\mathbf{x}), \dots, \mathbf{v}_d(\mathbf{x}) \in \mathbb{R}^d$  and eigenvalues  $\lambda_1(\mathbf{x}), \dots, \lambda_d(\mathbf{x})$ . By construction  $\Sigma(\mathbf{x})\mathbf{x} = 0$ , hence  
 1387 we can set  $\mathbf{v}_d(\mathbf{x}) := \mathbf{x}/\|\mathbf{x}\|$  and  $\lambda_d(\mathbf{x}) \equiv 0$ . Moreover, by the rank condition A2,  $\lambda_i \neq 0$  for  $i \neq d$ .  
 1388 By orthonormality of the eigenvectors  $\mathbf{v}_1(\mathbf{x}), \dots, \mathbf{v}_{d-1}(\mathbf{x})$  then span the tangent plane  $\mathbf{x}^\perp$  at  $\mathbf{x}$  on  
 1389  $\mathbb{S}^{d-1}$ . For any  $i = 1, \dots, d-1$ , we have that

$$1390 \lambda_i(\mathbf{x}) = \mathbf{v}_i(\mathbf{x})^\top \Sigma(\mathbf{x}) \mathbf{v}_i(\mathbf{x}) = \|\mathbf{G}^\top(\mathbf{x}) \mathbf{v}_i(\mathbf{x})\|^2 \geq \min_{\mathbf{y} \in \mathbf{x}^\perp} \frac{\|\mathbf{G}^\top(\mathbf{x}) \mathbf{y}\|^2}{\|\mathbf{y}\|^2}. \quad (\text{D.67})$$

1393 The polynomial  $(\mathbf{x}, \mathbf{y}) \mapsto P(\mathbf{x}, \mathbf{y}) = \|\mathbf{G}^\top(\mathbf{x}) \mathbf{y}\|^2$  on the compact  $S = \{(\mathbf{x}, \mathbf{y}) \in \mathbb{S}^{d-1} \times$   
 1394  $\mathbb{S}^{d-1} \mid \mathbf{x} \perp \mathbf{y}\}$  attains its minimum  $P^*$ , which from the rank condition satisfies  $P(\mathbf{x}, \mathbf{y}) \geq P^* > 0$  for  
 1395 all  $(\mathbf{x}, \mathbf{y}) \in S$ . As a consequence  $\lambda_i(\mathbf{x}) \geq P^*$  for  $i = 1, \dots, d-1$  and  $\mathbf{x} \in \mathbb{S}^{d-1}$ , which implies for  
 all  $\mathbf{y} \in \mathbf{x}^\perp$  that

$$1396 \mathbf{y}^\top \Sigma(\mathbf{x}) \mathbf{y} = \|\mathbf{G}^\top(\mathbf{x}) \mathbf{y}\|^2 \geq P^* \|\mathbf{y}\|^2. \quad (\text{D.68})$$

1397 Therefore, combining equation D.63, equation D.64 and equation D.66, we obtain

$$1399 \frac{1}{2} \frac{d}{dt} \|e_t^n\|_{L^2(\mathbb{S}^{d-1})}^2 \leq -P^* \|\nabla_\perp e_s^n\|_{L^2(\mathbb{S}^{d-1})}^2 \leq -P^*(d-1) \|e_s^n\|_{L^2(\mathbb{S}^{d-1})}^2. \quad (\text{D.69})$$

1401 Then, by Gronwall for  $\alpha = P^*(d-1) > 0$ , we conclude that

$$1402 \|p_s^n - p_\infty^n\|_{L^2(\mathbb{S}^{d-1})}^2 = \|e_s^n\|_{L^2(\mathbb{S}^{d-1})}^2 \leq \|e_0^n\|_{L^2(\mathbb{S}^{d-1})}^2 \exp(-\alpha s). \quad (\text{D.70})$$

1403  $\square$

1404 D.5 PROOF OF THEOREM 3.3.1 : CONVERGENCE OF FOKKER-PLANCK EQUATION  
1405

1406 This section is devoted to the analysis of the Fokker-Planck equation in the whole domain  $\mathbb{R}^d$ . Due to  
1407 the fact that the norm of a point does not change in the SDE process as shown in equation 3.7 and the  
1408 fact that  $\Sigma(\mathbf{x}) = 0$  for  $\mathbf{x} = 0$ , we exclude the origin in the analysis.

1409 **Theorem D.5.1.** *Let  $D = \mathbb{R}^d \setminus \{0\}$  for  $d > 1$ . Let assumptions A1 and A2 hold. Let  $\vec{\mathbf{x}}_0 \sim p_0 \in \mathcal{C}^2(D)$   
1410 and let  $p_{|\cdot|}$  be the (radial) density of  $\|\vec{\mathbf{x}}_0\|$ . Then, the Fokker-Planck equation*

$$1412 \quad \frac{\partial}{\partial s} p_s(\mathbf{x}) = \nabla_{\perp} \cdot \left( \frac{1}{2} \Sigma(\mathbf{x}) \nabla_{\perp} p_s(\mathbf{x}) \right), \quad \mathbf{x} \in D, \quad (\text{D.71})$$

1414 has a unique solution  $p_s \in \mathcal{C}^2(D) \cap L^2(D)$  for all  $s > 0$ . Moreover, the Fokker-Planck equation has  
1415 the stationary distribution  
1416

$$1417 \quad p_{\infty}(\mathbf{x}) = \frac{p_{|\cdot|}(\|\mathbf{x}\|)}{\|\mathbf{x}\|^{d-1}} \frac{1}{|\mathbb{S}^{d-1}|}. \quad (\text{D.72})$$

1419 In particular,  $\|\vec{\mathbf{x}}_s\|$  and  $\vec{\mathbf{x}}_s^n$  are asymptotically independent for  $s \rightarrow +\infty$ . Moreover, there exists  
1420  $\alpha = \alpha(\mathbf{G}, d) > 0$  such that  
1421

$$1422 \quad \|p_s - p_{\infty}\|_{L^2(\mathbb{R}^d)}^2 \leq \exp(-\alpha s) \|p_0 - p_{\infty}\|_{L^2(\mathbb{R}^d)}^2.$$

1424 The convergence rate  $\alpha$  is given as

$$1425 \quad \alpha(\mathbf{G}, d) = (d-1) \min_{(\mathbf{x}, \mathbf{y}) \in S} \|\mathbf{G}^T(\mathbf{x})\mathbf{y}\|^2, \quad S = \{(\mathbf{x}, \mathbf{y}) \in \mathbb{S}^{d-1} \times \mathbb{S}^{d-1} \mid \mathbf{x} \perp \mathbf{y}\}. \quad (\text{D.73})$$

1428 *Proof.* We will proof existence, uniqueness, regularity, invariant property and convergence separately.

1429 *Existence:* Let  $p_0(\mathbf{x}^n \|\vec{\mathbf{x}}_0\| = r)$  be the start value of the FP equation D.54 on  $\mathbb{S}^{d-1}$  of Lemma D.4.1.  
1430 This gives rise to a smooth unique density solution  $p_s^n(\mathbf{x}^n \|\vec{\mathbf{x}}_0\| = r)$  for  $s > 0$  and any  $r > 0$ .  
1431 Moreover,  $p_s^n(\mathbf{x}^n \|\vec{\mathbf{x}}_0\| = r) = p_s^n(\mathbf{x}^n \|\vec{\mathbf{x}}_s\| = r)$  since  $d\|\vec{\mathbf{x}}_s\| = 0$ . Now define  
1432

$$1434 \quad \rho_s(\mathbf{x}) = p_s^n(\mathbf{x}^n \|\vec{\mathbf{x}}_s\| = \|\mathbf{x}\|) p_{|\cdot|}(\|\mathbf{x}\|) \|\mathbf{x}\|^{1-d},$$

1435 where we denote  $\mathbf{x}^n = \frac{\mathbf{x}}{\|\mathbf{x}\|}$ .  $\rho_s$  is a density since  
1436

$$1437 \quad \int_{\mathbb{R}^d} \rho_s(\mathbf{x}) d\mathbf{x} = \int_{\mathbb{R}^d} p_s^n(\mathbf{x}^n \|\vec{\mathbf{x}}_s\| = \|\mathbf{x}\|) p_{|\cdot|}(\|\mathbf{x}\|) \|\mathbf{x}\|^{1-d} d\mathbf{x}, \quad (\text{D.74})$$

$$1440 \quad = \int_{\mathbb{R}_+} \int_{\mathbb{S}^{d-1}} p_s^n(\mathbf{x}^n \|\vec{\mathbf{x}}_s\| = r) p_{|\cdot|}(r) r^{1-d} r^{d-1} dr d\mathbf{x}^n, \quad (\text{D.75})$$

$$1443 \quad = \int_{\mathbb{R}_+} \int_{\mathbb{S}^{d-1}} p_s^n(\mathbf{x}^n \|\vec{\mathbf{x}}_s\| = r) p_{|\cdot|}(r) dr d\mathbf{x}^n, \quad (\text{D.76})$$

$$1446 \quad = \int_{\mathbb{R}_+} p_{|\cdot|}(r) \left( \int_{\mathbb{S}^{d-1}} p_s^n(\mathbf{x}^n \|\vec{\mathbf{x}}_s\| = r) d\mathbf{x}^n \right) dr, \quad (\text{D.77})$$

$$1449 \quad = 1. \quad (\text{D.78})$$

1451 We have  $\nabla_{\perp} = \frac{1}{\|\mathbf{x}\|} \nabla_{\mathbb{S}^{d-1}}$  and  $\nabla_{\perp}$  does not act on radial functions. Besides,  $\Sigma(\mathbf{x}) := \mathbf{G}(\mathbf{x})\mathbf{G}(\mathbf{x})^T$   
1452 with  $\mathbf{G}$  linear so  $\Sigma(\mathbf{x}) = \Sigma(\|\mathbf{x}\| \frac{\mathbf{x}}{\|\mathbf{x}\|}) = \|\mathbf{x}\|^2 \Sigma(\mathbf{x}^n)$ . Hence  
1453

$$1454 \quad \nabla_{\perp} \rho_s(\mathbf{x}) = \nabla_{\perp} p_s^n(\mathbf{x}^n \|\vec{\mathbf{x}}_s\| = \|\mathbf{x}\|) p_{|\cdot|}(\|\mathbf{x}\|) \|\mathbf{x}\|^{1-d}, \quad (\text{D.79})$$

$$1455 \quad = p_{|\cdot|}(\|\mathbf{x}\|) \|\mathbf{x}\|^{1-d} \nabla_{\perp} p_s^n(\mathbf{x}^n \|\vec{\mathbf{x}}_s\| = \|\mathbf{x}\|), \quad (\text{D.80})$$

$$1456 \quad = p_{|\cdot|}(\|\mathbf{x}\|) \|\mathbf{x}\|^{1-d} \left( \frac{1}{\|\mathbf{x}\|} \nabla_{\mathbb{S}^{d-1}} \right) p_s^n(\mathbf{x}^n \|\vec{\mathbf{x}}_s\| = \|\mathbf{x}\|), \quad (\text{D.81})$$

1458

and

$$\Sigma(\mathbf{x}) \nabla_{\perp} \rho_s(\mathbf{x}) = \Sigma(\mathbf{x}) p_{\perp}(\|\mathbf{x}\|) \|\mathbf{x}\|^{1-d} \frac{1}{\|\mathbf{x}\|} \nabla_{\mathbb{S}^{d-1}} p_s^n(\mathbf{x}^n \|\vec{\mathbf{x}}_s\| = \|\mathbf{x}\|), \quad (\text{D.82})$$

$$= \|\mathbf{x}\|^2 \Sigma(\mathbf{x}^n) p_{\perp}(\|\mathbf{x}\|) \|\mathbf{x}\|^{1-d} \frac{1}{\|\mathbf{x}\|} \nabla_{\mathbb{S}^{d-1}} p_s^n(\mathbf{x}^n \|\vec{\mathbf{x}}_s\| = \|\mathbf{x}\|), \quad (\text{D.83})$$

$$= \|\mathbf{x}\|^2 p_{\perp}(\|\mathbf{x}\|) \|\mathbf{x}\|^{1-d} \frac{1}{\|\mathbf{x}\|} \Sigma(\mathbf{x}^n) \nabla_{\mathbb{S}^{d-1}} p_s^n(\mathbf{x}^n \|\vec{\mathbf{x}}_s\| = \|\mathbf{x}\|) \quad (\text{D.84})$$

$$\nabla_{\perp} \cdot (\Sigma(\mathbf{x}) \nabla_{\perp} \rho_s(\mathbf{x})) = \frac{1}{\|\mathbf{x}\|} \nabla_{\mathbb{S}^{d-1}} \cdot \left( \|\mathbf{x}\| p_{\perp}(\|\mathbf{x}\|) \|\mathbf{x}\|^{1-d} \Sigma(\mathbf{x}^n) \nabla_{\mathbb{S}^{d-1}} p_s^n(\mathbf{x}^n \|\vec{\mathbf{x}}_s\| = \|\mathbf{x}\|) \right), \quad (\text{D.85})$$

$$= p_{\perp}(\|\mathbf{x}\|) \|\mathbf{x}\|^{1-d} \nabla_{\mathbb{S}^{d-1}} \cdot \left( \Sigma(\mathbf{x}^n) \nabla_{\mathbb{S}^{d-1}} p_s^n(\mathbf{x}^n \|\vec{\mathbf{x}}_s\| = \|\mathbf{x}\|) \right), \quad (\text{D.86})$$

$$= p_{\perp}(\|\mathbf{x}\|) \|\mathbf{x}\|^{1-d} 2 \frac{\partial}{\partial s} p_s^n(\mathbf{x}^n \|\vec{\mathbf{x}}_s\| = \|\mathbf{x}\|), \quad (\text{D.87})$$

$$= 2 \frac{\partial}{\partial s} \left( p_{\perp}(\|\mathbf{x}\|) \|\mathbf{x}\|^{1-d} p_s^n(\mathbf{x}^n \|\vec{\mathbf{x}}_s\| = \|\mathbf{x}\|) \right), \quad (\text{D.88})$$

$$= 2 \frac{\partial}{\partial s} \rho_s(\mathbf{x}), \quad (\text{D.89})$$

i.e.  $\frac{\partial}{\partial s} \rho_s(\mathbf{x}) = \frac{1}{2} \nabla_{\perp} \cdot (\Sigma(\mathbf{x}) \nabla_{\perp} \rho_s(\mathbf{x}))$ . Then,  $\rho_s$  solves the Fokker-Planck equation on  $\mathbb{R}^d$ .

1479

1480 *Uniqueness:* Assume there exists another  $\tilde{\rho}$  solving the FP on  $\mathbb{R}^d$  verify

$$1481 \quad \tilde{\rho}_s(\mathbf{x}) = \rho_{1,s}(\mathbf{x}^n \|\mathbf{x}\|) \rho_{2,s}(\|\mathbf{x}\|).$$

1483 Since  $d\|\vec{\mathbf{x}}_s\| = 0$ , by marginalizing  $\tilde{\rho}_s$  (integrating on  $\mathbb{S}^{d-1}$ ), we have the uniqueness of the radial  
1484 density  $\rho_{2,s}(r) = \int_{\mathbb{S}^{d-1}} \tilde{\rho}_s(r \mathbf{x}^n) d\mathbf{x}^n = p_{\|\vec{\mathbf{x}}_s\|}(r) r^{1-d} = p_{\perp}(\|\mathbf{x}\|) r^{1-d}$ .  
1485

1486 Since  $d\|\vec{\mathbf{x}}_s\| = 0$ , we have  $\frac{\partial}{\partial s} \rho_{2,s}(\|\mathbf{x}\|) = 0$ . Therefore,  
1487

$$\frac{\partial}{\partial s} \tilde{\rho}_s(\mathbf{x}) = \frac{\partial}{\partial s} (\rho_{1,s}(\mathbf{x}^n \|\mathbf{x}\|) \rho_{2,s}(\|\mathbf{x}\|)), \quad (\text{D.90})$$

$$= \rho_{2,s}(\|\mathbf{x}\|) \frac{\partial}{\partial s} \rho_{1,s}(\mathbf{x}^n \|\mathbf{x}\|) + \rho_{1,s}(\mathbf{x}^n \|\mathbf{x}\|) \frac{\partial}{\partial s} \rho_{2,s}(\|\mathbf{x}\|), \quad (\text{D.91})$$

$$= \rho_{2,s}(\|\mathbf{x}\|) \frac{\partial}{\partial s} \rho_{1,s}(\mathbf{x}^n \|\mathbf{x}\|). \quad (\text{D.92})$$

1494 In addition,

$$2 \frac{\partial}{\partial s} \tilde{\rho}_s(\mathbf{x}) = \nabla_{\perp} \cdot (\Sigma(\mathbf{x}) \nabla_{\perp} \tilde{\rho}_s(\mathbf{x})), \quad (\text{D.93})$$

$$= \nabla_{\perp} \cdot (\Sigma(\mathbf{x}) \nabla_{\perp} \rho_{1,s}(\mathbf{x}^n \|\mathbf{x}\|) \rho_{2,s}(\|\mathbf{x}\|)), \quad (\text{D.94})$$

$$= \rho_{2,s}(\|\mathbf{x}\|) \|\mathbf{x}\|^2 \nabla_{\perp} \cdot (\Sigma(\mathbf{x}^n) \nabla_{\perp} \rho_{1,s}(\mathbf{x}^n \|\mathbf{x}\|)), \quad (\text{D.95})$$

$$= \rho_{2,s}(\|\mathbf{x}\|) \nabla_{\mathbb{S}^{d-1}} \cdot (\Sigma(\mathbf{x}^n) \nabla_{\mathbb{S}^{d-1}} \rho_{1,s}(\mathbf{x}^n \|\mathbf{x}\|)), \quad (\text{D.96})$$

1501 and finally,

$$1502 \quad \rho_{2,s}(\|\mathbf{x}\|) \left( 2 \frac{\partial}{\partial s} \rho_{1,s}(\mathbf{x}^n \|\mathbf{x}\|) - \nabla_{\mathbb{S}^{d-1}} \cdot (\Sigma(\mathbf{x}^n) \nabla_{\mathbb{S}^{d-1}} \rho_{1,s}(\mathbf{x}^n \|\mathbf{x}\|)) \right) = 0. \quad (\text{D.97})$$

1504 Then,  $\rho_{1,s}(\mathbf{x}^n \|\mathbf{x}\|)$  is a solution of the de Fokker-Planck equation on the sphere, for any  $\mathbf{x}$  such that  
1505  $\|\mathbf{x}\| \in A := \{r \in \mathbb{R}^+ | \rho_{2,s}(r) > 0\}$ . If  $\|\mathbf{x}\| \notin A$ , then  $\rho_{2,s}(\|\mathbf{x}\|) = 0$  and

$$1507 \quad \rho_s(\mathbf{x}) = p_s^n(\mathbf{x}^n \|\vec{\mathbf{x}}_s\| = \|\mathbf{x}\|) p_{\perp}(\|\mathbf{x}\|) \|\mathbf{x}\|^{1-d}.$$

1508 For  $\|\mathbf{x}\| \in A$ , then  $\rho_{2,s}(\|\mathbf{x}\|) \neq 0$  and  $\rho_{1,s}(\|\mathbf{x}\|)$  is solution of the Fokker Planck equation  
1509 D.54. According to [lemma D.4.1](#), the Fokker Planck equation D.54 has a unique density  
1510 solution  $p_s^n(\mathbf{x}^n \|\vec{\mathbf{x}}_s\| = \|\mathbf{x}\|)$ . Hence, for any  $\mathbf{x}$  such that  $p_{\perp}(\|\mathbf{x}\|) > 0$ , we have  
1511

$$\rho_s(\mathbf{x}) = p_s^n(\mathbf{x}^n \|\vec{\mathbf{x}}_s\| = \|\mathbf{x}\|) p_{\perp}(\|\mathbf{x}\|) \|\mathbf{x}\|^{1-d}.$$

1512 It is true for any  $\mathbf{x}$ . So,  $\rho_s(\mathbf{x})$  is the unique solution of the Fokker Planck in  $\mathbb{R}^d$ .  
 1513

1514 *Regularity:* By definition of the marginal density, we have  
 1515

$$1518 p_{|\cdot|}(r) := \int_{\mathbb{S}^{d-1}} p_0(\Phi(r, \boldsymbol{\theta})) r^{d-1} d\boldsymbol{\theta} = r^{d-1} \int_{\mathbb{S}^{d-1}} p_0(\Phi(r, \boldsymbol{\theta})) d\boldsymbol{\theta}.$$

1522 with  $\Phi(r, \boldsymbol{\theta}) = r\boldsymbol{\theta}$ . According to the assumption  $\vec{\mathbf{x}}_0 \sim p_0 \in \mathcal{C}^2(\mathbb{R}^d \setminus \{0\})$  and compactness of  $\mathbb{S}^{d-1}$ ,  
 1523 one can conclude that  $p_{|\cdot|} \in \mathcal{C}^2([0, \infty[)$ .  
 1524

1525 Since  $p_0(\mathbf{x}^n \mid \|\vec{\mathbf{x}}_0\| = r)$  is  $\mathcal{C}^2$ , we have that  $p_s^n(\mathbf{x}^n \mid \|\vec{\mathbf{x}}_s\| = r)$  is smooth by Lemma D.4.1 for any  
 1526  $s > 0$ . Consequently,  $\rho_s(\mathbf{x})$  is smooth on  $D$  for any  $s > 0$ .  
 1527

1528 *Invariant distribution:* The distribution  
 1529

$$1532 p_\infty(\mathbf{x}) = \frac{p_{|\cdot|}(\|\mathbf{x}\|)}{\|\mathbf{x}\|^{d-1}} \frac{1}{|\mathbb{S}^{d-1}|}.$$

1536 is radial function in  $\|\mathbf{x}\|$ . The operator  $\nabla_\perp$  does not act on radial functions and  $\frac{1}{|\mathbb{S}^{d-1}|}$  is in the kernel  
 1537 of  $\nabla_\perp$  such that  $\nabla_\perp(\frac{1}{|\mathbb{S}^{d-1}|}) = 0$ . Hence  
 1538

$$1541 \frac{\partial}{\partial s} p_\infty(\mathbf{x}) = \nabla_\perp \cdot \left( \frac{1}{2} \boldsymbol{\Sigma}(\mathbf{x}) \nabla_\perp p_\infty(\mathbf{x}) \right), \quad \mathbf{x} \in D, \quad (D.98)$$

$$1543 = \nabla_\perp \cdot \left( \frac{1}{2} \boldsymbol{\Sigma}(\mathbf{x}) \nabla_\perp \left( \frac{p_{|\cdot|}(\|\mathbf{x}\|)}{\|\mathbf{x}\|^{d-1}} \frac{1}{|\mathbb{S}^{d-1}|} \right) \right), \quad (D.99)$$

$$1545 = \nabla_\perp \cdot \left( \frac{1}{2} \frac{p_{|\cdot|}(\|\mathbf{x}\|)}{\|\mathbf{x}\|^{d-1}} \boldsymbol{\Sigma}(\mathbf{x}) \nabla_\perp \left( \frac{1}{|\mathbb{S}^{d-1}|} \right) \right), \quad (D.100)$$

$$1548 = 0. \quad (D.101)$$

1550 Therefore, the Fokker-Planck distribution  $p_\infty$  is the stationary . In addition ,  $p_\infty$  is a density since  
 1551

$$1554 \int_{\mathbb{R}^d} p_\infty(\mathbf{x}) d\mathbf{x} = \int_{\mathbb{R}^d} \frac{p_{|\cdot|}(\|\mathbf{x}\|)}{\|\mathbf{x}\|^{d-1}} \frac{1}{|\mathbb{S}^{d-1}|} d\mathbf{x}, \quad (D.102)$$

$$1557 = \int_{\mathbb{R}_+} \int_{\mathbb{S}^{d-1}} \frac{p_{|\cdot|}(r)}{r^{d-1}} \frac{1}{|\mathbb{S}^{d-1}|} r^{d-1} dr d\mathbf{x}^n, \quad (D.103)$$

$$1560 = \int_{\mathbb{R}_+} \int_{\mathbb{S}^{d-1}} p_{|\cdot|}(r) \frac{1}{|\mathbb{S}^{d-1}|} dr d\mathbf{x}^n, \quad (D.104)$$

$$1563 = \int_{\mathbb{R}_+} p_{|\cdot|}(r) dr \int_{\mathbb{S}^{d-1}} \frac{1}{|\mathbb{S}^{d-1}|} d\mathbf{x}^n, \quad (D.105)$$

$$1565 = 1. \quad (D.106)$$

1566 *Convergence:* Hence, we obtain for  $p_s = \rho_s$  that, we can bound the speed of convergence

$$\|p_s - p_\infty\|_{L^2(\mathbb{R}^d)}^2 = \int_{\mathbb{R}^d} \left| p_s^n(\mathbf{x}^n \mid |\vec{\mathbf{x}}_s| = \|\mathbf{x}\|) p_{|\cdot|}(\|\mathbf{x}\|) \|\mathbf{x}\|^{1-d} - \frac{p_{|\cdot|}(\|\mathbf{x}\|)}{\|\mathbf{x}\|^{d-1}} \frac{1}{|\mathbb{S}^{d-1}|} \right|^2 d\mathbf{x}, \quad (\text{D.107})$$

$$= \int_{\mathbb{R}^d} \left| p_s^n(\mathbf{x}^n \mid |\vec{\mathbf{x}}_s| = \|\mathbf{x}\|) - \frac{1}{|\mathbb{S}^{d-1}|} \right|^2 \frac{p_{|\cdot|}(\|\mathbf{x}\|)^2}{\|\mathbf{x}\|^{2d-2}} d\mathbf{x}, \quad (\text{D.108})$$

$$1575 \quad = \int_{\mathbb{R}_+} \left( \int_{\mathbb{S}^{d-1}} \left| p_s(\boldsymbol{\theta} \mid |\vec{\mathbf{x}}_s| = r) - \frac{1}{|\mathbb{S}^{d-1}|} \right|^2 d\boldsymbol{\theta} \right) \frac{p_{|\cdot|}(r)^2}{r^{d-1}} dr, \quad (D.109)$$

$$1576$$

$$1577$$

$$= \int_{\mathbb{R}_+} \left( \left\| p_s(\cdot \mid |\vec{\mathbf{x}}_s| = r) - \frac{1}{|\mathbb{S}^{d-1}|} \right\|_{L^2(\mathbb{S}^{d-1})}^2 \right) \frac{p_{|\cdot|}(r)^2}{r^{d-1}} dr, \quad (\text{D.110})$$

$$\leq \exp(-\alpha s) \int_{\mathbb{R}_+} \left( \left\| p_0(\theta \mid \|\vec{x}_0\| = r) - \frac{1}{|\mathbb{S}^{d-1}|} \right\|_{L^2(\mathbb{S}^{d-1})}^2 \right) \frac{p_{|\cdot|}(r)^2}{r^{d-1}} dr, \quad (\text{D.111})$$

$$= \exp(-\alpha s) \int_{\mathbb{R}^d} \left| p_0(\mathbf{x}^n \|\vec{\mathbf{x}}_0\| = \|\mathbf{x}\|) - \frac{1}{|\mathbb{S}^{d-1}|} \right|^2 \frac{p_{|\cdot|}(\|\mathbf{x}\|)^2}{\|\mathbf{x}\|^{2d-2}} d\mathbf{x}, \quad (\text{D.112})$$

$$= \exp(-\alpha s) \int_{\mathbb{R}^d} \left| p_0(\mathbf{x}^n \mid \|\vec{\mathbf{x}}_0\| = \|\mathbf{x}\|) p_{|\cdot|}(\|\mathbf{x}\|) \|\mathbf{x}\|^{1-d} - \frac{p_{|\cdot|}(\|\mathbf{x}\|)}{\|\mathbf{x}\|^{d-1}} \frac{1}{|\mathbb{S}^{d-1}|} \right|^2 d\mathbf{x}, \quad (\text{D.113})$$

$$= \exp(-\alpha s) \|p_0 - p_\infty\|_{L^2(\mathbb{R}^d)}^2, \quad (\text{D.114})$$

where in the inequality we used Theorem D.4.2. The upper bound is finite since  $p_\infty \in L^2(\mathbb{R}^d)$ . In order to see this, we will show that the function  $p_{|\cdot|}(r)r^{\frac{1-d}{2}}$  is in  $L^2(0, \infty)$ . Recall that

$$p_{|\cdot|}(r) := \int_{\mathbb{S}^{d-1}} p_0(\Phi(r, \theta)) r^{d-1} d\theta = r^{d-1} \int_{\mathbb{S}^{d-1}} p_0(\Phi(r, \theta)) d\theta.$$

Then, application of Jensen inequality leads

$$\int_{\mathbb{R}_+} p_{|\cdot|}(r)^2 r^{1-d} dr = \int_{\mathbb{R}_+} \left( r^{d-1} \int_{\mathbb{S}^{d-1}} p_0(\Phi(r, \boldsymbol{\theta})) d\boldsymbol{\theta} \right)^2 r^{1-d} dr, \quad (\text{D.115})$$

$$= \int_{\mathbb{R}_+} \left( \int_{\mathbb{S}^{d-1}} p_0(\Phi(r, \theta)) d\theta \right)^2 r^{d-1} dr, \quad (\text{D.116})$$

$$\leq |\mathbb{S}^{d-1}| \int_{\mathbb{B}^d} \int_{\mathbb{S}^{d-1}} p_0(\Phi(r, \theta))^2 r^{d-1} d\theta dr, \quad (\text{D.117})$$

$$= |\mathbb{S}^{d-1}| \|p_0\|_{L^2(\mathbb{P}_d)}^2. \quad (\text{D.118})$$

Consequently,

$$\|p_\infty\|_{L^2(\mathbb{R}^d)}^2 = \left\| \frac{p_{|\cdot|}(\|\boldsymbol{x}\|)}{\|\boldsymbol{x}\|^{d-1}} \frac{1}{|\mathbb{S}^{d-1}|} \right\|_{L^2(\mathbb{R}^d)}^2, \quad (\text{D.119})$$

$$= \frac{1}{|\mathbb{S}^{d-1}|^2} \int_{\mathbb{S}^{d-1}} \int_{B_+} \frac{p_{|\cdot|}(r)^2}{r^{d-1}} dr d\theta \leq \frac{1}{|\mathbb{S}^{d-1}|} \|p_0\|_{L^2(\mathbb{R}^d)}^2 < \infty. \quad (\text{D.120})$$

1

1620 D.6 BEYOND PURE STRATONOVICH NOISE  
16211622 A possible extension to the described diffusion in equation 3.1 would be to add a drift term, i.e.  
1623 considering

1624 
$$d\vec{\mathbf{x}}_s = \mathbf{A}\vec{\mathbf{x}}_s ds + \mathbf{G}(\vec{\mathbf{x}}_s) \circ d\vec{\mathbf{B}}_s,$$

1625 with a skew-symmetric matrix  $\mathbf{A} \in \mathbb{R}^{d,d}$ . Then, the associated Fokker-Planck equations will  
1626 additional involve an advection term  $(\mathbf{A}\mathbf{x}) \cdot \nabla_{\perp} p_s$ , which can be used to improve the speed of  
1627 convergence of the dynamics.  
16281629 E LATENT DISTRIBUTION  
16301631 The latent vectors  $\vec{\mathbf{x}}_{\infty} \sim p_{\infty}$  of additive SGM are Gaussian white noises. This is not the case for  
1632 MSGM in general. This appendix will elaborate on this point. First, we will show that MSGM latent  
1633 vectors are white noise in the weak sense. Then, we will discuss the conditions for these latent vectors  
1634 to be Gaussian, how to sample them, and how to transform map them to another latent space which  
1635 is Gaussian. We also show that the MSGM latent distribution is always closer than the SGM latent  
1636 distribution to the data distribution. Finally, we focus on the case of Cauchy data distribution, where  
1637 SGM leads to singularity, unlike MSGM.  
16381639 E.1 THE INVARIANT MEASURES DEFINE WHITE NOISES IN THE WEAK SENSE  
16401641 In additive SGM, latent vectors  $\vec{\mathbf{x}}_{\infty} \sim p_{\infty}$  are Gaussian white noise in the strong sense, i.e. for any  
1642  $i \neq j$ , the coordinates  $(\vec{\mathbf{x}}_{\infty})_i$  and  $(\vec{\mathbf{x}}_{\infty})_j$  are centered, independent, and identically distributed. In  
1643 contrast, the latent vectors of MSGM are white noises in the weak sense, as stated by the following  
1644 proposition. For any  $i \neq j$ , the coordinates  $(\vec{\mathbf{x}}_{\infty})_i$  and  $(\vec{\mathbf{x}}_{\infty})_j$  are uncorrelated but neither Gaussian  
1645 nor independent, in general.1646 **Proposition E.1.1.** *Let the assumptions A1 and A2 hold,  $\mathbb{E}\|\vec{\mathbf{x}}_{\infty}\|^2 < +\infty$ , and  $p_{\infty}$  be a stationary  
1647 density of the Fokker-Planck equation D.22. Then,  $\vec{\mathbf{x}}_{\infty} \sim p_{\infty}$  is a white noise in the weak sense,  
1648 i.e.  $\mathbb{E}\vec{\mathbf{x}}_{\infty} = 0$ ,  $\mathbb{E}(\vec{\mathbf{x}}_{\infty})_i^2 < +\infty$  independent of  $i$ , and  $\mathbb{E}(\vec{\mathbf{x}}_{\infty})_i(\vec{\mathbf{x}}_{\infty})_j = 0, \forall i, j \in \{1, \dots, d\}$  with  
1649  $i \neq j$ .*  
16501651 *Proof.* From Theorem D.2.1,  $p_{\infty}$  is rotation-variant. So there exist a function  $h : \mathbb{R}^+ \rightarrow \mathbb{R}^+$  such  
1652 that for any  $\mathbf{x} \in \mathbb{R}^d$ ,  $p_{\infty}(\mathbf{x}) = h(\|\mathbf{x}\|)$ . Then,

1653 
$$\mathbb{E}(\vec{\mathbf{x}}_{\infty})_i = \int_{\mathbb{R}^d} x_i h(\|\mathbf{x}\|) d\mathbf{x} = \int_{\mathbb{R}^{d-1}} \left( \int_{\mathbb{R}} x_i h(\|\mathbf{x}\|) dx_i \right) \Pi_{k \neq i} dx_k = 0, \quad (\text{E.1})$$

1656 since the function  $x_i \rightarrow x_i h(\|\mathbf{x}\|)$  is even.1657 Similarly, for  $i \neq j$  in  $\{1, \dots, d\}$ 

1658 
$$\mathbb{E}(\vec{\mathbf{x}}_{\infty})_i(\vec{\mathbf{x}}_{\infty})_j = \int_{\mathbb{R}^d} x_i x_j h(\|\mathbf{x}\|) d\mathbf{x}, \quad (\text{E.2})$$

1659 
$$= \int_{\mathbb{R}^{d-1}} x_j \underbrace{\left( \int_{\mathbb{R}} x_i h(\|\mathbf{x}\|) dx_i \right)}_{=0} \Pi_{k \neq i} dx_k, \quad (\text{E.3})$$

1660 
$$= 0. \quad (\text{E.4})$$

1661 oreover, for  $i$  in  $\{1, \dots, d\}$ , we have

1662 
$$+\infty > \mathbb{E}\|\vec{\mathbf{x}}_{\infty}\|^2, \quad (\text{E.5})$$

1663 
$$= \mathbb{E} \sum_{i=1}^d (\vec{\mathbf{x}}_{\infty})_i^2, \quad (\text{E.6})$$

1664 
$$\geq \mathbb{E}(\vec{\mathbf{x}}_{\infty})_i^2, \quad (\text{E.7})$$

1665 
$$= \int_{\mathbb{R}^{d-1}} \left( \int_{\mathbb{R}} x_i^2 h(\|\mathbf{x}\|) dx_i \right) \Pi_{k \neq i} dx_k, \quad (\text{E.8})$$

1674 which does not depends of  $i$ . □  
 1675

1676 **Remark 1.** Since  $\mathbb{E}(\vec{\mathbf{x}}_\infty)_i^2$  does not depend on  $i$ , we can easily evaluate it from Theorem 3.3.1 and  
 1677 Proposition D.3.2

1678 
$$\mathbb{E}(\vec{\mathbf{x}}_\infty)_i^2 = \frac{1}{d}\mathbb{E}\|\vec{\mathbf{x}}_\infty\|^2 = \lim_{s \rightarrow +\infty} \frac{1}{d}\mathbb{E}\|\vec{\mathbf{x}}_s\|^2 = \frac{1}{d}\mathbb{E}\|\vec{\mathbf{x}}_0\|^2, \quad (\text{E.9})$$
  
 1679  
 1680

1681 and thus

1682 
$$\mathbb{E}(\vec{\mathbf{x}}_\infty \vec{\mathbf{x}}_\infty^\top) = \frac{1}{d}\mathbb{E}\|\vec{\mathbf{x}}_0\|^2 \mathbf{I}_d. \quad (\text{E.10})$$
  
 1683

1684 Therefore, monitoring the covariance of  $\vec{\mathbf{x}}_T$  and its distance to  $\frac{1}{d}\mathbb{E}\|\vec{\mathbf{x}}_0\|^2 \mathbf{I}_d$  are convenient proxies  
 1685 of the forward SDE convergence.  
 1686

## 1687 E.2 CONDITION OF GAUSSIANITY FOR THE LATENT VECTOR

1688 **Proposition E.2.1.** Let assumptions A1 and A2 hold and  $p_{|\cdot|}$  be the density of  $\|\vec{\mathbf{x}}_0\|^2$ . Then, the  
 1689 latent distribution  $p_\infty$  is Gaussian if and only if  $p_{|\cdot|}$  is a scaled  $\chi^2$  distribution with  $d$  degrees of  
 1690 freedom, denoted  $\alpha^2 \chi_d^2$  with  $\alpha \geq 0$ .  
 1691

1692 *Proof.* From Theorem D.2.1, we know that  $p_\infty$  is rotation invariant, i.e. it is a function of  $\|\mathbf{x}\|$ .  
 1693 If this distribution is Gaussian, it has to be of the form  $\mathcal{N}(0, \alpha^2 \mathbf{I}_d)$  with  $\alpha \geq 0$ . Then,  $\|\vec{\mathbf{x}}_0\|^2 =$   
 1694  $\|\mathbf{x}_\infty\|^2 \sim \alpha^2 \chi_d^2$ . Reciprocally, if there exists  $\alpha \geq 0$  such that  $p_{|\cdot|} = \alpha^2 \chi_d^2$  then  $p_{|\cdot|} = \alpha \chi_d$ , where  
 1695 we denote by  $\alpha \chi_d$  the distribution of a positive random variable  $X = \sqrt{\alpha^2 R}$  such that  $R \sim \chi_d^2$ .  
 1696 From Theorem 3.3.1, we know that  
 1697

1698 
$$p_\infty(\mathbf{x}) = p_{|\cdot|}(\|\mathbf{x}\|) \frac{\|\mathbf{x}\|^{1-d}}{|\mathbb{S}^{d-1}|} = p_{\alpha \chi_d}(\|\mathbf{x}\|) \frac{\|\mathbf{x}\|^{1-d}}{|\mathbb{S}^{d-1}|}. \quad (\text{E.11})$$
  
 1699  
 1700

1701 It is the distribution  $\mathcal{N}(0, \alpha^2 \mathbf{I}_d)$  written in spherical form. So, the latent distribution  $p_\infty$  is Gaussian.  
 1702 □  
 1703

1704 **Remark 2.** Isotropic Gaussian data  $\vec{\mathbf{x}}_0 \sim \mathcal{N}(0, \alpha^2 \mathbf{I}_d)$  will hence leads to Gaussian latent space.  
 1705 But the contrapositive is not true. To see this, let us consider a general spherical decomposition of  
 1706 the data distribution  $p_0$  :

1707 
$$p_0(\mathbf{x}) = p^\otimes \left( \|\mathbf{x}\|, \frac{\mathbf{x}}{\|\mathbf{x}\|} \right) \|\mathbf{x}\|^{1-d} = p_{|\cdot|}(\|\mathbf{x}\|) p_0^n \left( \frac{\mathbf{x}}{\|\mathbf{x}\|} \middle| \|\mathbf{x}\| \right) \|\mathbf{x}\|^{1-d}. \quad (\text{E.12})$$
  
 1708  
 1709

1710 The latent distribution would be Gaussian as long as the distribution of norm is  $p_{|\cdot|} = p_{\alpha \chi_d}$ . But the  
 1711 conditional distribution of direction can be any valid conditional distribution on the  $d$ -sphere. For  
 1712 instance,

1713 
$$p_0^n \left( \frac{\mathbf{x}}{\|\mathbf{x}\|} \middle| \|\mathbf{x}\| \right) = \delta \left( \frac{\mathbf{x}}{\|\mathbf{x}\|} - \mathbf{e}^{(1)} \right), \quad \text{with} \quad \mathbf{e}^{(1)} = (1, 0, \dots, 0), \quad (\text{E.13})$$
  
 1714  
 1715

1716 is a valid candidate even though  $p_0$  is not Gaussian (since its support is  $\mathbb{R}^+ \times \{0\}^{d-1}$ ).  
 1717

## 1718 E.3 A TRACTABLE ALGORITHM TO SAMPLE LATENT VECTORS

1719 With the following proposition, if we know the distribution of norms,  $p_{|\cdot|}$ , we can sample latent  
 1720 vectors from  $p_\infty$ .  
 1721

1722 **Proposition E.3.1.** Let  $\overset{\leftarrow}{\mathbf{x}}_0 \sim \mathcal{N}(0, \mathbf{I}_d)$  and  $\overset{\leftarrow}{\mathbf{x}}_0 = F^{-1} \left( \overset{\leftarrow}{\mathbf{x}}_0 \right)$  with  $F^{-1}(\mathbf{x}) := f(\|\mathbf{x}\|) \frac{\mathbf{x}}{\|\mathbf{x}\|}$  if  
 1723  $\mathbf{x} \neq 0$  and 0 otherwise,

1724 
$$f(r) := F_{|\cdot|}^{-1}(F_{\chi^2(d)}(r^2)), \quad \forall r > 0, \quad (\text{E.14})$$
  
 1725

1726 for the generalized inverse CDF  $F_{|\cdot|}^{-1}$  of  $p_{|\cdot|}$  and  $F_{\chi^2}$  is the CDF of the  $\chi^2$  distribution with  $d$  degrees  
 1727 of freedom. Then  $\overset{\leftarrow}{\mathbf{x}}_0 \sim p_\infty$ .

1728 *Proof.* Since  $\overset{\leftarrow}{\mathbf{x}}_0 \sim \mathcal{N}(0, \mathbf{I}_d)$ , we know that  $\|\overset{\leftarrow}{\mathbf{x}}_0\|^2 \sim \chi_{d-1}^2$ , i.e.  $F_{\chi^2}(\|\overset{\leftarrow}{\mathbf{x}}_0\|^2) \sim \mathcal{U}(0, 1)$  and  
1729 then  $R := f(\|\overset{\leftarrow}{\mathbf{x}}_0\|) = F_{|\cdot|}^{-1}(F_{\chi^2}(\|\overset{\leftarrow}{\mathbf{x}}_0\|^2)) \sim p_{|\cdot|}$ . In addition, the normalized vector is  
1730  $\frac{\overset{\leftarrow}{\mathbf{x}}_0}{\|\overset{\leftarrow}{\mathbf{x}}_0\|} \sim \mathcal{U}(\mathbb{S}^{d-1})$ . The norm  $\|\overset{\leftarrow}{\mathbf{x}}_0\|$  and the direction  $\frac{\overset{\leftarrow}{\mathbf{x}}_0}{\|\overset{\leftarrow}{\mathbf{x}}_0\|}$  are independent. Therefore,  $R$  and  
1731  $\frac{\overset{\leftarrow}{\mathbf{x}}_0}{\|\overset{\leftarrow}{\mathbf{x}}_0\|}$  are also independent. We can conclude that  $\overset{\leftarrow}{\mathbf{x}}_0 = R \frac{\overset{\leftarrow}{\mathbf{x}}_0}{\|\overset{\leftarrow}{\mathbf{x}}_0\|}$  follows the correct distribution.  $\square$   
1732  
1733  
1734  
1735

1736 In practice, we do not exactly know the distribution of the data norm  $p_{|\cdot|}$ . So, we do not have  
1737 access to  $F_{|\cdot|}$  or  $f$ . Instead, we approximate the distribution of  $\log \|\overset{\rightarrow}{\mathbf{x}}_0\|_\epsilon$  with  $\|\mathbf{x}\|_\epsilon := \|\mathbf{x}\| + \epsilon$ ,  
1738 denoted  $p_{\log |\cdot|_\epsilon}$ , by a model  $\hat{p}_{\log |\cdot|_\epsilon}$ , or equivalently  $F_{\log |\cdot|_\epsilon}$  by a model  $\hat{F}_{\log |\cdot|_\epsilon}$  (see Appendix C).  
1739 We perform a similar sampling procedure for the latent vectors, replacing  $F$  by our approximation.  
1740 We obtain samples of an approximate latent distribution  $\hat{p}_\infty$ , as stated by Proposition E.3.2.  
1741

1742 **Proposition E.3.2.** *Let  $\overset{\leftarrow}{\mathbf{x}}_0 \sim \mathcal{N}(0, \mathbf{I}_d)$  and  $\overset{\leftarrow}{\mathbf{x}}_0 = \hat{F}^{-1}(\overset{\leftarrow}{\mathbf{x}}_0)$  with  $\hat{F}^{-1}(\mathbf{x}) := \hat{f}(\|\mathbf{x}\|) \frac{\mathbf{x}}{\|\mathbf{x}\|}$  if  
1743  $\mathbf{x} \neq 0$  and 0 otherwise,*

$$1744 \hat{f}(r) := \exp\left(\hat{F}_{\log |\cdot|_\epsilon}^{-1}(F_{\chi^2(d)}(r^2))\right) - \epsilon, \quad \forall r > 0, \quad (\text{E.15})$$

1745 for the generalized inverse of the approximated CDF  $\hat{F}_{\log |\cdot|_\epsilon}^{-1}$  associated to the approximated PDF  
1746  $\hat{p}_{\log |\cdot|_\epsilon}$ , and  $F_{\chi^2}$  is the CDF of the  $\chi^2$  distribution with  $d$  degrees of freedom. Then  $\overset{\leftarrow}{\mathbf{x}}_0 \sim \hat{p}_\infty$ , where  
1747  $\hat{p}_\infty$  is the empirical approximation of  $p_\infty$ , that is  $\hat{p}_\infty(\mathbf{x}) := \hat{p}_{\log |\cdot|_\epsilon}(\log \|\mathbf{x}\|_\epsilon) \frac{\|\mathbf{x}\|^{1-d}}{|\mathbb{S}^{d-1}|}, \forall \mathbf{x} \in \mathbb{R}^d$ .  
1748  
1749

1750 *Proof.* We can follow the same proof that for Proposition E.3.1 replacing  $F_{|\cdot|}$ ,  $f$ ,  $p_{|\cdot|}$ , and  $p_\infty$  by  
1751  $\hat{F}_{\log |\cdot|_\epsilon}$ ,  $\hat{f}$ ,  $\hat{p}_{\log |\cdot|_\epsilon}$ , and  $\hat{p}_\infty$  respectively.  $\square$

#### 1752 E.4 GAUSSIANIZATION OF THE LATENT VECTORS

1753 If needed, we can easily build a second latent space with standard Gaussian vectors. As stated by the  
1754 following proposition, for any (non-Gaussian) latent vector  $\overset{\rightarrow}{\mathbf{x}}_T$ , we can create a Gaussian vector  $\overset{\rightarrow}{\mathbf{x}}_T^N$   
1755

$$1756 \overset{\rightarrow}{\mathbf{x}}_T^N = R_T \overset{\rightarrow}{\mathbf{x}}_T^n, \quad \text{with} \quad \overset{\rightarrow}{\mathbf{x}}_T^n = \overset{\rightarrow}{\mathbf{x}}_T / \|\overset{\rightarrow}{\mathbf{x}}_T\|, \quad \text{and} \quad R_T = \hat{f}^{-1}(\|\overset{\rightarrow}{\mathbf{x}}_T\|). \quad (\text{E.16})$$

1757 If  $\overset{\rightarrow}{\mathbf{x}}_T$  is zero, we just set  $\overset{\rightarrow}{\mathbf{x}}_T^N$  to zero.

1758 **Proposition E.4.1.** *Let  $\overset{\rightarrow}{\mathbf{x}}_T \sim \hat{p}_\infty$ , where  $\hat{p}_\infty$  is the empirical approximation of  $p_\infty$ , that is  $\hat{p}_\infty(\mathbf{x}) :=$   
1759  $\hat{p}_{\log |\cdot|_\epsilon}(\log \|\mathbf{x}\|_\epsilon) \frac{\|\mathbf{x}\|^{1-d}}{|\mathbb{S}^{d-1}|}, \forall \mathbf{x} \in \mathbb{R}^d$ , and  $\overset{\rightarrow}{\mathbf{x}}_T^N = \hat{F}(\overset{\rightarrow}{\mathbf{x}}_T)$  with  $\hat{F}(\mathbf{x}) := \hat{f}^{-1}(\|\mathbf{x}\|) \frac{\mathbf{x}}{\|\mathbf{x}\|}$  if  $\mathbf{x} \neq 0$   
1760 and 0 otherwise,*

$$1761 \hat{f}^{-1}(r) = \sqrt{(F_{\chi^2}^{-1}(\hat{F}_{\log |\cdot|_\epsilon}(r)))}, \quad \forall r > 0, \quad (\text{E.17})$$

1762 for the approximated CDF  $\hat{F}_{\log |\cdot|_\epsilon}$  associated to the approximated PDF  $\hat{p}_{\log |\cdot|_\epsilon}$ , and  $F_{\chi^2}$  is the CDF  
1763 of the  $\chi^2$  distribution with  $d$  degrees of freedom. Then  $\overset{\rightarrow}{\mathbf{x}}_T^N \sim \mathcal{N}(0, \mathbf{I}_d)$ .  
1764

1765 *Proof.* We can follow the same proof that for Proposition E.3.1 replacing  $F_{|\cdot|}^{-1}$ ,  $f$ ,  $\chi^2$ ,  $\mathcal{N}(0, \mathbf{I}_d)$ ,  $p_{|\cdot|}$ ,  
1766 and  $p_\infty$  by  $\hat{F}_{\log |\cdot|_\epsilon}$ ,  $\hat{f}^{-1}$ ,  $\hat{p}_{\log |\cdot|_\epsilon}$ ,  $\hat{p}_\infty$ ,  $\chi^2$ , and  $\mathcal{N}(0, \mathbf{I}_d)$  respectively.  $\square$

#### 1767 E.5 A SHORTER DISTANCE BETWEEN LATENT AND DATA DISTRIBUTION

1768 The following result states, that the latent space of MSGM is closer to the data distribution compared  
1769 to the SGM latent distribution in KL-divergence.

1782 **Proposition E.5.1.** *Let the assumptions A1 and A2 hold,  $p_{|\cdot|^2}$  be the density of  $\|\vec{\mathbf{x}}_0\|^2$ ,  $p_\infty$  and  
1783  $p_\infty^{\mathcal{N}} = \mathcal{N}(0, \mathbf{I}_d)$  be the MSGM and the SGM latent distributions respectively, then  
1784*

$$1785 \quad D_{KL}(p_\infty \| p_0) \leq D_{KL}(p_\infty^{\mathcal{N}} \| p_0), \quad (\text{E.18})$$

1786 with equality if and only if  $p_{|\cdot|^2}$  is a  $\chi^2$  distribution with  $d$  degrees of freedom.  
1787

1788 *Proof.* We recall that the MSGM latent pdf is  
1789

$$1790 \quad p_\infty(\mathbf{x}) = \frac{p_{|\cdot|}(\|\mathbf{x}\|)}{\|\mathbf{x}\|^{d-1}} \frac{1}{|\mathbb{S}^{d-1}|}. \quad (\text{E.19})$$

1792 and the data distribution reads  
1793

$$1794 \quad p_0(\mathbf{x}) = \frac{p_{|\cdot|}(\|\mathbf{x}\|)}{\|\mathbf{x}\|^{d-1}} p_0(\mathbf{x}^n \| \|\vec{\mathbf{x}}_0\| = \|\mathbf{x}\|). \quad (\text{E.20})$$

1795 Let denotes  $p_{\chi_d^2}$  the  $\chi^2$  distribution with  $d$  degrees of freedom  
1796

$$1797 \quad p_0^{\mathcal{LN}}(\mathbf{x}) = \frac{p_{\chi_d^2}(\|\mathbf{x}\|)}{\|\mathbf{x}\|^{d-1}} p_0(\mathbf{x}^n \| \|\vec{\mathbf{x}}_0\| = \|\mathbf{x}\|). \quad (\text{E.21})$$

1800 It is the distribution of  $\vec{\mathbf{x}}_0^{\mathcal{LN}} = F(\vec{\mathbf{x}}_0)$  with  $F(\mathbf{x}) := f^{-1}(\|\mathbf{x}\|) \frac{\mathbf{x}}{\|\mathbf{x}\|}$  if  $\mathbf{x} \neq 0$  and 0 otherwise, and  
1801

$$1802 \quad f^{-1}(r) = \sqrt{(F_{\chi_d^2}^{-1}(F_{|\cdot|}(r))}), \quad \forall r > 0, \quad (\text{E.22})$$

1804 and  $F_{|\cdot|}(R) = \int_0^R p_{|\cdot|}(r) dr$  the cdf associated to  $p_{|\cdot|}$ .  
1805

1806 We have

$$1807 \quad 0 \leq D_{KL}(p_0 \| p_0^{\mathcal{LN}}), \quad (\text{E.23})$$

$$1808 \quad = \int p_0(\mathbf{x}) \log \frac{p_0}{p_0^{\mathcal{LN}}} d\mathbf{x}, \quad (\text{E.24})$$

$$1811 \quad = \int p_0(\mathbf{x}) \log \frac{p_{|\cdot|}(\|\mathbf{x}\|)}{p_{\chi_d^2}(\|\mathbf{x}\|)} d\mathbf{x}, \quad (\text{E.25})$$

$$1813 \quad = \int p_0(\mathbf{x}) \log \frac{p_{|\cdot|}(\|\mathbf{x}\|)}{\|\mathbf{x}\|^{d-1} |\mathbb{S}^{d-1}|} \frac{\|\mathbf{x}\|^{d-1} |\mathbb{S}^{d-1}|}{p_{\chi_d^2}(\|\mathbf{x}\|)} d\mathbf{x}, \quad (\text{E.26})$$

$$1816 \quad = \int p_0(\mathbf{x}) \log \frac{p_\infty(\mathbf{x})}{p_\infty^{\mathcal{N}}(\mathbf{x})} d\mathbf{x}, \quad (\text{E.27})$$

$$1818 \quad = \int p_0(\mathbf{x}) \log \frac{p_0(\mathbf{x})}{p_\infty^{\mathcal{N}}(\mathbf{x})} \frac{p_\infty(\mathbf{x})}{p_0(\mathbf{x})} d\mathbf{x}, \quad (\text{E.28})$$

$$1821 \quad = \int p_0(\mathbf{x}) \log \frac{p_0(\mathbf{x})}{p_\infty^{\mathcal{N}}(\mathbf{x})} d\mathbf{x} - \int p_0(\mathbf{x}) \log \frac{p_0(\mathbf{x})}{p_\infty(\mathbf{x})} d\mathbf{x}, \quad (\text{E.29})$$

$$1823 \quad = D_{KL}(p_0 \| p_\infty^{\mathcal{N}}) - D_{KL}(p_0 \| p_\infty), \quad (\text{E.30})$$

1824 with equality if and only if  $p_0 = p_0^{\mathcal{LN}}$  i.e.  $p_{|\cdot|} = p_{\chi_d^2}$ .  $\square$   
1825

## 1826 E.6 RELEVANCE OF MSGM LATENT SPACE FOR HEAVY-TAIL DISTRIBUTIONS.

1828 This appendix provides an analysis of why the latent space of MSGM is better suited to heavy-  
1829 tailed data distribution as compared to the latent space of SGM. This subsection can be viewed  
1830 as an extension of Proposition E.5.1. In particular the derived inequality in Proposition E.5.1  
1831 becomes meaning less if both sides are not finite. However, as we will see for example of heavy tail  
1832 distribution such as the (product) Cauchy distribution, this is not the case. To this end we will show  
1833 in Appendix E.6.1 that the KL divergence of data distribution and SGM latent space is not finite and  
1834 that it is finite for the data distribution and the MSGM latent space in Appendix E.6.2.

1835 We note that the analysis can be extended to a broader class of heavy tailed distributions and more  
1836 general SGM latent spaces such as general Gaussian distributions.

1836 E.6.1 INFINITE KL DIVERGENCE BETWEEN CAUCHY DISTRIBUTION AND STANDARD  
 1837 GAUSSIAN  
 1838

1839 Let  $\phi(\mathbf{x}) = \frac{1}{\sqrt{2\pi}} e^{-\mathbf{x}^2/2}$  be the density of the standard Gaussian  $\mathcal{N}(0, I)$ , and let  $p_0(\mathbf{x}) = \prod_{i=1}^d \frac{1}{\pi(1+x_i^2)}$   
 1840 be the product density of univariate Cauchy distributions. Then, the following holds.  
 1841

1842 **Lemma E.6.1.**

1843 
$$D_{\text{KL}}(p_0 \parallel \phi) = \infty.$$
  
 1844

1845 *Proof.* Let  $L > 1$  and define the set  
 1846

1847 
$$M = \{\mathbf{x} \in \mathbb{R}^d \mid x_1 \geq L, |x_j| \leq 1, \quad j = 2, \dots, d\}.$$
  
 1848

1849 Then for  $\mathbf{x} \in M$  and  $C := \frac{1}{\pi^d 2^{d-1}}$

1850 
$$p_0(\mathbf{x}) = \prod_{i=1}^d \frac{1}{\pi(1+x_i^2)} \geq \frac{1}{\pi^d} \cdot \frac{1}{1+x_1^2} \cdot \prod_{i=2}^d \frac{1}{1+1} = \frac{1}{\pi^d 2^{d-1}} \cdot \frac{1}{1+x_1^2} = C \frac{1}{1+x_1^2}.$$
  
 1851  
 1852  
 1853

1854 Moreover, for any  $\mathbf{x} \in \mathbb{R}^d$ , it holds that  
 1855

1856 
$$\phi(\mathbf{x}) = (2\pi)^{-d/2} e^{-(x_1^2 + \sum_{i=2}^d x_i^2)/2} \leq (2\pi)^{-d/2} e^{-x_1^2/2}.$$
  
 1857

1858 Consequently, for  $L$  large enough,  
 1859

1860 
$$p_0(\mathbf{x}) \log \frac{p_0(\mathbf{x})}{\phi(\mathbf{x})} \geq \frac{x_1^2}{2} + \mathcal{O}(\log x_1),$$
  
 1861

1862 where  $\mathcal{O}$  refers to Landau-symbol of big-O notation. Together, for  $\mathbf{x} \in M$  and  $L$  large enough, there  
 1863 exists  $\underline{C} > 0$  such that  
 1864

1865 
$$p_0(\mathbf{x}) \log \frac{p_0(\mathbf{x})}{\phi(\mathbf{x})} \geq \frac{C}{1+x_1^2} \frac{x_1^2}{4} \geq \underline{C} > 0.$$
  
 1866

1867 Consequently,  
 1868

1869 
$$\int_M p_0(\mathbf{x}) \log \frac{p_0(\mathbf{x})}{\phi(\mathbf{x})} d\mathbf{x} \geq \int_T^\infty \left( \int \cdots \int_{|x_j| \leq 1, j \geq 2} \underline{C} dx_2 \cdots dx_d \right) dx_1 = \infty.$$
  
 1870  
 1871  
 1872

1873 By Lebesgue decomposition, we conclude  $D_{\text{KL}}(p_0 \parallel \phi) = \infty$ .  $\square$   
 1874

1875 E.6.2 FINITE KL DIVERGENCE BETWEEN CAUCHY DISTRIBUTION AND ITS RELATED  $\rho_\infty$   
 1876

1877 Let  $d \geq 2$  and again consider the product of Cauchy densities  
 1878

1879 
$$p_0(\mathbf{x}) = \prod_{i=1}^d \frac{1}{\pi(1+x_i^2)}.$$
  
 1880  
 1881

1882 Let  $\mathbf{x}_0 \sim p_0$  and let  $p_R$  be the density of  $R = \|\vec{\mathbf{x}}_0\|$ . Then, motivated by our latent space distribution  
 1883 equation 3.8, consider the density  
 1884

1885 
$$\rho_\infty(\mathbf{x}) = \frac{p_R(\|\mathbf{x}\|)}{\|\mathbf{x}\|^{d-1} |\mathbb{S}^{d-1}|}, \quad \mathbf{x} \in \mathbb{R}^d \setminus \{0\}, \quad (\text{E.31})$$
  
 1886

1887 Then, the following holds  
 1888

1889 **Lemma E.6.2.**

$$D_{\text{KL}}(p_0 \parallel \rho_\infty) < \infty.$$

1890 *Proof.* It holds that  
 1891

$$1892 \log \frac{p_0(\mathbf{x})}{p_\infty(\mathbf{x})} = \log p_0(\mathbf{x}) - \log p_R(\|\mathbf{x}\|) + (d-1) \log \|\mathbf{x}\| + \log |\mathbb{S}^{d-1}|.$$

$$1893$$

1894 Hence,  
 1895

$$1896 D_{\text{KL}}(p_0\|p_\infty) = \mathbb{E}_p[\log p_0(\vec{\mathbf{x}}_0)] - \mathbb{E}_p[\log p_R(\|\vec{\mathbf{x}}_0\|)] + (d-1)\mathbb{E}_p[\log \|\vec{\mathbf{x}}_0\|] + \log |\mathbb{S}^{d-1}|,$$

1897 where  $\mathbb{E}_p$  denotes the expectation with respect to the probability measure  $p_0 d\mathbf{x}$ . We will show, that  
 1898 each term separately is finite. We start with the first term, followed by the the third. The finiteness of  
 1899 the second term turns out to be a consequence of the finiteness of the second term.

1900 • *First term:* It holds that  
 1901

$$1902 \log p_0(\vec{\mathbf{x}}_0) = -d \log \pi - \sum_{i=1}^d \log(1 + (\vec{\mathbf{x}}_0)_i^2)$$

$$1903$$

$$1904$$

1905 for  $\vec{\mathbf{x}}_0 \sim p_0$ . Since coordinates of  $(\vec{\mathbf{x}}_0)_i$  are iid it is enough to check the marginal integrals  
 1906 for finiteness. In particular it holds that  
 1907

$$1908 \int_{-\infty}^{\infty} \frac{\log(1+x^2)}{\pi(1+x^2)} dx = \log(4) < \infty.$$

$$1909$$

$$1910$$

1911 Consequently  
 1912

$$1913 |\mathbb{E}_p[\log p_0(\vec{\mathbf{x}}_0)]| < \infty. \quad (\text{E.32})$$

1914 • *Third term:* For the second term, let  $R = \|\vec{\mathbf{x}}_0\|$  and  $M = \max_{i=1,\dots,d} |(\vec{\mathbf{x}}_0)_i|$ . Then, almost  
 1915 surely  
 1916

$$1917 \leq R \leq \sqrt{d}M \quad \Rightarrow \quad \log M \leq \log R \leq \log M + \frac{1}{2} \log d.$$

$$1918$$

1919 Consequently,  
 1920

$$1921 |\mathbb{E}_p[\log R] - \mathbb{E}_p[\log M]| \leq \frac{1}{2} \log d.$$

$$1922$$

$$1923$$

1924 Thus if we show  $\mathbb{E}_p[\log M] < \infty$ , then  $\mathbb{E}_p[\log R] < \infty$  as well, since both expectation only  
 1925 differ up to a finite factor. Using the CDF  $F$  of  $(\vec{\mathbf{x}}_0)_1$  e.g. for  $(\vec{\mathbf{x}}_0)_1$  it holds that  
 1926

$$1927 \mathbb{P}(\|(\vec{\mathbf{x}}_0)_1\| \leq t) = F(t) - F(-t) = \frac{2}{\pi} \arctan t, \quad t \geq 0.$$

$$1928$$

$$1929$$

$$1930$$

1931 Consequently, since  $(\vec{\mathbf{x}}_0)_1, \dots, (\vec{\mathbf{x}}_0)_d$  are iid, the CDF  $F_M$  of  $M$  satisfies  
 1932

$$1933 F_M(t) = \mathbb{P}(M \leq t) = \left( \frac{2}{\pi} \arctan t \right)^d, \quad t \geq 0.$$

$$1934$$

1935 Hence, the density  $f_M$  of  $M$  is given (for  $d \geq 2$ ) as  
 1936

$$1937 f_M(t) = \frac{\partial}{\partial t} F_M(t) = d \left( \frac{2}{\pi} \right)^d (\arctan t)^{d-1} \frac{1}{1+t^2}.$$

$$1938$$

$$1939$$

1940 Now, by a integral splitting we find that  
 1941

$$1942 \mathbb{E}_p[\log M] = \int_0^\infty \log t f_M(t) dt = \int_0^1 \log t f_M(t) dt + \int_1^\infty \log(t) f_M(t) dt. \quad (\text{E.33})$$

$$1943$$

1944 By noting that for  $0 \leq t$ ,  $f_M(t) \leq Ct^{d-1}$  for some  $C > 0$  and  
 1945

$$1946 \int_0^1 f_M(t)(-\log(t)) dt \leq \int_0^1 t^{a-1}(-\log(t)) dt = \frac{1}{a^2}, \quad a > 0,$$

$$1947$$

$$1948$$

1944 the first integrant of equation E.33 is finite using  $a = d$ . For  $t \geq 1$   $\arctan(t) \leq \pi/2$  and  
 1945 hence  $f_M(t) \leq C' \frac{1}{1+t^2}$  for some  $C' > 0$  and the second integral of equation E.33 is finite  
 1946 since

$$1947 \int_1^\infty \frac{\log(t)}{1+t^2} dt = 1 < \infty.$$

1950 It follows that  $\mathbb{E}_p[\log M]$  is finite.

1952 • *Second term:* Recall that

$$1954 p_R(r) = \int_{\mathbb{S}^{d-1}} p_0(r\theta) r^{d-1} d\sigma(\theta) = r^{d-1} \int_{\mathbb{S}^{d-1}} p_0(r\theta) d\sigma(\theta).$$

1957 Since for  $\mathbf{x} = r\theta$  with  $\theta = (\theta_1, \dots, \theta_d)$ , with  $\theta_i^2 \leq 1$  and using the fact that

$$1959 p_0(r\theta) = \prod_{i=1}^d \frac{1}{\pi(1+r^2\theta_i^2)}$$

1962 we conclude

$$1964 p_0(r\theta) \geq \prod_{i=1}^d \frac{1}{\pi(1+r^2)} = \frac{1}{\pi^d(1+r^2)^d}.$$

1966 Therefore,

$$1968 p_R(r) \geq r^{d-1} \frac{1}{\pi^d(1+r^2)^d} \cdot |\mathbb{S}^{d-1}| =: C_d \frac{r^{d-1}}{(1+r^2)^d}.$$

1970 Hence,

$$1971 \log p_R(r) \geq \log C_d + (d-1) \log r - d \log(1+r^2),$$

1973 which yields

$$1975 \mathbb{E}_p[\log p_R(\|\vec{x}_0\|)] \geq \log C_d + (d-1)\mathbb{E}_p[\log R] - d\mathbb{E}_p[\log(1+R^2)]. \quad (\text{E.34})$$

1976 For the third term in equation E.34 it holds that  $R^2 = \sum_{i=1}^d (\vec{x}_0)_i^2$ . Now for  $M \leq 1$  we have  
 1977 since  $R \leq \sqrt{d}M \leq \sqrt{d}$  that  $\log(1+R^2) \leq \log(1+\sqrt{d})$  is independent of  $R$ . For  $M \geq 1$ ,  
 1979  $\log(1+R^2) \leq \log(1+dM^2) \leq \log(dM^2 + dM^2) = \log(2d) + 2\log(M)$ . Since we  
 1980 already showed that  $\mathbb{E}_p[\log R]$  is finite, we conclude that the lower bound in equation E.34  
 1981 is finite. For the upper bound, note that

$$1983 p_0(r\theta) \leq \frac{1}{\pi^d}, \quad \forall r > 0.$$

1985 Thus,

$$1987 p_R(r) \leq r^{d-1} \frac{1}{\pi^d} |\mathbb{S}^{d-1}| =: C_d r^{d-1}$$

1988 for some  $C_d > 0$ . So

$$1989 \log p_R(r) \leq \log C_d + (d-1) \log r.$$

1991 And finally,

$$1992 \mathbb{E}_p[\log p_R(r)] \leq \log C_d + (d-1)\mathbb{E}_p[\log r] < \infty$$

1994 since  $\mathbb{E}_p[\log r] < \infty$

1995 • *Fourth term:* Finite since volume of the finite dimensional hypersphere.

1996

1997

□

1998 **F BACKWARD DIFFUSION**  
 1999

2000 This section is devoted to the derivation of the reverse SDE and ODE of our proposed MSGM in Itô  
 2001 and Stratonovich form.

2002 **Proposition F.1. (Backward SDE)** *Let the skew-symmetry assumption A1 hold. Then, the Itô form  
 2003 of the reverse SDE associated to the forward SDE 3.1 is given by the SDE*

$$2005 d\overleftarrow{\mathbf{x}}_t = \frac{1}{2}(\nabla \cdot \Sigma)(\overleftarrow{\mathbf{x}}_t)dt + \mathbf{G}(\overleftarrow{\mathbf{x}}_t)\mathbf{G}(\overleftarrow{\mathbf{x}}_t)^\top \nabla \log p_{T-t}(\overleftarrow{\mathbf{x}}_t)dt + \mathbf{G}(\overleftarrow{\mathbf{x}}_t)d\overleftarrow{\mathbf{B}}_t. \quad (\text{F.1})$$

2006 In the Stratonovich form, it reads:

$$2008 d\overleftarrow{\mathbf{x}}_t = \mathbf{G}(\overleftarrow{\mathbf{x}}_t) \left( \mathbf{G}(\overleftarrow{\mathbf{x}}_t)^\top \nabla \log p_{T-t}(\overleftarrow{\mathbf{x}}_t)dt + \circ d\overleftarrow{\mathbf{B}}_t \right). \quad (\text{F.2})$$

2011 *Proof.* From Anderson (1982); Song et al. (2021) and the Itô forward SDE (see Lemma D.1.2), we  
 2012 know that the Itô reverse SDE with negative  $ds$  writes

$$2013 d\overleftarrow{\mathbf{x}}_s = \frac{1}{2}(\nabla \cdot \Sigma)(\overleftarrow{\mathbf{x}}_s)ds - (\nabla \cdot \Sigma)(\overleftarrow{\mathbf{x}}_s)ds - \mathbf{G}(\overleftarrow{\mathbf{x}}_s)\mathbf{G}(\overleftarrow{\mathbf{x}}_s)^\top \nabla \log p_s(\overleftarrow{\mathbf{x}}_s)ds  
 2014 + \mathbf{G}(\overleftarrow{\mathbf{x}}_s)d\overleftarrow{\mathbf{B}}_s, \quad (\text{F.3})$$

$$2017 = -\frac{1}{2}(\nabla \cdot \Sigma)(\overleftarrow{\mathbf{x}}_s)ds - \mathbf{G}(\overleftarrow{\mathbf{x}}_s)\mathbf{G}(\overleftarrow{\mathbf{x}}_s)^\top \nabla \log p_s(\overleftarrow{\mathbf{x}}_s)ds + \mathbf{G}(\overleftarrow{\mathbf{x}}_s)d\overleftarrow{\mathbf{B}}_s. \quad (\text{F.4})$$

2018 Replacing the decreasing  $s \in [0, T]$  by  $s = T - t$  with increasing  $t \in [0, T]$  and using another  
 2019 Brownian motion  $\overleftarrow{\mathbf{B}}$ , we obtain the Itô backward SDE with positive  $dt$

$$2021 d\overleftarrow{\mathbf{x}}_t = \frac{1}{2}(\nabla \cdot \Sigma)(\overleftarrow{\mathbf{x}}_t)dt + \mathbf{G}(\overleftarrow{\mathbf{x}}_t)\mathbf{G}(\overleftarrow{\mathbf{x}}_t)^\top \nabla \log p_{T-t}(\overleftarrow{\mathbf{x}}_t)dt + \mathbf{G}(\overleftarrow{\mathbf{x}}_t)d\overleftarrow{\mathbf{B}}_t. \quad (\text{F.5})$$

2023 Then, Lemma D.1.1 and the standard Stratonovich-to-Itô formula (e.g. Kunita, 1997) yields the  
 2024 Stratonovich form of the backward SDE:

$$2025 d\overleftarrow{\mathbf{x}}_t = -\frac{1}{2}d\langle \mathbf{G}(\overleftarrow{\mathbf{x}}_t), \overleftarrow{\mathbf{B}}_t \rangle_t + \frac{1}{2}(\nabla \cdot \Sigma)(\overleftarrow{\mathbf{x}}_t)dt + \mathbf{G}(\overleftarrow{\mathbf{x}}_t)\mathbf{G}(\overleftarrow{\mathbf{x}}_t)^\top \nabla \log p_{T-t}(\overleftarrow{\mathbf{x}}_t)dt  
 2026 + \mathbf{G}(\overleftarrow{\mathbf{x}}_t) \circ d\overleftarrow{\mathbf{B}}_t, \quad (\text{F.6})$$

$$2028 = -\frac{1}{2}(\nabla \cdot \Sigma)(\overleftarrow{\mathbf{x}}_t)dt + \frac{1}{2}(\nabla \cdot \Sigma)(\overleftarrow{\mathbf{x}}_t)dt  
 2029 + \mathbf{G}(\overleftarrow{\mathbf{x}}_t) \left( \mathbf{G}(\overleftarrow{\mathbf{x}}_t)^\top \nabla \log p_{T-t}(\overleftarrow{\mathbf{x}}_t)dt + \circ d\overleftarrow{\mathbf{B}}_t \right), \quad (\text{F.7})$$

$$2032 = \mathbf{G}(\overleftarrow{\mathbf{x}}_t) \left( \mathbf{G}(\overleftarrow{\mathbf{x}}_t)^\top \nabla \log p_{T-t}(\overleftarrow{\mathbf{x}}_t)dt + \circ d\overleftarrow{\mathbf{B}}_t \right). \quad (\text{F.8})$$

2034  $\square$

2036 **Proposition F.2. (Backward probability flow ODE)** *Let the skew-symmetry assumption A1 hold.  
 2037 Then, the reverse probability flow associated to the forward SDE 3.1 is given by the ODE*

$$2038 \frac{d\overleftarrow{\mathbf{x}}_t}{dt} = \frac{1}{2}\mathbf{G}(\overleftarrow{\mathbf{x}}_t)\mathbf{G}(\overleftarrow{\mathbf{x}}_t)^\top \nabla \log p_{T-t}(\overleftarrow{\mathbf{x}}_t). \quad (\text{F.9})$$

2041 *Proof.* From Song et al. (2021) and the Itô forward SDE (see Lemma D.1.2), we know that the  
 2042 reverse probability flow writes with negative  $ds$

$$2043 d\overleftarrow{\mathbf{x}}_s = \frac{1}{2}(\nabla \cdot \Sigma)(\overleftarrow{\mathbf{x}}_s)ds - \frac{1}{2}(\nabla \cdot \Sigma)(\overleftarrow{\mathbf{x}}_s)ds - \frac{1}{2}\mathbf{G}(\overleftarrow{\mathbf{x}}_s)\mathbf{G}(\overleftarrow{\mathbf{x}}_s)^\top \nabla \log p_s(\overleftarrow{\mathbf{x}}_s)dt, \quad (\text{F.10})$$

$$2045 = -\frac{1}{2}\mathbf{G}(\overleftarrow{\mathbf{x}}_s)\mathbf{G}(\overleftarrow{\mathbf{x}}_s)^\top \nabla \log p_s(\overleftarrow{\mathbf{x}}_s)dt. \quad (\text{F.11})$$

2046 Replacing the decreasing  $s \in [0, T]$  by  $s = T - t$  with increasing  $t \in [0, T]$  and using another  
 2047 Brownian motion  $\overleftarrow{\mathbf{B}}$ , we obtain the Itô backward SDE with positive  $dt$

$$2049 \frac{d\overleftarrow{\mathbf{x}}_t}{dt} = \frac{1}{2}\mathbf{G}(\overleftarrow{\mathbf{x}}_t)\mathbf{G}(\overleftarrow{\mathbf{x}}_t)^\top \nabla \log p_{T-t}(\overleftarrow{\mathbf{x}}_t). \quad (\text{F.12})$$

2051  $\square$

2052 **G PROOF OF THEOREM 3.4.1: EQUIVALENCE BETWEEN ELBO AND SCORE  
2053 MATCHING**  
2054

2055 This appendix derives a score-matching-based ELBO for MSGM training. In this work, we focus on  
2056 the simple forward multiplicative SDE equation 3.1. Nevertheless, we here derive a slightly more  
2057 general theorem, where we include a possibly non-zero Stratonovich drift  $f_S$ .  
2058

2059 **G.1 STATEMENT OF THE THEOREM**  
2060

2061 **Theorem G.1.1.** *Let us consider the forward SDE*  
2062

2063 
$$d\vec{\mathbf{x}}_s = f_S(\vec{\mathbf{x}}_s)ds + \mathbf{G}(\vec{\mathbf{x}}_s) \circ d\vec{B}_s, \quad (\text{G.1})$$
  
2064

2065 where assumption A1 holds. Then, we have  
2066

2067 
$$p_0(\mathbf{x}|\theta) \geq \mathcal{E}_\infty(\mathbf{x}|\theta), \quad (\text{G.2})$$
  
2068

2069 with the following ELBO  
2070

2071 
$$\begin{aligned} \mathcal{E}_\infty(\mathbf{x}|\theta) &:= \mathbb{E} \left[ \log p_T(\vec{\mathbf{x}}_T) \mid \vec{\mathbf{x}}_0 = \mathbf{x} \right] \\ 2072 &\quad - \int_0^T \mathbb{E}_{\vec{\mathbf{x}}_s} \left[ \frac{1}{2} \|\mathbf{a}_\theta(\vec{\mathbf{x}}_s, s)\|^2 + \nabla \cdot (\mathbf{G}(\vec{\mathbf{x}}_s) \mathbf{a}_\theta(\vec{\mathbf{x}}_s, s)) - f_S(\vec{\mathbf{x}}_s) \mid \vec{\mathbf{x}}_0 = \mathbf{x} \right] ds. \end{aligned} \quad (\text{G.3})$$
  
2073  
2074

2075 *Proof.* Here, we review the work of Huang et al. (2021) on SGM and generalize some  
2076 of their results to derive an ELBO and justify score matching for MSGM. Note that  
2077 Benton et al. (2024); Ren et al. (2025) proposes a very general SGM framework with associated  
2078 ELBO and score matching losses. The MSGM ELBO and thus the above theorem can be understood  
2079 as a particular case of their work. The explicit dependence in  $\theta$  is omitted for readability.  
2080

2081 **G.2 NOTATIONS CORRESPONDENCE**  
2082

2083 The forward and backward processes are denote  $Y_s$  and  $X_t$  in Huang et al. (2021) and  $\vec{\mathbf{x}}_s$  and  $\overleftarrow{\mathbf{x}}_t$  in  
2084 this paper. The forward Itô equation of Huang et al. (2021) is denoted:  
2085

2086 
$$dY_s = f(Y_s, s)ds + g(Y_s, s)d\hat{B}_s. \quad (\text{G.4})$$
  
2087

2088 Lemma D.1.1 gives the forward Itô equation of MSGM. It yields the following notation correspon-  
2089 dence:  
2090

2091 
$$g(\mathbf{x}, s) = \mathbf{G}(\mathbf{x}), \quad (\text{G.5})$$
  
2092 
$$D(\mathbf{x}) = \frac{1}{2}g(\mathbf{x})g(\mathbf{x})^\top = \frac{1}{2}\Sigma(\mathbf{x}), \quad (\text{G.6})$$
  
2093 
$$f(\mathbf{x}) = \frac{1}{2}(\nabla \cdot \Sigma)^\top(\mathbf{x}) + f_S(\mathbf{x}). \quad (\text{G.7})$$
  
2094

2095 And the backward equation is :  
2096

2097 
$$d\overleftarrow{\mathbf{x}}_t = \mu(\overleftarrow{\mathbf{x}}_t, t)dt + \mathbf{G}(\overleftarrow{\mathbf{x}}_t, t)d\overleftarrow{B}_t, \quad (\text{G.8})$$
  
2098

2099 with a drift  
2100

2101 
$$\mu(\mathbf{x}, t) = -f(\mathbf{x}) + 2(\nabla \cdot D)^\top(\mathbf{x}) + 2D(\mathbf{x})\nabla \log p_{T-t}(\mathbf{x}), \quad (\text{G.9})$$
  
2102

2103 
$$= -f_S(\mathbf{x}) + \frac{1}{2}(\nabla \cdot \Sigma)^\top(\mathbf{x}) + \Sigma(\mathbf{x})\nabla \log p_{T-t}(\mathbf{x}), \quad (\text{G.10})$$
  
2104

2105 where we would arrive at the approximate backward SDE of Figure 1 if we replace  $\nabla \log p_{T-t}(\overleftarrow{\mathbf{x}}_t)$   
2106 by  $\mathbf{s}_\theta(\overleftarrow{\mathbf{x}}_t, T-t)$  also parametrized as  $\mathbf{a}_\theta = \mathbf{G}^\top \mathbf{s}_\theta$ . We note that in our case,  $f_S = 0$ , the drift reads  
2107 
$$\mu = \frac{1}{2}(\nabla \cdot \Sigma)^\top + \Sigma \nabla \log p_{T-t}$$
, and the SDE simplifies with Stratonovich notations equation 3.12.  
2108

2106 G.3 MARGINAL DENSITY FROM FEYNMAN-KAC REPRESENTATION  
21072108 The Appendix D of Huang et al. (2021) treats the general case of multiplicative noise. It states that  
2109

2110 
$$p_0(\mathbf{x}) = \mathbb{E} \left[ p_T(\vec{\mathbf{x}}_T) \exp \left( \int_0^T (-\nabla \cdot \boldsymbol{\mu}(\vec{\mathbf{x}}_s, T-s) + \nabla \cdot \frac{1}{2}(\nabla \cdot \boldsymbol{\Sigma})^\top(\vec{\mathbf{x}}_s, T-s)) ds \right) \middle| \vec{\mathbf{x}}_0 = \mathbf{x} \right], \quad (G.11)$$
  
2111  
2112

2113 
$$= \mathbb{E} \left[ p_T(\vec{\mathbf{x}}_T) \exp \left( - \int_0^T \nabla \cdot (\boldsymbol{\mu} - \frac{1}{2}(\nabla \cdot \boldsymbol{\Sigma})^\top)(\vec{\mathbf{x}}_s, T-s) ds \right) \middle| \vec{\mathbf{x}}_0 = \mathbf{x} \right], \quad (G.12)$$
  
2114  
2115

2116 where  
2117

2118 
$$d\vec{\mathbf{x}}_s = -\tilde{\boldsymbol{\mu}}(\vec{\mathbf{x}}_s, T-s) ds + \mathbf{G}(\vec{\mathbf{x}}_s, T-s) d\mathbf{B}'_s, \quad (G.13)$$
  
2119

2120 
$$\tilde{\boldsymbol{\mu}}(\mathbf{x}, t) = \boldsymbol{\mu}(\mathbf{x}, t) - (\nabla \cdot \boldsymbol{\Sigma})^\top(\mathbf{x}), \quad (G.14)$$

2121 and  $\mathbf{B}'_s$  is a Brownian motion.  
21222123 **Remark 3.** In our case,  $\tilde{\boldsymbol{\mu}}(\mathbf{x}, t) = \boldsymbol{\mu}(\mathbf{x}, t) - (\nabla \cdot \boldsymbol{\Sigma})^\top(\mathbf{x}) = \boldsymbol{\Sigma}(\mathbf{x}) \nabla \log p_{T-t}(\mathbf{x}) - \frac{1}{2}(\nabla \cdot \boldsymbol{\Sigma})^\top(\mathbf{x})$ .  
21242125 **Remark 4.** Note that  $\tilde{\boldsymbol{\mu}} - \boldsymbol{\mu} = -(\nabla \cdot \boldsymbol{\Sigma})^\top = -(\nabla \cdot \boldsymbol{\Sigma})^\top$  is twice the Itô to Stratonovich correction  
2126 of the backward SDE equation G.8 (see [Lemma D.1.2](#)). It is expected since this SDE can be reversed  
2127 in time once written with Stratonovich notations equation 3.12 (Kunita, 1997). Then, changing back  
2128 from Stratonovich to Itô notations but with a different sign in front of the drift, we obtain the forward  
2129 SDE equation G.14 verified by  $\vec{\mathbf{x}}_s$  including twice the Itô to Stratonovich correction.  
21302130 G.4 CHANGE OF MEASURE AND JENSEN'S INEQUALITY  
21312132 From the Feynman-Kac representation equation G.12 and Jensen's inequality, we obtain an ELBO as  
2133 in Huang et al. (2021).  
21342135 Let  $(\Omega, \mathcal{F}, \mathbb{P})$  be the underlying probability space for which  $\mathbf{B}'$  is a Brownian motion. Suppose  $\mathbb{Q}$  is  
2136 another probability measure on  $(\Omega, \mathcal{F})$  equivalent to  $\mathbb{P}$  (i.e., they have the same measure zero sets).  
2137 We can hence apply the change-of-measure  
2138

2139 
$$p_0(\mathbf{x}) = \mathbb{E} \left[ \frac{d\mathbb{P}}{d\mathbb{Q}} p_T(\vec{\mathbf{x}}_T) \exp \left( - \int_0^T \nabla \cdot (\boldsymbol{\mu} - \frac{1}{2}(\nabla \cdot \boldsymbol{\Sigma})^\top)(\vec{\mathbf{x}}_s, T-s) ds \right) \middle| \vec{\mathbf{x}}_0 = \mathbf{x} \right] \quad (G.15)$$
  
2140

2141 Then, we apply Jensen's inequality:  
2142

2143 
$$\log p_0(\mathbf{x}) \geq \underbrace{\mathbb{E} \left[ \log \frac{d\mathbb{P}}{d\mathbb{Q}} + \log p_T(\vec{\mathbf{x}}_T) - \int_0^T \nabla \cdot (\boldsymbol{\mu} - \frac{1}{2}(\nabla \cdot \boldsymbol{\Sigma})^\top)(\vec{\mathbf{x}}_s, T-s) ds \middle| \vec{\mathbf{x}}_0 = \mathbf{x} \right]}_{= \mathcal{E}^\infty} .. \quad (G.16)$$
  
2144  
2145  
2146  
2147

2148 Compared to Huang et al. (2021), we have the additional term  $-\frac{1}{2}(\nabla \cdot \boldsymbol{\Sigma})^\top$ , that is,  $-\frac{1}{2}(\nabla \cdot \boldsymbol{\Sigma})^\top$ .  
21492150 G.5 GIRSANOV THEOREM  
21512152 Huang et al. (2021) apply the Girsanov theorem to the following forward SDE equation (17) of Huang  
2153 et al. (2021):  
2154

2155 
$$d\vec{\mathbf{x}}_s = (-\boldsymbol{\mu} + \mathbf{G}\mathbf{a}) ds + \mathbf{G}d\hat{\mathbf{B}}_s, \quad (G.17)$$
  
2156

2157 since the Itô to Stratonovich correction  $\frac{1}{2}(\boldsymbol{\mu} - \tilde{\boldsymbol{\mu}}) = \frac{1}{2}(\nabla \cdot \boldsymbol{\Sigma})^\top$  is zero in Huang et al. (2021).  
2158 However, it is not the case in MSGM and here we use the Girsanov theorem to this forward SDE  
2159 instead:  
2160

2161 
$$d\vec{\mathbf{x}}_s = (-\tilde{\boldsymbol{\mu}} + \mathbf{G}\mathbf{a}) ds + \mathbf{G}d\hat{\mathbf{B}}_s. \quad (G.18)$$
  
2162

The Girsanov theorem (Oksendal, 1998, Theorem 8.6.3) states the following. Let  $\hat{B}$  be an Itô process solving

$$d\hat{B}_s = -\mathbf{a}(\omega, s)ds + dB'_s, \quad (\text{G.19})$$

for  $\omega \in \Omega$  and  $\hat{B}_0 = 0$  where  $\mathbf{a}$  satisfies the Novikov's condition. Then  $\hat{B}$  is a Brownian motion with respect to  $\mathbb{Q}$  and :

$$\mathbb{E} \left[ \log \frac{d\mathbb{P}}{d\mathbb{Q}} \middle| \vec{\mathbf{x}}_0 = \mathbf{x} \right] = \mathbb{E} \left[ \int_0^T \mathbf{a}(\omega, s) \cdot dB'_s - \frac{1}{2} \int_0^T \|\mathbf{a}(\omega, s)\|_2^2 ds \middle| \vec{\mathbf{x}}_0 = \mathbf{x} \right], \quad (\text{G.20})$$

$$= -\frac{1}{2} \int_0^T \mathbb{E}_{\vec{\mathbf{x}}_s} \left[ \|\mathbf{a}(\omega, s)\|_2^2 \middle| \vec{\mathbf{x}}_0 = \mathbf{x} \right] ds, \quad (\text{G.21})$$

since  $T \mapsto \int_0^T \mathbf{a}(\omega, s) \cdot dB'_s$  is a martingale and thus  $\mathbb{E} \left[ \int_0^T \mathbf{a}(\omega, s) \cdot dB'_s \right] = 0$  (Oksendal, 1998, Theorem 3.2.1).

## G.6 ELBO EVALUATION

Equation G.21 enable us to evaluate the ELBO  $\mathcal{E}^\infty$  given by equation G.16. To evaluate the divergence term, we note that:

$$(\mu - \frac{1}{2}(\nabla \cdot \Sigma)^\top)(\mathbf{x}, T - s) = -\mathbf{f}_S(\mathbf{x}) + \frac{1}{2}(\nabla \cdot \Sigma)^\top(\mathbf{x}) + \Sigma(\mathbf{x})\mathbf{s}_\theta(\mathbf{x}, s) - \frac{1}{2}(\nabla \cdot \Sigma)^\top(\mathbf{x}), \quad (\text{G.22})$$

$$= -\mathbf{f}_S(\mathbf{x}) + \mathbf{G}(\mathbf{x})\mathbf{a}_\theta(\mathbf{x}, s). \quad (\text{G.23})$$

Then, the ELBO simplifies to:

$$\begin{aligned} \mathcal{E}^\infty(\mathbf{x}) &= \mathbb{E} \left[ \log \frac{d\mathbb{P}}{d\mathbb{Q}} \middle| \vec{\mathbf{x}}_0 = \mathbf{x} \right] + \mathbb{E} \left[ \log p_T(\vec{\mathbf{x}}_T) \middle| \vec{\mathbf{x}}_0 = \mathbf{x} \right] \\ &\quad + \int_0^T \mathbb{E}_{\vec{\mathbf{x}}_s} \left[ -\nabla \cdot (\mu - \frac{1}{2}(\nabla \cdot \Sigma)^\top) \middle| \vec{\mathbf{x}}_0 = \mathbf{x} \right] ds, \end{aligned} \quad (\text{G.24})$$

$$= \mathbb{E} \left[ \log p_T(\vec{\mathbf{x}}_T) \middle| \vec{\mathbf{x}}_0 = \mathbf{x} \right] \quad (\text{G.25})$$

$$- \int_0^T \mathbb{E}_{\vec{\mathbf{x}}_s} \left[ \frac{1}{2} \|\mathbf{a}_\theta(\vec{\mathbf{x}}_s, s)\|_2^2 + \nabla \cdot (\mathbf{G}(\vec{\mathbf{x}}_s)\mathbf{a}_\theta(\vec{\mathbf{x}}_s, s) - \mathbf{f}_S(\vec{\mathbf{x}}_s)) \middle| \vec{\mathbf{x}}_0 = \mathbf{x} \right] ds.$$

□

We recall that in our case,  $\mathbf{f}_S$  cancels out. The first term  $\mathbb{E} \left[ \log p_T(\vec{\mathbf{x}}_T) \middle| \vec{\mathbf{x}}_0 = \mathbf{x} \right]$  is a constant w.r.t. to  $\theta$ . So, if when maximizing the ELBDO, this term has no effect on the optimization procedure. Therefore, even with our multiplicative noise, the minimization of the ELBO corresponds precisely to Implicit Score Matching (ISM), which is itself equivalent to Explicit Score Matching (ESM), Sliced Score Matching (SSM) and Denoising Score Matching (DSM) (Huang et al., 2021).

## G.7 FROM ELBO TO OUR SSM LOSS

Here we show how to derive our practical SSM loss equation 3.14 from Theorem 3.4.1. We assume the skew-symmetry condition A1 and zero Stratonovich drift, i.e.  $f_s = 0$ . The theorem states the

$$p_0(\mathbf{x}_0|\theta) \geq \mathcal{E}_\infty(\mathbf{x}_0|\theta) := C(\mathbf{x}_0) - \mathcal{L}_\infty(\mathbf{x}_0|\theta) \quad (\text{G.26})$$

with  $C$  being a constant with respect to the parameters  $\theta$  to be learned. More precisely,

$$C(\mathbf{x}_0) = \mathbb{E} \left[ \log p_T(\vec{\mathbf{x}}_T) \middle| \vec{\mathbf{x}}_0 = \mathbf{x}_0 \right], \quad (\text{G.27})$$

$$\mathcal{L}_\infty(\mathbf{x}_0|\theta) = \int_0^T \mathbb{E}_{\vec{\mathbf{x}}_s} \left[ \frac{1}{2} \|\mathbf{a}_\theta(\vec{\mathbf{x}}_s, s)\|_2^2 + \nabla \cdot (\mathbf{G}(\vec{\mathbf{x}}_s)\mathbf{a}_\theta(\vec{\mathbf{x}}_s, s) - \mathbf{f}_S(\vec{\mathbf{x}}_s)) \middle| \vec{\mathbf{x}}_0 = \mathbf{x}_0 \right] ds. \quad (\text{G.28})$$

2214 Then, we average over the data  $\mathbf{x}_0$  to obtain the following lower bound for the likelihood of the  
 2215 dataset:

$$\mathbb{E}_{\mathbf{x}_0} p_0(\mathbf{x}_0|\boldsymbol{\theta}) \geq \mathbb{E}_{\mathbf{x}_0} \mathcal{E}_\infty(\mathbf{x}_0|\boldsymbol{\theta}) = \mathbb{E}_{\mathbf{x}_0} C(\mathbf{x}_0) - \mathbb{E}_{\mathbf{x}_0} \mathcal{L}_\infty(\mathbf{x}_0|\boldsymbol{\theta}). \quad (\text{G.29})$$

2218 Our objective is to find the neural network parameters  $\boldsymbol{\theta}$ , that try to maximize the likelihood  
 2219 of the data set,  $\mathbb{E}_{\mathbf{x}_0} p_0(\mathbf{x}_0|\boldsymbol{\theta})$ . Since  $\mathbb{E}_{\mathbf{x}_0} C(\mathbf{x}_0)$  is a constant with respect to  $\boldsymbol{\theta}$ , we maximize  
 2220  $-\mathbb{E}_{\mathbf{x}_0} \mathcal{L}_\infty(\mathbf{x}_0|\boldsymbol{\theta})$ . Let us explicit the two terms above with the Hutchinson trick,  $\mathbb{E}_{\mathbf{v} \sim \text{Rad}(d)} [\mathbf{v} \mathbf{v}^\top] =$   
 2221  $\mathbf{I}_d$  (Song et al., 2020)

$$\mathbb{E}_{\mathbf{x}_0} C(\mathbf{x}_0) = \mathbb{E}_{\mathbf{x}_T} \left[ \log p_T(\vec{\mathbf{x}}_T) \right], \quad (\text{G.30})$$

$$\begin{aligned} \mathbb{E}_{\mathbf{x}_0} \mathcal{L}_\infty(\mathbf{x}_0|\boldsymbol{\theta}) &= \int_0^T \mathbb{E}_{\vec{\mathbf{x}}_s} \left[ \frac{1}{2} \|\mathbf{a}_\boldsymbol{\theta}(\vec{\mathbf{x}}_s, s)\|^2 + \nabla \cdot (\mathbf{G}(\vec{\mathbf{x}}_s) \mathbf{a}_\boldsymbol{\theta}(\vec{\mathbf{x}}_s, s) - f_S(\vec{\mathbf{x}}_s)) \right] ds, \end{aligned} \quad (\text{G.31})$$

$$= T \int_0^T \mathbb{E}_{\vec{\mathbf{x}}_s} \left[ \frac{1}{2} \|\mathbf{a}_\boldsymbol{\theta}(\vec{\mathbf{x}}_s, s)\|^2 + \nabla \cdot (\mathbf{G}(\vec{\mathbf{x}}_s) \mathbf{a}_\boldsymbol{\theta}(\vec{\mathbf{x}}_s, s)) \right] \frac{1}{T} ds, \quad (\text{G.32})$$

$$= T \mathbb{E}_{s \sim \mathcal{U}[0, T]} \mathbb{E}_{\vec{\mathbf{x}}_s} \left[ \frac{1}{2} \|\mathbf{a}_\boldsymbol{\theta}(\vec{\mathbf{x}}_s, s)\|^2 + \nabla \cdot (\mathbf{G}(\vec{\mathbf{x}}_s) \mathbf{a}_\boldsymbol{\theta}(\vec{\mathbf{x}}_s, s)) \right], \quad (\text{G.33})$$

$$= T \mathbb{E}_{s \sim \mathcal{U}[0, T]} \mathbb{E}_{\vec{\mathbf{x}}_s} \left[ \frac{1}{2} \|\mathbf{a}_\boldsymbol{\theta}(\vec{\mathbf{x}}_s, s)\|^2 + \nabla \cdot (\mathbb{E}_{\mathbf{v} \sim \text{Rad}(d)} [\mathbf{v} \mathbf{v}^\top] \mathbf{G}(\vec{\mathbf{x}}_s) \mathbf{a}_\boldsymbol{\theta}(\vec{\mathbf{x}}_s, s)) \right], \quad (\text{G.34})$$

$$= T \mathbb{E}_{s \sim \mathcal{U}[0, T]} \mathbb{E}_{\vec{\mathbf{x}}_s} \mathbb{E}_{\mathbf{v} \sim \text{Rad}(d)} \left[ \frac{1}{2} \|\mathbf{a}_\boldsymbol{\theta}(\vec{\mathbf{x}}_s, s)\|^2 + (\mathbf{v} \cdot \nabla) (\mathbf{G}(\vec{\mathbf{x}}_s) \mathbf{a}_\boldsymbol{\theta}(\vec{\mathbf{x}}_s, s)) \cdot \mathbf{v} \right]. \quad (\text{G.35})$$

$$= T \mathcal{L}_{\text{SSM}}(\boldsymbol{\theta}). \quad (\text{G.36})$$

2239 Therefore, maximizing the ELBO,  $\mathbb{E}_{\mathbf{x}_0} \mathcal{E}_\infty(\mathbf{x}_0|\boldsymbol{\theta}) = \mathbb{E}_{\mathbf{x}_0} C(\mathbf{x}_0) - \mathbb{E}_{\mathbf{x}_0} \mathcal{L}_\infty(\mathbf{x}_0|\boldsymbol{\theta})$ , is equivalent to  
 2240 minimizing our practical score-matching loss,  $\mathcal{L}_{\text{SSM}}(\boldsymbol{\theta})$ .

## 2241 G.8 REMARK ON THE SCORE PARAMETRIZATION

2243 Following Huang et al. (2021), we directly model  $\mathbf{G}(\vec{\mathbf{x}}_t)^\top \nabla \log p_s(\mathbf{x})$  by a neural network  $\mathbf{a}_\boldsymbol{\theta}(\mathbf{x}, s)$ .  
 2244 If needed, the projected score,  $\nabla_\perp \log p_s$ , can be retrieved directly from  $\mathbf{a}_\boldsymbol{\theta}$  as shown below. Note  
 2245 that the full score,  
 2246

$$\nabla \log p_s = \nabla_\perp \log p_s + (\mathbf{x}^n \cdot \nabla) \log p_s, \quad (\text{G.37})$$

2247 involves a radial term,  $(\mathbf{x}^n \cdot \nabla) \log p_s$  that cannot be directly estimated in MSGM.

2249 **Proposition G.1.** *We assume that assumptions A1 and A2 hold, and that we have an approximation,  
 2250  $\mathbf{a}_\boldsymbol{\theta}$ , of the scaled score and an orthonormal basis  $\mathbf{u}_2(\mathbf{x}), \dots, \mathbf{u}_d(\mathbf{x})$  of  $\mathbf{x}^\perp$ , that we concatenate in  
 2251  $\mathbf{U}(\mathbf{x}) = [\mathbf{u}_2(\mathbf{x}), \dots, \mathbf{u}_d(\mathbf{x})] \in \mathbb{R}^{d \times (d-1)}$ . Then,*

$$[\mathbf{U}^\top(\mathbf{x}) \boldsymbol{\Sigma}(\mathbf{x}) \mathbf{U}(\mathbf{x})]^{-1} \mathbf{U}^\top(\mathbf{x}) \mathbf{G}(\mathbf{x}) \mathbf{a}_\boldsymbol{\theta}(\mathbf{x}, s). \quad (\text{G.38})$$

2254 approximates the projected score

$$\mathbf{U}^\top(\mathbf{x}) \nabla_\perp \log p_s(\mathbf{x}). \quad (\text{G.39})$$

2257 *Proof.* Since  $\mathbb{R}^d = \mathbb{R} \mathbf{x}^n \overset{\perp}{\oplus} \mathbf{x}^\perp$ , we have  $\mathbf{I}_d = \mathbf{x}^n (\mathbf{x}^n)^\top + \mathbf{U}(\mathbf{x}) \mathbf{U}^\top(\mathbf{x})$ . Using  $\boldsymbol{\Sigma}(\mathbf{x}) \mathbf{x}^n = 0$ , we  
 2258 obtain  
 2259

$$\mathbf{U}^\top(\mathbf{x}) \mathbf{G}(\mathbf{x}) \mathbf{a}_\boldsymbol{\theta}(\mathbf{x}, s) \approx \mathbf{U}^\top(\mathbf{x}) \mathbf{G}(\mathbf{x}) \mathbf{G}(\mathbf{x})^\top \nabla \log p_s(\mathbf{x}), \quad (\text{G.40})$$

$$= \mathbf{U}^\top(\mathbf{x}) \boldsymbol{\Sigma}(\mathbf{x}) [\mathbf{x}^n (\mathbf{x}^n)^\top + \mathbf{U}(\mathbf{x}) \mathbf{U}^\top(\mathbf{x})] \nabla \log p_s(\mathbf{x}), \quad (\text{G.41})$$

$$= \mathbf{U}^\top(\mathbf{x}) \boldsymbol{\Sigma}(\mathbf{x}) \mathbf{U}(\mathbf{x}) \mathbf{U}^\top(\mathbf{x}) \nabla \log p_s(\mathbf{x}), \quad (\text{G.42})$$

$$= \mathbf{U}^\top(\mathbf{x}) \boldsymbol{\Sigma}(\mathbf{x}) \mathbf{U}(\mathbf{x}) \mathbf{U}^\top(\mathbf{x}) \nabla_\perp \log p_s(\mathbf{x}). \quad (\text{G.43})$$

2264  $\mathbf{U}^\top(\mathbf{x}) \boldsymbol{\Sigma}(\mathbf{x}) \mathbf{U}(\mathbf{x}) \in \mathbb{R}^{(d-1) \times (d-1)}$  is full rank, so

$$\mathbf{U}^\top(\mathbf{x}) \nabla_\perp \log p_s(\mathbf{x}) \approx [\mathbf{U}^\top(\mathbf{x}) \boldsymbol{\Sigma}(\mathbf{x}) \mathbf{U}(\mathbf{x})]^{-1} \mathbf{U}^\top(\mathbf{x}) \mathbf{G}(\mathbf{x}) \mathbf{a}_\boldsymbol{\theta}(\mathbf{x}, s). \quad (\text{G.44})$$

□

2268 It is also possible to model the score,  $\nabla \log p_s(\mathbf{x})$  directly by a neural network,  $\mathbf{s}_\theta(\mathbf{x}, s)$  using the  
 2269 following score-matching loss:  
 2270

$$\mathcal{L}_{\text{SSM}}(\theta) = \mathbb{E}_{s \sim \mathcal{U}[0, T]} \mathbb{E}_{\vec{\mathbf{x}}_s} \mathbb{E}_{\mathbf{v} \sim \text{Rad}(d)} \left[ \frac{1}{2} \|\mathbf{a}_\theta(\vec{\mathbf{x}}_s, s)\|^2 + (\mathbf{v} \cdot \nabla)(\mathbf{G}(\vec{\mathbf{x}}_s) \mathbf{a}_\theta(\vec{\mathbf{x}}_s, s) - \mathbf{f}_S(\vec{\mathbf{x}}_s)) \cdot \mathbf{v} \right], \quad (\text{G.45})$$

$$\mathcal{L}_{\text{SSM}}(\theta) = \mathbb{E}_{s \sim \mathcal{U}[0, T]} \mathbb{E}_{\vec{\mathbf{x}}_s} \mathbb{E}_{\mathbf{v} \sim \text{Rad}(d)} \left[ \frac{1}{2} \|\mathbf{s}_\theta(\vec{\mathbf{x}}_s, s)\|_{\Sigma(\vec{\mathbf{x}}_s)}^2 + (\mathbf{v} \cdot \nabla)(\Sigma(\vec{\mathbf{x}}_s) \mathbf{s}_\theta(\vec{\mathbf{x}}_s, s) - \mathbf{f}_S(\vec{\mathbf{x}}_s)) \cdot \mathbf{v} \right] ds. \quad (\text{G.46})$$

2277 However, for any  $\alpha \in \mathbb{R}$ ,  $\mathcal{L}_{\text{SSM}}(\theta)(s_\theta) = \mathcal{L}_{\text{SSM}}(\theta)(s_\theta + \alpha \mathbf{x}^n)$ , i.e. our loss function is insensible to  
 2278 the radial component of the score  $(\mathbf{x}^n \cdot \nabla) \log p_s$ . Therefore, our MSGM framework does not provide  
 2279 estimation for the radial score  $(\mathbf{x}^n \cdot \nabla) \log p_s$ . Moreover, the optimization problem parametrized by  
 2280  $s_\theta$  is ill-defined, and the loss should probably be regularized as follows:

$$\mathcal{L}_{\text{SSM}}^{\text{reg}}(\theta) = \mathcal{L}_{\text{SSM}}(\theta) + \gamma \mathbb{E}_{s \sim \mathcal{U}[0, T]} \mathbb{E}_{\vec{\mathbf{x}}_s} [(\mathbf{x} \cdot \mathbf{s}_\theta)^2], \quad (\text{G.47})$$

2281 with  $\gamma > 0$  large, says  $\gamma = 10^6$ .  
 2282

## 2285 G.9 GIRSANOV THEOREM IN THE TRANSPORT NOISE LITERATURE

2287 Following the work done by Huang et al. (2021) for additive noise, we have relied on the Girsanov  
 2288 theorem (Oksendal, 1998) to prove the equivalence between score matching and ELBO maximization  
 2289 for MSGM. Girsanov theorem is widely used, we may cite here its recent uses in the transport noise  
 2290 literature. In a Bayesian context, Cotter et al. (2020a; 2023); González et al. (2025); Singh et al.  
 2291 (2025) introduce nudging in their particle filter. Also used with other type of noises, nudging biases  
 2292 the noise to make the solution closer to the observations. Similarly, in our case, the weighted score,  
 2293  $\mathbf{a}_\theta(\vec{\mathbf{x}}_t, T-t)$ , biases the noise,  $d\vec{\mathbf{B}}_t/dt$ , in our backward SDE to make its solution closer to the  
 2294 forward SDE solution (see equation 3.12). This noise change is the core of Girsanov theorem (see  
 2295 equation G.19). Ressegueir (2023) also proposed to fit a parametric model for the transport noise by  
 2296 maximum likelihood estimation.

## 2297 H COMPARISON WITH DIFFUSIONS ON RIEMANNIAN MANIFOLDS

2300 This appendix describes the similarities between MSGM on  $\mathbb{R}^d$  and SGMs on manifolds. To introduce  
 2301 the subject, we first recall some theoretical elements related to Riemannian manifolds. The link with  
 2302 SGMs on manifolds also suggests a particular neural network architecture that we exploit in this  
 2303 work.

### 2304 H.1 RIEMANNIAN MANIFOLDS AND DIFFERENTIATION

2306 This section is devoted to a brief introduction to Riemannian manifolds and the associated differential  
 2307 calculus. For a more comprehensive discussion, we refer to Lee (2018). Let  $\mathcal{M}$  be a smooth  $n$ -  
 2308 dimensional embedded submanifold of  $\mathbb{R}^d$ , where  $n \leq d$ . For any  $\mathbf{x} \in \mathcal{M}$  we denote by  $T_x \mathcal{M}$  the  
 2309 tangential (linear) space of  $\mathcal{M}$  at  $\mathbf{x}$ . We denote by  $g$  a Riemannian metric on  $\mathcal{M}$ , which assigns to  
 2310 each  $\mathbf{x} \in \mathcal{M}$  an inner product

$$g_x : T_x \mathcal{M} \times T_x \mathcal{M} \rightarrow \mathbb{R}.$$

2312 In the case of a smooth embedded manifold in the Euclidean space, the induced metric is given by  
 2313

$$g_x(u, v) = \langle u, v \rangle_{\mathbb{R}^d}, \quad \forall u, v \in T_x \mathcal{M}.$$

2315 This makes  $(\mathcal{M}, g)$  a Riemannian manifold. Let  $\{\mathbf{e}^{(1)}, \dots, \mathbf{e}^{(n)}\}$  be an orthonormal basis of  $T_x \mathcal{M}$ .  
 2316 Then, the orthogonal projection onto  $T_x \mathcal{M}$  is the linear operator  $P_x : \mathbb{R}^d \rightarrow T_x \mathcal{M}$  that satisfies  
 2317

$$P_x(v) = \arg \min_{w \in T_x \mathcal{M}} \|v - w\|_{\mathbb{R}^d} = \sum_{i=1}^n \langle v, \mathbf{e}^{(i)} \rangle \mathbf{e}^{(i)}.$$

2318 While the concept of Riemannian gradients can be derived for general manifolds, here we limit  
 2319 ourselves to the simpler presentation of embedded manifolds in the Euclidean space. In this setup,  
 2320

the Riemannian manifold can be defined as the classical gradient projected to the tangential space. In particular, for  $f : \mathbb{R}^d \rightarrow \mathbb{R}$  smooth, its *Riemannian gradient* can be computed as

$$\nabla_{\mathcal{M}} f(\mathbf{x}) = P_x(\nabla f(\mathbf{x})),$$

where  $\nabla f(\mathbf{x})$  is the Euclidean gradient. Furthermore, we want to define the Riemannian divergence in this framework. For a tangent vector field  $\mathbf{f} : \mathcal{M} \rightarrow \mathbb{R}^d$  with  $\mathbf{f}(\mathbf{x}) \in T_x \mathcal{M}$ , the *Riemannian divergence* is given as

$$\text{div}_{\mathcal{M}} \mathbf{f}(\mathbf{x}) = \sum_{i=1}^n \langle \partial_{\mathbf{e}^{(i)}} \mathbf{f}(\mathbf{x}), \mathbf{e}^{(i)} \rangle,$$

where  $\partial_{\mathbf{e}^{(i)}} \mathbf{f}$  is the Euclidean directional derivative. Finally, the *Laplace-Beltrami operator*  $\Delta_{\mathcal{M}}$  can be defined as

$$\Delta_{\mathcal{M}} f = \text{div}_{\mathcal{M}}(\nabla_{\mathcal{M}} f),$$

which generalizes the Laplacian to  $\mathcal{M}$ .

In the special case that  $\mathcal{M} = r\mathbb{S}^{d-1}$ , for a radius  $r > 0$  then  $n = d - 1$  and

$$T_x \mathcal{M} = T_x r\mathbb{S}^{d-1} = \{v \in \mathbb{R}^d \mid \langle v, \mathbf{x} \rangle = 0\},$$

and  $P_x(v) = v - \frac{1}{r^2} \langle v, \mathbf{x} \rangle \mathbf{x}$ . Since  $\mathbf{x}^n = \frac{\mathbf{x}}{r}$  we obtain  $P_x(v) = (I - \mathbf{x}^n(\mathbf{x}^n)^\top)v$  and as a result

$$\nabla_{\mathcal{M}} f(\mathbf{x}) = P_x(\nabla f(\mathbf{x})) = (I - \mathbf{x}^n(\mathbf{x}^n)^\top) \nabla f(\mathbf{x}) = \nabla_{\perp} f(\mathbf{x}). \quad (\text{H.1})$$

Regarding the Riemannian divergence, we note that  $\mathbf{x}^n, \mathbf{e}^{(1)}, \dots, \mathbf{e}^{(n)}$  defines an orthonormal basis of  $\mathbb{R}^d$ . By Lemma D.2.1

$$\nabla \cdot f(\mathbf{x}) = (\mathbf{x}^n \cdot \nabla)(\mathbf{x}^n \cdot f(\mathbf{x})) + \nabla_{\perp} \cdot f(\mathbf{x}).$$

For  $\mathbf{f}(\mathbf{x}) \in T_x \mathcal{M}$ , we have  $\mathbf{f}(\mathbf{x}) \cdot \mathbf{x}^n = 0$ . Thus:

$$\nabla_{\perp} \cdot \mathbf{f}(\mathbf{x}) = \nabla \cdot \mathbf{f}(\mathbf{x}) - \underbrace{(\mathbf{x}^n \cdot \nabla)(\mathbf{f}(\mathbf{x}) \cdot \mathbf{x}^n)}_{=0} = \nabla \cdot \mathbf{f}(\mathbf{x}).$$

Differentiating the tangency condition  $\mathbf{f}(\mathbf{x}) \cdot \mathbf{x}^n = 0$  along  $\mathbf{x}^n$  leads

$$0 = \partial_{\mathbf{x}^n}(\mathbf{f}(\mathbf{x}) \cdot \mathbf{x}^n) = \langle \partial_{\mathbf{x}^n} \mathbf{f}(\mathbf{x}), \mathbf{x}^n \rangle + \langle \mathbf{f}(\mathbf{x}), \partial_{\mathbf{x}^n} \mathbf{x}^n \rangle.$$

Since  $\partial_{\mathbf{x}^n} \mathbf{x}^n = 0$ , we conclude that  $\langle \partial_{\mathbf{x}^n} \mathbf{f}(\mathbf{x}), \mathbf{x}^n \rangle = 0$ . Finally, expanding  $\nabla \cdot \mathbf{f}(\mathbf{x})$  in  $\mathbf{x}^n, \mathbf{e}^{(1)}, \dots, \mathbf{e}^{(n)}$  leads to

$$\nabla_{\perp} \cdot \mathbf{f}(\mathbf{x}) = \nabla \cdot \mathbf{f}(\mathbf{x}) = \sum_{i=1}^n \langle \partial_{\mathbf{e}^{(i)}} \mathbf{f}(\mathbf{x}), \mathbf{e}^{(i)} \rangle + \underbrace{\langle \partial_{\mathbf{x}^n} \mathbf{f}(\mathbf{x}), \mathbf{x}^n \rangle}_{=0} = \text{div}_{\mathcal{M}} \mathbf{f}(\mathbf{x}). \quad (\text{H.2})$$

In our setting  $\text{Im}(\boldsymbol{\Sigma}(\mathbf{x})) = \mathbf{x}^{\perp} = T_x \mathcal{M}$ . Hence, the right-hand side of the Fokker-Planck equation 3.4

$$\text{div}_{\mathcal{M}}(\boldsymbol{\Sigma}(\mathbf{x}) \nabla_{\mathcal{M}} f(\mathbf{x})) = \nabla_{\perp} \cdot (\boldsymbol{\Sigma}(\mathbf{x}) \nabla_{\perp} f(\mathbf{x})), \quad (\text{H.3})$$

generalizes the notion of a divergence-form operator to the manifold setup.

## H.2 CONDITIONAL DIFFUSIONS ON SCALED $d$ -SPHERES

Several authors have recently developed SGM on Riemannian manifolds (De Bortoli et al., 2022; Huang et al., 2022; Benton et al., 2024) in order to generate data lying on a particular manifold. Clearly different, our goal is more classical: generating data in  $\mathbb{R}^d$ . However, each solution path of our forward and backward SDE lies on its scaled  $d$ -sphere  $\|\vec{\mathbf{x}}_0\| \mathbb{S}^{d-1}$ . Clearly,  $d$ -spheres are particular cases of Riemannian manifolds and possibly the most studied. De Bortoli et al. (2022) describes diffusions of  $\vec{\mathbf{x}}^n$  in the  $d$ -sphere  $\mathbb{S}^{d-1}$ . The simplest one involves a Brownian motion on the  $d$ -sphere that converges to the uniform distribution on the  $d$ -sphere,  $p_{\infty}^n$ . Unfortunately, this appealing proposal does not directly apply to our framework: the Brownian motion on the  $d$ -sphere is not a solution of our forward SDE of  $\vec{\mathbf{x}}^n$ . Indeed, in general, there exists

2376  $\vec{\mathbf{x}}^n \in \mathbb{S}^{d-1}$  such that  $\Sigma(\mathbf{x}^n) = \sum_{k=1}^d (\mathbf{G}^k \mathbf{x}^n)(\mathbf{G}^k \mathbf{x}^n)^\top \neq I_{\mathbb{S}^{d-1}}$ . So, the Fokker-Planck equation  
 2377 of De Bortoli et al. (2022),  
 2378

$$2379 \frac{\partial}{\partial s} p^n(\mathbf{x}^n) = \text{div}_{\mathbb{S}^{d-1}}(\nabla_{\mathbb{S}^{d-1}} p^n(\mathbf{x}^n)), \quad \forall \mathbf{x}^n \in \mathbb{S}^{d-1}, \quad (\text{H.4})$$

2381 and our Fokker-Planck equation for the direction,  
 2382

$$2383 \frac{\partial}{\partial s} p^n(\mathbf{x}^n) = \text{div}_{\mathbb{S}^{d-1}}(\Sigma(\mathbf{x}^n) \nabla_{\mathbb{S}^{d-1}} p^n(\mathbf{x}^n)), \quad \forall \mathbf{x}^n \in \mathbb{S}^{d-1}, \quad (\text{H.5})$$

2385 do not coincide. However, the analyses from the SGM-on-manifold community on the finite-time  
 2386 distribution, its score, approximations, and score-matching losses choices could certainly facilities  
 2387 the MSGM training process in the future.

2388 In our case, the norm of solution being constant along path, we can write both the forward and the  
 2389 backward equations of the direction on the unit  $d$ -sphere from equation 3.1 and equation 3.12:

$$2391 d\vec{\mathbf{x}}_t^n = \mathbf{G}(\vec{\mathbf{x}}_t^n) \circ d\vec{\mathbf{B}}_t, \quad (\text{H.6})$$

$$2393 d\vec{\mathbf{x}}_t^n = \frac{1}{\|\vec{\mathbf{x}}_t\|} \mathbf{G}(\vec{\mathbf{x}}_t) \left( \mathbf{G}(\vec{\mathbf{x}}_t)^\top \nabla \log p_{T-t} \left( \|\vec{\mathbf{x}}_t\| \vec{\mathbf{x}}_t^n \right) dt + \circ d\vec{\mathbf{B}}_t \right), \quad (\text{H.7})$$

$$2395 = \mathbf{G}(\vec{\mathbf{x}}_t^n) \left( \mathbf{G}(\vec{\mathbf{x}}_t^n)^\top \left( \|\vec{\mathbf{x}}_t\| \nabla_{\perp} \log p_{T-t} \left( \|\vec{\mathbf{x}}_t\| \vec{\mathbf{x}}_t^n \right) \right) dt + \circ d\vec{\mathbf{B}}_t \right). \quad (\text{H.8})$$

2397 We note that  $\|\mathbf{x}\| \nabla_{\perp} = \nabla_{\mathbb{S}^{d-1}} = \partial_{\mathbf{x}^n}$  is the Riemannian gradient on the scaled  $d$ -sphere  $\|\mathbf{x}\| \mathbb{S}^{d-1}$ .  
 2398 Therefore, using  $p_s^\otimes$ , the density of the couple of variables  $(\|\vec{\mathbf{x}}_s\|, \vec{\mathbf{x}}_s^n) \in \mathbb{R}^+ \times \mathbb{S}^{d-1}$ ,

$$2400 \|\vec{\mathbf{x}}_t\| \nabla_{\perp} \log p_{T-t} \left( \|\vec{\mathbf{x}}_t\| \vec{\mathbf{x}}_t^n \right) = \frac{\partial}{\partial \mathbf{x}^n} \log p_{T-t} \left( \|\vec{\mathbf{x}}_t\| \vec{\mathbf{x}}_t^n \right) \quad (\text{H.9})$$

$$2403 = \frac{\partial}{\partial \mathbf{x}^n} \log \left( p_{T-t}^\otimes \left( \|\vec{\mathbf{x}}_t\|, \vec{\mathbf{x}}_t^n \right) \|\vec{\mathbf{x}}_t\|^{1-d} \right) \quad (\text{H.10})$$

$$2405 = \frac{\partial}{\partial \mathbf{x}^n} \log \left( p_{T-t}^n \left( \vec{\mathbf{x}}_t^n \mid \|\vec{\mathbf{x}}_t\| \right) p_{\|\cdot\|} \left( \|\vec{\mathbf{x}}_t\| \right) \|\vec{\mathbf{x}}_t\|^{1-d} \right), \quad (\text{H.11})$$

$$2408 = \frac{\partial}{\partial \mathbf{x}^n} \log p_{T-t}^n \left( \vec{\mathbf{x}}_t^n \mid \|\vec{\mathbf{x}}_t\| \right) \quad (\text{H.12})$$

$$2410 = \frac{\partial}{\partial \mathbf{x}^n} \log p_{T-t}^n \left( \vec{\mathbf{x}}_t^n \mid \|\vec{\mathbf{x}}_0\| \right) \quad (\text{H.13})$$

$$2412 = \nabla_{\mathbb{S}^{d-1}} \log p_{T-t}^n \left( \vec{\mathbf{x}}_t^n \mid \|\vec{\mathbf{x}}_0\| \right) \quad (\text{H.14})$$

2413 and finally  
 2414

$$2415 d\vec{\mathbf{x}}_t^n = \mathbf{G}(\vec{\mathbf{x}}_t^n) \left( \mathbf{G}(\vec{\mathbf{x}}_t^n)^\top \nabla_{\mathbb{S}^{d-1}} \log p_{T-t}^n \left( \vec{\mathbf{x}}_t^n \mid \|\vec{\mathbf{x}}_0\| \right) dt + \circ d\vec{\mathbf{B}}_t \right). \quad (\text{H.15})$$

2418 In contrast, forward and backward SDEs of De Bortoli et al. (2022) read  
 2419

$$2420 d\vec{\mathbf{x}}_t^n = d\vec{\mathbf{B}}_t^{\mathbb{S}^{d-1}}, \quad (\text{H.16})$$

$$2422 d\vec{\mathbf{x}}_t^n = \nabla_{\mathbb{S}^{d-1}} \log p_{T-t}^n \left( \vec{\mathbf{x}}_t^n \right) dt + d\vec{\mathbf{B}}_t^{\mathbb{S}^{d-1}}, \quad (\text{H.17})$$

2424 where  $\vec{\mathbf{B}}_t^{\mathbb{S}^{d-1}}$  and  $\vec{\mathbf{B}}_t^{\mathbb{S}^{d-1}}$  are Brownian motions on the  $d$ -sphere. They can be defined from Stroock's  
 2425 representation (Hsu, 2002, Example 3.3.2) as  
 2426

$$2427 d\vec{\mathbf{B}}_t^{\mathbb{S}^{d-1}} = (\mathbf{I}_d - (\vec{\mathbf{x}}_t^n)(\vec{\mathbf{x}}_t^n)^\top) \circ d\vec{\mathbf{B}}_t, \quad (\text{H.18})$$

$$2429 d\vec{\mathbf{B}}_t^{\mathbb{S}^{d-1}} = (\mathbf{I}_d - (\vec{\mathbf{x}}_t^n)(\vec{\mathbf{x}}_t^n)^\top) \circ d\vec{\mathbf{B}}_t. \quad (\text{H.19})$$

The first main difference with MSGM is that the projection on the tangent plane,  $(\mathbf{I}_d - (\mathbf{x}^n)(\mathbf{x}^n)^\top)$ , (quadratic in  $\mathbf{x}^n$ ) is replaced in our approach by  $\mathbf{G}(\overleftarrow{\mathbf{x}}_t^n)$  (linear in  $\mathbf{x}^n$ ). Accordingly the noise (conditional) covariance,  $(\mathbf{I}_d - (\mathbf{x}^n)(\mathbf{x}^n)^\top)^2 = (\mathbf{I}_d - (\mathbf{x}^n)(\mathbf{x}^n)^\top)$  (projection property), is replaced by  $\mathbf{G}(\overleftarrow{\mathbf{x}}_t^n)\mathbf{G}(\overleftarrow{\mathbf{x}}_t^n)^\top = \Sigma(\overleftarrow{\mathbf{x}}_t^n)$ . To make our diffusion coincide with equation H.16, we would have to consider

$$\mathbf{G}(\mathbf{x}) := \|\mathbf{x}\|(\mathbf{I}_d - \mathbf{x}^n(\mathbf{x}^n)^\top), \quad (\text{H.20})$$

which is Lipchitz continuous but nonlinear. As such, the noise covariance would be

$$\Sigma(\mathbf{x}) = \|\mathbf{x}\|^2 \mathbf{I}_d - \mathbf{x}\mathbf{x}^\top. \quad (\text{H.21})$$

In general, we can hardly expect such a simple form from MSGM noise covariance. However, for the random tensor equation 6.1, we can show (see equation J.10) that:

$$2\mathbb{E}\Sigma(\mathbf{x}) = \|\mathbf{x}\|^2 \mathbf{I}_d - \mathbf{x}\mathbf{x}^\top. \quad (\text{H.22})$$

In addition, our score involved in the backward SDE equation H.15 depends on the norm  $\|\overleftarrow{\mathbf{x}}_t\|$ . The norm  $\|\overleftarrow{\mathbf{x}}_t\| = \|\overleftarrow{\mathbf{x}}_0\|$  appears as a covariate – with prior distribution  $p_{|\cdot|}$  – for the diffusion on the unit  $d$ -sphere. This is another major difference of our approach compared to SGM on manifolds. Besides, from this point of view, we can better understand how the direction and magnitude are re-coupled during MSGM generation. Along the reverse diffusion, the conditional score direction H.14 will focus along some orientations, counterbalancing the direction equiprobability of the latent space, i.e. reversing the "whitening" of the forward process. On different scaled  $d$ -sphere  $\|\mathbf{x}_0\|\mathbb{S}^{d-1}$ , the conditional score direction will be oriented differently, pushing along some orientations on some spheres and along other directions on spheres of larger radius. Accordingly, along the backward diffusion, the directions tend to align differently on different hyperspheres. The distribution of direction become more and more radius-dependent.

If data samples  $\overrightarrow{\mathbf{x}}_0$  are snapshots of a conservative dynamical system, all data points probably have the similar energy  $E = \|\overrightarrow{\mathbf{x}}_0\|^2$ , i.e.  $\text{Var}(E)/\mathbb{E}[E]^2$  is small. All data points are on closed scaled  $d$ -spheres  $\sqrt{E}\mathbb{S}^{d-1}$  and our approach becomes even closer to De Bortoli et al. (2022).

### H.3 LINK WITH NEURAL NETWORK ARCHITECTURE

Form equation H.14, we also note that

$$\mathbf{G}(\overleftarrow{\mathbf{x}}_t)^\top \nabla \log p_{T-t}(\overleftarrow{\mathbf{x}}_t) = \mathbf{G}(\overleftarrow{\mathbf{x}}_t^n)^\top \nabla_{\mathbb{S}^{d-1}} \log p_{T-t}^n(\overleftarrow{\mathbf{x}}_t^n \mid \|\overleftarrow{\mathbf{x}}_0\|), \quad (\text{H.23})$$

justifying our neural network spherical architecture equation L.33

$$\mathbf{G}(\overleftarrow{\mathbf{x}}_t)^\top \nabla \log p_{T-t}(\overleftarrow{\mathbf{x}}_t) \approx \mathbf{a}_\theta(\overleftarrow{\mathbf{x}}_t, T-t) = \tilde{\mathbf{a}}_\theta \left( \frac{\|\overleftarrow{\mathbf{x}}_t\|}{\|\overleftarrow{\mathbf{x}}_t\|_\epsilon} \overleftarrow{\mathbf{x}}_t^n, \log \|\overleftarrow{\mathbf{x}}_t\|_\epsilon, T-t \right). \quad (\text{H.24})$$

## I ANALYTIC ILLUSTRATIONS ON SIMPLIFIED CASES

### I.1 THE TWO-DIMENSIONAL CASE

We note here that for  $d = 2$ , we can find an analytic solution for our multiplicative forward SDE. Moreover, it corresponds to the Brownian motion on the circle.

Let us recall this forward SDE:

$$d\overrightarrow{\mathbf{x}}(t) = \mathbf{G}(\overrightarrow{\mathbf{x}}(t)) \circ d\overrightarrow{\mathbf{B}}_t = \sum_{k=1}^K \mathbf{G}^k \overrightarrow{\mathbf{x}}(t) \circ d\overrightarrow{\mathbf{B}}_t^k = \left( \sum_{k=1}^K \mathbf{G}^k \circ d\overrightarrow{\mathbf{B}}_t^k \right) \overrightarrow{\mathbf{x}}(t), \quad (\text{I.1})$$

In dimension 2,

$$d\overrightarrow{\mathbf{x}}(t) = \alpha J \overrightarrow{\mathbf{x}}(t) \circ d\overrightarrow{\mathbf{B}}_t^1, \quad (\text{I.2})$$

2484 where  $\vec{x} = \begin{pmatrix} \vec{x}_1 \\ \vec{x}_2 \end{pmatrix} \in \mathbb{R}^2$ ,  $J = \begin{pmatrix} 0 & -1 \\ 1 & 0 \end{pmatrix}$  is the  $\frac{\pi}{2}$ -rotation.  
 2485  
 2486

$$2487 \quad d\begin{pmatrix} \vec{x}_1 \\ \vec{x}_2 \end{pmatrix} = \alpha \begin{pmatrix} -\vec{x}_2 \\ \vec{x}_1 \end{pmatrix} \circ d\vec{B}_t^1, \quad (I.3)$$

2489 Then, in the complex plane,  $\vec{x}^C = \vec{x}_1 + i\vec{x}_2 \in \mathbb{C}$ , with  $i = \sqrt{-1}$  and we have:  
 2490  
 2491

$$2492 \quad d\vec{x}^C(t) = \alpha i \vec{x}^C \circ d\vec{B}_t^1, \quad (I.4)$$

2493 since  
 2494

$$2495 \quad d\vec{x}_1 + id\vec{x}_2 = \alpha i(\vec{x}_1 + i\vec{x}_2) \circ d\vec{B}_t^1 = \alpha(-\vec{x}_2 + i\vec{x}_1) \circ d\vec{B}_t^1. \quad (I.5)$$

2496 The solution is the Brownian motion on the circle:  
 2497  
 2498

$$2499 \quad \vec{x}^C(t) = \vec{x}^C(0) \exp(\alpha i \vec{B}_t^1), \quad (I.6)$$

2500 i.e.  
 2501

$$2502 \quad \vec{x}(t) = R(\alpha \vec{B}_t^1) \vec{x}(0) = \begin{pmatrix} \cos(\alpha \vec{B}_t^1) & -\sin(\alpha \vec{B}_t^1) \\ \sin(\alpha \vec{B}_t^1) & \cos(\alpha \vec{B}_t^1) \end{pmatrix} \vec{x}(0), \quad (I.7)$$

2503 i.e.  
 2504

$$2505 \quad \vec{x}_1(t) = \vec{x}_1(0) \cos(\alpha \vec{B}_t^1) - \vec{x}_2(0) \sin(\alpha \vec{B}_t^1), \quad (I.8)$$

$$2506 \quad \vec{x}_2(t) = \vec{x}_1(0) \sin(\alpha \vec{B}_t^1) + \vec{x}_2(0) \cos(\alpha \vec{B}_t^1). \quad (I.9)$$

2507 The key element of the proof was the possibility to write the forward diffusion with a single skew-  
 2508 symmetric matrix in equation I.2. Below we generalize this idea to larger dimension  $d \geq 2$ .  
 2509  
 2510

## 2512 I.2 TENSOR BUILT FROM A SINGLE SKEW-SYMMETRIC MATRIX

2513 Here we assume that whole tensor  $\mathbf{G}$  is built from the same dense skew-symmetric matrix  $\mathbf{G}^1$  i.e.  
 2514

$$2515 \quad \mathbf{G}^k = \mathbf{G}^1, \quad \forall k \in \{1, \dots, d\}, \quad (I.10)$$

2516 with  $\mathbf{G}^1$  a skew-symmetric matrix. As explained in Appendix K.2.1, this tensor respect the condition  
 2517 A1 but not the A2. Nevertheless, this case and its analytic solution may be insightful.  
 2518  
 2519

### 2520 I.2.1 MATRIX EXPONENTIAL

2521 Here the full Brownian matrix  $\mathbf{Z}$  can be simply factorized as  
 2522

$$2523 \quad \mathbf{Z}_s = \sum_{k=1}^d \mathbf{G}^k (\vec{B}_s)_k = \mathbf{G}^1 \sum_{k=1}^d (\vec{B}_s)_k. \quad (I.11)$$

2524 It has the same distribution than  
 2525  
 2526

$$2527 \quad \mathbf{Z}'_s = \sqrt{d} \mathbf{G}^1 \vec{B}'_s, \quad (I.12)$$

2528 with  $\vec{B}'$  another single Brownian motion. The forward diffusion simplify to  
 2529  
 2530

$$2531 \quad d\vec{x}_s = \sqrt{d} \mathbf{G}^1 \vec{x}_s \circ d\vec{B}'_s, \quad (I.13)$$

2532 with solution  
 2533

$$2534 \quad \vec{x}_s = \exp(\mathbf{Z}'_s) \vec{x}_0 = \exp\left(\sqrt{d} \mathbf{G}^1 \vec{B}'_s\right) \vec{x}_0, \quad (I.14)$$

2535 since  $\mathbf{Z}'_s$  and  $d\mathbf{Z}'_s$  commute.  
 2536  
 2537

2538 I.2.2 DIAGONALIZATION IN THE COMPLEX PLANE  
25392540  $G^1$  has pure imaginary eigenvalues and can be diagonalized in  $\mathbb{C}$  on an orthonormal basis  
2541

2542 
$$G^1 = \mathbf{U}_{\mathbb{C}}(i\Lambda)\mathbf{U}_{\mathbb{C}}^H, \quad (I.15)$$
  
2543

2544 with  $\mathbf{U}_{\mathbb{C}}$  a complex unitary matrix,  $\Lambda$  a real diagonal matrix, and the superscript  $H$  denotes the  
2545 conjugate transpose. Then, the solution can be easily evaluate as follow  
2546

2547 
$$\vec{\mathbf{x}}_s = \mathbf{U}_{\mathbb{C}} \exp\left(i\sqrt{d} \Lambda \vec{\mathbf{B}}'_s\right) \mathbf{U}_{\mathbb{C}}^H \vec{\mathbf{x}}_0, \quad (I.16)$$
  
2548

2549 For an even dimension  $d$ , and for all  $j \in \{1, \dots, d/2\}$ , there exists  $\lambda_j \in \mathbb{R}$  such that  
2550

2551 
$$(\mathbf{U}_{\mathbb{C}}^H \vec{\mathbf{x}}_s)_{2j-1} = \exp\left(i\sqrt{d} \lambda_j \vec{\mathbf{B}}'_s\right) (\mathbf{U}_{\mathbb{C}}^H \vec{\mathbf{x}}_0)_{2j-1}, \quad (I.17)$$
  
2552

2553 
$$(\mathbf{U}_{\mathbb{C}}^H \vec{\mathbf{x}}_s)_{2j} = \exp\left(-i\sqrt{d} \lambda_j \vec{\mathbf{B}}'_s\right) (\mathbf{U}_{\mathbb{C}}^H \vec{\mathbf{x}}_0)_{2j}. \quad (I.18)$$
  
2554

2555 For an odd dimension  $d$ ,  $G^1$  has at least one zero eigenvalue. Without loss of generality, we consider  
2556  $\Lambda_{d,d} = 0$  and for all  $j \in \{1, \dots, (d-1)/2\}$ , there exists  $\lambda_j \in \mathbb{R}$  such that  
2557

2558 
$$(\mathbf{U}_{\mathbb{C}}^H \vec{\mathbf{x}}_s)_{2j-1} = \exp\left(i\sqrt{d} \lambda_j \vec{\mathbf{B}}'_s\right) (\mathbf{U}_{\mathbb{C}}^H \vec{\mathbf{x}}_0)_{2j-1}, \quad (I.19)$$
  
2559

2560 
$$(\mathbf{U}_{\mathbb{C}}^H \vec{\mathbf{x}}_s)_{2j} = \exp\left(-i\sqrt{d} \lambda_j \vec{\mathbf{B}}'_s\right) (\mathbf{U}_{\mathbb{C}}^H \vec{\mathbf{x}}_0)_{2j}, \quad (I.20)$$
  
2561

2562 
$$(\mathbf{U}_{\mathbb{C}}^H \vec{\mathbf{x}}_s)_d = (\mathbf{U}_{\mathbb{C}}^H \vec{\mathbf{x}}_0)_d. \quad (I.21)$$
  
2563

2564 I.2.3 REAL SOLUTION WITH SINE AND COSINE  
25652566 The diagonalization matrix,  $\mathbf{U}$ , is complex but we can find a real unitary matrix,  $\mathbf{U}_{\mathbb{R}}$ , to make  
2567  $G_1$  block diagonal, and then expressing the solution with cosinus and sinus as in equation I.8 and  
2568 equation I.9:

2569 
$$(\mathbf{U}_{\mathbb{R}}^T \vec{\mathbf{x}}_s)_{2j-1} = \cos\left(\sqrt{d} \lambda_j \vec{\mathbf{B}}'_s\right) (\mathbf{U}_{\mathbb{R}}^T \vec{\mathbf{x}}_0)_{2j-1} - \sin\left(\sqrt{d} \lambda_j \vec{\mathbf{B}}'_s\right) (\mathbf{U}_{\mathbb{R}}^T \vec{\mathbf{x}}_0)_{2j}, \quad (I.22)$$
  
2570

2572 
$$(\mathbf{U}_{\mathbb{R}}^T \vec{\mathbf{x}}_s)_{2j} = \sin\left(\sqrt{d} \lambda_j \vec{\mathbf{B}}'_s\right) (\mathbf{U}_{\mathbb{R}}^T \vec{\mathbf{x}}_0)_{2j-1} + \cos\left(\sqrt{d} \lambda_j \vec{\mathbf{B}}'_s\right) (\mathbf{U}_{\mathbb{R}}^T \vec{\mathbf{x}}_0)_{2j}. \quad (I.23)$$
  
2573

2574 For an odd dimension  $d$ , the real solution reads  
2575

2576 
$$(\mathbf{U}_{\mathbb{R}}^T \vec{\mathbf{x}}_s)_{2j-1} = \cos\left(\sqrt{d} \lambda_j \vec{\mathbf{B}}'_s\right) (\mathbf{U}_{\mathbb{R}}^T \vec{\mathbf{x}}_0)_{2j-1} - \sin\left(\sqrt{d} \lambda_j \vec{\mathbf{B}}'_s\right) (\mathbf{U}_{\mathbb{R}}^T \vec{\mathbf{x}}_0)_{2j}, \quad (I.24)$$
  
2577

2579 
$$(\mathbf{U}_{\mathbb{R}}^T \vec{\mathbf{x}}_s)_{2j} = \sin\left(\sqrt{d} \lambda_j \vec{\mathbf{B}}'_s\right) (\mathbf{U}_{\mathbb{R}}^T \vec{\mathbf{x}}_0)_{2j-1} + \cos\left(\sqrt{d} \lambda_j \vec{\mathbf{B}}'_s\right) (\mathbf{U}_{\mathbb{R}}^T \vec{\mathbf{x}}_0)_{2j}, \quad (I.25)$$
  
2580

2581 
$$(\mathbf{U}_{\mathbb{R}}^T \vec{\mathbf{x}}_s)_d = (\mathbf{U}_{\mathbb{R}}^T \vec{\mathbf{x}}_0)_d. \quad (I.26)$$
  
2582

2583 Figure 5 illustrates the solution for  $d = 4$  with 20000 realizations of  $\vec{\mathbf{x}}_T$  at large time  $T = 100$ , with  
2584  $\lambda_1 = 1, \lambda_2 = 10$ ,  $\vec{\mathbf{x}}_0 = (1, 1, 1, 1)$ , and  $\mathbf{U}_{\mathbb{R}} = \mathbf{I}_4$ . A rotation-invariant distribution,  $p_{\infty}$ , would  
2585 induce rotation-invariant marginals and hence point cloud projections appearing rotation-invariant.  
2586 This is clearly not the case here. This counter example shows that low-rank tensors as defined in  
2587 equation I.10 cannot guarantee rotation-invariant latent distribution, and thus prevent the use of our  
2588 simple eCDF-based sampling procedure.  
25892590 Figure 7 illustrates the latent vector support for a random initial condition  $\vec{\mathbf{x}}_0 = N((1, 1, 1, 1), 0.01\mathbf{I}_4)$ . The supporting manifold is not one-dimensional anymore, but still depend  
2591 on the initial direction distribution,  $p_0^n$ .

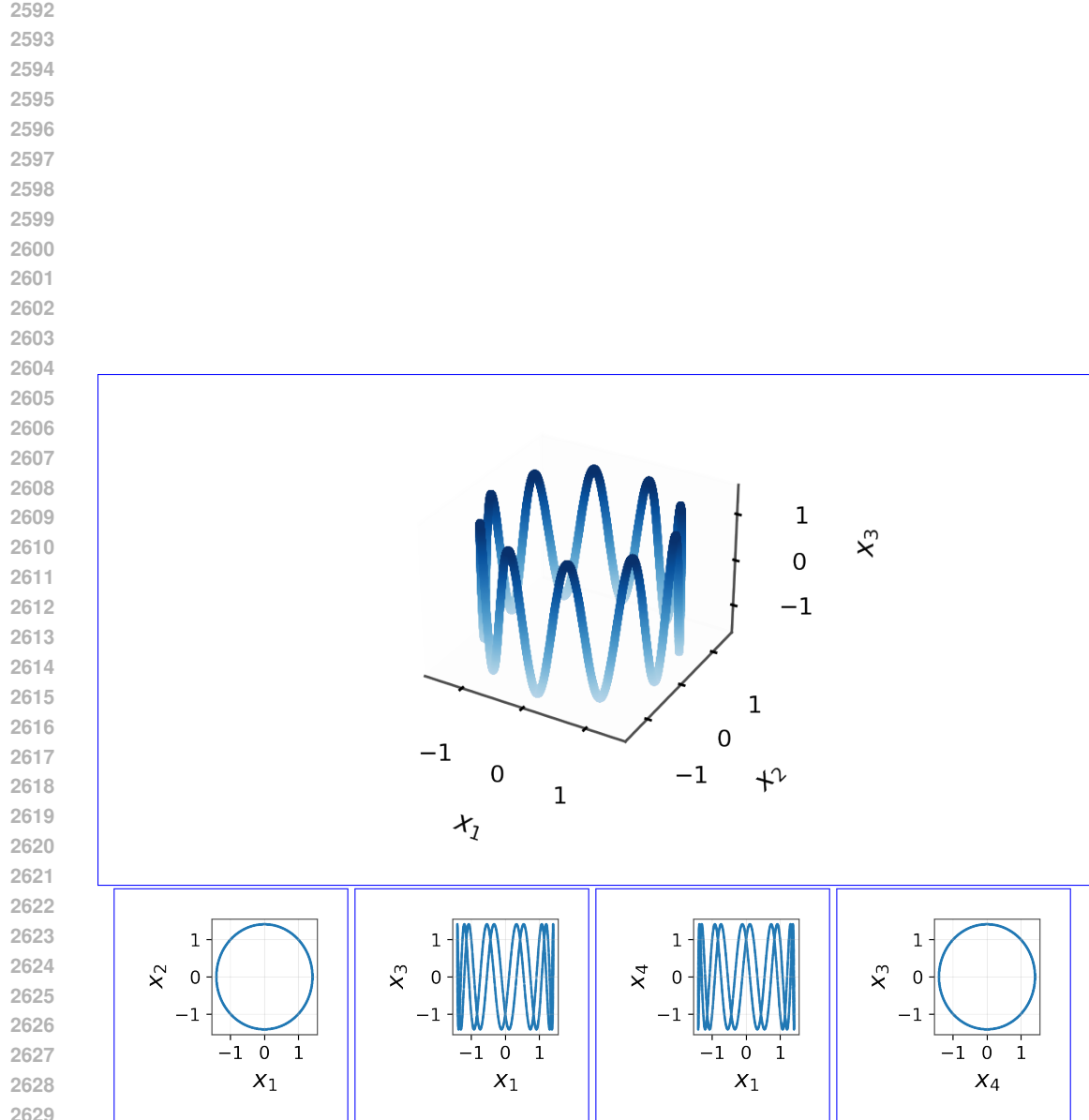
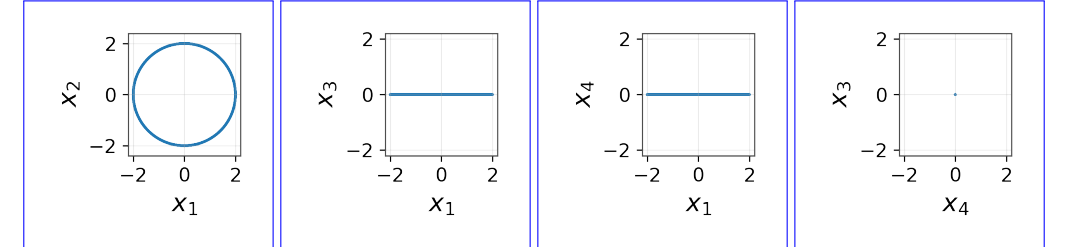


Figure 5: Projection of samples,  $\vec{x}_T$ , sketching the support of the invariant measure,  $p_\infty$ , for a low-rank tensor I.10,  $d = 4$  and  $\vec{x}_0 = (1, 1, 1, 1)$ . The top plot is in space  $(x_1, x_2, x_3)$ , the bottom plots are, from left to right, in space  $(x_1, x_2)$ ,  $(x_1, x_3)$ ,  $(x_1, x_4)$ , and  $(x_4, x_3)$ .

2646  
 2647  
 2648  
 2649  
 2650  
 2651  
 2652  
 2653  
 2654

2655 Moreover, as expected from the expression above, the initial norm,  $\|\vec{x}_0\|$ , scales the one-dimensional  
 2656 manifold supporting the invariant measure (not shown) and the initial direction,  $\vec{x}_0^n$ , has an influence  
 2657 at large time. Figure 6 shows the same example with  $\vec{x}_0 = (\sqrt{2}, \sqrt{2}, 0, 0)$ . The initial norm is the  
 2658 same but the initial direction is different. Therefore, the limit distribution,  $p_\infty$ , if it exists does depend  
 2659 on the initial direction,  $\vec{x}_0^n$ , making the latent sampling intractable.  
 2660

2661  
 2662  
 2663  
 2664  
 2665  
 2666  
 2667  
 2668  
 2669  
 2670  
 2671  
 2672  
 2673  
 2674  
 2675  
 2676  
 2677  
 2678



2679  
 2680 Figure 6: Projection of samples,  $\vec{x}_T$ , sketching the support of the invariant measure,  $p_\infty$ , for a  
 2681 low-rank tensor  $I.10$ ,  $d = 4$  and  $\vec{x}_0 = (\sqrt{2}, \sqrt{2}, 0, 0)$ . The top plot is in space  $(x_1, x_2, x_3)$ , the  
 2682 bottom plots are, from left to right, in space  $(x_1, x_2)$ ,  $(x_1, x_3)$ ,  $(x_1, x_4)$ , and  $(x_4, x_3)$ .  
 2683  
 2684  
 2685  
 2686  
 2687

2688  
 2689  
 2690  
 2691  
 2692  
 2693  
 2694  
 2695  
 2696  
 2697  
 2698  
 2699

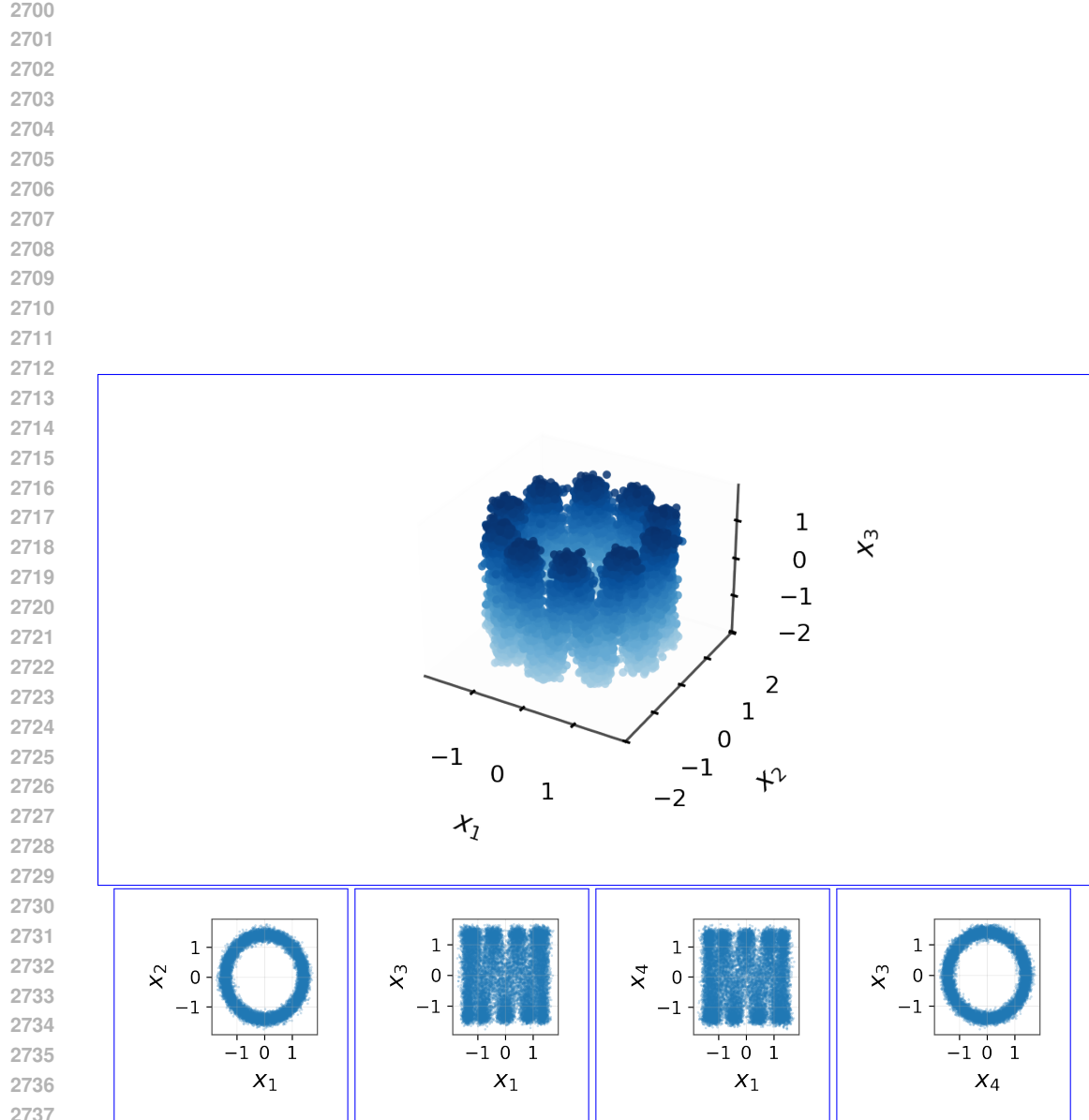


Figure 7: Projection of samples,  $\vec{x}_T$ , sketching the support of the invariant measure,  $p_\infty$ , for a low-rank tensor  $\mathbf{I.10}$ ,  $d = 4$  and  $\vec{x}_0 = \mathcal{N}((1, 1, 1, 1), 0.01\mathbf{I}_4)$ . The top plot is in space  $(x_1, x_2, x_3)$ , the bottom plots are, from left to right, in space  $(x_1, x_2)$ ,  $(x_1, x_3)$ ,  $(x_1, x_4)$ , and  $(x_4, x_3)$ .

2754 I.3 NON-COMMUTATIVITY IN THE GENERAL CASE  
27552756 For a general tensor  $\mathbf{G}$  in dimension  $d > 2$ , it is tempting to look for a solution  $\vec{\mathbf{x}}_s$  of the forward  
2757 SDE

2758 
$$d\vec{\mathbf{x}}_s = \circ d\mathbf{Z}_s \vec{\mathbf{x}}_s,$$

2759 of the form  $\exp(\mathbf{Z}_s) \vec{\mathbf{x}}_0$  with  $\mathbf{Z} = \sum_{k=1}^d \mathbf{G}^k (\vec{\mathbf{B}}_s)_k$ .  $\mathbf{Z}_s$  being skew-symmetric,  $\exp(\mathbf{Z}_s)$  is unitary  
2760 and such a solution would be reminiscent of the rotation form of equation I.6 and equation I.16 derived  
2761 above. However,  $\exp(\mathbf{Z}_s) \vec{\mathbf{x}}_0$  is not a solution of equation 3.1 in general, since  $d\mathbf{Z}_s \mathbf{Z}_s \neq \mathbf{Z}_s d\mathbf{Z}_s$ .  
27622763 J RANK AND SKEW-SYMMETRY CONDITIONS FOR RANDOM TENSOR  $G$   
27642765 In this appendix, we treat the case of random tensor  $\mathbf{G}$  as defined by equation 6.1. We will show that  
2766 this tensor respects both assumptions A1 and A2 almost surely. Then, we will discuss the speed of  
2767 contraction of the Fokker-Planck equation with this tensor.  
27682769 J.1 PROOF OF THE RANK CONDITION  
27702771 **Proposition J.1.** Let  $M^k \in \mathbb{R}^{d,d}$  be iid random matrices with entries drawn independently from  
2772  $\mathcal{N}(0, 1)$ . Define the skew-symmetric matrices  $\mathbf{G}^k = \frac{1}{2}(\mathbf{M}^k - (\mathbf{M}^k)^\top)$  and for  $\mathbf{x} \in \mathbb{R}^d \setminus \{0\}$  define  
2773 the (random) matrix

2774 
$$\mathbf{G}(\mathbf{x}) := [\mathbf{G}^1 \mathbf{x}, \mathbf{G}^2 \mathbf{x}, \dots, \mathbf{G}^d \mathbf{x}] \in \mathbb{R}^{d,d}.$$

2775 Then, almost surely  $\text{rank}(\mathbf{G}(\mathbf{x})) = d - 1$ .  
27762777 *Proof.* Let  $\mathbf{x} \neq 0$ . Let  $\mathbf{M}$  be a random standard Gaussian matrix. Then, let  $\mathbf{D} = \mathbf{M} - \mathbf{M}^\top$ . Then,  
2778  $\mathbf{D}$  is Gaussian matrix with entries drawn from  $\mathcal{N}(0, 2)$ , in particular  
2779

2780 
$$\mathbb{E}[D_{ij} D_{k\ell}] = \mathbb{E}[(M_{ij} - M_{ij})(M_{k\ell} - M_{k\ell})] = 2(\delta_{ik}\delta_{j\ell} - \delta_{i\ell}\delta_{jk}). \quad (\text{J.1})$$
  
2781

2782 Consequently,

2783 
$$\mathbb{E}[(\mathbf{M} - \mathbf{M}^\top) \mathbf{x} \mathbf{x}^\top (\mathbf{M}^\top - \mathbf{M})] = -\mathbb{E}[\mathbf{D} \mathbf{x} \mathbf{x}^\top \mathbf{D}]. \quad (\text{J.2})$$
  
2784

2785 Now, for the covariance structure it holds

2786 
$$-(\mathbb{E}[\mathbf{D} \mathbf{x} \mathbf{x}^\top \mathbf{D}])_{ik} = \mathbb{E}[(\mathbf{D} \mathbf{x})_i (\mathbf{D} \mathbf{x})_k], \quad (\text{J.3})$$
  
2787

2788 
$$= \sum_{j=1}^d \sum_{\ell=1}^d \mathbb{E}[D_{ij} x_j D_{k\ell} x_\ell], \quad (\text{J.4})$$
  
2789

2790 
$$= \sum_{j=1}^d \sum_{\ell=1}^d x_j x_\ell \mathbb{E}[D_{ij} D_{k\ell}], \quad (\text{J.5})$$
  
2791

2792 
$$= 2 \sum_{j=1}^d \sum_{\ell=1}^d x_j x_\ell (\delta_{ik}\delta_{j\ell} - \delta_{i\ell}\delta_{jk}), \quad (\text{J.6})$$
  
2793

2794 
$$= 2\delta_{ik} \sum_{j=1}^d \sum_{\ell=1}^d x_j x_\ell \delta_{j\ell} - 2 \sum_{j=1}^d \sum_{\ell=1}^d x_j x_\ell \delta_{i\ell} \delta_{jk}, \quad (\text{J.7})$$
  
2795

2796 
$$= 2\delta_{ik} \|\mathbf{x}\|^2 - 2x_i x_k. \quad (\text{J.8})$$
  
2797

2798 Hence  $\mathbb{E}[\mathbf{D} \mathbf{x} \mathbf{x}^\top \mathbf{D}] = 2(\|\mathbf{x}\| \mathbf{I}_d - \mathbf{x} \mathbf{x}^\top)$ . Consequently for any  $k = 1, \dots, d$  it holds that  
2799

2800 
$$\mathbb{E}[(\mathbf{G}^k \mathbf{x})(\mathbf{G}^k \mathbf{x})^\top] = \frac{1}{4} \mathbb{E}[(\mathbf{M}^k - (\mathbf{M}^k)^\top) \mathbf{x} \mathbf{x}^\top ((\mathbf{M}^k)^\top - \mathbf{M}^k)] = \frac{1}{2}(\|\mathbf{x}\|^2 \mathbf{I}_d - \mathbf{x} \mathbf{x}^\top). \quad (\text{J.9})$$
  
2801

2802 As a result, the matrix  $\mathbf{G}(\mathbf{x})$  has columns  $\mathbf{G}^k \mathbf{x} \stackrel{iid}{\sim} \mathcal{N}(0, \mathbf{V})$  with  
2803

2804 
$$\mathbf{V} = \mathbf{V}(\mathbf{x}) = \mathbb{E}\Sigma(\mathbf{x}) = \frac{1}{2}(\|\mathbf{x}\|^2 \mathbf{I}_d - \mathbf{x} \mathbf{x}^\top), \quad (\text{J.10})$$
  
2805

2808 of rank  $d - 1$ . Therefore,  $\Sigma(\mathbf{x}) = \mathbf{G}(\mathbf{x})\mathbf{G}(\mathbf{x})^\top \sim W_d(\mathbf{V}(\mathbf{x}), d)$  is a Wishart matrix.  
 2809

2810 Let  $\mathbf{K} = \mathbf{K}(\mathbf{x})$  be a matrix

$$2811 \quad \mathbf{K} = [\mathbf{K}_1, \dots, \mathbf{K}_{d-1}], \quad (J.11)$$

2812 with column vectors  $\mathbf{K}_i$  forming an orthonormal basis of the hyperplane  $\mathbf{x}^\perp$ . Then by construction,  
 2813 we have

$$2814 \quad \frac{2}{\|\mathbf{x}\|^2} \mathbf{K} \mathbf{V} \mathbf{K}^\top = \mathbf{I}_{d-1}. \quad (J.12)$$

2815 This means, that

$$2817 \quad \frac{\sqrt{2}}{\|\mathbf{x}\|} \mathbf{K} \mathbf{G}(\mathbf{x}) = \left( \frac{\sqrt{2}}{\|\mathbf{x}\|} \mathbf{K} \mathbf{G}^1 \mathbf{x} \dots \frac{\sqrt{2}}{\|\mathbf{x}\|} \mathbf{K} \mathbf{G}^d \mathbf{x} \right), \quad \frac{\sqrt{2}}{\|\mathbf{x}\|} \mathbf{K} \mathbf{G}^k \mathbf{x} \stackrel{iid}{\sim} \mathcal{N}(0, \mathbf{I}_{d-1}). \quad (J.13)$$

2819 Therefore,

$$2821 \quad \frac{\sqrt{2}}{\|\mathbf{x}\|} \mathbf{K} \Sigma(\mathbf{x}) \left( \frac{\sqrt{2}}{\|\mathbf{x}\|} \mathbf{K} \right)^\top = \left( \frac{\sqrt{2}}{\|\mathbf{x}\|} \mathbf{K} \mathbf{G}(\mathbf{x}) \right) \left( \frac{\sqrt{2}}{\|\mathbf{x}\|} \mathbf{K} \mathbf{G}(\mathbf{x}) \right)^\top \sim W_{d-1}(\mathbf{I}_{d-1}, d), \quad (J.14)$$

2823 is a Wishart matrix, in particular  $W_p(C, n)$  denotes the Wishart distribution with  $n$  degrees of freedom.  
 2824 In the case  $n \geq p$ , such matrix is invertible almost surely (Muirhead, 2009, Theorem 3.1.4). In our  
 2825 case  $n = d > p = d - 1$  thus almost surely

$$2826 \quad \text{rank} \left( \frac{\sqrt{2}}{\|\mathbf{x}\|} \mathbf{K} \mathbf{G}(\mathbf{x}) \right) = \text{rank} \left( \left( \frac{\sqrt{2}}{\|\mathbf{x}\|} \mathbf{K} \mathbf{G}(\mathbf{x}) \right)^\top \right) = d - 1. \quad (J.15)$$

2828 Now, since  $\mathbf{G}(\mathbf{x})^\top \mathbf{x} = 0$  we obtain almost surely that

$$2830 \quad d - 1 = \text{rank} \left( \frac{\sqrt{2}}{\|\mathbf{x}\|} \mathbf{K} \mathbf{G}(\mathbf{x}) \right) \leq \text{rank}(\mathbf{G}(\mathbf{x})) \leq d - 1, \quad (J.16)$$

2832 which yields the claim. □

## 2835 J.2 TENSOR RENORMALIZATION

2836 In practice, we renormalize the tensor  $\mathbf{G}$  as follows:

$$2838 \quad \mathbf{G} = \frac{\sqrt{d}}{\|\mathbf{G}\|_2} \tilde{\mathbf{G}} \quad \text{with} \quad \tilde{\mathbf{G}}_{ij}^k = \frac{1}{2} (\mathbf{M}_{i,j}^k - \mathbf{M}_{j,i}^k). \quad (J.17)$$

2841 The normalization ensures that the trace of matrix defining the **Itô** term of our forward SDE – i.e. the  
 2842 term driving the exponential decreases of  $\mathbb{E} \vec{\mathbf{x}}_s$  (see the forward **Itô** SDE equation D.9) – is

$$2844 \quad \text{tr} \left( \frac{1}{2} \sum_k \mathbf{G}^k \mathbf{G}^k \right) = -\text{tr} \left( \frac{1}{2} \sum_k \mathbf{G}^k (\mathbf{G}^k)^\top \right) = -\frac{1}{2} \sum_k \|\mathbf{G}^k\|_2^2 = -\frac{1}{2} \|\mathbf{G}\|_2^2 = -\frac{1}{2} d, \quad (J.18)$$

2846 similarly to the trace of the matrix defining the **Itô** term of classical **Ornstein Uhlenbeck** forward SDE  
 2847 :

$$2849 \quad \text{tr}(-\mathbf{I}_d) = -d. \quad (J.19)$$

2850 This normalization helps to better control the speed of convergence of the forward SDE without  
 2851 changing its skew-symmetry nor its rank.

## 2853 J.3 MEAN SPEED OF CONVERGENCE WITH RENORMALIZED TENSOR

2855 Note that in this case, for  $(\mathbf{x}, \mathbf{y}) \in S = \{(\mathbf{x}, \mathbf{y}) \in \mathbb{S}^{d-1} \times \mathbb{S}^{d-1} \mid \mathbf{x} \perp \mathbf{y}\}$ ,

$$2857 \quad \mathbb{E} \|\mathbf{G}(\mathbf{x}) \mathbf{y}\|^2 = \mathbf{y}^\top \mathbb{E} \Sigma(\mathbf{x}) \mathbf{y} = \mathbf{y}^\top \mathbb{E} \left( \sum_{k=1}^d (\mathbf{G}^k \mathbf{x})(\mathbf{G}^k \mathbf{x})^\top \right) \mathbf{y} = \mathbf{y}^\top \frac{d}{2} (\|\mathbf{x}\|^2 \mathbf{I}_d - \mathbf{x} \mathbf{x}^\top) \mathbf{y} = \frac{d}{2}. \quad (J.20)$$

2859 So, we can expect exponential convergence of the Fokker-Planck equation with the speed

$$2861 \quad \mathbb{E}[\alpha(\mathbf{G}, d)] = (d - 1) \mathbb{E} \min_{(\mathbf{x}, \mathbf{y}) \in S} \|\mathbf{G}^\top(\mathbf{x}) \mathbf{y}\|^2 = (d - 1) \mathbb{E} \|\mathbf{G}^\top(\vec{\mathbf{x}}_0) \mathbf{y}_0\|^2 = \frac{1}{2} d(d - 1). \quad (J.21)$$

2862 Therefore, the convergence gets faster when the dimension increases.  
 2863

2864 However, the tensor  $\mathbf{G}$  is normalized (see equation J.17), so the evaluation of the convergence speed  
 2865 is modified. We note first that:

$$2866 \mathbb{E}\|\tilde{\mathbf{G}}\|^2 = d\mathbb{E}\|\tilde{\mathbf{G}}^1\|^2 = \frac{d}{4}\mathbb{E}\|M^1 - (M^1)^\top\|^2 = \frac{d}{2}\sum_{ij}(\mathbb{E}(M_{ij}^1)^2 - \mathbb{E}M_{ij}^1M_{ji}^1), \quad (\text{J.22})$$

$$2867 = \frac{d}{2}\sum_{ij}(1 - \delta_{ij}^2) = \frac{1}{2}d^2(d - 1). \quad (\text{J.23})$$

2871 So, we obtain an estimate by Cauchy-Schwartz and Jensen's inequality  
 2872

$$2873 \mathbb{E}\|\mathbf{G}(\mathbf{x})\mathbf{y}\|^2 = \mathbb{E}\left\|\frac{\sqrt{d}}{\|\tilde{\mathbf{G}}\|}\tilde{\mathbf{G}}(\mathbf{x})\mathbf{y}\right\|^2 = \mathbb{E}\left[\frac{d}{\|\tilde{\mathbf{G}}\|^2}\|\tilde{\mathbf{G}}(\mathbf{x})\mathbf{y}\|^2\right], \quad (\text{J.24})$$

$$2874 \leq \mathbb{E}\left[\frac{d}{\|\tilde{\mathbf{G}}\|^2}\right]\mathbb{E}\|\tilde{\mathbf{G}}(\mathbf{x})\mathbf{y}\|^2, \quad (\text{J.25})$$

$$2875 \leq \frac{d}{\mathbb{E}\|\tilde{\mathbf{G}}\|^2}\mathbb{E}\|\tilde{\mathbf{G}}(\mathbf{x})\mathbf{y}\|^2, \quad (\text{J.26})$$

$$2876 = d\frac{d/2}{d^2(d-1)/2}, \quad (\text{J.27})$$

$$2877 = \frac{1}{d-1}, \quad (\text{J.28})$$

2885 and finally we obtain the following bound  
 2886

$$2887 \mathbb{E}\alpha(\mathbf{G}, d) \leq (d-1)\mathbb{E}\|\mathbf{G}^\top(\vec{\mathbf{x}}_0)\mathbf{y}_0\|^2 = 1. \quad (\text{J.29})$$

## 2889 K GOING BEYOND THE RANK CONDITION FOR MSGM SCALABILITY

2891 The dense tensor of Appendix J imposes a computational complexity as  $O(d^3)$ . To scale up the  
 2892 method, we shall consider sparse tensor  $\mathbf{G}$ . However, the rank condition A2 makes it difficult to find  
 2893 sparse tensors. Therefore, we here open the discussions to a weaker set of assumptions.  
 2894

### 2895 K.1 WEAKER ASSUMPTIONS

2897 We recall here the two main assumptions of the paper

2898 Skew-symmetry : For any  $k \in \{1, \dots, d\}$ , the matrix  $\mathbf{G}^k = (\mathbf{G}_{i,j}^k)_{i,j}$  is skew-symmetric. (A1)

2899 Rank condition : For any  $\mathbf{x} \in \mathbb{R}^d \setminus \{0\}$ ,  $\text{rank}(\mathbf{G}(\mathbf{x})) = d - 1$ . (A2)

2900 Note that the Fokker-Planck equation 3.4, Proposition F.2, Proposition F.1, and Theorem 3.4.1 re-  
 2901 quire only the assumption A1. So, the backward SDE, ODE and score-matching loss are general  
 2902 enough and do not prevent the use of sparse tensor  $\mathbf{G}$ . In contrast, our current proof of the asymptotic  
 2903 results Theorem 3.1.1, Theorem D.4.1, and Theorem 3.3.1 rely on the restrictive assumption A2, and  
 2904 unfortunately, it seems difficult to find a sparse tensor  $\mathbf{G}$  matching this assumption.  
 2905

#### 2906 K.1.1 RANK CONDITION ALMOST EVERYWHERE

2907 Therefore, we discuss here a weaker set of assumptions where the noise rank condition A2 is verified  
 2908 for almost all  $\mathbf{x} \in \mathbb{R}^d$  only. This set of assumptions will yield a definition of a sparse tensor in  
 2909 Appendix K.2.2 providing satisfactory numerical results in practice.  
 2910

2911 Skew-symmetry : For any  $k \in \{1, \dots, d\}$ , the matrix  $\mathbf{G}^k = (\mathbf{G}_{i,j}^k)_{i,j}$  is skew-symmetric. (A1)

2912 Rank condition almost everywhere: For almost all  $\mathbf{x} \in \mathbb{R}^d$ ,  $\text{rank}(\mathbf{G}(\mathbf{x})) = d - 1$ . (A3)

2913 The assumption A3 means the set  $A_G = \{\mathbf{x} \in \mathbb{R}^d | \mathbf{G}(\mathbf{x}) < d - 1\}$  has zero Lebesgue measure, i.e.  
 2914  $\int_{A_G} d\mathbf{x} = 0$ . Obviously, the assumption A2 implies the assumption A3.  
 2915

The right-hand side of the Fokker-Planck equation 3.4 is a function of  $\nabla_{\perp} p_{\infty}$  only. Hence, under the weaker assumptions A1 and A3, rotational invariant distributions are still invariant measures of the Fokker-Planck equation. Following the proof of Theorem D.2.1, we saw that the invariant density is characterized by  $\|\mathbf{G}(\mathbf{x})^{\top} \nabla_{\perp} p_{\infty}(\mathbf{x})\| = 0$  almost surely. So, if  $\mathbf{G}(\mathbf{x})$  has rank  $d - 1$  for almost all  $\mathbf{x}$  with respect to the Lebesgue measure, then this requires  $\nabla_{\perp} p_{\infty}(\mathbf{x}) = 0$  almost everywhere. Therefore, the invariant measures of Fokker-Planck equation 3.4 must be rotational invariant almost everywhere.

However, the existence and uniqueness of a classical solution (Lemma D.4.1) and the convergence guarantees to the invariant distribution (Theorem D.4.1) need more careful analysis. We only sketch some challenges involved, the full analysis will be carried out in a follow up work.

If the diffusion process enters the area of points  $\mathbf{x}$ , such that  $\text{rank}(\mathbf{G}(\mathbf{x})) < d - 1$ , one has to make sure that the Diffusion process is not trapped in such an area, even if it has a measure zero. In particular, let  $D \subset \mathbb{S}^{d-1}$  be defined as

$$D = \{\mathbf{x}^n \in \mathbb{S}^{d-1} \mid \text{rank}(G(\mathbf{x}^n)) < d - 1\}.$$

Then, we call  $D$  a trap set. If the process  $\vec{\mathbf{x}}_s^n$  once ever entering  $D$  with positive probability, it cannot leave  $D$  again, i.e.

$$\mathbb{P}(\vec{\mathbf{x}}_s^n \in D, \forall s \geq s_0 \mid \vec{\mathbf{x}}_{s_0}^n \in D) > 0.$$

Hence, in this case, convergence to the correct invariant measure has to ensure that the trap set is not invariant under the diffusion-controlled dynamic. Such a analysis then sufficiently can be implied by Hörmander / bracket-generating conditions, i.e. hypoellipticity analysis. Based on this, the asymptotic results Theorem 3.1.1, Theorem D.4.1, and Theorem 3.3.1 must be adapted. In this case we expect the convergence rate to the invariant distribution to be slower compared to the exponential convergence rate obtained in the case of strong rank condition, see also Appendix K.3 for a related discussion.

Although a detailed analysis of this research question is out of the scope of the current manuscript, we want to stress its relevance related to the *scalability* of the proposed method for the high-dimensional case. The standard construction via a random dense tensor  $\mathbf{G}$  poses scalability problems. On the other side, sparse tensors provide a tool to enable such scalability provided that they satisfy the (weaker) rank conditions. While the non-local sparse tensor discussed in Appendix K.2.3, satisfy the strong rank condition, the local sparse tensors from Appendix K.2.2 only satisfy the weak rank conditions. Still, the latter have been applied in our numerical investigation for the high-dimensional test cases with Particle Image Velocimetry measurements as discussed in Appendix M.7 yielding first very promising results.

### K.1.2 ITÔ TERM RANK CONDITION

Now, we discuss another weaker set of assumptions where the noise rank condition A2 is replaced by an Itô drift rank condition. Although attractive, a detailed analysis in Appendix K.2.1 will lead us to consider this set of assumptions as insufficient for the MSGM sampling procedure.

Skew-symmetry : For any  $k \in \{1, \dots, d\}$ , the matrix  $\mathbf{G}^k = (\mathbf{G}_{i,j}^k)_{i,j}$  is skew-symmetric. (A1)

Itô term rank condition : the matrix  $\mathbf{S} := \frac{1}{2} \sum_{k=1}^d (\mathbf{G}^k)(\mathbf{G}^k)^{\top}$  is full rank (A4)

From Lemma D.1.1, we note that  $\mathbf{S} = -\nabla \nabla \cdot \Sigma$ . Lemma D.1.2 gives the Itô forward diffusion which can be expressed with  $\mathbf{S}$ . The assumption A2 is not needed for these lemmas. These results are true as long as the assumption A1 is verified. Taking the expectation of the Itô diffusion, we get:

$$\frac{d}{ds} \mathbb{E} \vec{\mathbf{x}}_s = -\mathbf{S} \mathbb{E} \vec{\mathbf{x}}_s. \quad (\text{K.1})$$

Instead of controlling the convergence of the full distribution  $p_s$ , the assumption A4 controls the convergence of the mean only. It leads to the following property justifying our assumption choice.

**Proposition K.1.1.** *Let the assumption A1 holds. Then, the following assertions are equivalent*

- The assumption A4 holds.

2970     •  $\mathbb{E}[\vec{x}_s | \vec{x}_0] \xrightarrow[s \rightarrow \infty]{} 0$ .  
 2971  
 2972     •  $\text{Var}[\vec{x}_s | \vec{x}_0] \xrightarrow[s \rightarrow \infty]{} \|\vec{x}_0\|^2$ .

2974  
 2975 *Proof.*  $S$  is positive semi-definite, so it is diagonalizable in an orthonormal basis, and from equa-  
 2976 tion K.1,  $\mathbb{E}\vec{x}_s \xrightarrow[s \rightarrow \infty]{} 0$  if and only if  $S$  is positive definite, i.e. the assumption A4 is verified.  
 2977

2978 Besides, by assumption A1, the norm  $\|\vec{x}_s\|$  is conserved along the diffusion, so  
 2979

$$2980 \quad \text{Var}[\vec{x}_s | \vec{x}_0] = \|\vec{x}_s\|^2 - \|\mathbb{E}[\vec{x}_s | \vec{x}_0]\|^2 = \|\vec{x}_0\|^2 - \|\mathbb{E}[\vec{x}_s | \vec{x}_0]\|^2 \quad (\text{K.2})$$

2981 which converges to  $\|\vec{x}_0\|^2$  if and only if  $\mathbb{E}[\vec{x}_s | \vec{x}_0] \xrightarrow[s \rightarrow \infty]{} 0$ .  $\square$   
 2982

2983  
 2984 We highlight the fact that the assumption A4 is weaker than the assumption A2 as stated  
 2985 by Proposition K.1.2. It is actually a strictly weaker assumption since the tensors defined in  
 2986 Appendix K.2.1 and Appendix K.2.2 respect assumption A4 but not assumption A2.  
 2987

**Proposition K.1.2.** *Let the assumption A1 holds. Then, the assumption A2 implies the assumption A4.*

2990 *Proof.* If the assumption A2 holds, then, Theorem 3.3.1 implies that  $\vec{x}_s \xrightarrow[s \rightarrow 0]{\mathcal{L}} \vec{x}_\infty = \|\vec{x}_\infty\| \vec{x}_\infty^n$ .  
 2991 The asymptotic latent direction,  $\vec{x}_\infty^n$ , is independent of the initial condition  $\vec{x}_0$  and has zero mean.  
 2992 Therefore,  
 2993

$$2994 \quad \mathbb{E}[\vec{x}_s | \vec{x}_0] \xrightarrow[s \rightarrow \infty]{} \mathbb{E}[\vec{x}_\infty | \vec{x}_0] = \mathbb{E}[\|\vec{x}_\infty\| \vec{x}_\infty^n | \vec{x}_0] = \|\vec{x}_0\| \mathbb{E}[\vec{x}_\infty^n | \vec{x}_0] = \|\vec{x}_0\| \mathbb{E}[\vec{x}_\infty^n] = 0, \quad (\text{K.3})$$

2996 and by Proposition K.1.1, the assumption A4 holds.  $\square$   
 2997

## 2998 K.2 SPARSE TENSORS

3000 Here we propose several possible choices of sparse tensors.

3001 First, we will consider a simple low-rank tensor in Appendix K.2.1 and show that it makes the latent  
 3002 distribution untractable. Then, we will introduce a sparse local tensor in Appendix K.2.2, which  
 3003 is adapted to MSGM and leads to good generative skills in practice. Finally, we propose a sparse  
 3004 nonlocal tensor in Appendix K.2.3 that involves more Brownian motions but meets the original  
 3005 assumptions A1 and A2 of our paper.

### 3006 K.2.1 LOW-RANK TENSOR

3008 A simple choice of tensor with  $d^2 = O(d^2)$  non-zero coefficients would be to take  $d$  times the same  
 3009 dense random skew-symmetric matrix  $\mathbf{G}^1$  i.e.  
 3010

$$3011 \quad \mathbf{G}_{i,j}^k = \mathbf{G}_{i,j}^1 = \frac{1}{2}(\mathbf{M}_{i,j}^1 - \mathbf{M}_{j,i}^1), \quad (\text{K.4})$$

$$3012 \quad \mathbf{M}_{i,j}^1 \stackrel{iid}{\sim} \mathcal{N}(0, 1). \quad (\text{K.5})$$

3014 Appendix I.2 provides an analytic solution for the forward diffusion in this case. Such a solution  
 3015 would be a strong advantage for our learning procedure, bypassing the need for numerical integration  
 3016 of the forward diffusion, and enabling denoising score matching instead of sliced score matching.  
 3017 However, Proposition K.2.1 below shows that there is a rank deficiency, probably inducing the  
 3018 existence of non-rotation-invariant latent distribution,  $p_\infty$ , preventing MSGM sampling in practice.  
 3019 Indeed, numerically illustrated in dimension  $d = 4$ , the analytic solution of Appendix I.2 shows a  
 3020 latent distribution intractable in practice. The latent distribution is not rotation-invariant and does  
 3021 depends on the initial direction distribution,  $p_0^n$ . It seems to be a direct consequence of the rank  
 3022 deficiency.

3023 We conclude that low-rank tensors as in equation K.4 is not a suitable choice for MSGM. oreover, it  
 3024 suggests that assumptions A1 and A4 as in Appendix K.1.2 are not sufficient for MSGM.

3024  
 3025 **Proposition K.2.1.** *If  $\mathbf{G}$  is defined from equation K.4 and equation K.5, then, for any  $\mathbf{x} \in \mathbb{R}^d$ ,  
 3026  $\text{rank}(\mathbf{G}(\mathbf{x})) \leq 1$ . Assumption A1 is verified, assumptions A2 and A3 are not for  $d \geq 3$ , and  
 3027 assumption A4 is verified almost surely if and only if the dimension  $d$  is even. Moreover, we have  
 3028  $\mathbf{S} = \frac{d}{2} \mathbf{G}^1 (\mathbf{G}^1)^\top$  and  $\mathbb{E} \mathbf{S} = \frac{d(d-1)}{4} I_d$ .*

3029 *Proof.* The tensor defined by equation K.4 and equation K.5 obviously matches the skew-symmetric  
 3030 condition A1.

3031 For odd dimension  $d$ ,  $\mathbf{G}^1$  – like all skew-symmetric matrix – is singular. Thus  $\mathbf{S}$  is singular and even  
 3032 the weak condition A4 is not satisfied.

3034 For even  $d$  the polynomial  $p: \mathbb{R}^{d \times d} \rightarrow \mathbb{R}$ ,  $\mathbf{M} \mapsto \det(\frac{1}{2}(\mathbf{M} - \mathbf{M}^\top))$ , which is non-zero since  
 3035 there exists invertible skew-symmetric matrices. As a non-zero polynomial, the set  $\{\mathbf{M} \in \mathbb{R}^{d,d} \mid$   
 3036  $\det(\mathbf{M} - \mathbf{M}^\top) = 0\}$  forms a proper algebraic variety with zero Lebesgue measure. Hence, since the  
 3037 Gaussian distribution is absolutely continuous w.r.t. to the Lebesgue measure, it holds

$$3038 \quad \mathbb{P}(\det(\mathbf{G}^1) = 0) = 0, \quad (\text{K.6})$$

3039 and so  $\mathbf{G}^1$  is invertible with full rank with probability 1. Thus

$$3041 \quad \mathbf{S} = \frac{d}{2} \mathbf{G}^1 (\mathbf{G}^1)^\top. \quad (\text{K.7})$$

3043 is positive definite. Therefore, A4 is verified for even dimension  $d$ .

3044 However, for any  $d \geq 3$ , neither conditions A2 nor condition A3 is satisfied. Indeed, for any  
 3045  $\mathbf{x} \in \mathbb{R}^d \setminus \{0\}$ ,  $\text{rank}(\mathbf{G}(\mathbf{x})) = \text{rank}[\mathbf{G}^1 \mathbf{x}, \dots, \mathbf{G}^1 \mathbf{x}] \leq 1$ . This is expected since the diffusion involves  
 3046 a single Brownian motion (see Appendix I.2).

3047 Since the entries in  $\mathbf{M}^1$  are independent standard normal Gaussian, we have  $\mathbb{V}(G_{i,j}^1) = \frac{1}{4}(\mathbb{V}(M_{i,j}^1) +$   
 3048  $\mathbb{V}(M_{j,i}^1)) = \frac{1}{2}$ . Then,  $[\mathbf{G}^1 (\mathbf{G}^1)^\top]_{ik} = \sum_{j=1}^d G_{ij}^1 G_{kj}^1$ . Hence for  $i = k$

$$3052 \quad \mathbb{E}[[\mathbf{G}^1 (\mathbf{G}^1)^\top]_{ik}] = \sum_{j=1}^d \mathbb{E}[(G_{ij}^1)^2] = \sum_{j \neq i} \frac{1}{2} = \frac{d-1}{2},$$

3055 since  $G_{ii}^1 = 0$ . For  $i \neq k$ ,  $G_{ij}^1$  and  $G_{kj}^1$  involve independent entries of  $\mathbf{M}^1$ , leading to  $\mathbb{E}[G_{ij}^1 G_{kj}^1] = 0$ .  
 3056 As a consequence

$$3057 \quad \mathbb{E}[\mathbf{S}] = \frac{d}{2} \mathbb{E}[\mathbf{G}^1 (\mathbf{G}^1)^\top] = \frac{d(d-1)}{4} I_d \in \mathbb{R}^{d,d}.$$

3059  $\square$

## 3060 K.2.2 LOCAL SPARSE TENSOR

3063 Let us define a tensor with only  $2d = O(d)$  non-zero coefficients.

$$3064 \quad \mathbf{G}_{i,j}^k = \begin{cases} 1 & \text{if } i = j \text{ and } [d] = k \\ -1 & \text{if } i - 1[d] = j = k \\ 0 & \text{otherwise.} \end{cases}, \quad 1 \leq i, j, k \leq d, \quad (\text{K.8})$$

3067 with  $[d]$  stands for modulo  $d$ . It is built from a subset of the canonical basis of skew-symmetric  
 3068 matrices, keeping only  $d$  matrices with most non-zero values close to the diagonal. It ensures a strong  
 3069 sparsity and a local structure for  $\mathbf{x} \rightarrow \mathbf{G}^k \mathbf{x}$ .

3071 The skew-symmetry assumption A1 is obviously fulfilled from the definition K.8. However, the strict  
 3072 rank condition assumption A2 is not in general. Fortunately, the assumptions A3 and A4 still hold. In  
 3073 particular, the Itô term matrix simplifies as shown by the following proposition.

3074 We implemented this version of sparse tensor. For small dimension applications in Appendix M.6.2  
 3075 and Appendix M.6.1, it has been found to provide numerical results as good as the dense tensor im-  
 3076 plementation (see Figures 29 and 43). For large dimension applications, dense tensor can complicate  
 3077 or even prevent MSGM applications. There, we obtained satisfactory results with local sparse tensor  
 (see Figure 49 in Appendix M.6.2).

3078 **Proposition K.2.2.** *If  $\mathbf{G}$  is defined from equation K.8, then, for any  $\mathbf{x} \in (\mathbb{R} \setminus \{0\})^d$ ,  $\text{rank}(\mathbf{G}(\mathbf{x})) =$   
 3079  $d - 1$ . Moreover, we have  $\mathbf{S} = \mathbf{I}_d$  and the assumptions A1, A3, and A4 are verified.*

3080  
 3081 *Proof.* For any  $\mathbf{x} \in (\mathbb{R} \setminus \{0\})^d$ , we have

$$3082 \quad \mathbf{G}(\mathbf{x}) = [\mathbf{G}^1 \mathbf{x}, \dots, \mathbf{G}^d \mathbf{x}] = \begin{pmatrix} x_2 & 0 & \cdots & 0 & -x_d \\ -x_1 & x_3 & \cdots & 0 & 0 \\ 0 & -x_2 & \ddots & \vdots & \vdots \\ \vdots & \vdots & \ddots & x_d & 0 \\ 0 & 0 & \cdots & -x_{d-1} & x_1 \end{pmatrix}. \quad (\text{K.9})$$

3083 To simplify notations, all the indices in this proof will be defined modulo  $d$ . For instance,  $x_{i+1}$  for  
 3084  $i = d$  stands for  $x_1$ .

3085 For any  $\mathbf{y} \in \mathbb{R}^d$ ,  $\mathbf{G}(\mathbf{x})^T \mathbf{y} = 0$  ( $\in \mathbb{R}^d$ ) if and only if, for all  $i \leq d$ ,  $x_{i+1}y_i - x_iy_{i+1} = 0$  and  
 3086  $y_{i+1} = \frac{x_{i+1}}{x_i}y_i$ . Finally,

$$3087 \quad y_i = \prod_{j=1}^{i-1} \frac{x_{i+1}}{x_i} y_1 = \frac{x_i}{x_1} y_1. \quad (\text{K.10})$$

3088 Therefore,  $\mathbf{y} \in \mathbb{R}\mathbf{x}$ . Reciprocally, we can verify that  $\mathbb{R}\mathbf{x} \subset \text{Ker}(\mathbf{G}(\mathbf{x}))$ . We conclude that  
 3089  $\text{rank}(\mathbf{G}(\mathbf{x})) = d - \dim(\text{Ker}(\mathbf{G}(\mathbf{x}))) = d - 1$ .

3090 To evaluate the matrix  $\mathbf{S}$ , we note that

$$3091 \quad \mathbf{G}^k = \mathbf{e}_k \mathbf{e}_{k+1}^\top - \mathbf{e}_{k+1} \mathbf{e}_k^\top, \quad (\text{K.11})$$

3092 with  $(\mathbf{e}_k)_k$  the canonical basis of  $\mathbb{R}^d$ . Then,

$$3093 \quad \mathbf{S} = -\frac{1}{2} \sum_{k=1}^d (\mathbf{G}^k)^2, \quad (\text{K.12})$$

$$3094 \quad = -\frac{1}{2} \sum_{k=1}^d (\mathbf{e}_k \mathbf{e}_{k+1}^\top - \mathbf{e}_{k+1} \mathbf{e}_k^\top)^2, \quad (\text{K.13})$$

$$3095 \quad = -\frac{1}{2} \sum_{k=1}^d (0 - \mathbf{e}_k \mathbf{e}_k^\top - \mathbf{e}_{k+1} \mathbf{e}_{k+1}^\top + 0), \quad (\text{K.14})$$

$$3096 \quad = \frac{1}{2} (\mathbf{I}_d + \mathbf{I}_d), \quad (\text{K.15})$$

$$3097 \quad = \mathbf{I}_d. \quad (\text{K.16})$$

3098  $\square$

### 3114 K.2.3 NON-LOCAL SPARSE TENSOR

3115 We also propose another tensor with  $d(d - 1) = O(d^2)$  non-zero coefficients.

$$3116 \quad \mathbf{G}_{i,j}^{k,k'} = \begin{cases} 1 & \text{if } i - k'[d] = j = k \\ -1 & \text{if } i = j - k'[d] = k \\ 0 & \text{otherwise.} \end{cases}, \quad 1 \leq i, j, k \leq d, \quad 1 \leq k' \leq \lceil \frac{d-1}{2} \rceil, \quad (\text{K.17})$$

3117 where  $\lceil \frac{d-1}{2} \rceil$  is the least integer greater than or equal to  $\frac{d-1}{2}$ . It is the canonical basis for skew-  
 3118 symmetric matrices. It ensures a relative sparsity and encodes a non-local structure for  $\mathbf{x} \rightarrow \mathbf{G}^{k,k'} \mathbf{x}$ .

3119 Here, the sparse tensor  $\mathbf{G}$  is of size  $d \times d \times d(d - 1)/2$  instead of  $d \times d \times d$ . Our theoretical framework  
 3120 differs slightly. The forward diffusion involves  $d(d - 1)/2$  one-dimensional Brownian motions.  
 3121 Consequently, the neural network,  $\mathbf{a}_\theta(\mathbf{x}, s)$ , approximating the scaled score,  $\mathbf{G}(\mathbf{x}) \nabla \log p_s(\mathbf{x})$ ,  
 3122 has  $d(d - 1)/2$  coefficients. The size of the neural network parameters  $\theta$  can increase and may  
 3123 complicate the training procedure. An alternative could be to work with a neural network,  $\mathbf{s}_\theta(\mathbf{x}, s)$ ,  
 3124 which approximates the true score,  $\nabla \log p_s(\mathbf{x})$ , having  $d$  coefficients only.

3125 This choice of tensor meets all the assumptions, including A1 and A2 as proofed below. However,  
 3126 because of the additional implementation complexity mentioned above, we postpone its numerical  
 3127 evaluation to MSGM for future work.

3132 **Proposition K.2.3.** *If  $\mathbf{G}$  is defined from equation K.17, then, for any  $\mathbf{x} \in \mathbb{R}^d \setminus \{0\}$ ,  $\text{rank}(\mathbf{G}(\mathbf{x})) =$   
 3133  $d - 1$ . Moreover, we have  $\mathbf{S} = \mathbf{I}_d$  and the assumptions A1, A2, A3, and A4 are verified.*

3135 *Proof.* For any  $\mathbf{x} \in \mathbb{R}^d \setminus \{0\}$ , we have

$$3137 \quad \mathbf{G}(\mathbf{x}) = [\mathbf{G}^{1,1}\mathbf{x}, \dots, \mathbf{G}^{d,\lceil \frac{d-1}{2} \rceil}\mathbf{x}] \quad (\text{K.18})$$

3139 We already know that  $\text{Im}(\mathbf{G}(\mathbf{x})) \subset \mathbf{x}^\perp$  since  $\mathbf{x}^\top \mathbf{G}(\mathbf{x}) = 0$ . Now we assume that  $\mathbf{y} \in \mathbf{x}^\perp$ , and we  
 3140 define

$$3141 \quad \mathbf{Q} = \frac{1}{\|\mathbf{x}\|^2} (\mathbf{y}\mathbf{x}^\top - \mathbf{x}\mathbf{y}^\top). \quad (\text{K.19})$$

3143 Applying on  $\mathbf{x}$ , we get:

$$3145 \quad \mathbf{Q}\mathbf{x} = \frac{1}{\|\mathbf{x}\|^2} (\mathbf{y}\|\mathbf{x}\|^2 - \mathbf{x}\mathbf{y}\cdot\mathbf{x}) = \mathbf{y}. \quad (\text{K.20})$$

3147 Besides,  $(\mathbf{G}^{k,k'})_{k,k'}$  is the canonical basis of skew-symmetric matrices and  $\mathbf{Q}$  is skew-symmetric so  
 3148 there exists  $\alpha \in \mathbb{R}^{\frac{d(d-1)}{2}}$  such that

$$3150 \quad \mathbf{Q} = \sum_{k'=1}^{\lceil \frac{d-1}{2} \rceil} \sum_{k=1}^d \alpha_{k,k'} \mathbf{G}^{k,k'} \quad (\text{K.21})$$

3153 and thus

$$3155 \quad \mathbf{y} = \mathbf{Q}\mathbf{x} = \sum_{k'=1}^{\lceil \frac{d-1}{2} \rceil} \sum_{k=1}^d \alpha_{k,k'} \mathbf{G}^{k,k'} \mathbf{x} = \mathbf{G}(\mathbf{x})\alpha \in \text{Im}(\mathbf{G}(\mathbf{x})). \quad (\text{K.22})$$

3158 We conclude that  $\text{Im}(\mathbf{G}(\mathbf{x})) = \mathbf{x}^\perp$  and  $\text{rank}(\mathbf{G}(\mathbf{x})) = d - 1$ .

3159 To evaluate the matrix  $\mathbf{S}$ , we note that

$$3161 \quad \mathbf{G}^{k,k'} = \mathbf{e}_k \mathbf{e}_{k+k'}^\top - \mathbf{e}_{k+k'} \mathbf{e}_k^\top, \quad (\text{K.23})$$

3163 with  $(\mathbf{e}_k)_k$  the canonical basis of  $\mathbb{R}^d$ , and defining again all the indices modulo  $d$ .

$$3164 \quad \mathbf{S} = -\frac{1}{2} \sum_{k'=1}^{\lceil \frac{d-1}{2} \rceil} \sum_{k=1}^d (\mathbf{G}^{k,k'})^2, \quad (\text{K.24})$$

$$3168 \quad = -\frac{1}{2} \sum_{k'=1}^{\lceil \frac{d-1}{2} \rceil} \sum_{k=1}^d (\mathbf{e}_k \mathbf{e}_{k+k'}^\top - \mathbf{e}_{k+k'} \mathbf{e}_k^\top)^2, \quad (\text{K.25})$$

$$3171 \quad = -\frac{1}{2} \sum_{k'=1}^{\lceil \frac{d-1}{2} \rceil} \sum_{k=1}^d \sum_{k=1}^d (0 - \mathbf{e}_k \mathbf{e}_k^\top - \mathbf{e}_{k+k'} \mathbf{e}_{k+k'}^\top + 0), \quad (\text{K.26})$$

$$3174 \quad = \frac{1}{2} (\mathbf{I}_d + \mathbf{I}_d), \quad (\text{K.27})$$

$$3176 \quad = \mathbf{I}_d. \quad (\text{K.28})$$

3177  $\square$

### 3179 K.3 DISCUSSION ABOUT LOCAL AND NON LOCAL STRUCTURE

3181 The random tensor of Appendix J and the large sparse tensor of Appendix K.2.3 may be interpreted  
 3182 as non-local since  $\mathbf{x} \rightarrow \mathbf{G}^k \mathbf{x}$  changes coefficients  $x_i$  of  $\mathbf{x}$  which are not sorted next to each other in  
 3183  $\mathbf{x}$ . For large dimension  $d$ , we believe that this can accelerate the convergence in comparison with  
 3184 local tensors, like the sparse tensor of Appendix K.2.2 or a discretized version of transport noise  
 3185 SPDEs. Indeed, for local dynamics the randomness may take time to spread by going from one  
 coefficient to the next whereas in non-local dynamics the randomness can spread directly in the whole

state space at each time step. Our preliminary numerical results (not shown) seems to confirm this intuition. Moreover, the stronger theoretical properties of those non-local tensors – rank condition A2 and thus exponential convergence of the distribution – also tends to confirm our conjecture. However, diffusion models in large dimension strongly rely on the powerful skills of convolutional neural networks (CNN), which have – up to attention layers – an intrinsic local structures. Accordingly, it may be difficult for a CNN to learn how to denoise a non-local noising process. More theoretical and experimental works would be needed to confirm this intuition. This is out of the scope of this already lengthy paper and is currently under investigation by the authors.

## L NUMERICAL SCHEME

### L.1 NUMERICAL INTEGRATION OF SDEs

#### L.1.1 STOCHASTIC RUNGE-KUTTA METHOD FOR STRATONOVICH SDEs

We consider the Stratonovich stochastic differential equation (SDE):

$$dx_t = f_S(t, x_t) dt + \tilde{\mathbf{G}}(t, x_t) \circ dB_t, \quad (\text{L.1})$$

where  $f_S : \mathbb{R} \times \mathbb{R}^d \rightarrow \mathbb{R}^d$  is the drift,  $\tilde{\mathbf{G}} : \mathbb{R} \times \mathbb{R}^d \rightarrow \mathbb{R}^{d \times m}$  is the diffusion term, and  $B_t$  is an  $d$ -dimensional Wiener process.

The following Runge-Kutta (RK) method (Kloeden et al., 1992) approximates the solution  $x_{n+1} \approx x(t_{n+1})$  over the interval  $[t_n, t_{n+1}]$ , with time step  $\Delta t = t_{n+1} - t_n$  and Wiener increment  $\Delta B_n = B_{t_{n+1}} - B_{t_n}$ :

$$\mathbf{K}_1 = f_S(t_n, x_n) \Delta t + \tilde{\mathbf{G}}(t_n, x_n) \Delta B_n, \quad (\text{L.2})$$

$$\mathbf{K}_2 = f_S\left(t_n + \frac{\Delta t}{2}, x_n + \frac{\mathbf{K}_1}{2}\right) \Delta t + \tilde{\mathbf{G}}\left(t_n + \frac{\Delta t}{2}, x_n + \frac{\mathbf{K}_1}{2}\right) \Delta B_n, \quad (\text{L.3})$$

$$\mathbf{K}_3 = f_S\left(t_n + \frac{\Delta t}{2}, x_n + \frac{\mathbf{K}_2}{2}\right) \Delta t + \tilde{\mathbf{G}}\left(t_n + \frac{\Delta t}{2}, x_n + \frac{\mathbf{K}_2}{2}\right) \Delta B_n, \quad (\text{L.4})$$

$$\mathbf{K}_4 = f_S(t_n + \Delta t, x_n + \mathbf{K}_3) \Delta t + \tilde{\mathbf{G}}(t_n + \Delta t, x_n + \mathbf{K}_3) \Delta B_n, \quad (\text{L.5})$$

$$x_{n+1} = x_n + \frac{1}{6}(\mathbf{K}_1 + 2\mathbf{K}_2 + 2\mathbf{K}_3 + \mathbf{K}_4). \quad (\text{L.6})$$

This method leverages the structure of Stratonovich SDEs and their differential geometry properties. It is particularly well-suited to our SDE equation 3.1 with skew-symmetric noise and no Stratonovich drift.

#### L.1.2 RENORMALISATION

Both our forward SDE equation 3.1 and backward SDE equation 2.2 preserve the solution norm  $\|x_t\|$ . However, even the above Runge-Kutta discretization can break this symmetry. To enforce it numerically, we normalize after each time step.

The final integration scheme is summarized in Algorithm 2. Here, we highlight the differences compared to the classical RK4 in color. Note that the optional of normalization in line 10 of the Algorithm is relevant only for MSGM but not for SGM.

## L.2 SCHEDULING

In order to enable both a sufficient statistical convergence of the forward SDE at time  $s = T$  and a convenient time step, we implemented a time scheduling for both SGM and MSGM. We first recall the basic principle of scheduling in continuous time, then propose a method for MSGM, and finally discuss the theoretical consequences.

3240  
3241**Algorithm 2:** SRK4 for conservative Stratonovich SDEs with renormalization.

3242

---

**Input:** Integration time  $T$ , number of time step  $N_T$ , initial condition  $\mathbf{x}_0$ , drift  $\mathbf{f}_S$ , diffusion  $\tilde{\mathbf{G}}$

1:  $\Delta t \leftarrow \frac{T}{N_T}$ ; {Time step}

2: **for**  $n = 0$  to  $N_T - 1$  **do**

3:    $\Delta \mathbf{B}_n \sim \mathcal{N}(0, \Delta t \mathbf{I}_d)$  {Wiener increment}

4:    $t_n \leftarrow n \Delta t$

5:    $\mathbf{K}_1 \leftarrow \mathbf{f}_S(t_n, \mathbf{x}_n) \Delta t + \tilde{\mathbf{G}}(t_n, \mathbf{x}_n) \Delta \mathbf{B}_n$

6:    $\mathbf{K}_2 \leftarrow \mathbf{f}_S(t_n + \frac{\Delta t}{2}, \mathbf{x}_n + \frac{\mathbf{K}_1}{2}) \Delta t + \tilde{\mathbf{G}}(t_n + \frac{\Delta t}{2}, \mathbf{x}_n + \frac{\mathbf{K}_1}{2}) \Delta \mathbf{B}_n$

7:    $\mathbf{K}_3 \leftarrow \mathbf{f}_S(t_n + \frac{\Delta t}{2}, \mathbf{x}_n + \frac{\mathbf{K}_2}{2}) \Delta t + \tilde{\mathbf{G}}(t_n + \frac{\Delta t}{2}, \mathbf{x}_n + \frac{\mathbf{K}_2}{2}) \Delta \mathbf{B}_n$

8:    $\mathbf{K}_4 \leftarrow \mathbf{f}_S(t_n + \Delta t_n, \mathbf{x}_n + \mathbf{K}_3) \Delta t + \tilde{\mathbf{G}}(t_n + \Delta t_n, \mathbf{x}_n + \mathbf{K}_3) \Delta \mathbf{B}_n$

9:    $\tilde{\mathbf{x}}_{n+1} \leftarrow \mathbf{x}_n + \frac{1}{6}(\mathbf{K}_1 + 2\mathbf{K}_2 + 2\mathbf{K}_3 + \mathbf{K}_4)$  {Classical RK4 blend}

10:    $\mathbf{x}_{n+1} \leftarrow \frac{\|\mathbf{x}_0\|}{\|\tilde{\mathbf{x}}_{n+1}\|} \tilde{\mathbf{x}}_{n+1}$  {Optional step : Enforce  $\|\mathbf{x}_{n+1}\| = \|\mathbf{x}_0\|$ }

11: **end for**

12: **return**  $\mathbf{x}_{N_T}$  {Approximation of  $\mathbf{x}_T$ }

---

3257

3258

## L.2.1 USUAL SCHEDULING

3260

3261  
3262

In continuous time (Song et al., 2021), a convenient way is to make a change of variable, replacing the time  $s$  by

3263  
3264

$$z(s) = \int_0^s g^2(s') ds'. \quad (\text{L.7})$$

with

3266  
3267

$$g^2(s) = \frac{1}{2} \beta(s) = \frac{1}{2} \left( \beta_m + (\beta_M - \beta_m) \frac{s}{T} \right), \quad (\text{L.8})$$

3268  
3269

and  $\beta_M > \beta_m > 0$ . We first describe the hyperparameters values chosen in our numerical experiments and then explain how scheduling affects SGM and MSGM theories.

3270  
3271  
3272  
3273  
3274  
3275  
3276

Since we built our code from an existing one (<https://github.com/CW-Huang/sdeflow-light>, Huang et al. (2021)), by default we choose the values provided there for SGM scheduling:  $\beta_m = 0.1$  and  $\beta_M = 20$ . We expect these values to be already finely tuned and we have verified that this couple of values gives indeed better results than many other choices (not shown). We believe that these default values of the SGM hyperparameters enable a fair comparison to MSGM. For some test cases, we found another SGM scheduling that works better and we use it instead. All scheduling hyperparameters are provided in the tables summarizing test cases in Appendix M.

3277  
3278  
3279

For small time  $s$ , the time remapping is linear :  $g^2(s) \underset{s \rightarrow 0}{\sim} \frac{1}{2}\beta_m$  and  $z(s) \underset{s \rightarrow 0}{\sim} \frac{1}{2}\beta_m s$  whereas for large time,  $g^2(s) \underset{s \rightarrow T}{\sim} \frac{1}{2}\beta_M$  and using the Taylor expansion around  $T$ , yielding

3280  
3281

$$z(s) = z(T) + z'(t)(s - T) + o(s - T),$$

3282

we find that

3283  
3284

$$z(s) = \frac{1}{2} \left( \beta_m + \frac{1}{2}(\beta_M - \beta_m) \frac{s}{T} \right) s, \quad (\text{L.9})$$

3285  
3286  
3287

$$= \frac{1}{2} \left( \frac{\beta_M + \beta_m}{2} T + \beta_M(s - T) \right) + \underset{s \rightarrow T}{o}(s - T), \quad (\text{L.10})$$

3288  
3289

$$\underset{s \rightarrow T}{\longrightarrow} \frac{\beta_M + \beta_m}{4} T. \quad (\text{L.11})$$

3290

As such, SGM forward and backward SDEs become:

3291  
3292

$$d\vec{\mathbf{x}}_s = -g^2(s) \vec{\mathbf{x}}_s ds + \sqrt{2}g(s) d\vec{\mathbf{B}}_s, \quad (\text{L.12})$$

3293

$$d\vec{\mathbf{x}}_t = g^2(T - t) \vec{\mathbf{x}}_t dt + \sqrt{2}g(T - t) \left( \mathbf{a}_\theta(T - t, \vec{\mathbf{x}}_t) dt + \circ d\vec{\mathbf{B}}_t \right), \quad (\text{L.13})$$

3294 where  $\mathbf{a}_\theta(T-t, \overleftarrow{\mathbf{x}}_t)$  approximates  $\sqrt{2}g(T-t)\nabla \log p_{T-t}(\overleftarrow{\mathbf{x}}_t)$ . The backward SDE can be integrated  
 3295 with the Stochastic Runge-Kutta Algorithm 2 where  
 3296

$$3297 \quad f_S(t, \overleftarrow{\mathbf{x}}_t) = g^2(T-t)\overleftarrow{\mathbf{x}}_t + \sqrt{2}g(T-t)\mathbf{a}_\theta(T-t, \overleftarrow{\mathbf{x}}_t) \quad \text{and} \quad \tilde{\mathbf{G}}(t, \overleftarrow{\mathbf{x}}_t) = \sqrt{2}g(T-t). \quad (\text{L.14})$$

### 3299 L.2.2 SCHEDULING FOR MSGM

3300 We propose a similar scheduling for MSGM. Scheduled forward and backward SDEs write:  
 3301

$$3302 \quad d\overrightarrow{\mathbf{x}}_s = g(s)\mathbf{G}(\overrightarrow{\mathbf{x}}_s) \circ d\overrightarrow{\mathbf{B}}_s, \quad (\text{L.15})$$

$$3304 \quad d\overleftarrow{\mathbf{x}}_t = g(T-t)\mathbf{G}(\overleftarrow{\mathbf{x}}_t) \left( \mathbf{a}_\theta(T-t, \overleftarrow{\mathbf{x}}_t) dt + \circ d\overleftarrow{\mathbf{B}}_t \right), \quad (\text{L.16})$$

3306 where  $\mathbf{a}_\theta(T-t, \overleftarrow{\mathbf{x}}_t)$  approximates  $g(T-t)\mathbf{G}(\overleftarrow{\mathbf{x}}_t)^\top \nabla \log p_{T-t}(\overleftarrow{\mathbf{x}}_t)$ . Numerically, following Algo-  
 3307 rithm 2 we can integrate the forward SDE with  
 3308

$$3309 \quad f_S(s, \overrightarrow{\mathbf{x}}_s) = 0 \quad \text{and} \quad \tilde{\mathbf{G}}(s, \overrightarrow{\mathbf{x}}_s) = g(s)\mathbf{G}(\overrightarrow{\mathbf{x}}_s), \quad (\text{L.17})$$

3310 and the backward SDE with  
 3311

$$3312 \quad f_S(t, \overleftarrow{\mathbf{x}}_t) = g(T-t)\mathbf{G}(\overleftarrow{\mathbf{x}}_t)\mathbf{a}_\theta(T-t, \overleftarrow{\mathbf{x}}_t) \quad \text{and} \quad \tilde{\mathbf{G}}(t, \overleftarrow{\mathbf{x}}_t) = g(T-t)\mathbf{G}(\overleftarrow{\mathbf{x}}_t). \quad (\text{L.18})$$

### 3314 L.2.3 THEORETICAL RESULTS

3315 We can verify that our theoretical results remain under this time scheduling. The new Fokker-Planck  
 3316 equation is

$$3318 \quad \frac{\partial}{\partial s} p_s = \nabla_\perp \cdot \left( \frac{1}{2} g^2(s) \boldsymbol{\Sigma}(\mathbf{x}) \nabla_\perp p_s(\mathbf{x}) \right). \quad (\text{L.19})$$

3320 which can be rewritten as

$$3321 \quad \frac{\partial}{\partial s} p_s^g = \nabla_\perp \cdot \left( \frac{1}{2} \boldsymbol{\Sigma}(\mathbf{x}) \nabla_\perp p_s^g(\mathbf{x}) \right). \quad (\text{L.20})$$

$$3323 \quad p_s^g = p_{z(s)}. \quad (\text{L.21})$$

3325 Besides, for  $0 \leq s' \leq z(T)$  for  $\beta_M > \beta_m$  Taylor expansion at  $s'_0 = \frac{\beta_M + \beta_m}{4}T$  yields

$$3327 \quad z^{-1}(s') = \frac{-\beta_m T + \sqrt{\beta_m^2 T^2 + 4T(\beta_M - \beta_m)z}}{\beta_M - \beta_m} \quad (\text{L.22})$$

$$3329 \quad = T + \frac{2}{\beta_M} (s' - s_0) \left( 1 + \underset{s' \rightarrow s'_0}{\mathcal{O}}(1) \right), \quad (\text{L.23})$$

$$3331 \quad \xrightarrow[s' \rightarrow s'_0]{} T. \quad (\text{L.24})$$

3333 Therefore, from the convergence of  $p_s^g$  (already proofed) we have the convergence of  $p_{s'} = p_{z^{-1}(s')}^g$ .  
 3334 The rate of convergence is still exponential:

$$3336 \quad \|p_{s'} - p_\infty\|_{L^2(\mathbb{R}^d)}^2 = \|p_{z^{-1}(s')}^g - p_\infty\|_{L^2(\mathbb{R}^d)}^2, \quad (\text{L.25})$$

$$3337 \quad \leq \|p_{z^{-1}(0)}^g - p_\infty\|_{L^2(\mathbb{R}^d)}^2 \exp(-\alpha(\mathbf{G}, d)z^{-1}(s')), \quad (\text{L.26})$$

$$3339 \quad = \|p_0 - p_\infty\|_{L^2(\mathbb{R}^d)}^2 \exp(-\alpha(\mathbf{G}, d)T) \quad (\text{L.27})$$

$$3340 \quad \left( 1 - \frac{\alpha(\mathbf{G}, d)}{\beta_M/2} \left( s' - \frac{\beta_M + \beta_m}{4}T \right) \left( 1 + \underset{s' \rightarrow \frac{\beta_M + \beta_m}{4}T}{\mathcal{O}}(1) \right) \right).$$

3343 Besides the ELBO remains valid :

$$3345 \quad p_0(\mathbf{x}) \geq \mathcal{E}_\infty(\mathbf{x}) := \mathbb{E} \left[ \log p_0(\overrightarrow{\mathbf{x}}_T) \mid \overrightarrow{\mathbf{x}}_0 = \mathbf{x} \right] \quad (\text{L.28})$$

$$3346 \quad - \int_0^T \mathbb{E}_{\overrightarrow{\mathbf{x}}_s} \left[ \frac{1}{2} \|\mathbf{a}_\theta(\overrightarrow{\mathbf{x}}_s, s)\|^2 + \nabla \cdot (g(s)\mathbf{G}(\overrightarrow{\mathbf{x}}_s)\mathbf{a}_\theta(\overrightarrow{\mathbf{x}}_s, s)) \mid \overrightarrow{\mathbf{x}}_0 = \mathbf{x} \right] ds.$$

3348 L.3 LOSS EVALUATION  
3349

3350 Following the existing code (<https://github.com/CW-Huang/sdeflow-light>, Huang  
3351 et al. (2021)), we sample final integration time  $s$  of the forward SDEs uniformly on  $[t_\epsilon, T]$  with  $T = 1$   
3352 with  $t_\epsilon$  small. According to Theorem 3.4.1, we consider the following SSM loss:

$$3353 \mathcal{L}_{\text{SSM}}(\boldsymbol{\theta}) = \hat{\mathbb{E}}_{\vec{\mathbf{x}}_0} \hat{\mathbb{E}}_{s \sim \mathcal{U}[t_\epsilon, T]} \hat{\mathbb{E}}_{\vec{\mathbf{x}}_s | \vec{\mathbf{x}}_0} \hat{\mathbb{E}}_{v_s \sim \text{Rad}(d)} \mathcal{L}_{\text{SSM}}(s, \vec{\mathbf{x}}_s, g\mathbf{G}, \mathbf{a}_{\boldsymbol{\theta}_n}, v_s), \quad (\text{L.29})$$

3355 with

$$3356 \mathcal{L}_{\text{SSM}}(s, \mathbf{x}, g\mathbf{G}, \mathbf{a}_{\boldsymbol{\theta}_n}, \mathbf{v}) = \frac{1}{2} \|\mathbf{a}_{\boldsymbol{\theta}}(\mathbf{x}, s)\|^2 + (\mathbf{v} \cdot \nabla)(g(s)\mathbf{G}(\mathbf{x})\mathbf{a}_{\boldsymbol{\theta}}(\mathbf{x}, s)) \cdot \mathbf{v}, \quad (\text{L.30})$$

3358 where  $\hat{\mathbb{E}}$  is the averaged over the generated samples. Each training sample  $\vec{\mathbf{x}}_0$  of a batch is chosen  
3359 randomly among the train set. For each of them, we sample one time  $s$ , one solution  $\vec{\mathbf{x}}_s$ , and one  
3360 slicing direction  $v_s \sim \text{Rad}(d)$ .

3361 For SGM, we take  $\mathbf{G} = \sqrt{2}$  in the above expressions and following Song et al. (2021), the solution  
3362  $\vec{\mathbf{x}}_s$  of the SGM scheduled forward SDE equation L.12 is

$$3364 \vec{\mathbf{x}}_s = \exp(-\frac{1}{2}z(s))\vec{\mathbf{x}}_0 + \sqrt{1 - \exp(-z(s))}\vec{\mathbf{x}}_\infty, \quad (\text{L.31})$$

3365 where  $z(s) := \int_0^s g^2(s')ds'$  is given by equation L.9,  $\vec{\mathbf{x}}_0$  is chosen randomly among the train set and  
3366  $\vec{\mathbf{x}}_\infty \sim \mathcal{N}(0, \mathbf{I}_d)$ .  
3367

3368 Unfortunately, to evaluate the MSGM loss, we cannot apply the same methodology, since, for  $d > 2$   
3369 we are not aware of an analytic expression for the solution of the MSGM forward SDE, neither  
3370 with nor without scheduling (equation L.15 and equation 3.1 respectively). We integrate that SDE  
3371 numerically with the stochastic Runge-Kutta method with renormalization (see Appendix L.1.1 and  
3372 Appendix L.1.2). Through this integration, we have to compute the solution  $\vec{\mathbf{x}}_{s_k}$  for many time steps  
3373  $s_k := kT/N_T \in [0, T]$ . Instead of sampling a random continuous time  $s \sim \mathcal{U}([t_\epsilon, T])$ , we choose a  
3374 random discrete time as follow

$$3375 s \sim \mathcal{U}(I(t_\epsilon, T)) \quad \text{with} \quad I(t_\epsilon, T) = \{s_k | s_k = k\frac{T}{N_T}, k \in \{1, \dots, N_T\}, s_k \geq t_\epsilon\}. \quad (\text{L.32})$$

3377 The numerical integration of the forward SDE implies a larger computational cost compared to  
3378 SGM. Therefore, as explained in Appendix M.3, for fair comparisons between SGM and MSGM, the  
3379 number of ADAMS iterations will be smaller.

3380 For two-dimensional test cases, we could have used the analytic example of Appendix I to integrate  
3381 the forward MSGM SDE. However, we prefer to propose and analyze an algorithm that is not tied to  
3382 the dimension 2. So, we perform all our numerical experiments with the same algorithm whatever  
3383 the dimension. SGM forward equation is integrated analytically, whereas the MSGM is integrated  
3384 numerically.

3385 L.4 NEURAL NETWORK ARCHITECTURE  
33863387 L.4.1 SPHERICAL DECOMPOSITION AS AN INPUT LAYER  
3388

3389 In line with our spherical decomposition equation 3.6, we add a fixed input layer to the network used  
3390 in MSGM:

$$3391 \mathbf{a}_{\boldsymbol{\theta}}(\mathbf{x}, s) = \tilde{\mathbf{a}}_{\boldsymbol{\theta}}(\mathbf{x}/\|\mathbf{x}\|_\epsilon, \log \|\mathbf{x}\|_\epsilon, s), \quad \text{with} \quad \|\mathbf{x}\|_\epsilon := \|\mathbf{x}\| + \epsilon. \quad (\text{L.33})$$

3393 The geometrical interpretation of Appendix H.3 also suggests that form.

3394 For SGM, if not stated otherwise, we use a default architecture:

$$3395 \mathbf{a}_{\boldsymbol{\theta}}(\mathbf{x}, s) = \tilde{\mathbf{a}}_{\boldsymbol{\theta}}(\mathbf{x}, s). \quad (\text{L.34})$$

3397 L.5  
33983399 L.4.1 NETWORK ARCHITECTURE FOR LOW-DIMENSIONAL TEST CASES (MLP)  
3400

3401 Following the existing code (<https://github.com/CW-Huang/sdeflow-light>, Huang  
et al. (2021)), we parameterize the vector field  $\tilde{\mathbf{a}}_{\boldsymbol{\theta}} : \mathbb{R}^{\tilde{d}} \times \mathbb{R} \rightarrow \mathbb{R}^d$  ( $\tilde{d} = d$  or  $d + 1$ ) with a 4-layer

3402 MLP conditioned on an index  $t \in \mathbb{R}$  by concatenation. Let  $H = 128$  be the hidden width. For input  
 3403  $\mathbf{x} \in \mathbb{R}^{\tilde{d}}$ , we form  $\mathbf{h}_0 = [\mathbf{x}; t] \in \mathbb{R}^{\tilde{d}+1}$  and compute  
 3404

$$\begin{aligned} \mathbf{h}_1 &= \text{swish}(\mathbf{W}_1 \mathbf{h}_0 + \mathbf{b}_1), & \mathbf{W}_1 &\in \mathbb{R}^{H \times (\bar{d}+1)}, \\ \mathbf{h}_2 &= \text{swish}(\mathbf{W}_2 \mathbf{h}_1 + \mathbf{b}_2), & \mathbf{W}_2 &\in \mathbb{R}^{H \times H}, \\ \mathbf{h}_3 &= \text{swish}(\mathbf{W}_3 \mathbf{h}_2 + \mathbf{b}_3), & \mathbf{W}_3 &\in \mathbb{R}^{H \times H}, \\ \mathbf{y} &= \mathbf{W}_4 \mathbf{h}_3 + \mathbf{b}_4, & \mathbf{W}_4 &\in \mathbb{R}^{d \times H}, \end{aligned}$$

3411 with  $(\text{swish}(z))_i = z_i \sigma(z_i)$  and  $\sigma$  the logistic sigmoid. We set  $\tilde{a}_\theta(x, t) = y \in \mathbb{R}^d$ . No residual  
 3412 connections, normalization, or dropout are used. Table 1 summarizes the hyperparameters of this  
 3413 default architecture.

Table 1: MLP architecture hyperparameters.

Hyperparameter	Value
Input dimension	$\tilde{d} = d$ or $d + 1$
Index dimension	1
Hidden width	128
Depth	3 hidden layers
Activation	Swish ( $x \mapsto x\sigma(x)$ )
Output dimension	$d$
Output layer	Linear
Residual connections	None
Normalization / Dropout	None

#### L.4.2 NETWORK ARCHITECTURE FOR HIGH-DIMENSIONAL TEST CASES (UNET FOR 32 × 32 VORTICITY FIELDS)

For high-dimensional experiments of Appendix M.6.2, we model the score field  $\tilde{a}_\theta(x, t)$  using a 2D UNet operating on images  $x'$  of size  $H \times W$  representing vorticity snapshots ( $H = W = 16$  or  $32$ ). Some part of our algorithm was built for vectors rather than images. So depending on the portion of the algorithm, images  $x' \in \mathbb{R}^{1 \times H \times W}$  are reshaped into vectors  $x \in \mathbb{R}^d$  with  $d = HW$  or vectors are reshaped as a one-channel images  $x' \in \mathbb{R}^{1 \times H \times W}$ .

**Optional spherical premodule.** When enabled, we apply the spherical decomposition of Appendix L.4.1:

$$(\mathbf{x}_\epsilon^n, \log \|\mathbf{x}\|_\varepsilon) = \text{NormalizeLogRadius}(x), \quad \mathbf{x}_\epsilon^n = \frac{x}{\|\mathbf{x}\|_\varepsilon}.$$

The normalized field  $x_\epsilon^n$  is passed to the UNet, while  $\log \|x\|_\epsilon$  is embedded through a small MLP and added to the temporal embedding, giving a conditioning mechanism analogous to the time embedding of diffusion models.

**UNet backbone.** The core architecture follows the DDPM UNet of Dhariwal & Nichol (2021): a fully convolutional encoder–decoder with skip connections, residual blocks, and optional attention at intermediate resolutions. We use one input channel and one output channel (vorticity). Let  $C_0$  denote the base width. The feature width at resolution level  $k$  is  $C_0 m_k$  where  $C_0$  is the base channel width and  $m_k$  is the channel multiplier.

The UNet receives  $(x, t)$  (and optionally  $\log \|x\|_e$ ) and computes:

$$\tilde{a}_\theta(x, t) \equiv \text{UNet}_\theta(\text{reshape}(x), \text{Emb}(t) \pm \text{Emb}_{\log}(\log \|x\|_c)),$$

followed by flattening back to dimension  $d$  if needed

3454 This UNet is used as a drop-in replacement for the small-dimensional MLP of Appendix L.4.1,  
 3455 enabling MSGM/SGM to scale to image-like vorticity fields up to dimension  $d = 1024$

3456  
3457  
3458 Table 2: UNet architecture hyperparameters.  
3459  
3460  
3461  
3462  
3463  
3464  
3465  
3466  
3467  
3468  
3469  
3470

Component	Setting
Input / output channels	1
Input resolution	$H = W \in \{16, 32\}$
Base channels width $C_0$	32
Channel multipliers	(1, 2, 4)
Residual blocks per stage	2
Attention resolutions	$8 \times 8$ and $4 \times 4$ (for $16 \times 16$ input)
Activation	SiLU
Time embedding	sinusoidal + MLP
Log-norm conditioning	optional MLP added to time embedding
Dropout	0
Upsampling / downsampling	convolutional
Output	1-channel vorticity field

3471  
3472  
3473 M DETAILS ABOUT OUR NUMERICAL EXPERIMENTS  
3474  
3475

3476 We will show that – for comparable training time – MSGM can generate distribution of better quality  
3477 than SGM when data distribution tails are heavy or close to being heavy. For distributions with lighter  
3478 tails such as Gaussian ones, SGM and MSGM produce similar results, except for a small number of  
3479 backward time steps where SGM can become unstable. MSGM is more robust in this aspect.

3480 Our code can be found here: [https://anonymous.4open.science/r/](https://anonymous.4open.science/r/MSGM-submission-6E1E)  
3481 MSGM-submission-6E1E and the preprocessed vorticity data we used in Appendix M.7  
3482 can be found here: <https://anonymous.4open.science/r/MSGM-data-6E64>.

3483  
3484 M.1 TEST CASES  
3485

3486 We will illustrate MSGM and compare it to SGM through different test cases. We first consider four  
3487 examples sampled from known distributions: the Swiss roll, a multidimensional Gaussian distribution,  
3488 and the multidimensional Cauchy distribution with and without correlations. Then, we will address  
3489 the experimental fluid dynamics data. For each test case, a table summarizes the nominal parameters  
3490 used in the experiments (see tables 3, 4, 5, 6, and 7). All are performed on CPU. In addition, we  
3491 additional cover a high-dimensional application with imagine processing, see section Appendix M.7  
3492 with a GPU A40 NVL with 48 Go of VRAM.

3493  
3494 M.2 DATA PREPROCESSING  
3495

3496 The data set and distribution are centered before processing. For SGM, data sets are renormalized,  
3497 component by component, by their estimated standard deviations. This preconditioning can signifi-  
3498 cantly reduce the number of conditioning of the covariance of the data set, and therefore facilitate the  
3499 SGM (Guth et al., 2022). Generated data are then re-scaled for plots and other post-processings. For  
3500 MSGM, it is not necessary and may even be counterproductive for conservative dynamical systems.  
3501 In fact, it changes the definition of energy  $\|\vec{x}_0\|^2$ . The modified energy has no physical meaning. It  
3502 may have a very different distribution, possibly much less relevant for the data structure. So, we do  
3503 not renormalize the data set before training MSGM.

3504  
3505 M.3 COMPARISON STRATEGY  
3506

3507 We will perform different qualitative visual comparisons with pairplots and quantitative assessment  
3508 with Maximum Mean Discrepancy (MMD) (Gretton et al., 2012). Given two ensembles  $\mathbb{X} = (x^{(i)}) \in$   
3509  $(\mathbb{R})^N$  and  $\mathbb{Y} = (y^{(i)}) \in (\mathbb{R})^N$  samples of random variables  $X$  and  $Y$  respectively, we define

3510  
3511  
3512 Table 3: Swiss roll test case: parameters of the nominal numerical experiments.  
3513  
3514  
3515  
3516  
3517  
3518  
3519  
3520  
3521  
3522  
3523  
3524  
3525  
3526  
3527  
3528  
3529  
3530  
3531  
3532  
3533  
3534  
3535  
3536  
3537  
3538  
3539  
3540  
3541  
3542  
3543  
3544  
3545  
3546  
3547  
3548  
3549  
3550  
3551  
3552  
3553  
3554  
3555  
3556  
3557  
3558  
3559  
3560  
3561  
3562  
3563

Parameter	SGM	MSGM
Dimension $d$	2	2
Number of used training data points ( $M$ )	$2^{20} \times 256$	$2^{20} \times 256$
Number of test data points	$10^4$	$10^4$
Reference number of ADAMS steps	$2^{20}$	$2^{20}$
Number of ADAMS steps ( $N_{\text{iter}}$ )	$2^{20}$	$2^{20}$
CPU time / ADAMS steps (in ms)	4	3
Batch size	256	256
Number of time steps (forward) $N_T^f$	1	16
Number of time steps (backward) $N_T^b$	16	16
$\beta_{\min}$	0.1	0.1
$\beta_{\max}$	20	20
$t_\varepsilon$	$10^{-3}$	$10^{-3}$
Learning rate	$10^{-3}$	$10^{-3}$
Neural network architecture	default	spherical (equation L.33)
MD (MMD(train)= $0.9 \times 10^{-2}$ )	$1.9 \times 10^{-2}$	$0.9 \times 10^{-2}$

3530 MMD( $x, y$ ) as:  
3531

$$3532 \quad \text{MMD}^2(\mathbb{X}, \mathbb{Y}) = \frac{1}{N^2} \sum_{i,j=1}^N \left( k(x^{(i)}, x^{(j)}) - 2k(x^{(i)}, y^{(j)}) + k(y^{(i)}, y^{(j)}) \right), \quad (\text{M.1})$$

$$3535 \quad k(u, v) = \exp(-\|u - v\|^2). \quad (\text{M.2})$$

3537 If  $\mathbb{X}^{\text{test}}$  is the test set and  $\mathbb{X}^{\text{gen}}$  our generated ensemble,  $\text{MMD}(\mathbb{X}^{\text{test}}, \mathbb{X}^{\text{gen}})$  is a metric of the precision  
3538 of our generated ensemble and hence our AI generative algorithm. A small MMD means close distributions.  
3539 However, MMD is a relative metric. So we compare  $\text{MMD}(\mathbb{X}^{\text{test}}, \mathbb{X}_{\text{SGM}}^{\text{gen}})$ ,  $\text{MMD}(\mathbb{X}^{\text{test}}, \mathbb{X}_{\text{MSGM}}^{\text{gen}})$   
3540 and  $\text{MMD}(\mathbb{X}^{\text{test}}, \mathbb{X}^{\text{train}})$  where  $\mathbb{X}_{\text{SGM}}^{\text{gen}}$  and  $\mathbb{X}_{\text{MSGM}}^{\text{gen}}$  are generated from SGM and MSGM respectively,  
3541 and  $\mathbb{X}^{\text{train}}$  is the train set.  $\text{MMD}(\mathbb{X}^{\text{test}}, \mathbb{X}^{\text{train}})$  provides a reference MMD, encoding in particular  
3542 possible distribution shifts between the train and the test sets.

3543 The numerical integration of the MSGM forward SDE is an additional significant computational cost  
3544 compared to SGM, and hence a slower training procedure. This cost scales linearly in  $N_T$  due to  
3545 the "for" loop in time. Empirically, it appears to scale as  $\zeta = \sqrt{d} N_t / 2^4$  (not shown), probably due  
3546 to the vectorized  $d \times d \times d$  tensor products involved in each integration time step. In most of the  
3547 numerical experiments below,  $N_t = 2^4$  and thus  $\zeta = \sqrt{d}$ . The SGM iteration steps are  $\zeta$  times faster  
3548 than the MSGM iteration steps. Consequently, the number of iterations for the SGM is  $\max(1, \lfloor \zeta \rfloor)$   
3549 times larger than the number of iterations for the MSGM. As such, we can compare the results of  
3550 SGM and MSGM at a similar training cost. By convention, we take the number of iterations for SGM  
3551 as a reference and refer to it as the reference number of iterations. Summary tables 3, 4, 5, 6, and  
3552 7 provide the values for the reference number of iterations, the true number of iterations, and the  
3553 execution time per ADAMS step.

#### 3554 M.4 SWISS ROLL

3556 We first illustrate our method with the Swiss roll distribution. It is a simple two-dimensional  
3557 distribution: <https://homepages.ecs.vu.ac.nz/~marslast/Code/Ch6/lle.py>.  
3558 Its curved shape makes it difficult to grasp by linear Gaussian approaches. Both MSGM and SGM  
3559 mimic the Swiss roll distribution well, as illustrated by the pairplot 8. However, the diffusion  
3560 distribution  $p_s$  differs from Figure 9 to Figure 10. In particular, latent distributions are completely  
3561 different. Figure 11 illustrates the convergence of the SGM and MSGM approaches as a function of  
3562 the reference number of ADAMS iterations and as a function of number of time steps for integrating  
3563 the backward SDE. The precision of each sampler is quantified through MMD and the confidence  
intervals of MMD are estimated from the samples of 10 MMD.

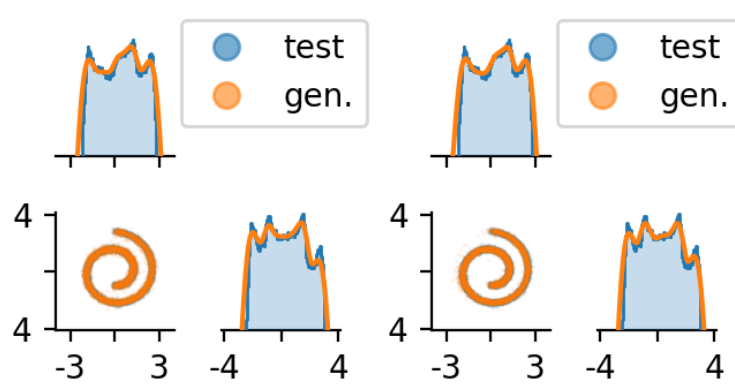


Figure 8: Pair plots of generated data (orange dots) compared to ground truth data (blue dots) with the SGM (left) and MSGM (right) for Swissroll data. On the diagonal, log-histogram of ground truth data (continuous blue line) and logarithm of the pdf KDE estimation of generated data (orange line) are superimposed.

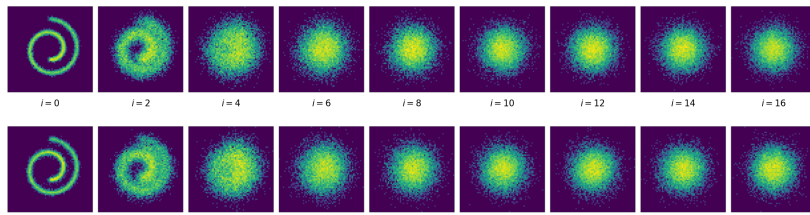


Figure 9: Evolution of the solution log-pdf  $\log(p_s(x_1, x_2))$  of SGM forward SDE (top) and backward SDE (bottom) for Swiss roll data.

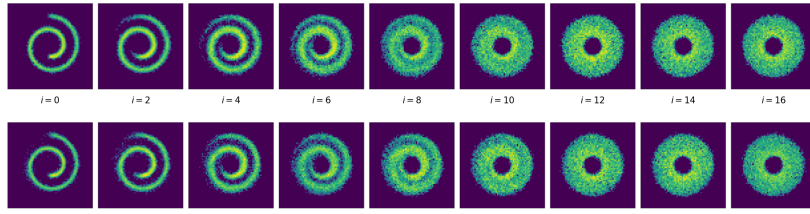


Figure 10: Evolution of the solution log-pdf  $\log(p_s(x_1, x_2))$  of MSGM forward SDE (top) and backward SDE (bottom) for Swiss roll data.

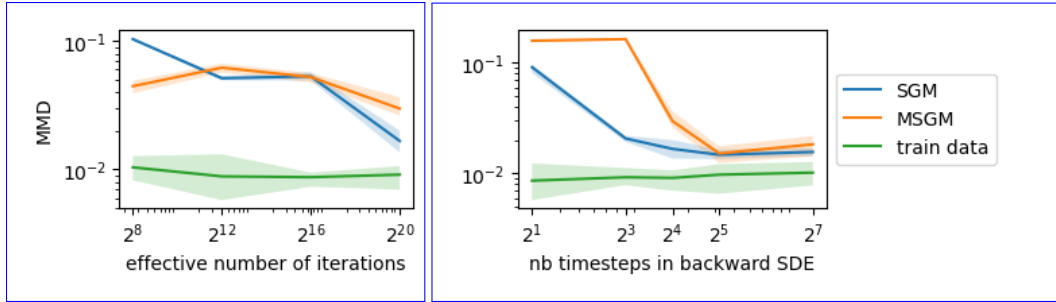


Figure 11: Convergence of MMD (mean and 80% confidence interval) for Swiss roll distribution as a function of reference number of ADAMs iterations (left) and as a function of number of time steps for integrating the backward SDE (right).

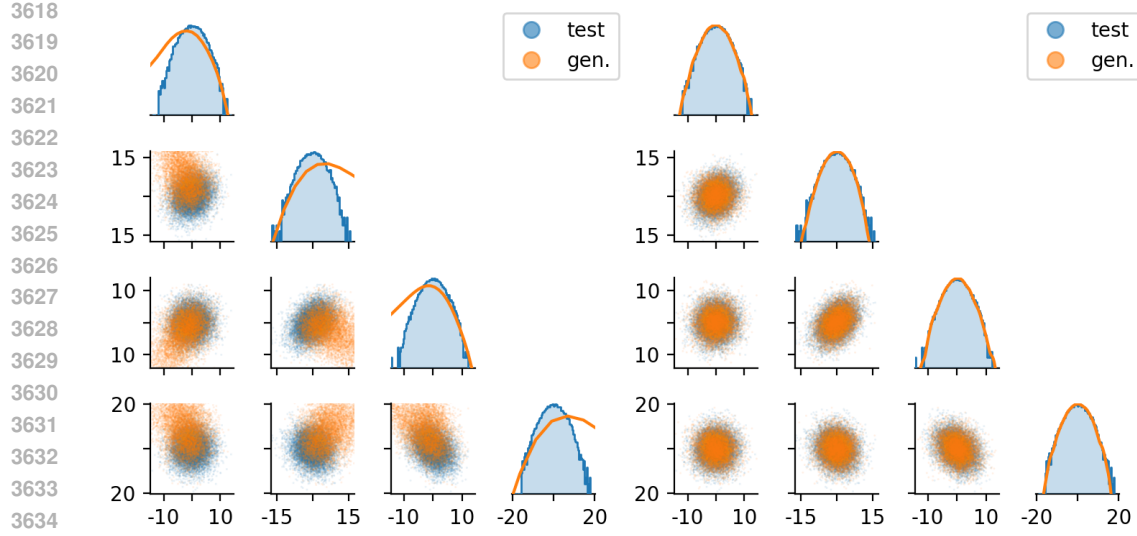


Figure 12: Pair plots of generated data (orange dots) compared to ground truth data (blue dots) with the SGM (left) and MSGM (right) with 8 time steps backward for a vector of 4 correlated Gaussian variables, among 16 correlated Gaussian variables used for training. On the diagonal, log-histogram of ground truth data (continuous blue line), and logarithm of the pdf KDE estimation of generated data (orange line) are superimposed.

#### M.4.1

### M.5 ANISOTROPIC GAUSSIAN DISTRIBUTION

Table 4: Gaussian test case: parameters of the nominal numerical experiments.

Parameter	SGM	MSGM
Dimension $d$	16	16
Number of used training data points ( $M$ )	$1048576 \times 256$	$262144 \times 256$
Number of test data points	$10^4$	$10^4$
Reference number of ADAMS steps	$2^{20}$	$2^{20}$
Number of ADAMS steps ( $N_{\text{iter}}$ )	$2^{20} = 1048576$	262144
CPU time / ADAMS steps (in ms)	3	23
Batch size	256	256
Number of time steps (forward) $N_T^f$	1	16
Number of time steps (backward) $N_T^b$	16	16
$\beta_{\min}$	0.1	0.1
$\beta_{\max}$	20	20
$t_{\varepsilon}$	$10^{-3}$	$10^{-3}$
Learning rate	$10^{-3}$	$10^{-3}$
Neural network architecture	default	spherical (equation L.33)
MD (MMD(train)= $1.5 \times 10^{-2}$ )	$11 \times 10^{-2}$	$2.5 \times 10^{-2}$

For a complete numerical analysis, we compare SGM and MSGM on correlated Gaussian data  $\mathbf{x}_0 \sim \mathcal{N}(0, \mathbf{A}\mathbf{A}^T)$ , with a fixed matrix,  $\mathbf{A}$ , initialized with i.i.d. coefficients  $A_{i,j} \sim \mathcal{N}(0, 1)$ . For 32 time steps backward, the pairplots in Figures 12, 13, and 14 present similar generative skills, but for 8 or 16 time steps backward, only MSGM gives good results. For 8 time steps backwards, MSGM still provides a good distribution, whereas the SGM backward SDE completely diverges. Figures 15, 16, and 17 also highlight this and show that the converged dynamics of the pdf  $p_s$  differs between SGM and MSGM. Figure 18 also confirms that MSGM converges faster with the number of time steps, and is generally more stable.

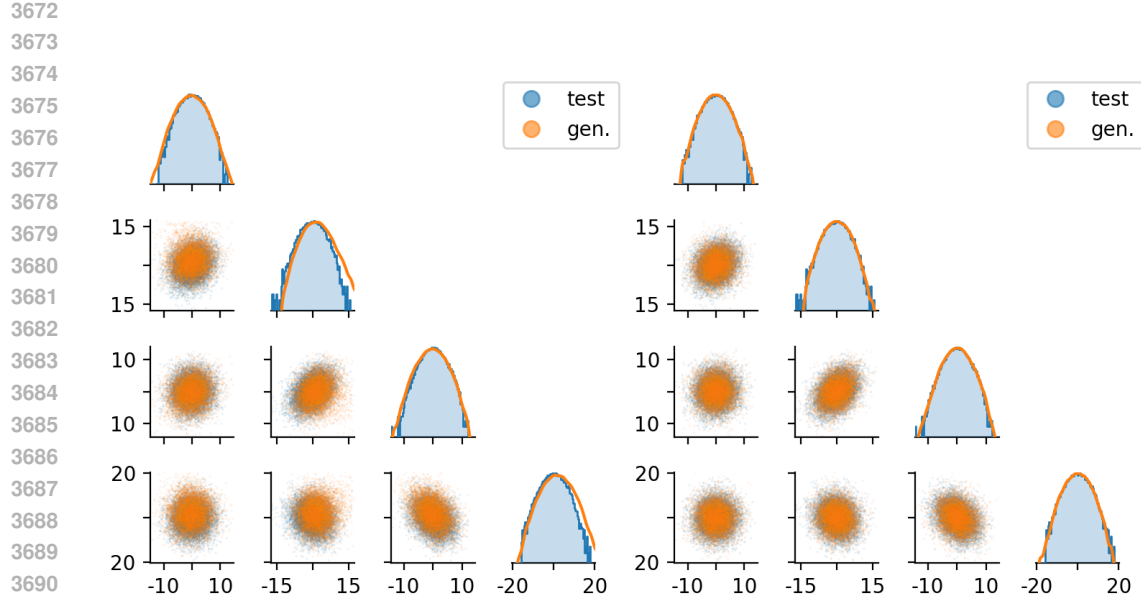


Figure 13: Pair plots of generated data (orange dots) compared to ground truth data (blue dots) with the SGM (left) and MSGM (right) with 16 time steps backward for a vector of 4 correlated Gaussian variables, among 16 correlated Gaussian variables used for training. On the diagonal, log-histogram of ground truth data (continuous blue line), and logarithm of the pdf KDE estimation of generated data (orange line) are superimposed.

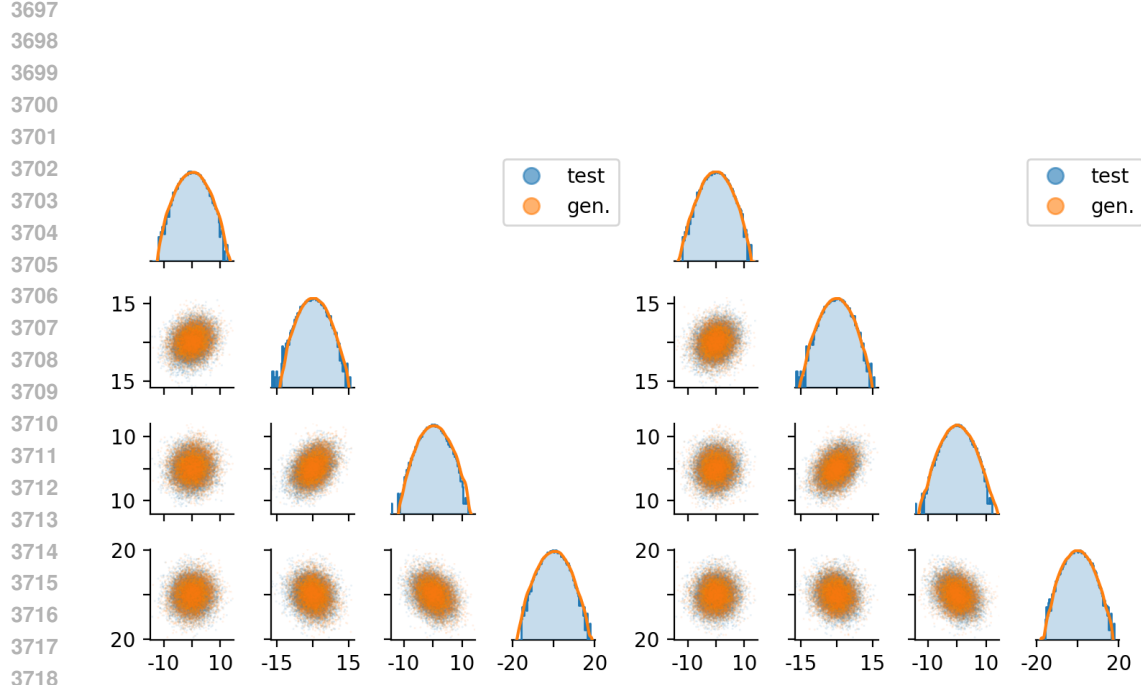


Figure 14: Pair plots of generated data (orange dots) compared to ground truth data (blue dots) with the SGM (left) and MSGM (right) with 32 time steps backward for a vector of 4 correlated Gaussian variables, among 16 correlated Gaussian variables used for training. On the diagonal, log-histogram of ground truth data (continuous blue line), and logarithm of the pdf KDE estimation of generated data (orange line) are superimposed.

3726

3727

3728

3729

3730

3731

3732

3733

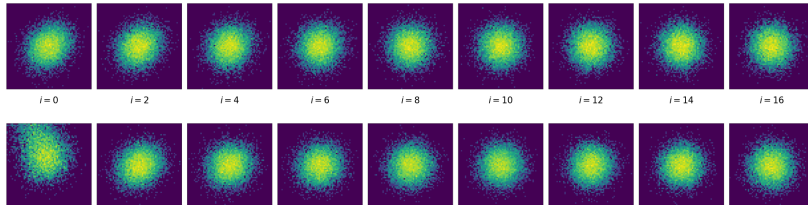
3734

3735

3736

3737

3738

Figure 15: Evolution of the solution log-pdf  $\log(p_s(x_1, x_2))$  of SGM forward SDE (top) and backward SDE (bottom, with 8 time steps) for Gaussian data.

3740

3741

3742

3743

3744

3745

3746

3747

3748

3749

3750

3751

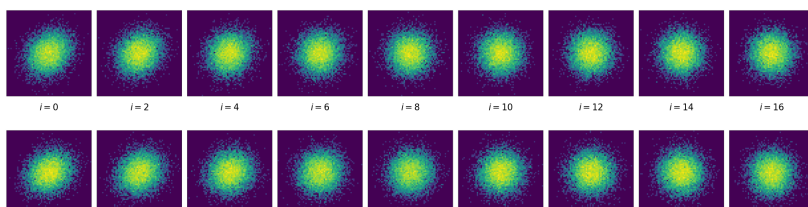
3752

3753

3754

3755

3756

Figure 16: Evolution of the solution log-pdf  $\log(p_s(x_1, x_2))$  of SGM forward SDE (top) and backward SDE (bottom, with 32 time steps) for Gaussian data.

3758

3759

3760

3761

3762

3763

3764

3765

3766

3767

3768

3769

3770

3771

3772

3773

3774

3775

Figure 17: Evolution of the solution log-pdf  $\log(p_s(x_1, x_2))$  of MSGM forward SDE (top) and backward SDE (bottom, with 16 time steps) for Gaussian data.

3776

3777

3778

3779

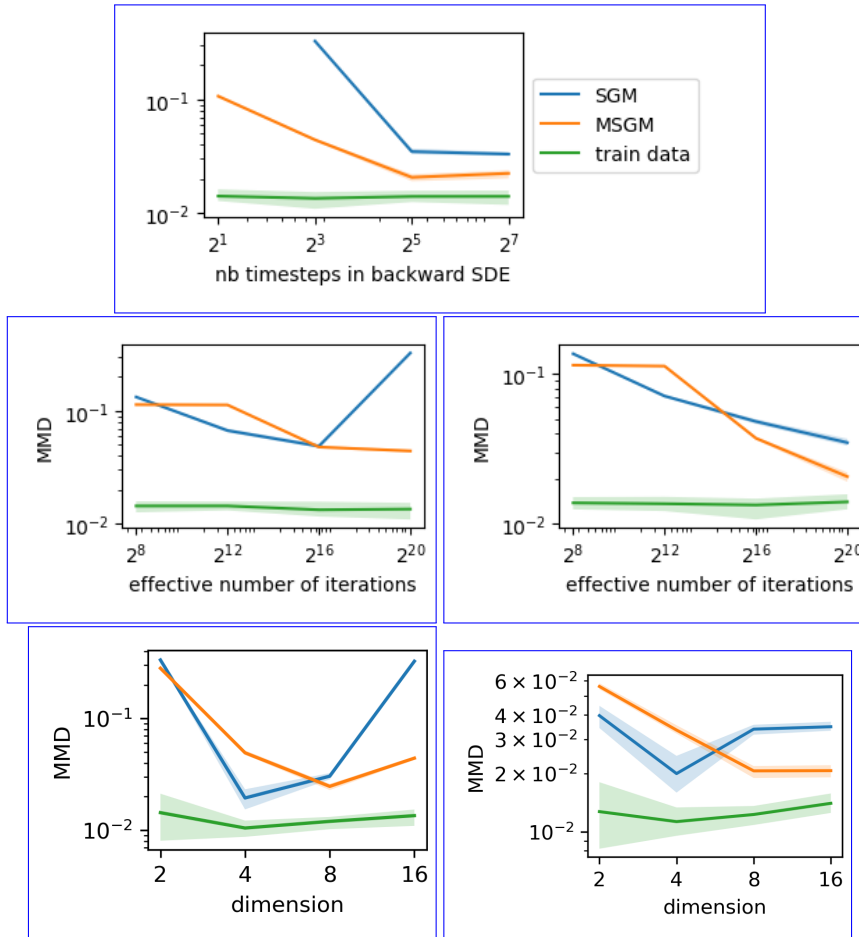


Figure 18: Convergence of MMD (mean and 80% confidence interval) for the Gaussian data as a function of number of time steps for integrating the backward SDE  $N_T^b$  (top), as a function of reference number of ADAM iterations (middle) for  $N_T^b = 8$  (left) and  $N_T^b = 32$  (right), and as a function of dimension (bottom) for  $N_T^b = 8$  (left) and  $N_T^b = 32$  (right).

3834 M.6 MULTIVARIATE CAUCHY DISTRIBUTION  
3835

3836 Cauchy distributions are worst-case heavy-tail distributions in the sense that they do not have finite  
3837 moments. Still, they appear in applications of hydrology, e.g. annual maximum one-day rainfalls and  
3838 river discharges. Consequently, we analyze the expressivity of MSGM in this extreme case. Note that  
3839 due to the absence of finite moments, convergence in common metrics such as Wasserstein- $p$  or total  
3840 variation is not well defined.

3841 M.6.1 VECTOR OF INDEPENDENT CAUCHY VARIABLES  
38423843 Table 5: Vector of independent Cauchy variables: parameters of the nominal numerical experiments.  
3844

3846 <b>Parameter</b>	3847 <b>SGM</b>	3848 <b>MSGM</b>
3849 Dimension $d$	3850 2	3851 2
3852 Number of used training data points ( $M$ )	3853 $2^{20} \times 256$	3854 $209715 \times 256$
3855 Number of test data points	3856 $10^5$	3857 $10^5$
3858 Reference number of ADAMS steps	3859 $2^{20}$	3860 $2^{20}$
3861 Number of ADAMS steps ( $N_{\text{iter}}$ )	3862 $2^{20} = 1048576$	3863 209715
3864 CPU time / ADAMS steps (in ms)	3865 3	3866 27
3867 Batch size	3868 256	3869 256
3870 Number of time steps (forward) $N_T^f$	3871 1	3872 64
3873 Number of time steps (backward) $N_T^b$	3874 128	3875 128
3876 $\beta_{\min}$	3877 0.1	3878 0.1
3879 $\beta_{\max}$	3880 20	3881 0.4
3882 $t_{\epsilon}$	3883 $10^{-3}$	3884 $10^{-3}$
3885 Learning rate	3886 $10^{-3}$	3887 $10^{-3}$
3888 Neural network architecture	3889 default	3890 spherical (equation L.33)
3891 MD (MMD(train)= $2.8 \times 10^{-3}$ )	3892 $7.5 \times 10^{-3}$	3893 $3.3 \times 10^{-3}$

3894 We first illustrate our method with a vector of independent Cauchy variables:  $\mathbf{x}_0 = \mathbf{x}_{\text{Ca}}$  with  $\mathbf{x}_{\text{Ca}}$   
3895 defined by equation 6.2 with scale parameter  $\gamma = 1/50$ . As expected, [Figure 19](#) and [Figure 20](#)  
3896 confirm that SGM does not reproduce fat tails unlike MSGM. Moreover, SGM misaligns the far data  
3897 points that have the coordinate  $x_1 < -3$ . An explanation of the superior skills is the similarity  
3898 between the data distribution and the latent distribution in MSGM: a property not shared by SGM, as  
3899 illustrated in Figures 21 and 22.

3900 [Figure 19](#) compares MSGM with fast scheduling ( $\beta_m = 0.1$ ,  $\beta_M = 0.4$ ) and a neural network  
3901 architecture based on spherical decomposition equation L.33 with SGM with default scheduling  
3902 ( $\beta_m = 0.1$ ,  $\beta_M = 20$ ) and default neural network architecture. For a fair comparison of MSGM,  
3903 we complement our numerical analysis with Figures 23-27: we test SGM with fast and default  
3904 scheduling, and with both spherical-decomposition-based and default network architectures. This  
3905 fast scheduling seems not adapted to SGM, making the sample generation highly inaccurate in  
3906 the pairplot of [Figure 24](#). In contrast, the network architecture with spherical decomposition does  
3907 improve the SGM sampling procedure, especially for distribution tails. However, even with this  
3908 architecture, SGM remains less efficient than MSGM. First, the estimated tail is less clean. Secondly,  
3909 the samples generated far are not properly aligned with the test samples, especially for  $x_2 < -3$ .  
3910 Third, outside the  $x_1$  and  $x_2$  axes, SGM generates too few samples close to the origin (say points  $\mathbf{x}$   
3911 with  $\|\mathbf{x}\|_{\frac{1}{2}} > 2$  and  $\|\mathbf{x}\|_1 < 2$ ).

3912 For Cauchy distributions, we still compare MMD values. However, it is not well defined mathematically  
3913 and is hardly relevant numerically. Indeed, the Gaussian kernel structure of the MMD is  
3914 probably not adapted to samples that are so far from each other. In our experiments, we used  $10^4$   
3915 samples to compute an approximate MMD. Other quantities of interest can also be utilized, such  
3916 as the survival function  $t \mapsto \mathbb{P}(\|\mathbf{x}\| > R)$ , illustrated in [Figure 20](#). As expected MSGM clearly  
3917 outperforms SGM on this metric. Indeed by construction our learning method is robust in terms of  
3918 the radial distribution  $\|\mathbf{x}\|$  obtained directly from the data and not after the noising process. This is  
3919 valid since the norm distribution does not change in time due to equation 3.7.

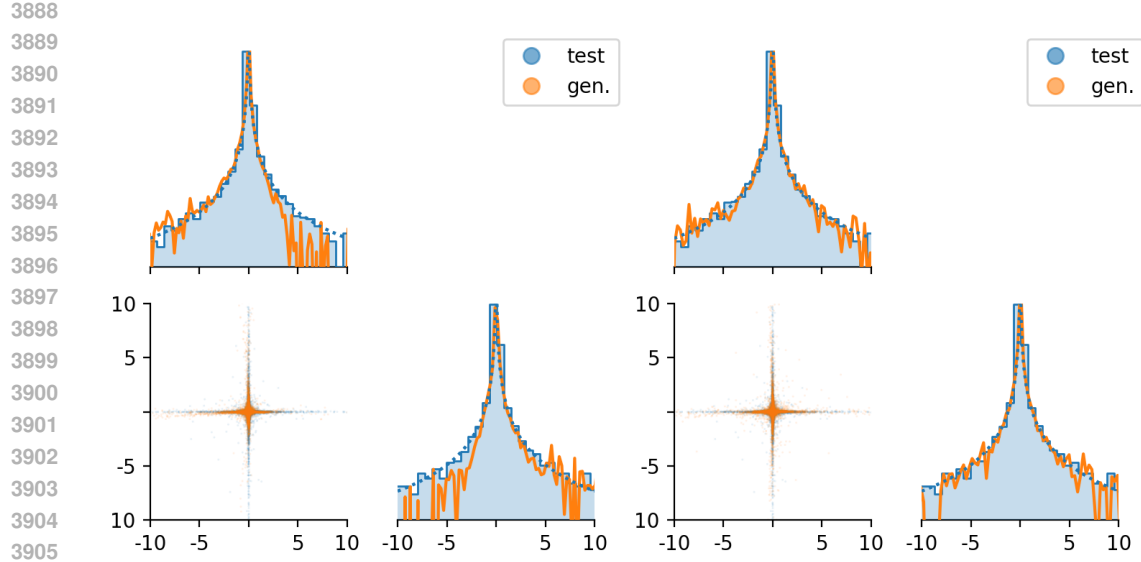


Figure 19: Pair plots of generated data (orange dots) compared to ground truth data (blue dots) with the SGM (left) and MSGM (right) for a vector of two independent Cauchy variables. On the diagonal, log-histogram of ground truth data (continuous blue line), theoretical log-pdf (dashed blue line), and logarithm of the pdf KDE estimation of generated data (orange line) are superimposed.

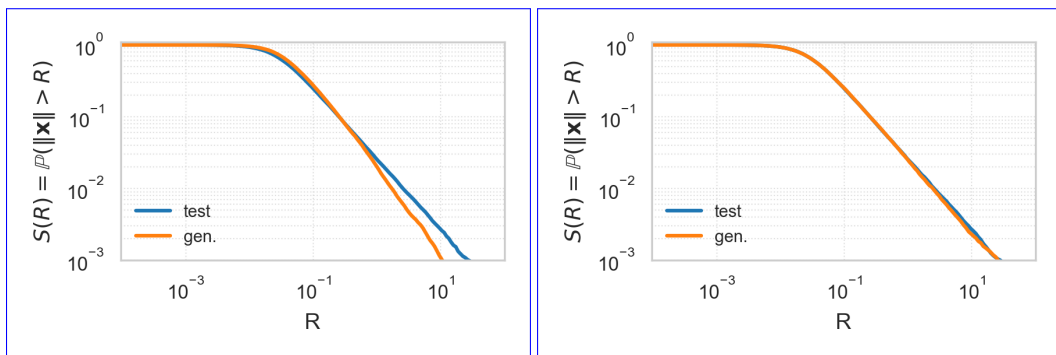


Figure 20: Survival function of generated data (orange line) compared to ground truth data (blue line) with the SGM (left) and MSGM (right) for a vector of two independent Cauchy variables.

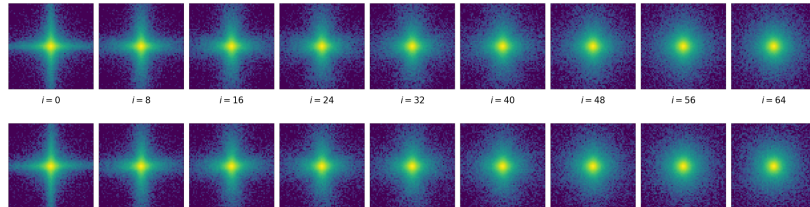
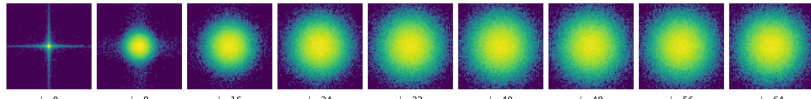


Figure 21: Evolution of the solution log-pdf  $\log(p_s(x_1, x_2))$  of MSGM forward SDE (top) and backward SDE (bottom) for a vector of two independent Cauchy variables, with fast scheduling:  $\beta_m = 0.1$ ,  $\beta_M = 0.4$  and our neural network architecture based on spherical decomposition equation L.33.

3942



3943

3944

3945

3946

3947

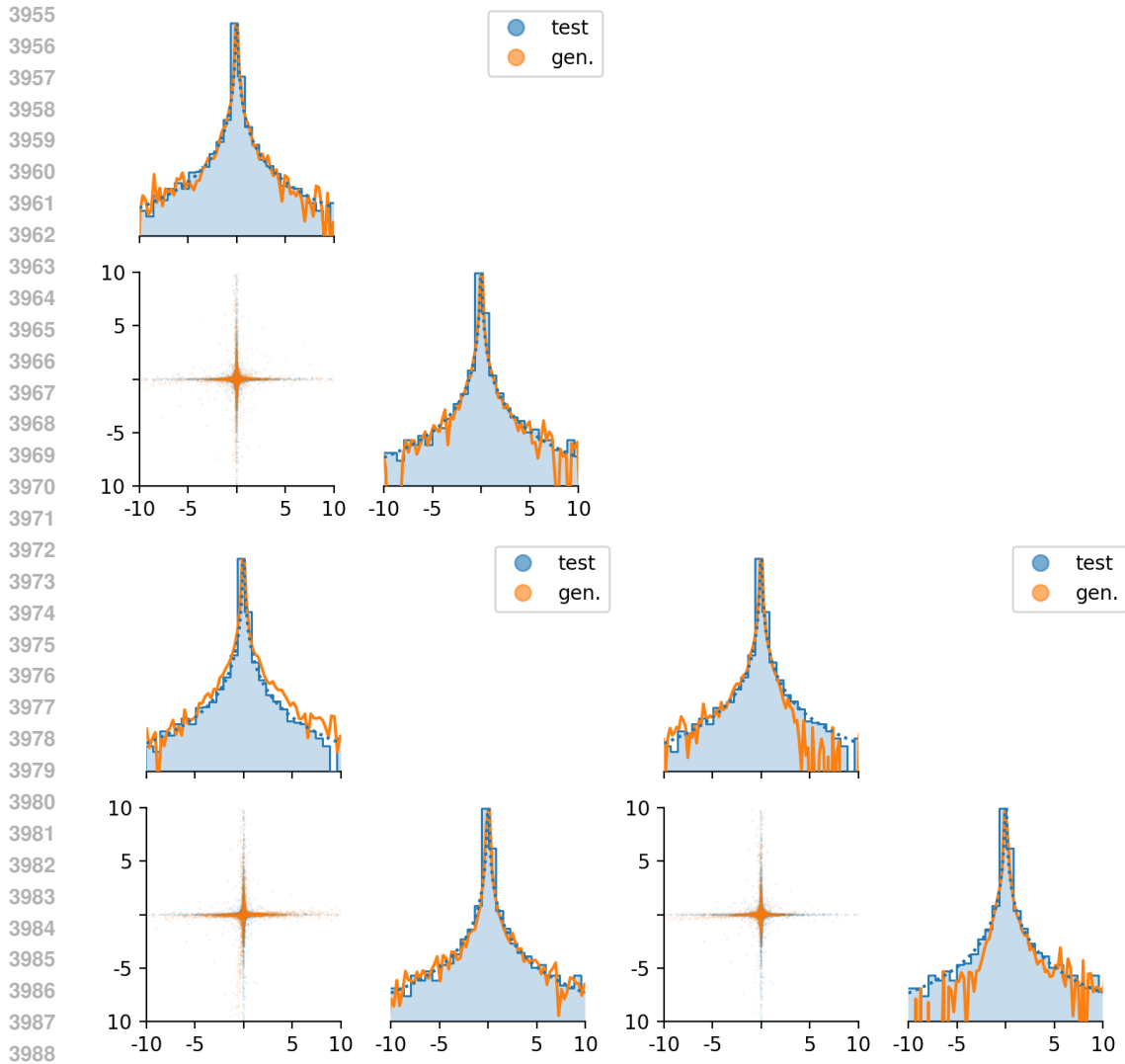
3948

3949

3950

3951 Figure 22: Evolution of the solution log-pdf  $\log(p_s(x_1, x_2))$  of SGM forward SDE (top) and backward  
 3952 SDE (bottom) for a vector of two independent Cauchy variables, with default scheduling:  $\beta_m = 0.1$ ,  
 3953  $\beta_M = 20$  and default neural network architecture.

3954



3989

3990 Figure 23: Generated data (orange lines and dots) compared to ground truth data (blue lines and dots)  
 3991 with the MSGM (top left corner) and the SGM (bottom) for two-dimensional Cauchy distribution.  
 3992 SGM plots correspond to a default scheduling:  $\beta_m = 0.1$ ,  $\beta_M = 20$ . Left plots correspond to our  
 3993 neural network architecture based on spherical decomposition equation L.33 whereas the right plot  
 3994 correspond to default neural network architecture. On the diagonal, log-histogram of ground truth  
 3995 data (continuous blue line), theoretical log-pdf (dashed blue line), and logarithm of the pdf KDE  
 estimation of generated data (orange line) are superimposed.

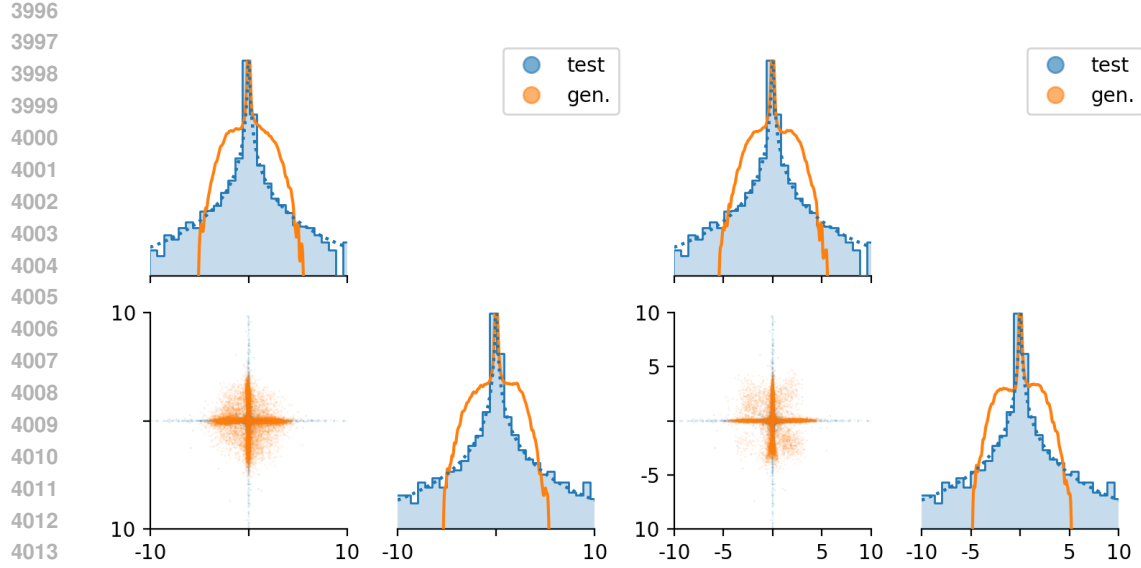


Figure 24: Generated data (orange lines and dots) compared to ground truth data (blue lines and dots) with the SGM for two-dimensional Cauchy distribution. Plots correspond to a fast scheduling:  $\beta_m = 0.1$ ,  $\beta_M = 0.4$ . The left plot corresponds to our neural network architecture based on spherical decomposition equation L.33 whereas right plot corresponds to default neural network architecture. On the diagonal, log-histogram of ground truth data (continuous blue line), theoretical log-pdf (dashed blue line), and logarithm of the pdf KDE estimation of generated data (orange line) are superimposed.

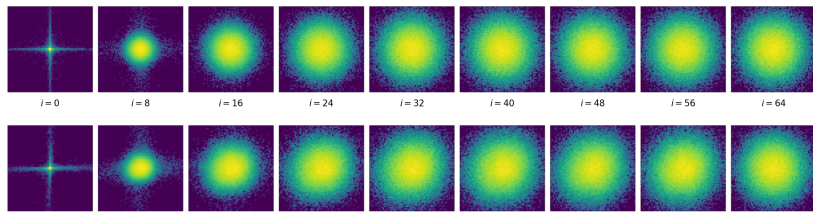


Figure 25: Evolution of the solution log-pdf  $\log(p_s(x_1, x_2))$  of SGM forward SDE (top) and backward SDE (bottom) for a vector of two independent Cauchy variables, with default scheduling:  $\beta_m = 0.1$ ,  $\beta_M = 20$  and our neural network architecture based on spherical decomposition equation L.33.

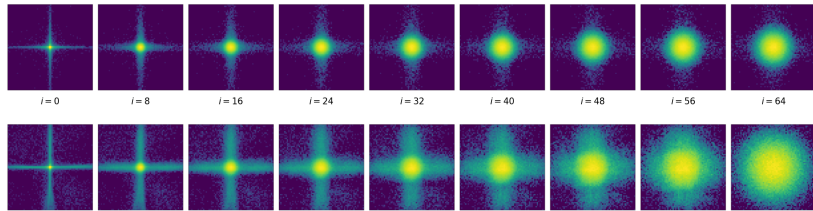


Figure 26: Evolution of the solution log-pdf  $\log(p_s(x_1, x_2))$  of SGM forward SDE (top) and backward SDE (bottom) for a vector of two independent Cauchy variables, with fast scheduling:  $\beta_m = 0.1$ ,  $\beta_M = 0.4$  and default neural network architecture.

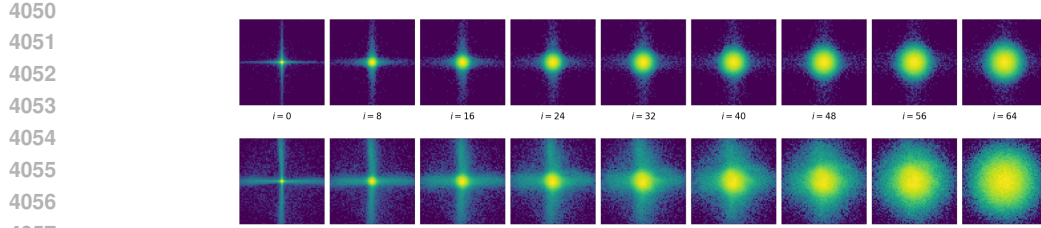


Figure 27: Evolution of the solution log-pdf  $\log(p_s(x_1, x_2))$  of SGM forward SDE (top) and backward SDE (bottom) for a vector of two independent Cauchy variables, with fast scheduling:  $\beta_m = 0.1$ ,  $\beta_M = 0.4$  and our neural network architecture based on spherical decomposition equation L.33.

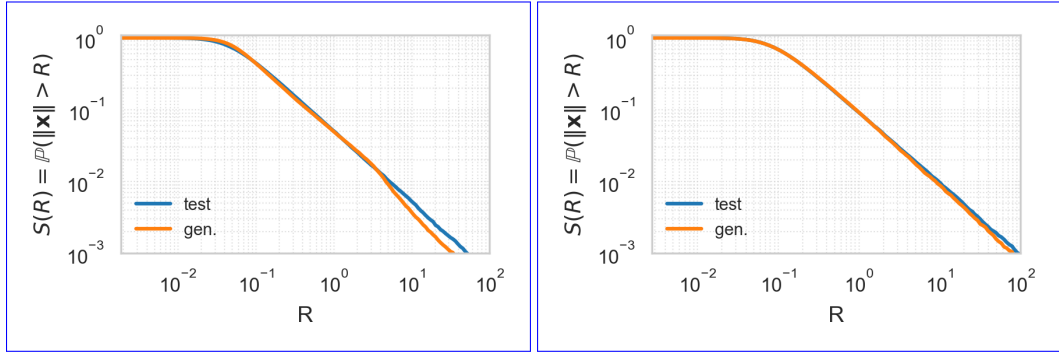


Figure 28: Survival function of generated data (orange line) compared to ground truth data (blue line) with the SGM (left) and MSGM (right) for a vector of 4 correlated Cauchy variables.

## M.6.2 VECTOR OF CORRELATED CAUCHY VARIABLES

Table 6: Vector of correlated Cauchy variables: parameters of the nominal numerical experiments.

Parameter	SGM	MSGM
Dimension $d$	4	4
Number of used training data points ( $M$ )	$2^{20} \times 256$	$2^{20} \times 256$
Number of test data points	$10^5$	$10^5$
Reference number of ADAMS steps	$2^{20}$	$2^{20}$
Number of ADAMS steps ( $N_{\text{iter}}$ )	$2^{20}$	$2^{20}$
CPU time / ADAMS steps (in ms)	3	45
Batch size	256	256
Number of time steps (forward) $N_T^f$	1	128
Number of time steps (backward) $N_T^b$	128	128
$\beta_{\min}$	0.1	0.01
$\beta_{\max}$	20	1
$t_\varepsilon$	$10^{-4}$	$10^{-4}$
Learning rate	$10^{-3}$	$10^{-3}$
Neural network architecture	default	spherical (equation L.33)
MD (MMD(train)= $3.5 \times 10^{-3}$ )	$11.2 \times 10^{-3}$	$5.2 \times 10^{-3}$

To address dimensionality issues, we consider the correlated Cauchy variables already presented in Section 6.1. In terms of survival function, MSGM is as expected more accurate than SGM (see Figure 28).

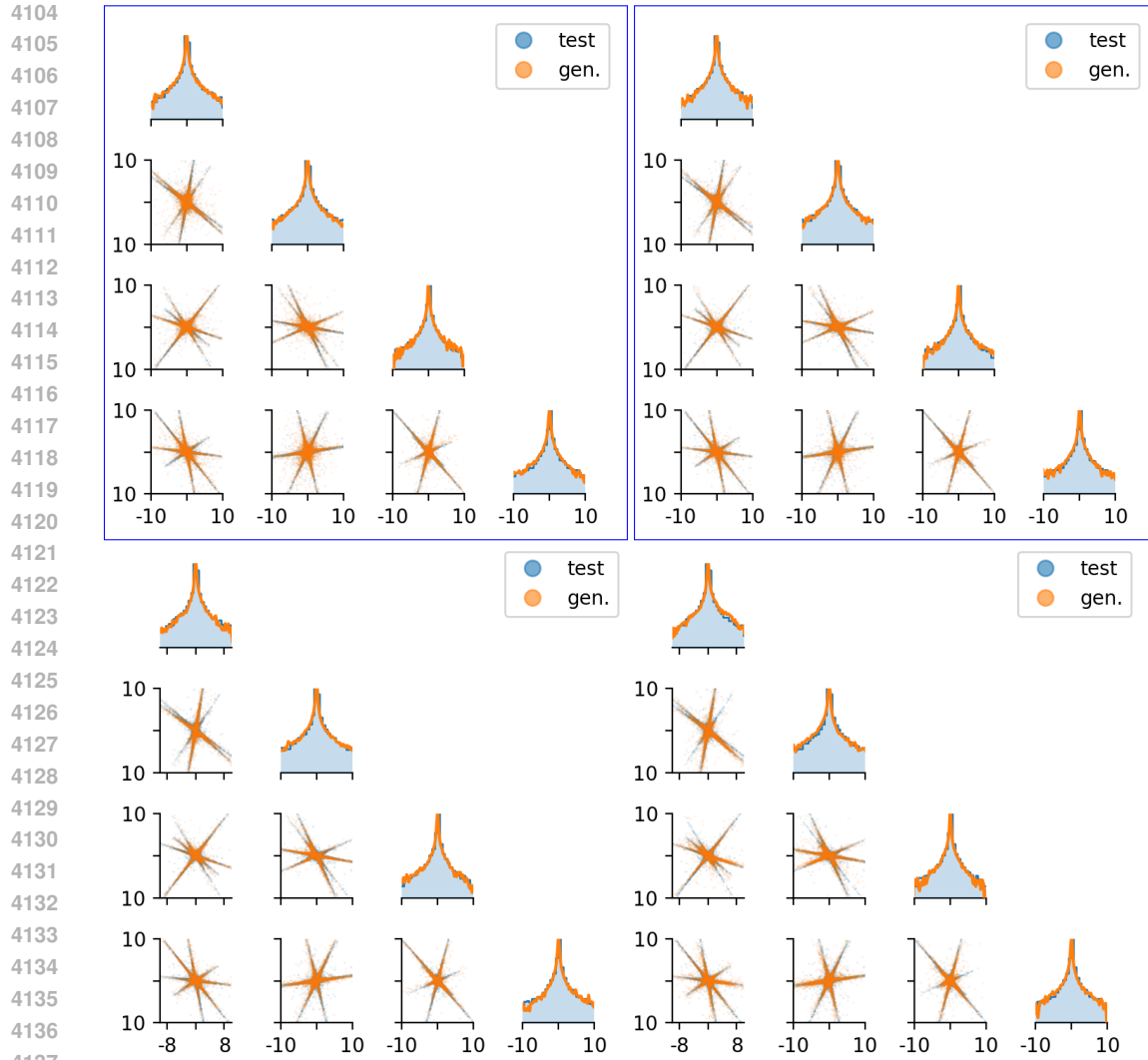


Figure 29: Generated data (orange lines and dots) compared to ground truth data (blue lines and dots) with the MSGM (top) with dense tensor  $\mathbf{G}$  (top left corner), with sparse local tensor  $\mathbf{G}$  (top right corner), and the SGM (bottom) for a vector of 4 correlated Cauchy variables. SGM correspond to a default scheduling:  $\beta_m = 0.1$ ,  $\beta_M = 20$ . Left and top plots correspond to our neural network architecture based on spherical decomposition equation L.33 whereas the right bottom plot corresponds to default neural network architecture. On the diagonal, log-histogram of ground truth data (continuous blue line), and logarithm of the pdf KDE estimation of generated data (orange line) are superimposed.

As for independent Cauchy variables, we present complementary numerical experiments with different scheduling and different neural network architectures in Figures 29 and 30. Figures 31-35 unveil the corresponding diffusion dynamics from  $s = 0$  to  $s = T$  and from  $t = 0$  to  $t = T$ . Again, the neural network architecture based on spherical decomposition significantly improves the SGM generative skills but MSGM remains a more efficient sampler. Not all the branches of the star-like pdf are well sampled and, outside the branches, the regions near the origin is not well sampled.

One can wonder if the poorer results of SGM would improve for a larger number of ADAMS iterations. To answer this question, we run longer experiments with  $2^{24} = 16777216$  ADAMS iterations. Figures 36, 37, and 4a show that MSGM slightly improves with an increasing number of iterations, whereas SGM diverges. For a fair comparison, the MMD convergence Figure 4a is expressed in terms of effective number of ADAMS iterations, i.e. we proportionally reduce the

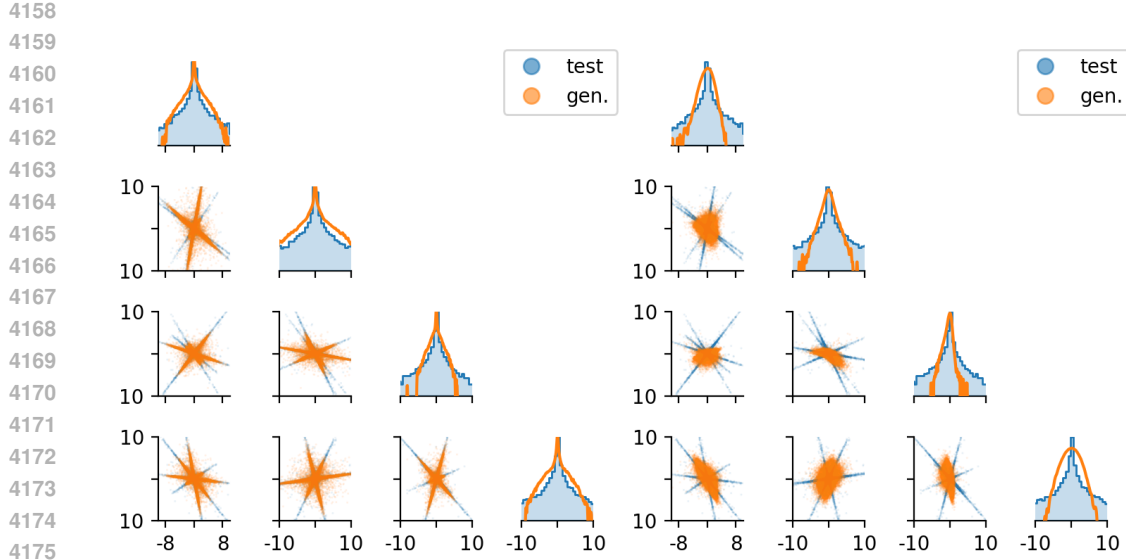


Figure 30: Generated data (orange lines and dots) compared to ground truth data (blue lines and dots) with the SGM for a vector of 4 correlated Cauchy variables with a fast scheduling:  $\beta_m = 0.01$ ,  $\beta_M = 1$ . The left plot corresponds to our neural network architecture based on spherical decomposition equation L.33 whereas the right plot corresponds to default neural network architecture. On the diagonal, log-histogram of ground truth data (continuous blue line), and logarithm of the pdf KDE estimation of generated data (orange line) are superimposed.

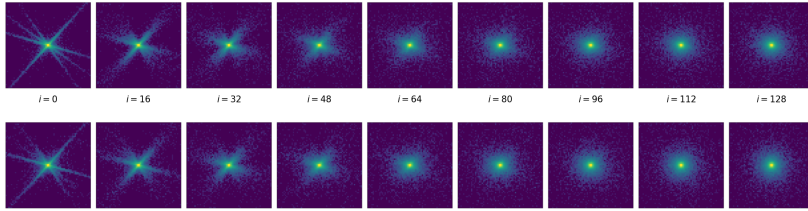


Figure 31: Evolution of the solution  $\log(p_s(x_1, x_3))$  of MSGM forward SDE (top) and backward SDE (bottom) for a vector of 4 correlated Cauchy variables, with fast scheduling:  $\beta_m = 0.01$ ,  $\beta_M = 1$  and our neural network architecture based on spherical decomposition equation L.33.

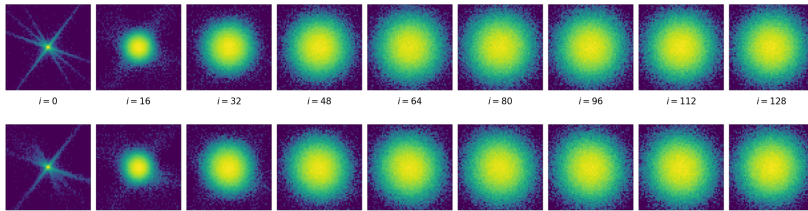


Figure 32: Evolution of the solution  $\log(p_s(x_1, x_3))$  of SGM forward SDE (top) and backward SDE (bottom) for a vector of 4 correlated Cauchy variables, with default scheduling:  $\beta_m = 0.1$ ,  $\beta_M = 20$  and default neural network architecture.

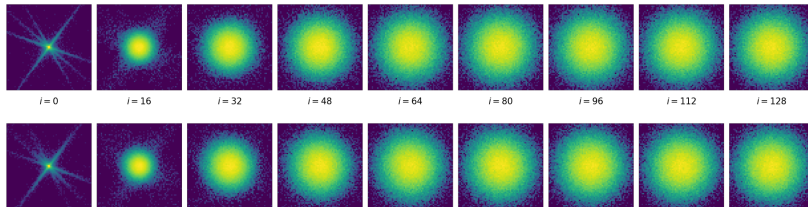


Figure 33: Evolution of the solution  $\log(p_s(x_1, x_3))$  of SGM forward SDE (top) and backward SDE (bottom) for a vector of 4 correlated Cauchy variables, with default scheduling:  $\beta_m = 0.1$ ,  $\beta_M = 20$  and our neural network architecture based on spherical decomposition equation L.33.

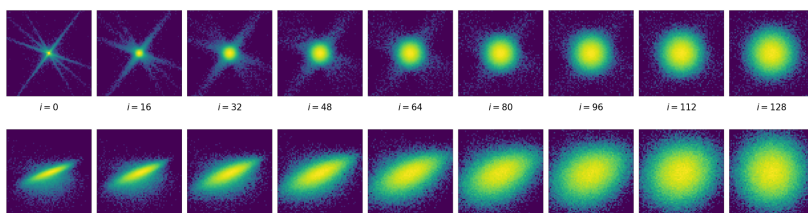


Figure 34: Evolution of the solution  $\log(p_s(x_1, x_3))$  of SGM forward SDE (top) and backward SDE (bottom) for a vector of 4 correlated Cauchy variables, with fast scheduling:  $\beta_m = 0.01$ ,  $\beta_M = 1$  and default neural network architecture.

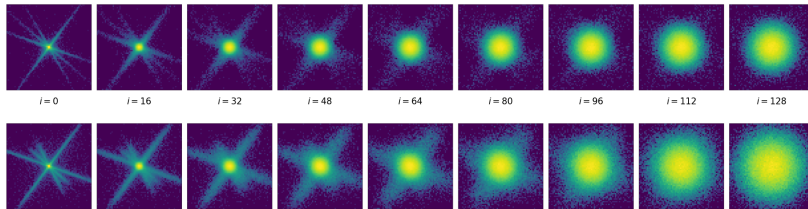


Figure 35: Evolution of the solution  $\log(p_s(x_1, x_3))$  of SGM forward SDE (top) and backward SDE (bottom) for a vector of 4 correlated Cauchy variables, with fast scheduling:  $\beta_m = 0.01$ ,  $\beta_M = 1$  and our neural network architecture based on spherical decomposition equation L.33.

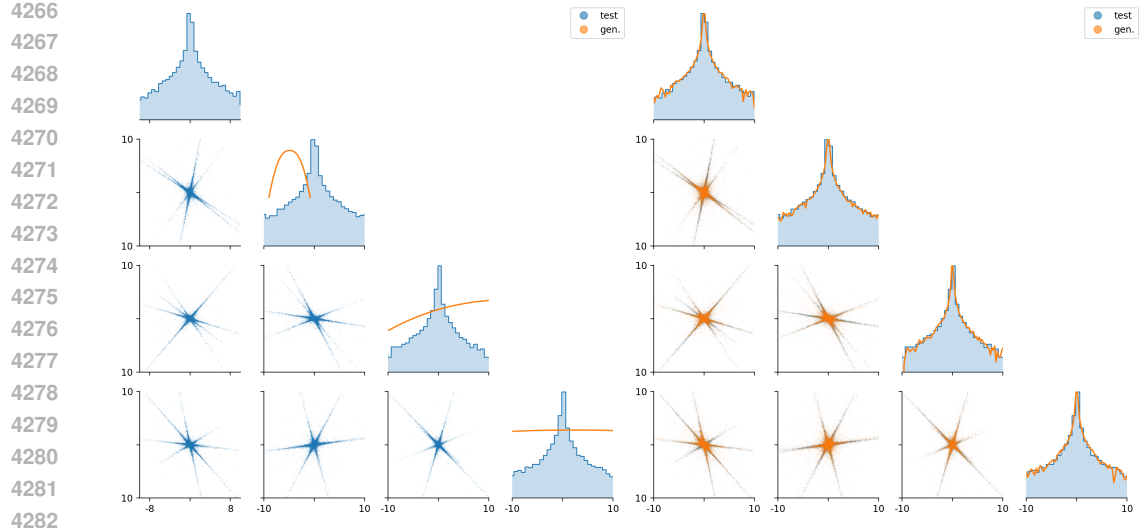


Figure 36: Pair plots of generated data (orange dots) compared to ground truth data (blue dots) with the SGM (left) and MSGM (right) with  $2^{24} = 16777216$  ADAMS iterations for a vector of 4 correlated Cauchy variables. On the diagonal, log-histogram of ground truth data (continuous blue line), and logarithm of the pdf KDE estimation of generated data (orange line) are superimposed.

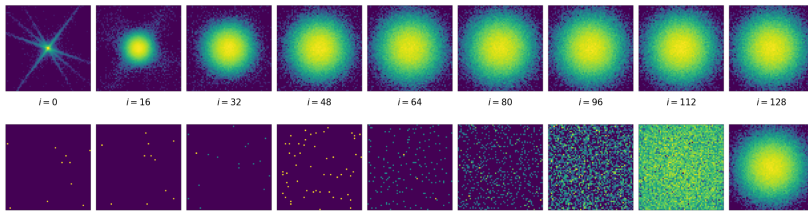


Figure 37: Evolution of the solution log-pdf  $\log(p_s(x_1, x_3))$  of SGM forward SDE (top) and backward SDE (bottom,  $2^{24} = 16777216$  ADAMS iterations and  $2^9 = 512$  time steps) for a vector of 4 correlated Cauchy variables, with default scheduling:  $\beta_m = 0.1$ ,  $\beta_M = 20$  and default neural network architecture.

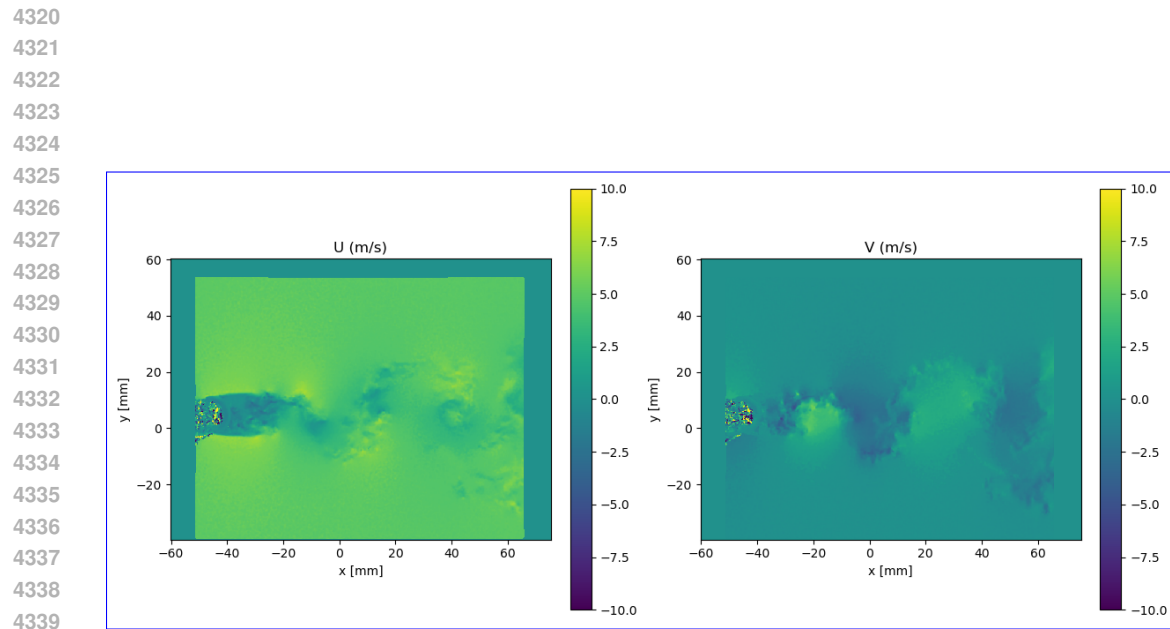
number of ADAMS iterations for MSGM in order to make the CPU training time of SGM and MSGM similar (see Appendix M.3 for details). For SGM with very large number of iterations ( $2^{24} = 16777216$ ), we use a larger number of time steps ( $2^9 = 512$ ) for the backward SDE to prevent all samples generated by SGM to diverge.

## M.7 VORTICITY FIELD FROM PARTICLE IMAGE VELOCIMETRY MEASUREMENTS

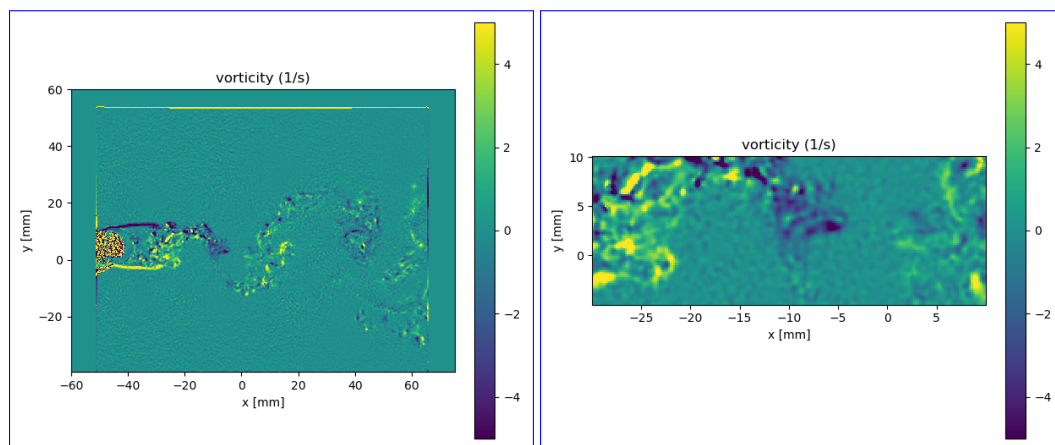
Particle Image Velocimetry (PIV) is an experimental technique to measure velocity fields in fluids by tracking the displacement of tracer particles between consecutive images illuminated with lasers (Adrian & Westerweel, 2011). We used two-dimensional, two-component (2D2C) PIV data of Figure 38, which provide both in-plane velocity components. Here PIV is not time-resolved, i.e. each velocity image is uncorrelated to the next. The flow observed is a benchmark configuration : a wake flow at Reynolds number  $Re = 3900$  created by a circular cylinder embedded in a mean stream (Parnaudeau et al., 2008). We compute the two-dimensional curl of the velocity. Named vorticity, it is presented in Figure 39.

### M.6.1 LOW-DIMENSIONAL TEST CASE: VORTICITY EVALUATED ON SEVERAL SPATIAL POINTS

To reduce the dimension  $d$  of the data, we severely crop the vorticity images and subsample them spatially, keeping only  $4 \times 4$  pixels by images as illustrated by Figure 40. Once reshaped as a vector,



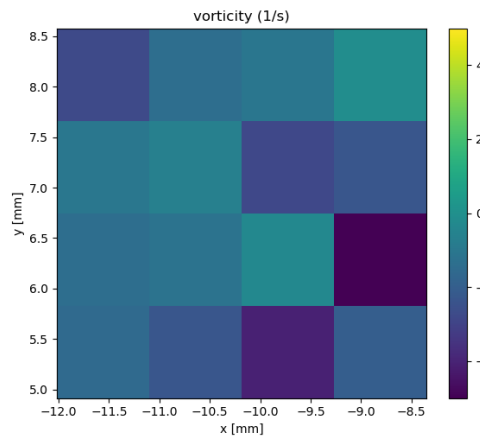
4341 Figure 38: 2D2C PIV velocity field: velocity component along  $x$  (left) and velocity component along  
 4342  $y$  (right).



4368 Figure 39: The full two-dimensional vorticity (left) and a zoom (right) of a PIV field  
 4369  
 4370  
 4371  
 4372  
 4373

Table 7: Low-dimensional vorticity test case: parameters of the nominal numerical experiments.

Parameter	SGM	MSGM
Dimension $d$	16	16
Number of used training data points ( $M$ )	$2^{10} = 1024$	1024
Number of test data points	6476	6476
Reference number of ADAMS steps	$2^{20}$	$2^{20}$
Number of ADAMS steps ( $N_{\text{iter}}$ )	$2^{20} = 1048576$	262144
CPU time / ADAMS steps (in ms)	4	32
Batch size	256	256
Number of time steps (forward) $N_T^f$	1	16
Number of time steps (backward) $N_T^b$	8	8
$\beta_{\min}$	0.025	0.025
$\beta_{\max}$	5	5
$t_{\epsilon}$	$10^{-4}$	$2.5 \times 10^{-5}$
Learning rate	$10^{-3}$	$10^{-3}$
Neural network architecture	default	spherical (equation L.33)
MD (MMD(train)= $0.9 \times 10^{-2}$ )	$1.5 \times 10^{-2}$	$1.3 \times 10^{-2}$

Figure 40: Spatial cropping and spatial subsampling of a vorticity field to obtain a data sample at low dimension  $d = 16$ .

each small image represents a data point of dimension 16. If we choose a dimension  $d \leq 16$ , we just keep the first  $d$  coefficients of the vector. For this experimental dataset, we investigate the influence of the amount of data available for learning. Our default experiments will train the models with  $2^{10} = 1024$  data points only.

As seen previously in Section 6.2, MSGM is more robust in low-data mode and better represents rare events, as also confirmed by the survival function Figure 41. We explain it by a latent distribution close to the data distribution as illustrated in Figure 42.

For a fair numerical comparison, we also test SGM with and without our neural network architecture based on spherical decomposition equation L.33 in Figures 43, 44, and 45. This architecture improves the quality of the generated samples. However, tails are still underestimated and some regions of the space remain clearly badly sampled. In contrast, MSGM samples fit well the data distribution both with dense and with sparse tensor,  $\mathbf{G}$ .

To complete the numerical study, we evaluated the MMD between generated samples and test samples for different values of the reference number of ADAMS iterations, different number of time steps to integrate the backward SDE, different dimension  $d$ , and different numbers of training data. The convergence plots are visible in Figures 46 and 47. Again, MMD may not be the best tool for studying

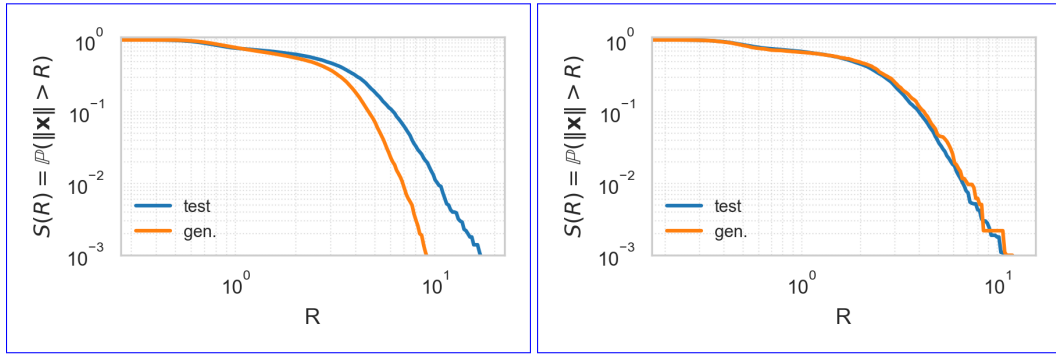


Figure 41: Survival function of generated data (orange line) compared to ground truth data (blue line) with the SGM (left) and MSGM (right) trained on 1024 16-dimensional data points representing PIV-based vorticity fields.

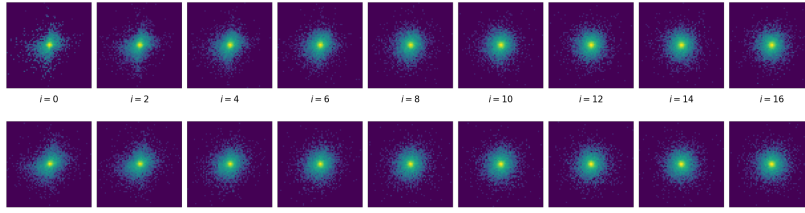


Figure 42: Evolution of the solution log-pdf  $\log(p_s(x_1, x_3))$  of MSGM forward SDE (top) and backward SDE (bottom) for the vorticity images distribution, with nominal scheduling ( $\beta_m = 0.025$ ,  $\beta_M = 5.0$ ) and our neural network architecture based on spherical decomposition equation L.33.

rare events. We can observe some tendencies, but definite conclusions may not be obtained from those convergence plots. For a very small training set ( $2^6 = 64$  data points), both SGM and MSGM fail and MMDs are similarly large. The biggest MMD gap between SGM and MSGM appears to be in the intermediate region:  $2^{10} = 1024$  data points. As expected, this gap seems to increase with dimension, even though this tendency is not fully clear for the plot. For small numbers of ADAMS iterations or small numbers of time steps, MSGM seems much better than SGM. This is expected since the MSGM latent space is already close to the data distribution. Without enough ADAMS iterations, neither the MSGM nor the SGM samples accurately mimic the data distribution, and in any case, it is better to let the optimization procedure run for a long enough time.

#### M.6.2 HIGH-DIMENSIONAL TEST CASE : VORTICITY IMAGE PROCESSING

To demonstrate that MSGM can address high-dimensional problems, we propose here an image generator based on the sparse local tensor of Appendix K.2.2 and the Unet detailed in Appendix L.4.2. From the original high-resolution PIV-based vorticity images of Figure 39, we crop, subsample at resolution  $64 \times 64$ , smooth and subsample again images them spatially, keeping  $32 \times 32$  pixels by images as illustrated by Figure 48. Once reshaped as a vector, each small image represents a data point of dimension 1024.

Figures 49 and 50 present generated images with MSGM and SGM respectively. Table 8 summarizes the parameters of our numerical experiment. The numerical evaluation of image generation skills of MSGM is beyond the scope of this paper and we postpone this study to future work.

## N SUMMARIZED COMPARISON OF MSGM AND SGM

This section is devoted to a brief comparison of these two concepts of generative modeling both from theoretical and empirical point of views.

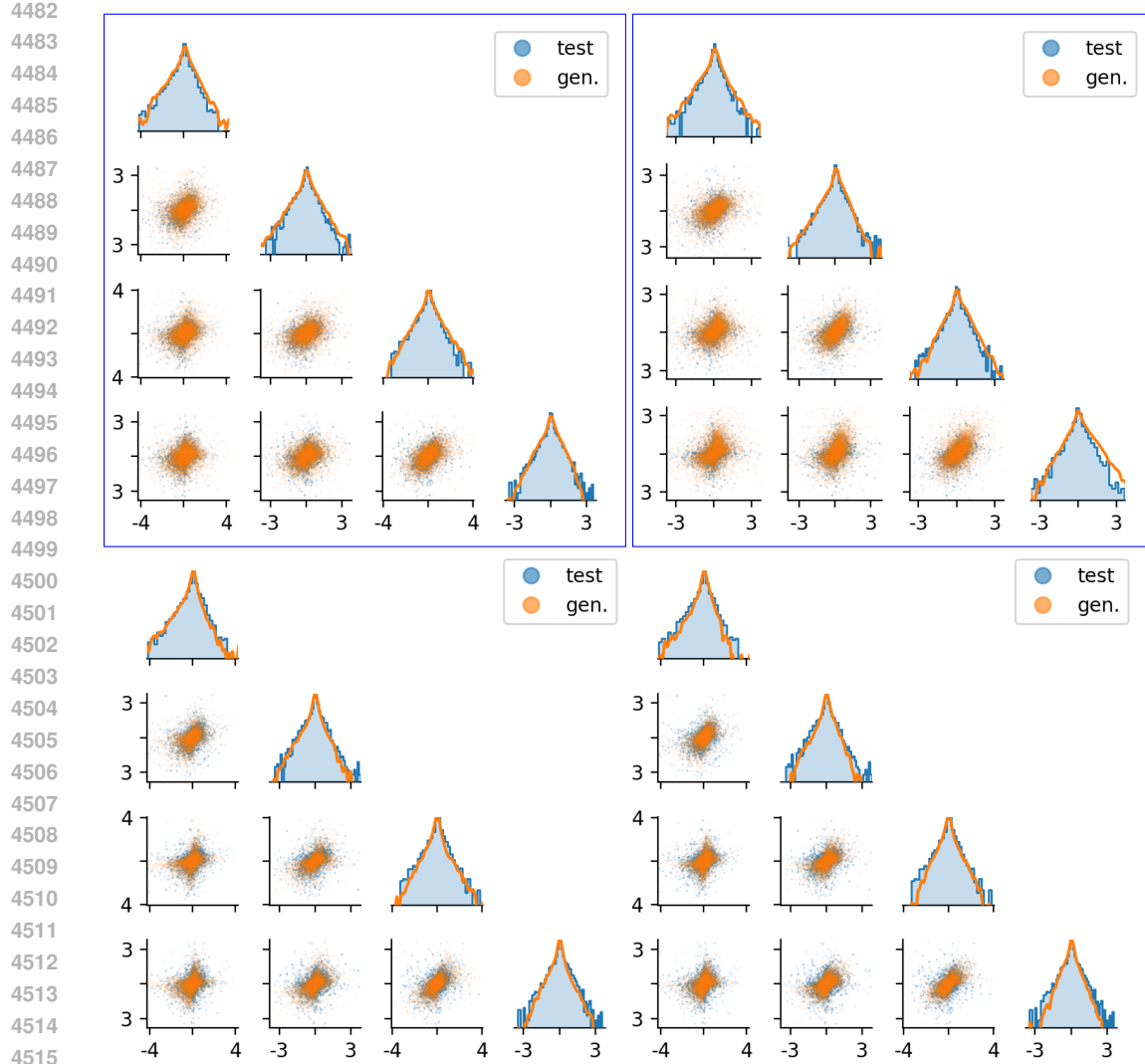


Figure 43: Pair plots of generated data (orange dots) compared to ground truth data (blue dots) with the MSGM with dense tensor  $\mathbf{G}$  (top left), sparse local tensor  $\mathbf{G}$  (top right), and SGM (bottom) trained on 1024 16-dimensional data points representing PIV-based vorticity fields. Left and top plots correspond to our neural network architecture based on spherical decomposition equation L.33 whereas the right bottom plot correspond to default neural network architecture. On the diagonal log-histogram of ground truth data (blue line) and logarithm of the pdf KDE estimation of generated data (orange line) are superimposed.

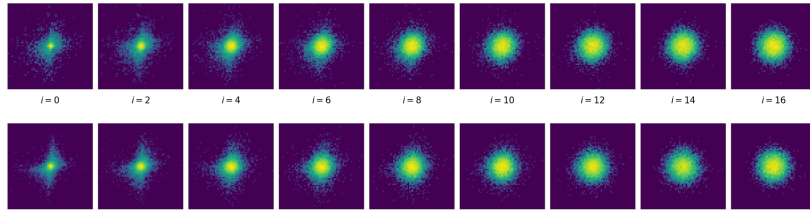


Figure 44: Evolution of the solution log-pdf  $\log(p_s(x_1, x_3))$  of SGM forward SDE (top) and backward SDE (bottom) for the vorticity images distribution, with nominal scheduling ( $\beta_m = 0.025$ ,  $\beta_M = 5.0$ ) and default neural network architecture.

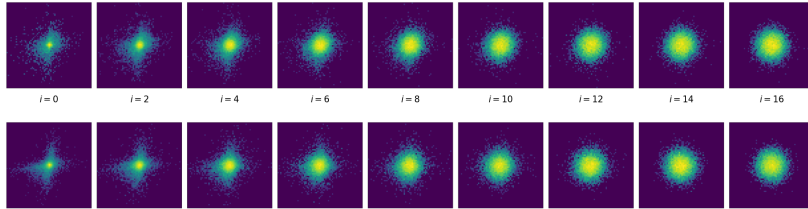


Figure 45: Evolution of the solution  $\log(p_s(x_1, x_3))$  of SGM forward SDE (top) and backward SDE (bottom) for the vorticity images distribution, with nominal scheduling ( $\beta_m = 0.025$ ,  $\beta_M = 5.0$ ) and our neural network architecture based on spherical decomposition equation L.33.

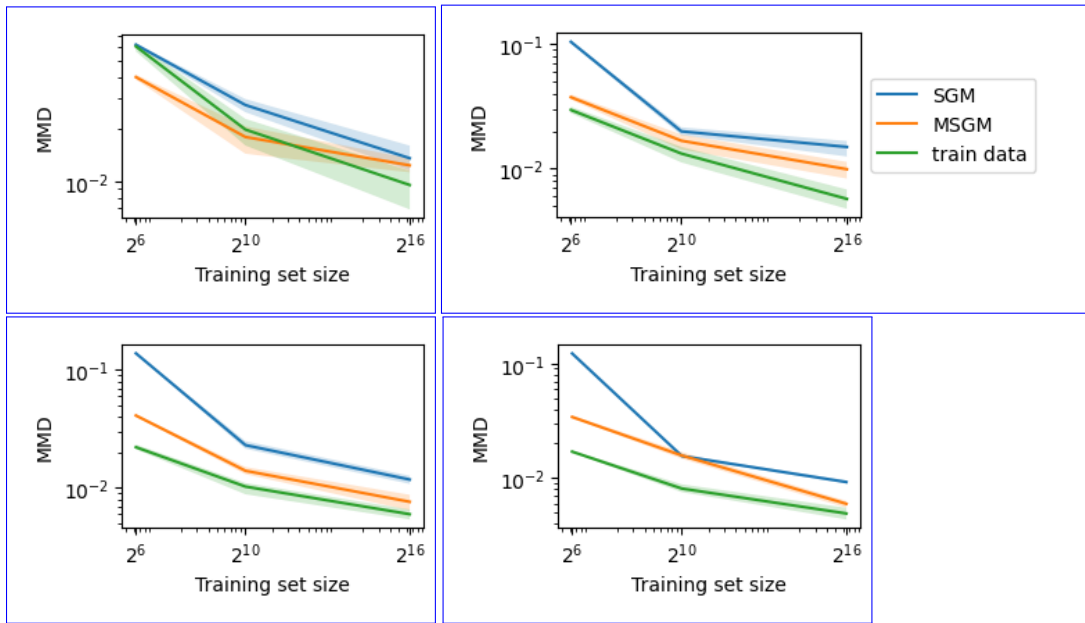
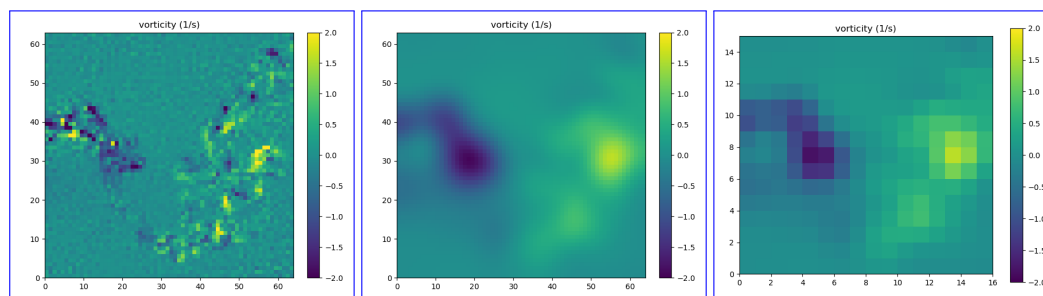
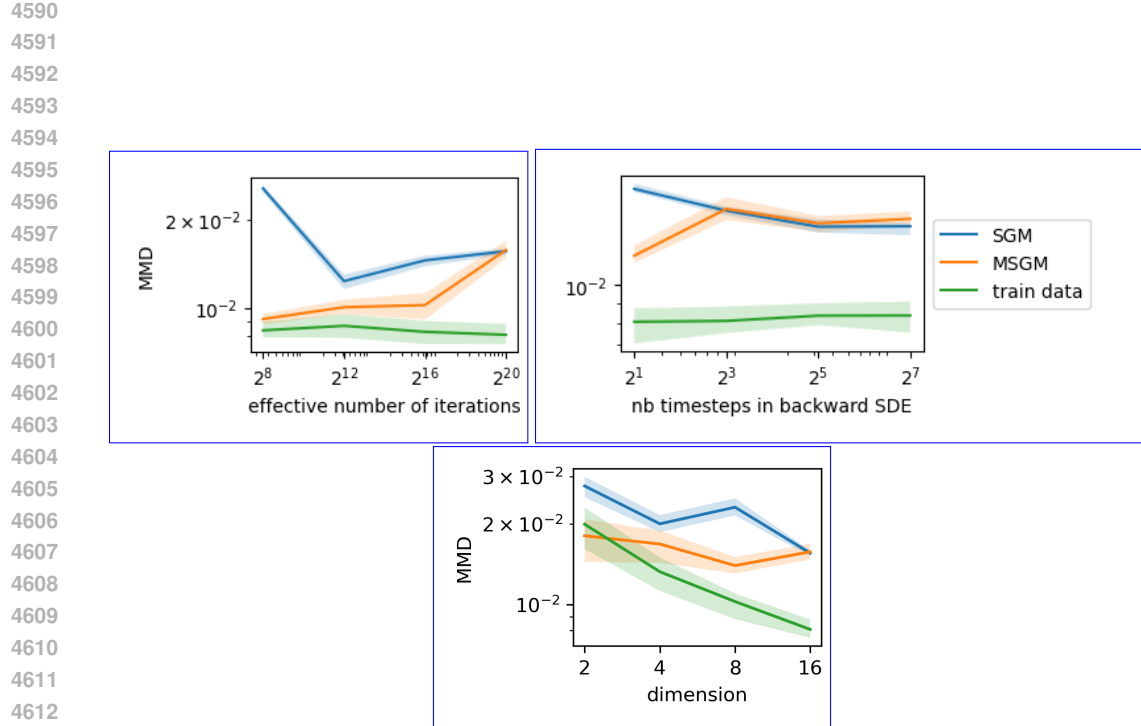


Figure 46: Convergence of MMD (mean and 80% confidence interval) for the vorticity images distribution as a function of number of training data for (from left to right and from top to bottom) dimension  $d = 2, 4, 8$ , and  $16$ .



4637 Figure 48: Spatial cropping and subsampling (left), spatial smoothing (middle), and spatial sub-  
4638 sampling again (right) of a vorticity field to obtain a data sample at lower but still high dimension  
4639  $d = 1024$ .

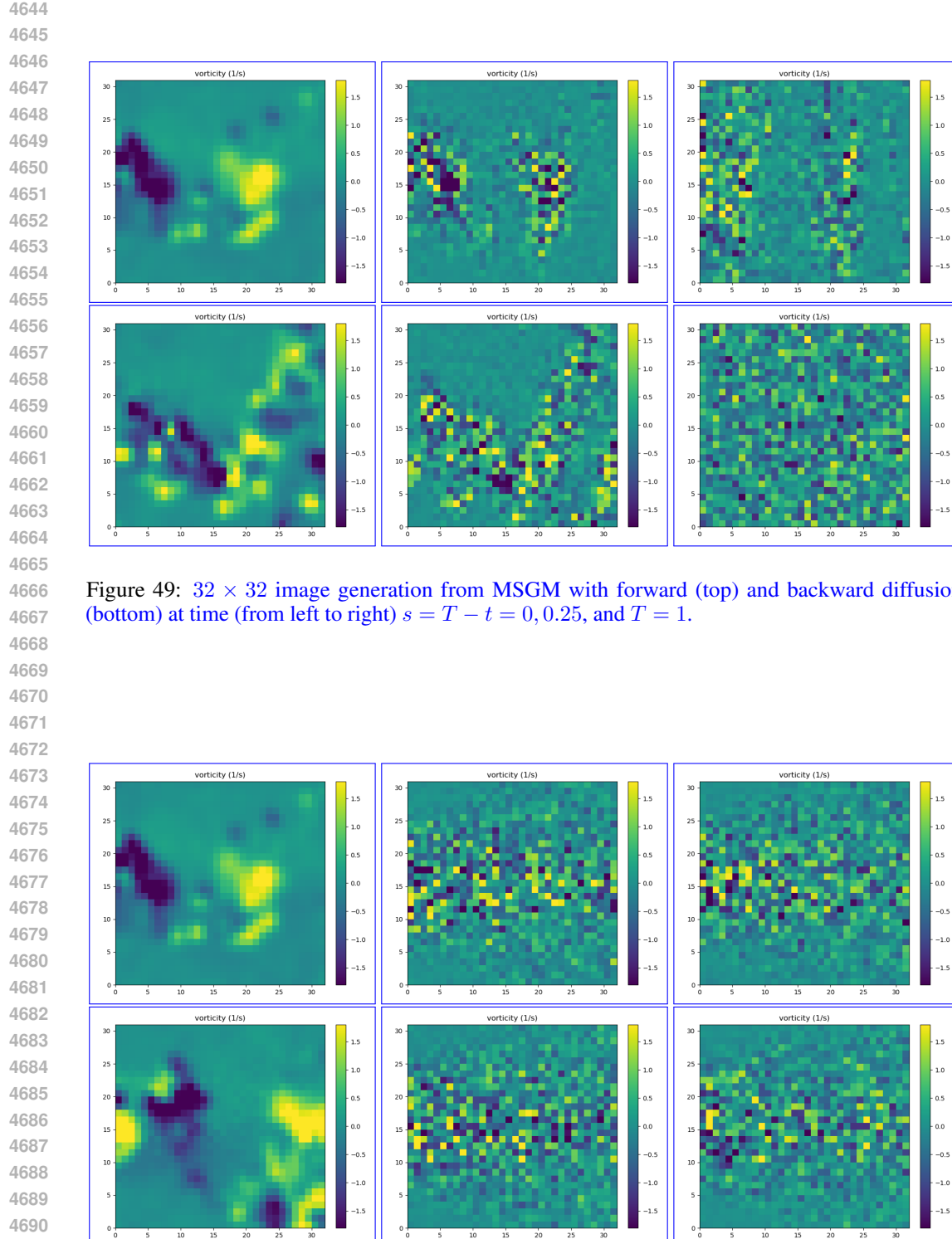


Figure 49:  $32 \times 32$  image generation from MSGM with forward (top) and backward diffusion (bottom) at time (from left to right)  $s = T - t = 0, 0.25$ , and  $T = 1$ .

Figure 50:  $32 \times 32$  image generation from SGM with forward (top) and backward diffusion (bottom) at time (from left to right)  $s = T - t = 0, 0.25$ , and  $T = 1$ . The apparent heteroskedasticity in the diffusion is due to the data normalization (pixel-wise variance is larger on top and bottom boundaries).

4698 Table 8: High-dimensional vorticity test case: parameters of the nominal numerical experiments.  
4699

4700 <b>Parameter</b>	4701 <b>SGM</b>	4702 <b>MSGM</b>
4703 Dimension $d$	4704 1024	4705 1024
4706 Number of used training data points ( $M$ )	4707 5000	4708 5000
4709 Number of test data points	4710 2500	4711 2500
4712 Reference number of ADAMS steps	4713 $10^5$	4714 $10^5$
4715 Number of ADAMS steps ( $N_{\text{iter}}$ )	4716 $10^5$	4717 $10^5$
4718 GPU time / ADAMS steps (in ms)	4719 410	4720 590
4721 Batch size	4722 128	4723 128
4724 Number of time steps (forward) $N_T^f$	4725 1	4726 128
4727 Number of time steps (backward) $N_T^b$	4728 2048	4729 2048
4730 $\beta_{\min}$	4731 0.8	4732 0.8
4733 $\beta_{\max}$	4734 160	4735 160
4736 $t_{\epsilon}$	4737 $8 \times 10^{-3}$	4738 $8 \times 10^{-3}$
4739 Learning rate	4740 $10^{-4}$	4741 $10^{-4}$
4742 Neural network architecture	4743 default	4744 spherical (equation L.33)
4745 MMD (MMD(train)= $1.4 \times 10^{-3}$ )	4746 $2.4 \times 10^{-3}$	4747 $3.2 \times 10^{-3}$

4718 Each strategy follows its own noising process, leading to different invariant distributions, i.e. Gaussian  
4719 for SGM and rotational invariant for MSGM. Both latent spaces are tractable, allowing for fast initial  
4720 sample generation for the reverse process. As a particular added on, the latent distribution of MSGM  
4721 allows for finite KL divergence when compared to heavy-tail distribution, e.g., as discussed and  
4722 motivated by Appendix E.6. From the convergence speed, both dynamics allow for exponential  
4723 convergence to the invariant distribution, assuming the rank condition A2 is satisfied for  $G$ . We will  
4724 conclude this section with a comparison discussion beyond the heavy tail case.

## 4725 N.1 THEORETICAL ASPECTS

4726 The latent space of MSGM is data aware, which ensures smaller KL-divergence of target distribution  
4727 and latent distribution compared to classical SGM, see Appendix E and Proposition E.5.1. The  
4728 method allows for inductive bias based on physics in the design of  $G$ . For example, in the context of  
4729 transport noise, making the noising/denoising process more physically relevant. This topic is part of  
4730 future work by the authors and is briefly discussed in Section 7. Moreover, the conservation of norm  
4731 in the denoising/backward process of MSGM serves as a stabilization tool, both for training and for  
4732 sampling stage. In particular, samples cannot diverge.

4733 At first glance, MSGM offers drawbacks compared to SGM. First, we have to rely on SSM and  
4734 cannot apply DSM since we do not have access to an analytic score solution of the noising process.  
4735 Second, we have to rely on numerical integration in the training because of no available analytic  
4736 solution; see also the empirical discussion N.2 below.

4737 When it comes to scalability, as  $d \rightarrow \infty$ , the current theoretical analysis is not yet complete. The  
4738 current analysis is built on the (strong) rank-condition which can be verified in the case of dense  
4739 tensors; see Appendix J. This is a limit in terms of scalability due to the  $d^3$  scaling of  $G$ . Here,  
4740 the sparse tensors discussed in Appendix K will serve as a solution when it comes to scalability.  
4741 However, in this context the rank condition has to be relaxed and new analysis is required as outlined  
4742 in Appendix K.1.1.

## 4743 N.2 EMPIRICAL ASPECTS

4744 SGM offers exact integration of the noising process, while MSGM relies on numerical integration.  
4745 Although this at first glance looks like a drawback in praxis, for most of our test cases, only a few  
4746 forward steps were needed in the training process, making the training traceable and comparable  
4747 to SGM training based on exact integration, while offering the same quality. For a more detailed  
4748 discussion, we refer to the *fair comparison* discussion in Appendix M.3. As our current experiments  
4749 suggest, MSGM requires less data in training. From approximation theory, learning the score reduces

4752 to training on a support that is the hyper-sphere in  $\mathbb{R}^d$ , with a conditioning variable  $\log \|\mathbf{x}\| \in \mathbb{R}$ .  
4753 In particular, the effective domain for learning a neuronal remains bounded in  $d$ . It may affect the  
4754 stability of the approximation using such an approximation class. Finally, the stabilization due to the  
4755 conservation of norm avoids divergence instabilities of SSM solvers for MSGM, when compared to  
4756 well known instabilities of SSM solvers for SGM.

4757

4758

4759

4760

4761

4762

4763

4764

4765

4766

4767

4768

4769

4770

4771

4772

4773

4774

4775

4776

4777

4778

4779

4780

4781

4782

4783

4784

4785

4786

4787

4788

4789

4790

4791

4792

4793

4794

4795

4796

4797

4798

4799

4800

4801

4802

4803

4804

4805